



**INSTITUTO POTOSINO DE INVESTIGACIÓN  
CIENTÍFICA Y TECNOLÓGICA, A.C.**

**POSGRADO EN CIENCIAS APLICADAS**

**Synthesis of nanocomposites from polyaniline,  
polypyrrole and carbon nanotubes, and unzipping of  
multi-walled carbon nanotubes for the obtention of  
new graphitic nanomaterials**

Tesis que presenta:

**Abraham Guadalupe Cano Márquez**

Para obtener el grado de:

**Doctor en Ciencias Aplicadas**

En la opción de:

**Nanociencias y Nanotecnología**

**Codirectores de la Tesis:**

**Dra. Yadira I. Vega Cantú**

**Dr. Fernando J. Rodríguez Macías**

**Dr. Mauricio Terrones Maldonado**

San Luis Potosí, S. L. P. Agosto de 2010

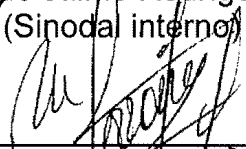


## Constancia de aprobación de la tesis

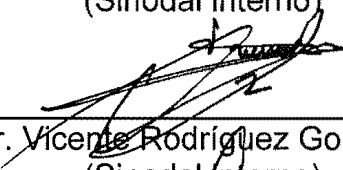
La tesis “**Synthesis of nanocomposites from polyaniline, polypyrrole and carbon nanotubes, and unzipping of multi-walled carbon nanotubes for the obtention of new graphitic nanomaterials**” presentada para obtener el grado de doctor en ciencias aplicadas en la opción de Nanociencias y Nanotecnología fue elaborada por **Abraham Guadalupe Cano Márquez** y aprobada el **27 de agosto de 2010** por los suscritos, designados por el Colegio de Profesores de la División de Materiales Avanzados del Instituto Potosino de Investigación Científica y Tecnológica, A.C.

  
 Dra. Yadira Itzel Vega Cantú  
 (Sinodal interno)

  
 Dr. Fernando Jaime Rodríguez Macías  
 (Sinodal interno)

  
 Dr. Mauricio Terrones Maldonado  
 (Sinodal interno hasta el 18 de diciembre de 2009 y externo a partir de esa fecha)

  
 Dr. Vladimir Alonso Escobar Barrios  
 (Sinodal interno)

  
 Dr. Vicente Rodríguez González  
 (Sinodal interno)

  
 Dra. Alma Gabriela Palestino Escobedo  
 (Sinodal externo)

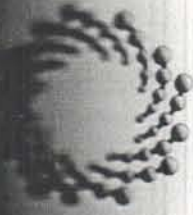


## **Créditos Institucionales**

Esta tesis fue elaborada en los Laboratorios de Polímeros y Nanoestructuras de la División de Materiales Avanzados del Instituto Potosino de Investigación Científica y Tecnológica, A.C., bajo la co-dirección de los doctores Yadira I. Vega Cantú, Fernando J. Rodríguez Macías y Mauricio Terrones Maldonado.

Durante la realización del trabajo el autor recibió una beca académica del Consejo Nacional de Ciencia y Tecnología 105490 y del Instituto Potosino de Investigación Científica y Tecnológica, A. C.

Adicionalmente, este trabajo se realizó con apoyo de los proyectos SEP-47338 (Y.I.V.C.), SEP-47337 (F.J.R.M.), 586787 (Laboratorio para la Investigación de Nanociencia y Nanotecnología - LINAN), 45772 (M.T.), 58899 – Colaboración Interamericana de Materiales (M.T.), 2004-01-013/ SALUD-CONACYT (M.T.), Fondo Mixto de San Luis Potosí 63001 S-3908 (M.T.) y Fuerzas Aéreas Polymer Composites S-3919 (M.T./Y.I.V.C.).



INSTITUTO POTOSINO DE INVESTIGACIÓN CIENTÍFICA Y TECNOLÓGICA, A.C.

IPICYT

1053

Sustentante:

ABRAHAM

GUADALUPE

CANO MARQUEZ



*Signature*

Firma

# Acta de Examen de Grado

En la ciudad de San Luis Potosí, a los 27 días, del mes de AGOSTO del año 2010, se reunió a las 17:00 horas, en las instalaciones del Instituto Potosino de Investigación Científica y Tecnológica, A.C., el Jurado integrado por:

|  |                   |
|--|-------------------|
| <u>DRA. ALMA GABRIELA PALESTINO ESCOBEDO</u> | <u>PRESIDENTE</u> |
| <u>DRA. YADIRA ITZEL VEGA CANTU</u>          | <u>SECRETARIA</u> |
| <u>DR. FERNANDO JAIME RODRIGUEZ MACIAS</u>   | <u>SINODAL</u>    |
| <u>DR. VICENTE RODRIGUEZ GONZALEZ</u>        | <u>SINODAL</u>    |
| <u>DR. VLADIMIR ALONSO ESCOBAR BARRIOS</u>   | <u>SINODAL</u>    |

a fin de efectuar el examen, que para obtener el Grado de Doctor (a) en Ciencias Aplicadas en la opción de Nanociencias y Nanotecnología, sustentó el (la)

C. ABRAHAM GUADALUPE CANO MARQUEZ

sobre la Tesis intitulada: SYNTHESIS OF NANOCOMPOSITES FROM POLYANILINE, POLYPYRROLE AND CARBON NANOTUBES AND UNZIPPING OF MULTI-WALLED CARBON NANOTUBES FOR THE OBTENTION OF NEW GRAPHITIC NANOMATERIALS

que se desarrolló bajo la dirección de: DRA. YADIRA VEGA CANTU, DR. FERNANDO JAIME RODRIGUEZ MACIAS, DR. MAURICIO TERRONES MALDONADO HASTA EL 17 DE DICIEMBRE DE 2009. El Jurado, después de deliberar, determinó: BAJO SU DIRECCION EXTERNA A PARTIR DEL 18 DE DICIEMBRE DE 2009  
APROBADO

Dándose por terminado el acto a las 20:00 horas, procediendo a la firma del Acta los integrantes del Jurado. Dando fé el Secretario Académico del Instituto.

*Signature*  
Presidente

*Signature*  
Secretario

*Signature*  
Sinodal

*Signature*  
Sinodal

*Signature*  
Sinodal



“If Science is great, how Great shall the Creator be!”

– A.G.C.M.

“To boldly go where no man has gone before...”

From the original TV series *Star Trek*

## Acknowledgements

I would like to thank:

God, for this life opportunity for walking through new paths in search of an answer to unknown phenomena, and that has opened new ones.

To my advisors, Dr. Yadira I. Vega, Dr. Fernando J. Rodríguez and Dr. Mauricio Terrones for their patience, discipline, vision, and example of how scientific research must be properly done. I also thank Dr. Emilio Muñoz and Dr. Florentino López for their valuable comments and guidance during thesis writing. I have learned a lot from them, and improved and developed new skills as a scientist and as a person. In addition, I would like to mention that this thesis was co-directed by Dr. Mauricio Terrones; nonetheless, due to political affairs, the IPICYT has refused to officially credit him.

Thanks to technicians M. Sc. Grisel Ramírez, Eng. Daniel Ramírez, Dr. Hugo Martínez, and Dr. Ferdinando Tristán for their valuable aid and training in both laboratory work and characterization. Thanks to Gabriela Pérez, Víctor Mata, and Karla Gómez for the logistics. To all my professors, teachers, friends and colleagues that in a way or another have helped me, and/or from which I have taken good counsel and/or attitudes. To CONACYT, IPICYT, and Mexico for their economic support to this doctoral research through CONACYT scholarship 105490.

To my parents, Abraham Cano and Diana Márquez for bringing me to life, for their guidance, comprehension, love, and for their unconditional support during all these years. I give special thanks to my beloved wife Elizabeth Serrano, to my children Eliakim Sebastián and Santiago, and to my brother Emmanuel, for their understanding and time, and for being my reason to follow this quest. This thesis is for you.

To John Ronald Reuel Tolkien (1892 – 1973) and Peter Jackson (1961 – ), for all those moments in which one can immerse in a distant world, from which humankind (including a part of the scientific community) has fled away in the search for goods, pleasure, power, and ravage to the environment, forgetting about looking for Truth and Life.

# Contents

|   |              |
|---|--------------|
| <b>Acknowledgements</b> .....   | <b>xi</b>    |
| <b>Contents</b> .....   | <b>xiii</b>  |
| <b>List of Figures</b> .....  | <b>xix</b>   |
| <b>List of Tables</b> .....   | <b>xxiii</b> |
| <b>List of Abbreviations</b> .....                                      | <b>xxv</b>   |
| <b>Resumen</b> .....  | <b>xxvii</b> |
| <b>Abstract</b> .....   | <b>xxix</b>  |
| <br>  |              |
| <b>Chapter 1. Introduction</b> .....                                    | <b>1</b>     |
| 1.1 Carbon Nanotubes.....   | 2            |
| 1.2 Doping of carbon nanotubes .....                                    | 6            |
| 1.3 Synthesis of carbon nanotubes: chemical vapor deposition (CVD)..... | 7            |
| 1.3.1 Growth mechanism of CVD carbon nanotubes.....                     | 9            |
| 1.4 Some properties of carbon nanotubes.....                            | 11           |
| 1.4.1 Conductivity .....  | 11           |
| 1.4.2 Infrared and Raman active modes.....                              | 11           |
| 1.5 Nanocomposites from carbon nanotubes .....                          | 13           |
| 1.6 Novel carbon materials: graphene and graphene ribbons .....         | 16           |
| 1.6.1 Importance of edges .....   | 16           |
| 1.6.2 Applications of graphene and ribbons.....                         | 18           |
| References .....  | 21           |

|  |           |
|--|-----------|
| <b>Chapter 2. Nanocomposites from polyaniline (PAni), polypyrrole (PPy), and multi-walled carbon nanotubes (MWNTs)</b> .....                             | <b>29</b> |
| 2.1 Introduction .....   | 29        |
| 2.2 Polyaniline (PAni), polypyrrole (PPy), and their composites with multi-walled carbon nanotubes (MWNTs) .....   | 33        |
| 2.2.1 Properties of electronically conducting polymers: PAni and PPy .....   | 33        |
| 2.2.2 Nanocomposites from carbon nanotubes (CNTs), PAni, and PPy .....   | 35        |
| 2.2.3 Synthesis methods for nanocomposites derived from CNTs, PAni and PPy .....   | 37        |
| 2.2.4 Nanocomposites from PAni, PPy, and MWNTs synthesized by the nanotube salts method.....   | 38        |
| 2.3 Experimental procedure for the synthesis of composites from polyanilines (PAnis), polypyrrole (PPy), and multi-walled carbon nanotubes (MWNTs) ..... | 41        |
| 2.3.1 Materials.....   | 41        |
| 2.3.2 Synthesis of nanocomposites.....   | 41        |
| 2.4 Results and discussion.....  | 43        |
| 2.4.1 Morphology of nanocomposites from MWNTs and sulfonated PAni .....  | 43        |
| 2.4.2 Morphology of nanocomposites from MWNTs and PAni.....  | 46        |
| 2.4.3 Morphology of nanocomposites from CN <sub>x</sub> and PPy .....  | 49        |
| 2.4.4 Spectroscopic studies on MWNT/PAni nanocomposites.....   | 51        |
| <i>Raman spectroscopy</i> .....  | 51        |
| <i>Fourier-Transform Infrared spectroscopy</i> .....   | 53        |
| 2.4.3 X-Ray powder diffraction of MWNTs/PAni nanocomposites.....   | 55        |
| 2.5 Conclusions.....   | 56        |
| References.....  | 59        |

|   |           |
|---|-----------|
| <b>Chapter 3. Nanoribbons and graphene generation from exfoliation of MWNTs.....</b>                          | <b>65</b> |
| 3.1 Introduction .....  | 65        |
| 3.1.1 Production methods for graphene and graphene ribbons.....   | 67        |
| 3.1.2 Graphene nanoribbons from multi-walled carbon nanotubes: the<br>nanotubes salt method .....             | 75        |
| 3.2 Experimental procedure for the synthesis of exfoliated multi-walled carbon<br>nanotubes (ex-MWNTs).....   | 78        |
| 3.2.1 Materials .....   | 78        |
| 3.2.2 Nanoribbons and graphene generation from lithium-ammonia intercalation<br>and exfoliation in MWNTs..... | 78        |
| 3.3 Results and discussion .....  | 81        |
| 3.3.1 Morphology .....  | 81        |
| <i>Electron Microscopy techniques</i> .....   | 81        |
| <i>Atomic Force Microscopy</i> .....  | 89        |
| 3.3.2 Spectroscopic studies on ex-MWNTs .....   | 92        |
| <i>Raman spectroscopy</i> .....   | 92        |
| <i>Fourier-Transform Infrared spectroscopy</i> .....  | 95        |
| 3.3.3 X-Ray powder diffraction .....  | 97        |
| 3.3.4 Reactivity of carbon structures towards oxidation. Thermogravimetric<br>analysis.....                   | 99        |
| 3.4 Mechanism for unzipping of MWNTs .....  | 101       |
| 3.5 Other methods for obtention of GNRs from CNTs .....   | 103       |
| 3.6 Other layered carbon materials.....   | 105       |
| 3.6.1 Morphology .....  | 105       |
| 3.6.2 Raman spectroscopy .....  | 107       |

|  |            |
|--|------------|
| 3.7 Conclusions.....   | 109        |
| References.....  | 111        |
| <b>Chapter 4. Conclusions, perspectives, and future work .....</b> | <b>117</b> |
| 4.1 Conclusions.....   | 117        |
| 4.2 Perspectives and future work.....                              | 119        |
| <b>Appendices .....</b>  | <b>123</b> |
| <b>A.1 Properties and synthesis of carbon nanotubes.....</b>       | <b>125</b> |
| A.1.1 Summary of properties .....                                  | 125        |
| A.1.2 Other synthesis methods for carbon nanotubes .....           | 127        |
| References.....  | 135        |
| <b>A.2 Graphite intercalation compounds (GICs).....</b>            | <b>137</b> |
| A.2.1 Introduction .....   | 137        |
| A.2.2 Ternary and higher order GICs .....                          | 140        |
| A.2.3 The intercalation of ammonia.....                            | 141        |
| A.2.4 Characterization techniques for GICs .....                   | 142        |
| References.....  | 145        |
| <b>A.3 Experimental conditions and exfoliation data .....</b>      | <b>149</b> |
| <b>A.4 Characterization techniques.....</b>                        | <b>163</b> |
| A.4.1 Scanning Electron Microscopy.....                            | 163        |
| A.4.2 Transmission Electron Microscopy .....                       | 165        |
| A.4.3 Atomic Force Microscopy.....                                 | 166        |

|  |     |
|--|-----|
| A.4.4 Raman Spectroscopy .....         | 168 |
| A.4.5 Thermogravimetric Analysis ..... | 170 |
| A.4.6 X-Ray Powder Diffraction .....   | 172 |
| References .....                       | 177 |



## List of Figures

|   |    |
|---|----|
| 1.1. Unrolled honeycomb lattice of a carbon nanotube .....                                    | 3  |
| 1.2. Unit cell and Brillouin zone of 2D graphite .....  | 3  |
| 1.3. Examples of carbon nanotubes .....   | 4  |
| 1.4. TEM micrographs of MWNTs with different number of layers .....                           | 5  |
| 1.5. HRTEM images of MWNTs .....  | 6  |
| 1.6. Experimental setup for CVD growth of MWNTs .....   | 7  |
| 1.7. MWNT synthesized by a CVD process.....   | 8  |
| 1.8. Growth mechanisms for carbon nanotubes by pyrolysis of organic precursors.....           | 10 |
| 1.9. Raman spectra of single-walled carbon nanotubes.....                                     | 12 |
| 1.10. Schematic representation of carbon nanoribbons .....                                    | 17 |
| 1.11. Unit cells and edge vectors of carbon nanoribbons.....                                  | 17 |
|   |    |
| 2.1. Detrimental effects observed in carbon nanotube-polymer composites .....                 | 31 |
| 2.2. Conductivity of emeraldine base as a function of the pH.....                             | 33 |
| 2.3. Conductivity comparison between electronic polymers and other materials.....             | 34 |
| 2.4. Main oxidation states of PANi .....  | 35 |
| 2.5. Raman spectra and X-ray diffraction patterns for MWNTs, PANi, and their composites ..... | 37 |
| 2.6. Scheme for nanotube-lithium salt formation in liquid ammonia .....                       | 39 |
| 2.7. Functionalization pathways for carbon nanotubes by the nanotube salts method...          | 40 |
| 2.8. Experimental setup for the synthesis of nanocomposites.....                              | 42 |
| 2.9. SEM images of MWNTs, and MWNTs/PoASA nanocomposites.....                                 | 44 |
| 2.10. SEM images of MWNT/PoASA nanocomposites .....   | 45 |
| 2.11. SEM images of MWNT/PAni nanocomposites .....  | 46 |
| 2.12. SEM images of MWNT/PAni nanocomposites .....  | 47 |
| 2.13. SEM images of a nanocomposite from nitrogen-doped MWNTs (CN <sub>x</sub> ) and PPy...50 |    |
| 2.14. SEM and STEM images of composites from CN <sub>x</sub> , PoASA, PANi, and PPy .....     | 50 |
| 2.15. Raman spectra of MWNTs and MWNTs/PAni nanocomposites.....                               | 52 |
| 2.16. FT-IR spectra for MWNTs and MWNTs/PAni nanocomposites .....                             | 54 |

|  |     |
|--|-----|
| 2.17. Diffraction patterns for MWNTs and MWNTs/PAni nanocomposites .....                                       | 55  |
| 3.1. Crystallographic structure of graphene .....  | 66  |
| 3.2. A graphene flake and a graphene-based FET device.....   | 67  |
| 3.3. Comparison of the G' Raman feature for graphite and graphene .....  | 68  |
| 3.4. STM images of epitaxial graphene on SiC(0001) .....   | 70  |
| 3.5. Raman spectra of CVD-grown graphene films on Ni/SiO <sub>2</sub> /Si.....                                 | 71  |
| 3.6. CVD-grown graphene nanoribbons.....   | 72  |
| 3.7. Multilayered, graphitic carbon nanoribbons from coalesced SWNTs .....                                     | 72  |
| 3.8. Suzuki-Miyaura coupling leading to carbon nanoribbons.....  | 73  |
| 3.9. SEM/STEM images of exfoliated MWNTs after washing MWNTs/PAni and MWNTs/PPy nanocomposites with acids..... | 76  |
| 3.10. TEM images of exfoliated MWNTs.....  | 76  |
| 3.11. Partial exfoliation and breakage in MWNTs and CN <sub>x</sub> .....                                      | 77  |
| 3.12. Experimental setup for lithium-ammonia intercalation in MWNTs.....                                       | 79  |
| 3.13. Exfoliation of lithium-intercalated MWNTs .....  | 80  |
| 3.14. STEM micrographs after lithium intercalation and exfoliation in MWNTs.....                               | 81  |
| 3.15. STEM micrographs of partially unwrapped MWNTs .....  | 83  |
| 3.16. TEM images of partially exfoliated MWNTs .....   | 84  |
| 3.17. Interlayer distances in a MWNT after Li intercalation and acid treatment .....                           | 84  |
| 3.18. STEM micrographs after lithium intercalation and exfoliation in MWNTs.....                               | 85  |
| 3.19. Cut MWNTs after exposing to liquid NH <sub>3</sub> without lithium .....                                 | 86  |
| 3.20. Width distribution for MWNTs .....   | 87  |
| 3.21. TEM images of exfoliated MWNTs.....  | 88  |
| 3.22. AFM images of an ex-MWNT and graphitic platelets over HOPG .....   | 90  |
| 3.23. Profile analysis of the surface of an ex-MWNT .....  | 91  |
| 3.24. Phase comparison of graphitic materials by AFM.....  | 92  |
| 3.25. Raman spectra for different types of MWNTs .....   | 94  |
| 3.26. FT-IR spectra for different types of MWNTs .....   | 96  |
| 3.27. Diffraction patterns for different types of MWNTs .....  | 98  |
| 3.28. Thermogravimetric measurements on MWNTs .....  | 100 |

|  |     |
|--|-----|
| 3.29. Intercalation mechanism in MWNTs and their exfoliation .....   | 102 |
| 3.30. SEM/TEM micrographs of non-intercalated pristine graphene nanoribbons.....   | 105 |
| 3.31. SEM/STEM micrographs of graphene nanoribbons after Li intercalation and thermal treatments .....                       | 106 |
| 3.32. Raman spectra of MWNTs and GNRs.....   | 107 |
|  |     |
| A.1.1. Cross-sectional view of a carbon arc generator .....  | 127 |
| A.1.2. TEM micrograph of an arc-grown MWNT.....  | 128 |
| A.1.3. Experimental setup for production of carbon nanotubes by laser ablation.....  | 129 |
| A.1.4. Fullerene branching paths.....  | 130 |
| A.1.5. TEM images of laser-ablation-grown MWNTs.....   | 130 |
| A.1.6. Schematic of a solar reactor for synthesis of carbon nanotubes.....   | 132 |
| A.1.7. Carbon nanotubes synthesized by solar energy .....  | 132 |
| A.1.8. MWNTs grown on lava.....  | 133 |
|  |     |
| A.2.1. Lithium intercalation in graphite .....   | 139 |
| A.2.2. Proposed schematic for $\text{Cs}(\text{THF})_{1.2}\text{C}_{24}$ and $\text{K}(\text{THF})_{2.5}\text{C}_{24}$ ..... | 141 |
|  |     |
| A.4.1. Schematic ray path for a scanning electron microscope (SEM).....  | 163 |
| A.4.2. Schematic ray path for a transmission electron microscope (TEM) .....   | 165 |
| A.4.3. Block diagram of a laser deflection contact AFM .....   | 167 |
| A.4.4. Jablonski energy diagram for Raman scattering.....  | 168 |
| A.4.5. Experimental setup of a micro-Raman spectrometer .....  | 169 |
| A.4.6. Schematic of a thermobalance.....   | 170 |
| A.4.7. Comparison of TGA and DTG curves .....  | 171 |
| A.4.8. X-ray diffraction by a crystal.....   | 173 |
| A.4.9. Formation of a diffracted cone of radiation in the powder method .....  | 174 |
| A.4.10. An X-ray spectrometer .....  | 175 |



## List of Tables

|  |     |
|--|-----|
| 1.1 Number and symmetries of Raman and IR-active modes for different types of carbon nanotubes.....    | 11  |
| 2.1 Conductivity for MWNTs/polyaniline nanocomposites.....   | 48  |
| 2.2 D and G Raman peak positions and relative intensities for MWNTs and MWNTs/PAni nanocomposites..... | 52  |
| 3.1 Characteristic Raman bands and shifts for different types of MWNTs .....                           | 93  |
| 3.2 Interplanar distance, crystallite size, and relative (002) intensities for MWNTs.....              | 99  |
| 3.3. Characteristic Raman bands and shifts for MWNTs and CNRs .....                                    | 108 |
| A.1 Most significant properties of carbon nanotubes and related materials .....                        | 125 |
| A.3.1 Experimental conditions for composites.....  | 151 |
| A.3.2 Experimental conditions for exfoliation of MWNTs.....  | 154 |
| A.3.3 Exfoliation data for selected experiments.....   | 161 |



## List of Abbreviations

|                 |   |
|-----------------|---|
| AFM             | Atomic force microscopy                               |
| Ani             | Aniline   |
| ARPES           | Angle-resolved photoemission spectroscopy             |
| ATR             | Attenuated total reflectance                          |
| ATRP            | Atomic-transfer radical polymerization                |
| BSE             | Backscattered electrons                               |
| CCD             | Charge-coupled diode                                  |
| CNRs            | Carbon nanoribbons                                    |
| CNTs            | Carbon nanotubes                                      |
| CN <sub>x</sub> | Nitrogen-doped multi-walled carbon nanotubes          |
| CRT             | Cathode-ray tube                                      |
| CVD             | Chemical vapor deposition                             |
| DR              | Double resonance                                      |
| DSC             | Differential scanning thermogravimetry                |
| DTA             | Differential thermal analysis                         |
| DTBP            | 4,4'-di- <i>tert</i> -butyl-biphenyl                  |
| DTG             | Differential or derivative thermogravimetry           |
| DMSO            | Dimethyl sulfoxide                                    |
| ECPs            | Electronically (or electrically) conducting polymers  |
| EG              | Epitaxially grown graphene                            |
| EGA             | Evolved gas analysis                                  |
| EMI             | Electromagnetic interference                          |
| Ex-MWNTs        | Exfoliated or unzipped MWNTs, also called nanoribbons |
| FET             | Field-effect transistor                               |
| FT-IR           | Fourier transform infrared spectroscopy               |
| FWHM            | Full-width at half maximum                            |
| GICs            | Graphite intercalation compounds                      |
| GNRs            | Graphene or graphitic nanoribbons, a type of CNRs     |

|        |  |
|--------|--|
| GOX    | Graphene oxide   |
| HOPG   | Highly oriented pyrolytic graphite   |
| HRTEM  | High resolution TEM  |
| ICDD   | International Centre for Diffraction Data  |
| MWNTs  | Multi-walled carbon nanotubes  |
| NMF    | N-methylformamide  |
| NMRP   | Nitroxide-mediated radical polymerization  |
| oASA   | <i>ortho</i> -aminobenzenesulfonic acid  |
| PAni   | Polyaniline  |
| PMMA   | Poly(methyl methacrylate)  |
| PoASA  | Poly(2-aminobenzene sulfonic acid) or poly( <i>ortho</i> -anilic acid), an SPAni |
| PPy    | Polypyrrole  |
| PS     | Polystyrene  |
| PTFE   | Polytetrafluoroethylene  |
| RBM    | Radial breathing modes   |
| RMS    | Root-mean-square   |
| ROMP   | Ring-opening metathesis polymerization   |
| ROP    | Ring-opening-polymerization  |
| SE     | Secondary electrons  |
| SEM    | Scanning electron microscopy   |
| SPAni  | Sulfonated polyaniline, for example, PoASA                                       |
| STEM   | Scanning transmission electron microscopy  |
| STM    | Scanning tunneling microscopy  |
| SWNTs  | Single-walled carbon nanotubes   |
| TEM    | Transmission electron microscopy   |
| TGA    | Thermogravimetric analysis   |
| THF    | Tetrahydrofuran  |
| UHV    | Ultra-high-vacuum  |
| UV-Vis | Ultraviolet-visible spectroscopy   |
| XPS    | X-ray photoelectron spectroscopy   |
| XRD    | X-ray diffraction  |

## Resumen

La síntesis de compositos a partir de nanotubos de carbono ha tenido como principal reto el lograr una buena dispersión de los primeros en la matriz polimérica y para ello se han utilizado diversos métodos de funcionalización. Así mismo, se busca obtener una buena interacción entre ambos componentes y que el composito resultante se beneficie de las propiedades presentes en los materiales de partida.

En este contexto, en la presente tesis presentamos los principales resultados concernientes a la síntesis de compositos a partir de nanotubos de carbono multicapa (MWNTs), MWNTs dopados con nitrógeno ( $CN_x$ ) y de polímeros conductores electrónicos, específicamente de polianilina (PAni), polianilina sulfonada (SPAni) y polipirrol (PPy). Dicho estudio surge a partir de nuestro interés en combinar las propiedades únicas de cada componente y así obtener nuevos materiales con propiedades electrónicas y mecánicas mejoradas. Por primera vez en el ámbito científico, sintetizamos estos compositos mediante la polimerización *in situ* de los monómeros correspondientes mediante un método de alquilación reductiva en amoníaco líquido, al cual se denomina *sales de nanotubos*, y que ha sido ampliamente utilizado para la funcionalización de fullerenos, nanotubos de una (SWNTs) y de varias capas (MWNTs). En este método se disuelve litio metálico en amoníaco líquido, al que se agregan los nanotubos de carbono formando entonces una sal de nanotubos.

Durante la síntesis de compositos encontramos que, ocasionalmente, tanto MWNTs como  $CN_x$  se exfoliaban en los extremos o en segmentos. Decidimos entonces seguir esta línea de investigación, logrando exitosamente la obtención de nanocintas de carbono a partir de MWNTs. Encontramos que los MWNTs pueden ser abiertos longitudinalmente mediante la intercalación de litio y amoníaco, seguida por exfoliación. Los mejores resultados se obtuvieron mediante intercalación en tubos cortados y abiertos en los extremos y exfoliación con tratamiento ácido y calentamiento abrupto. El material resultante consistió en: (i) estructuras gráficas de multicapa (nanocintas), (ii)

MWNTs parcialmente abiertos y (iii) hojuelas de grafeno. A los nanotubos completamente abiertos les llamamos ex-MWNTs, los cuales se caracterizan por su gran cantidad de bordes, lo cual los hace candidatos muy atractivos para muchas aplicaciones, tales como: elaboración de nanocompositos, adsorción de gases, baterías recargables, capacitores, etc. La caracterización de su morfología y propiedades vibracionales y estructurales nos permitió proponer un mecanismo para la exfoliación de MWNTs.

## Abstract

The synthesis of composites from carbon nanotubes has its most notable challenge in the good dispersion of carbon nanotubes within the polymer matrix. Moreover, a good interaction is also desired between both components and a synergic effect in the composite as well, resulting from the properties of each component.

On this respect, in this thesis we present the main results concerning the synthesis of composites from multi-walled carbon nanotubes (MWNTs), nitrogen-doped MWNTs ( $CN_x$ ), and electronic conducting polymers, specifically from polyaniline (PAni), sulfonated polyaniline (SPAni), and polypyrrole (PPy). This study was motivated by our interest to combine the unique properties of each component and the obtention of composites with improved electronic and mechanical properties. For first time in science, we synthesized these composites by *in situ* polymerization of the corresponding monomers by means of a reductive alkylation method in liquid ammonia which is called *nanotube salts*. This method has been widely used for functionalization of fullerenes, single- (SWNTs), and multi-walled carbon nanotubes (MWNTs). In this method, metallic lithium is dissolved in liquid ammonia, to which carbon nanotubes are added, thus forming nanotube salts.

During the synthesis of these composites we occasionally observed that both MWNTs and  $CN_x$  were opened at the tips or in segments. We thus decided to follow this research line, successfully obtaining carbon nanoribbons from MWNTs. We found that these MWNTs can be opened longitudinally by intercalation of lithium and ammonia followed by exfoliation. Intercalation of open-ended tubes and exfoliation with acid treatment and abrupt heating provided the best results. The resulting material consists of: (i) multilayered flat graphitic structures (nanoribbons), (ii) partially open MWNTs, and (iii) graphene flakes. We called the completely unwrapped nanotubes ex-MWNTs, which are characterized by a large number of edges that make them very attractive for many applications such as: composites, gas adsorption, rechargeable batteries, capacitors,

xxx

etc. Characterization of their morphology, vibrational, and structure properties allowed us to propose an exfoliation mechanism for MWNTs.

# Chapter 1 Introduction

Carbon nanotubes (CNTs) have acquired greater importance due to their remarkable properties [1], and have opened a vast field of study in nanoscience [2, 3]. CNTs are stronger than steel, since they have high break strengths (~200 GPa), and elastic moduli in the 1 TPa range [4]. Carbon nanotubes easily beat carbon fibers and microparticles due to properties such as high aspect-ratio, strength, low mass density, and thermal and electrical conductivity, properties that make them suitable for use as reinforcing materials in composites [5]. In this regard, the continuous research on carbon nanotubes has resulted in the development and improvement of new materials and applications like polymer composites [2-6]. Composites from carbon nanotubes and polymers often show enhanced properties in comparison to the starting materials; for example, the increase in the glass transition temperature (critical for many applications) in polystyrene-SWNT composites [7] occurs by addition of small loads of SWNTs (~1 wt%). The addition of nanotubes to polymers can also notably increase the electrical transport [7] (~0.5 wt%), which can be explained by a percolation process [3]. Major challenges in the elaboration of polymer-nanotube composites are [5]: the poor dispersion of individual nanotubes in polymer matrices (because of bundling), and the matrix-filler interaction, which can be notably improved by using *in situ* polymerization [6].

In addition, electronically conducting polymers (ECPs) show interesting electronic properties that make them attractive in the electronics field [8, 9]: organic LEDs, flexible electronics, actuators, rechargeable batteries, capacitors, electromagnetic absorbers, and others. Composites derived from carbon nanotubes and ECPs show improved properties inherited from both components [10], for example, stiffness and flexibility from carbon nanotubes and electrocatalytic activity from ECPs. On the other hand, the discovery and study of new carbon-based materials, such as graphene [11] and carbon nanoribbons [12], add a significant contribution to the field of nanomaterials and offers new research paths.

On this basis, in this thesis work we briefly discuss in chapter 1, some of the most relevant properties of carbon nanotubes, polymer composites, graphene and graphene

nanoribbons. Next, in chapter 2 we explain how we synthesized composites from multi-walled carbon nanotubes, polyaniline, and poly(2-aminobenzene sulfonic acid) (PoASA, a sulfonated polyaniline) by means of a covalent functionalization method which is called nanotube salts. We also study some of the most relevant properties and features of these nanocomposites, such as morphology, structure, and vibrational properties. This project was not continued further, due to lack of equipment, and to an unexpected finding that led us to a striking discovery: the opening of carbon nanotubes. We thus decided to perform a deeper study of this phenomenon, explained in chapter 3, which ultimately led us to the opening of multi-walled carbon nanotubes into carbon nanoribbons, which we called ex-MWNTs, and to the better understanding of their unzipping process. This novel method, first published in the world by our research group [13], could be exploited for the development of improved computer processors [14], super capacitors [15, 16], rechargeable batteries [17], hydrogen storage [18, 19], improved catalysts [20, 21], and polymer composites [22, 23]. We also explain some of the properties of ex-MWNTs, and we propose an unwrapping mechanism for ex-MWNTs. Nevertheless, more research is needed in order to better understand this mechanism and the properties of this new material, as well as to explore future applications.

## 1.1 Carbon nanotubes

The discovery of fullerenes by Kroto, Smalley, Curl [24] and co-workers set a strong background for the study of new carbon shapes. In 1991 and 1993, Iijima [25, 26] observed in detail the structure of arc-grown carbon filaments: carbon nanotubes, a novel material on which further research has been performed due to their unique properties and potential applications [2, 3]. A carbon nanotube, or elongated fullerene, can be viewed as a honey-comb lattice arrangement of  $sp^2$  hybridized carbon atoms, that is, a graphene sheet rolled up into a seamless cylinder, as depicted in figure 1.1.

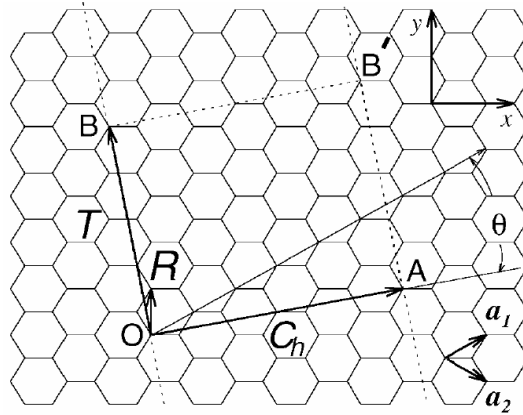


**Figure 1.1. Unrolled honeycomb lattice of a carbon nanotube**, constructed by connecting the points O and A, B and B'. Vectors OA and OB define the chiral vector  $C_h$  and the translational vector T of the nanotube, respectively. The vector R consists of a rotation around the nanotube axis, and is used for generating the coordinates of carbon atoms in the nanotube. The rectangle OAB'B defines the unit cell for the nanotube, and is rolled up so that points O and A coincide (and also points B and B'). Diagram constructed for a  $(n, m) = (4, 2)$  nanotube [1].

The orientation of a six-membered ring in the honey-comb lattice relative to the axis of the nanotube can be taken almost arbitrary, i. e., the graphene sheet may be rolled up in an almost any direction, defined by the chiral vector. The chiral vector is composed of two real space unit vectors  $a_1$  and  $a_2$  of the hexagonal lattice:

$$C_h = na_1 + ma_2 \equiv (n, m), \quad (n, m: \text{integers}, 0 \leq |m| \leq n) \quad 1.1$$

the two real space unit vectors  $a_1$  and  $a_2$  and their corresponding vectors  $b_1$  and  $b_2$  of the reciprocal lattice define both the unit cell and the Brillouin zone, which are shown at figure 1.2.

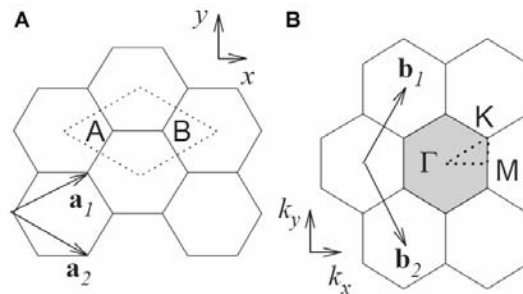


**Figure 1.2. Unit cell and Brillouin zone of 2D graphite**, shown as the dotted rhombus in (A) and the shaded hexagon in (B). The real and reciprocal lattice vectors are  $a_i$ , and  $b_i$ , respectively. Energy dispersion relations are obtained along the perimeter of the dotted triangle connecting the high symmetry points  $\Gamma$ , K and M of the Brillouin zone, and make possible the study of the electronic structure of carbon nanotubes [27].

Then, we may define the chirality of a carbon nanotube by its chiral indices, which tell us if a nanotube is achiral or chiral. Achiral nanotubes are classified as armchair  $(n, n)$  or zigzag  $(n, 0)$ ; chiral nanotubes are defined by two indices  $(n, m)$ , different to those of achiral nanotubes. Examples of each type of nanotube are shown at [figure 1.3](#). Another important parameter is the orientation or tilt angle of the hexagons with respect to the direction of the nanotube axis, which is defined by the chiral vectors as follows:

$$\cos\theta = \frac{\text{Ch} \cdot \mathbf{a}_1}{|\text{Ch}||\mathbf{a}_1|} = \frac{2n + m}{2\sqrt{n^2 + m^2 + nm}} \quad 1.2$$

in the particular cases of zigzag and armchair nanotubes,  $\theta$  corresponds to  $0^\circ$  and  $30^\circ$ , respectively [[1](#), [28](#)]. The diameter of the nanotube is expressed as:

$$d = \frac{a \cdot \sqrt{m^2 + mn + n^2}}{\pi} \quad 1.3$$

where  $a = 1.42 \times \sqrt{3} \text{ \AA}$  corresponds to the lattice constant in the graphite sheet, with a carbon-carbon bond distance of  $1.42 \text{ \AA}$ .

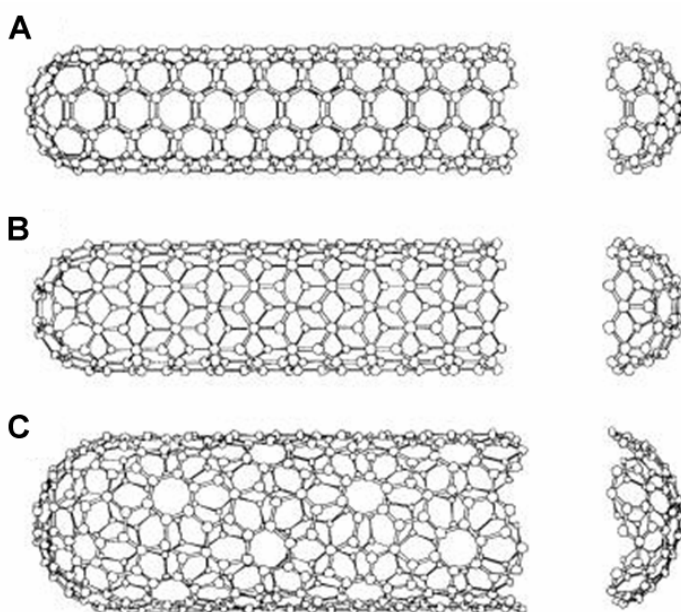


**Figure 1.3. Examples of carbon nanotubes: (A)** armchair,  $(5, 5)$ ; **(B)** zigzag  $(9, 0)$ ; **(C)** chiral,  $(10, 5)$ . Note that the tube can be rolled up in almost any direction. In theory, by joining the two caps of a nanotube, a fullerene can be obtained [[28](#)].

If we consider the large aspect ratio (length vs. diameter) of the cylinder, nanotubes can be considered as one-dimensional nanostructures, in comparison to zero-dimensional (fullerenes), 2D (graphene), or 3D (graphite) structures. In addition, a carbon nanotube may be formed by one, two, or more layers, being thus called single-walled carbon nanotubes (SWNTs), double-walled carbon nanotubes (DWNTs), or multi-walled carbon nanotubes (MWNTs); from which some examples are shown at [figure 1.4](#).

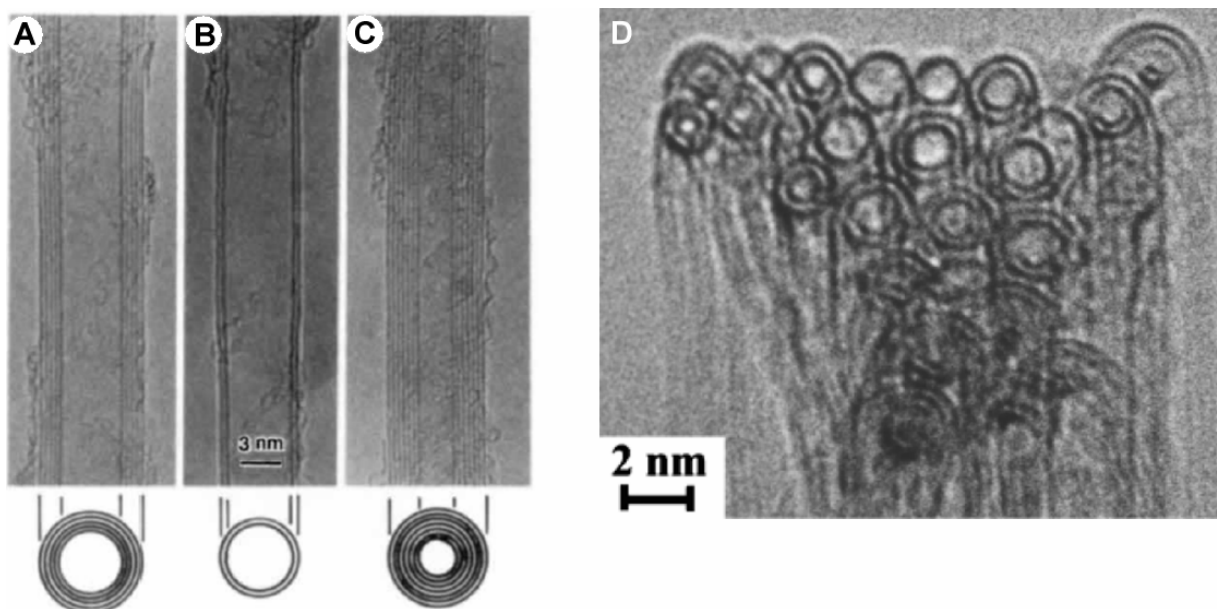


**Figure 1.4. TEM micrographs of MWNTs with different number of layers.** (A) Five graphitic sheets, diameter 6.7 nm; (B) two-sheet nanotube, diameter 5.5 nm; (C) seven-sheet tube, outer diameter 6.5 nm, inner diameter 2.2 nm; MWNTs were synthesized by the arc-discharge method [25]. (D) HRTEM of DWNTs synthesized by a chemical vapor deposition process [29]. The tips of the tubes are closed, formed by arrays of pentagons, which are positive surface disclinations ( $+60^\circ$ ) in the hexagonal lattice [30]. The inclusion of different types of topological defects such as pentagons and heptagons in a single nanotube changes its electrical properties.

The interlayer spacing among graphitic layers in MWNTs ( $d_{002} = 3.4 \text{ \AA}$ ) differs slightly from that of graphite ( $d_{002} = 3.35 \text{ \AA}$ ), due to curvature and Van der Waals interactions between successive layers [25]. Moreover, chirality varies within a MWNT after three to five graphitic layers [31], probably because the inner tubes are closer to the catalytic particle and thus the growth process is determined only by the nature of the catalytic particle [32], while for the outer layers chirality depends primarily on the tube diameter.

## 1.2 Doping of carbon nanotubes

Carbon nanotubes may be doped by replacement of carbon atoms by phosphor, boron, or nitrogen atoms [33-38]. Other potential substitutional dopants are silicon [39, 40], oxygen [41], and sulfur [42]. The dopant, which is often included in the synthesis solution, strongly changes the electronic, chemical and morphological properties of carbon nanotubes, such as: conductivity [35, 36] and p- or n-type doping [34, 43], field emission [44, 45], sensing [46, 47], magnetism [48-50], structure [37, 38], among others, thus allowing the tuning of the properties of carbon nanotubes. As an example, consider the nitrogen-doped carbon nanotubes obtained from pyrolysis of ferrocene-benzylamine solutions [37], in figure 1.5.

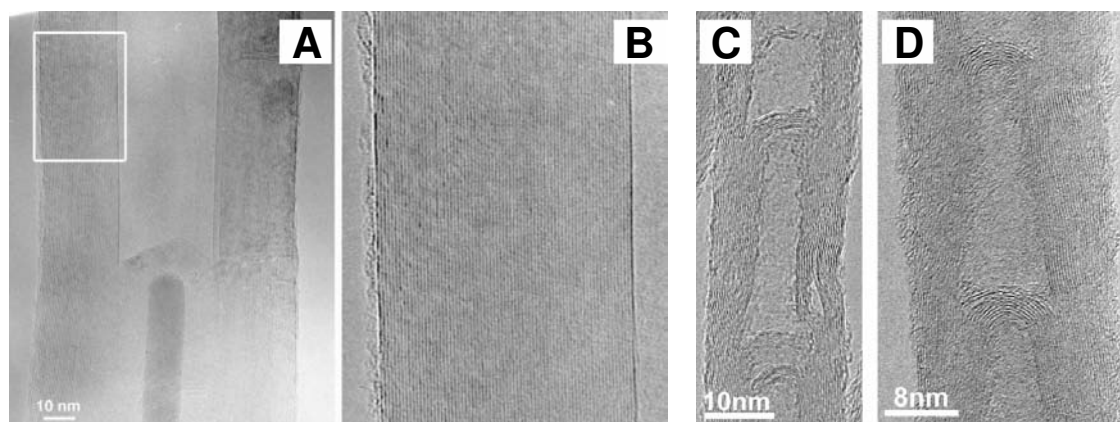


**Figure 1.5.** HRTEM images of MWNTs. (A, B) MWNTs show the high degree of perfection of the tube walls. Interlayer spacing is 3.4 Å [51]. (C) Nitrogen-doped MWNTs (CN<sub>x</sub>) produced by CVD process of a ferrocene-benzylamine solution at 850 °C, showing compartmentalized structure and (D) detailed continuous closure of the tubes [37].

Figures 1.5C and D clearly show structural changes upon inclusion of nitrogen into the organic precursor synthesis feedstock. Predictions [37] have shown that nitrogen promotes diameter reduction (which is energetically favored) and tube closure. Moreover, fast creation of pentagons and of positive curvature occurs, thus forming tube caps. If more nitrogen atoms are fed, the tube must re-open and start growing; as a result, bamboo-like or corrugated configurations are obtained [37]. On the other hand, the presence of nitrogen not only affects growth and structure [36, 37], but also influences the electronic properties of nitrogen-doped carbon nanotubes [36].

### 1.3 Synthesis of carbon nanotubes: chemical vapor deposition (CVD)

Despite the variety of synthesis methods [3, 51-53] (see appendix A.1), the pyrolysis of organic vapors at moderate temperature in the presence of a catalyst is an easy, simple, efficient, and relatively low-cost synthesis method. A typical CVD process [52, 53], which was used in this thesis work as a routine procedure for making multi-walled carbon nanotubes, is schematized at figure 1.6, and described below.

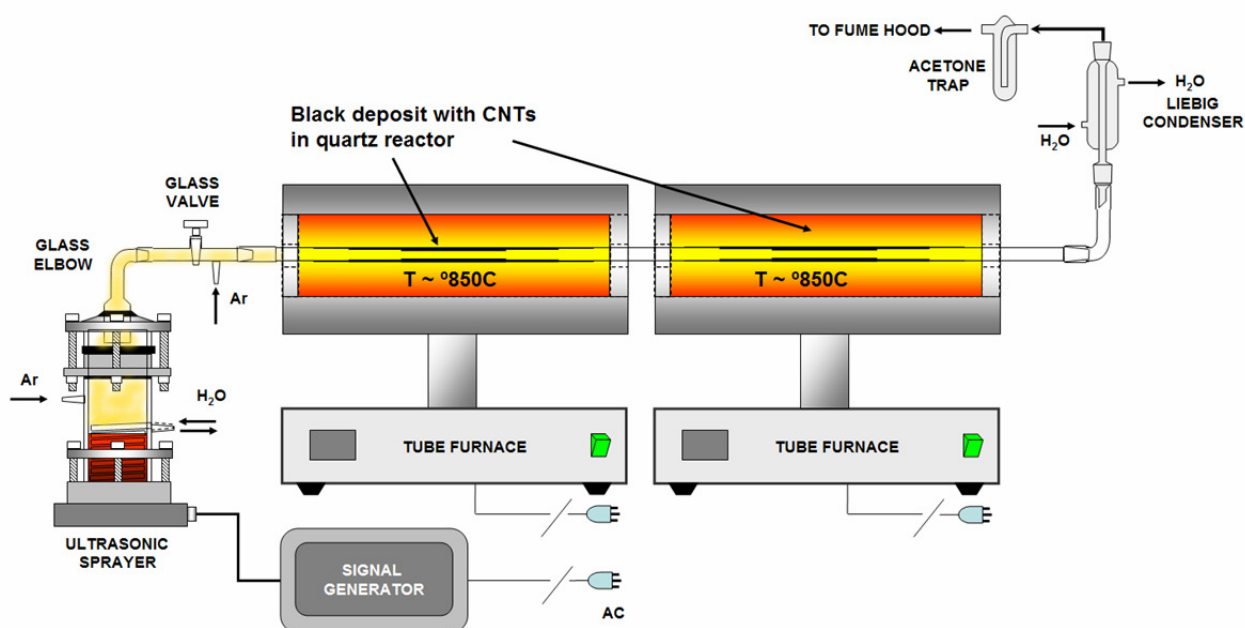


**Figure 1.6. Experimental setup for CVD growth of MWNTs.** A carbon source/catalyst liquid mixture is sonicated (by means of an electronic command and a piezoelectric ceramic), which produces a mist of hydrocarbons and of catalyst (e. g. a toluene/ferrocene solution). This mist is fed to a tube reactor placed inside a two-furnace set by flowing argon. Due to the high temperature (825–850 °C), hydrocarbons are pyrolyzed and then MWNTs are synthesized at the hot regions of the quartz tube (typically, during 15 minutes). Exhaust gases are passed through a water condenser and an acetone trap. The minimum distance between both furnaces should be 5 cm to avoid their damage.

The main parts of the setup consist of: an ultrasonic sprayer (QVF), a glass valve (Ace Glass), a quartz tube (45.75" L x 1.25" O.D.), and a tube furnace (Barnstead|Thermolyne 21100). To increase the production of carbon nanotubes, a two-oven setup was used. Care should be taken when mounting the system, and all glassware joints should be sealed with silicon grease and Teflon tape to avoid leaks (an important issue, since the hot mixture could ignite if in contact with air).

Before attempting the synthesis, it is strongly recommended to calibrate both furnaces at the desired temperature. First, the system is purged for 5 minutes with flowing argon (99.998%) at 0.5 L/min to remove oxygen. With the glass valve closed, both furnaces are set to the desired temperature (825 or 850 °C). The higher the temperature, the more crystalline will be the synthesized carbon nanotubes. The argon flux should then be increased to 2.5 L/min. Next, a toluene/ferrocene (for MWNTs) or benzylamine/ferrocene (for nitrogen-doped MWNTs) mixture (carbon source:catalyst 97.5:2.5 wt%) solution is nebulized by sonication with an electronic command and a piezoelectric. Once the desired temperature is reached in both furnaces, the valve is opened, which lets Ar gas to draw the mist into the quartz reactor. Excessive sonication during synthesis will increase the amount of amorphous carbon. A typical synthesis lasts up to 15 minutes; longer times may allow longer MWNTs, but more amorphous carbon will also be obtained. Next, the valve is closed, sonication is stopped, the argon flux is reduced to 0.5 L/min, and the heating cycle is turned off in both furnaces.

The system is allowed to cool at least to ~150 °C or less, since high temperatures may induce decomposition of nanotubes once they come in contact with air. The carbon soot is collected, weighted, and stored in glass vials. About 400–500 mg of product is obtained in each synthesis using the two-furnace setup. Examples of MWNTs synthesized by this method are shown in [figure 1.7](#).

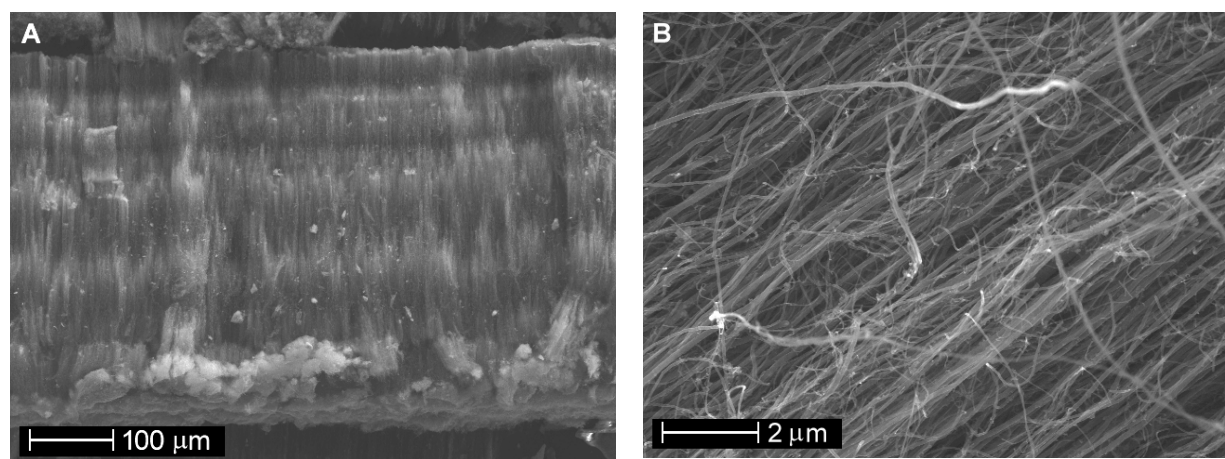


**Figure 1.7.** MWNTs synthesized by a CVD process, from a toluene/ferrocene 97.5:2.5 wt % solution, after 15 minutes of pyrolysis at 825 °C. (A) A mat of aligned MWNTs; (B) closer view of MWNTs.

The composition of the carbon source may be varied according to the characteristics of the desired material. As carbon source, practically any hydrocarbon is useful [3, 43]. The catalyst accelerates the decomposition of the organic molecules, and forms metallic catalyst particles which allow the deposition of decomposed precursors, and the growth of nanotubes onto a substrate (the reactor itself or another substrate) [52]. The catalyst, Fe, Co, Ni, Pt, Pd, Cu, Mo, or Ru [3, 54-56], not only promotes nanotube growth, but also defines other important features on the tubules such as pentagon-heptagon structural defects and tube closure [57], diameter [58], and helicity [59]. Catalysts are often mixed with the carbon source as coordination compounds (cobaltocene, ferrocene, nickelocene), which are decomposed at moderate temperatures, for example, ferrocene decomposes above 400 °C [60]. The catalyst may also be in oxidized form, and reduced with hydrogen [58] before the CVD synthesis, though under certain conditions it may also present high catalytic activity [52].

Temperature is another important variable, e. g., high temperatures (~950 °C) promote a greater size of catalyst particles and hence of diameter in SWNTs, favor the production of carbon nanotubes [45], and induce graphitization and morphological changes. Finally, the carrier gas flow also becomes an important factor when thick and crystalline MWNTs are desired [51]. Depending on the experimental conditions, either SWNTs [61] or MWNTs [51] can be obtained, and nitrogen-doped SWNTs [36]. For example, nitrogen-doped double and triple walled carbon nanotubes can be obtained as primary products from the pyrolysis of benzylamine in a ~830–870 °C temperature range; below this range their formation is greatly reduced [62]. Among its advantages, hydrocarbon pyrolysis allows the synthesis of relatively long, well aligned MWNTs [52], which may have applications such as: enhanced field emission [63], high-density magnetic storage [64], chemical separation and sensing [65, 66], and composites [5].

### **1.3.1 Growth mechanism of CVD carbon nanotubes**

Two types of growth mechanisms for CVD carbon nanotubes have been proposed [3], depicted in figure 1.8.

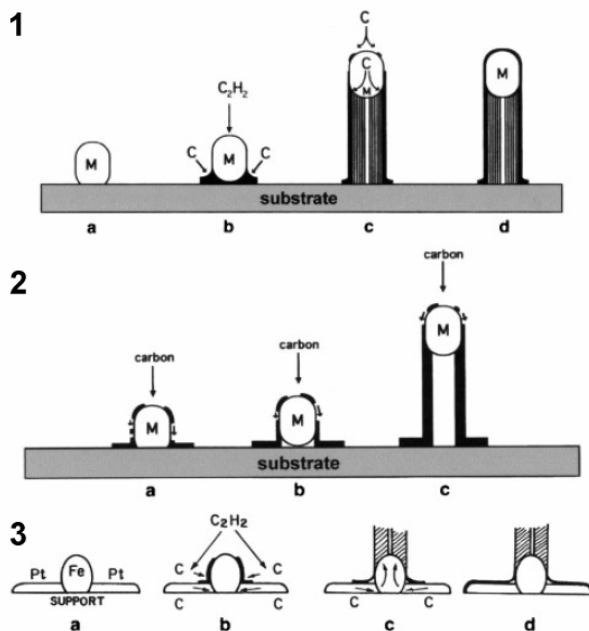


**Figure 1.8. Growth mechanisms for carbon nanotubes by pyrolysis of organic precursors. (1)** Carbon is cracked on the catalytic particle and diffuses through it, and precipitates at the opposite end in form of graphite. The catalyst particle remains always at top. **(2)** Benzene is cracked on the surface of the metal and diffuses on it, and precipitates at the colder end in form of graphitic domains. **(3)** From Fe-Pt/acetylene and stainless steel/natural gas systems; carbon also diffuses through the metal, but the particle remains at bottom of the filament. Scheme from [3].

The decomposition of hydrocarbons (figure 1.8, 1) on the exposed surfaces of the metal catalyst produces bimolecular hydrogen and carbon species [3]. Then, carbon diffuses through the catalytic particle and precipitates at the other end of the filament. The exothermic decomposition of the organic precursor results in a temperature gradient across the catalyst, which allows precipitation of carbon at the colder zone of the particle, and filament growth (figure 1.8, 1b, 1c). This continues until the catalyst particle is deactivated (figure 1.8, 1d). A similar mechanism (figure 1.8, 2), proposes that the carbon species diffuse on the surface of the metal particle [67]. Finally (figure 1.8, 3), growth may occur due to the rapid diffusion of carbon through the catalyst, thus generating a filament which grows from its base. A variant of this last method suggests that carbon species adsorb on iron clusters and diffuse rapidly along the axial direction, thus forming concentric carbon cylinders, which grow along the axial and radial directions as iron and carbon continue to react at the tube ends; finally, the catalytic particles at the tips may be drawn into the tube core by capillary action [51]. Accurate control over the experimental conditions, i. e., carbon source, metal catalyst, particle

size, flux of carrier gas, pyrolysis time, substrates, and temperature, has a strong effect on the growth mechanism and also on the characteristics of the resulting product [3].

## 1.4 Some properties of carbon nanotubes

### 1.4.1 Conductivity

Recalling equation 1.1, a single carbon nanotube shell is defined by the chiral indices  $(n, m)$ . The chiral indices (or chirality) define the direction in which the graphene sheet is rolled up in order to form the nanotube. Depending on their chiral indices, carbon nanotubes can be non-conducting, semiconducting, or metallic. By controlling the chirality of CNTs, it would be possible to finely tune up the conducting properties of single and multi-walled CNTs, for example, to design metal-insulator coaxial nanostructures without doping [28]. Electrical conductivity values [3] for individual MWNTs vary from  $\sim 8 \times 10^3 \text{ S}\cdot\text{cm}^{-1}$  to  $2 \times 10^5 \text{ S}\cdot\text{cm}^{-1}$ , and bundles of SWNTs have shown conductivities in the  $3 \times 10^4 \text{ S}\cdot\text{cm}^{-1}$  to  $1 \times 10^4 \text{ S}\cdot\text{cm}^{-1}$  range. For more details on this and other properties, see appendix 1.

### 1.4.2 Infrared and Raman active modes

Chirality not only defines the conducting properties of CNTs, but also gives rise to symmetry groups which determine the active vibrational infrared and Raman modes [28, 68]. Raman and IR-active modes can be predicted by group theory, for a given lattice structure and symmetry, and are shown for different types of carbon nanotubes at table 1.1.

**Table 1.1. Number and symmetries of Raman and IR-active modes for different types of carbon nanotubes.** For any nanotube chirality, there are only 6 or 7 intense Raman-active modes [27].

| Nanotube structure                | Point group | Raman-active modes            | IR-active modes     |
|-----------------------------------|-------------|-------------------------------|---------------------|
| Armchair $(n, n)$ $n$ even        | $D_{nh}$    | $4A_{1g} + 4E_{1g} + 8E_{2g}$ | $A_{2u} + 7E_{1u}$  |
| Armchair $(n, n)$ $n$ odd         | $D_{nd}$    | $3A_{1g} + 6E_{1g} + 6E_{2g}$ | $2A_{2u} + 5E_{1u}$ |
| Zigzag $(n, 0)$ $n$ even          | $D_{nh}$    | $3A_{1g} + 6E_{1g} + 6E_{2g}$ | $2A_{2u} + 5E_{1u}$ |
| Zigzag $(n, 0)$ $n$ odd           | $D_{nd}$    | $3A_{1g} + 6E_{1g} + 6E_{2g}$ | $2A_{2u} + 5E_{1u}$ |
| Chiral $(n, m)$ $n \neq m \neq 0$ | $C_N$       | $4A + 5E_1 + 6E_2$            | $4A + 5E_1$         |

These modes can be observed experimentally by Raman and Fourier-transformed infrared spectroscopies. Figure 1.9 shows typical examples of Raman spectra for SWNTs.

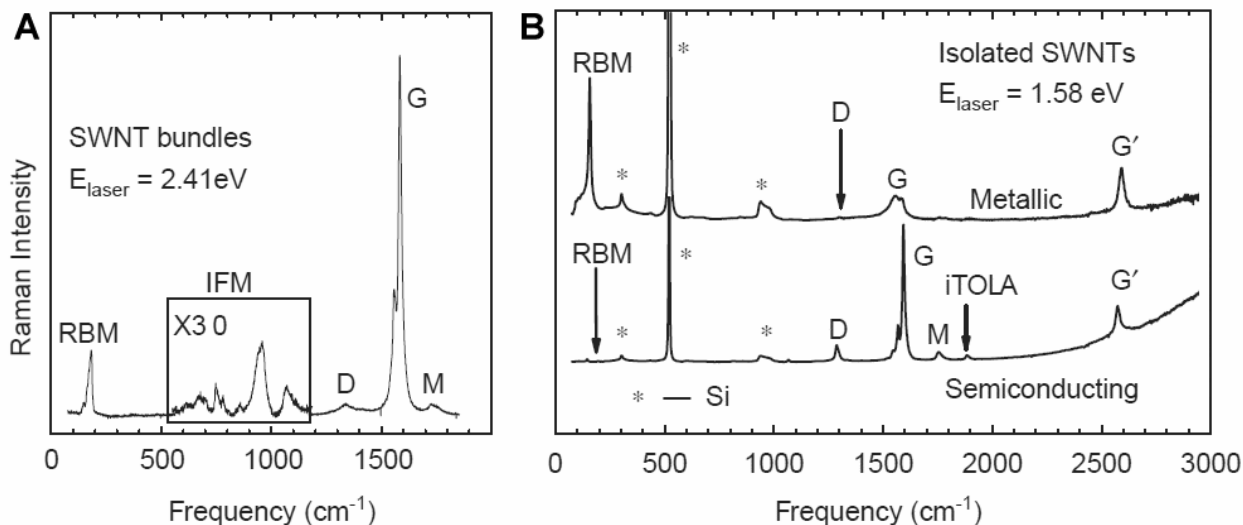


**Figure 1.9. Raman spectra of single-walled carbon nanotubes.** (A) HiPco SWNTs bundles. (B) Raman spectra of isolated metallic (top), and semiconducting (bottom) SWNTs. Besides the RBM, D, G, and G' bands, weak double resonance features appear such as those related to *M* and iTOLA second-order modes. The marked features (\*) are due to the SiO<sub>2</sub> substrate [69].

The most relevant features in the spectrum shown at figure 1.9A are the radial breathing modes (RBMs), which are radial motions (as if the tube were breathing), and unique features of SWNTs found at low frequencies. On the other hand, the tangential G band multi-feature (with G<sup>+</sup> and G<sup>-</sup> components) is observed at high frequencies. Other features are the D band, the *M* band (an overtone mode), the iTOLA band (a combination of optical and acoustic modes), the intermediate frequency phonon modes (IFM, inset at figure 1.9A), and the G' band (figure 1.9B), an overtone of the D mode, visible in the spectra of individual SWNTs. Raman spectra of individual SWNTs are useful when comparing the behavior of the different Raman features of SWNTs while varying diameter  $d_t$  and/or laser energy  $E_L$ . The dependency of the mode frequencies on the diameter for an individual SWNT can be expressed by [69]:

$$\omega = \omega_0 + \frac{\beta}{d_t^n} \quad 1.4$$

where  $\omega_0$  is the frequency of 2D graphite (graphite may be regarded as a tube with diameter  $d_t \rightarrow \infty$ ),  $\beta$  and  $n$  are the coefficient and exponent of the diameter dependence, respectively [69]. Raman frequencies may be affected by other factors, such as stress [70]. When a SWNT is subject to stress, which can be accomplished by anchoring both ends of the tube to a SiO<sub>2</sub> surface and by pushing the tube with an AFM tip, the additional displacement may be quite small (~0.06% to 1.65% strain). Nonetheless, downshift of the D, G (G<sup>+</sup> and G<sup>-</sup> components), and G' bands happens due to strain. Strain produces elongation of the carbon-carbon bonds, which makes the bonds weaker, thus lowering the vibrational frequencies. Relaxation (upshift) of the Raman signals occurs after certain time, and is immediate when the tubes are broken. In the case of MWNTs, some of the characteristic features which distinguish SWNTs from graphite cannot be seen (such as the RBMs), due to the large diameter distribution in MWNTs [70]. Full explanations of the Raman processes held in carbon nanotubes and other carbon materials can be found at references [27, 68, 69] and [71].

Carbon nanotubes present many other important properties, which are summarized in [appendix A.1](#). Such properties in most cases have a strong effect on the properties of composites, for example Young's modulus, and thermal and electrical conductivity.

## 1.5 Nanocomposites from carbon nanotubes

Due to their small size and exceptional physical and electronic properties such as high longitudinal elastic modulus, high thermal and electrical conductivity along the axial direction, and low density [3], carbon nanotubes (CNTs) have become important for improving the properties of polymers. Depending on the polymer matrix, conductive composites can be obtained with 5 wt% of CNTs or even less while avoiding or minimizing detrimental effects on properties. Some of the potential applications of polymer-carbon nanotube nanocomposites are [3, 5, 10, 72]: sensors and actuators, charge dissipation and electromagnetic shielding, electrochemical supercapacitors, photosensitive materials, photovoltaic cells and photodiodes, solar cells, Schottky contacts, logic gates and transistors, conductive inks, rechargeable batteries. Percolation, increase of strength, increase of Young's modulus and strain to failure,

enhancement of the interface strength, and increase in the glass transition temperature, can be obtained by incorporating very low CNT contents (0.1–1 wt%) [2, 3, 6].

Nonetheless, some of the most important problems that arise when making nanocomposites are [5]: CNTs tend to form clusters and bundles when dispersed in an aqueous medium or polymer matrix due to Van der Waals interactions; also, the matrix-filler interaction, i. e., the polymer-nanotube interaction is weak, thus lacking effective stress transfer. Other problems are: pull-out effects (sliding of nanotubes from the polymer matrix), nanotube alignment, the high viscosity of polymer-nanotube mixtures due to the large surface area of nanotubes, and poor dispersion of nanotubes in most solvents and polymers, which lead to heterogeneous dispersion of carbon nanotubes, and make composite molding and processing difficult.

For this reason, several methods have been aimed to obtain nanocomposites with strong interaction between nanotubes and the polymer matrix [5, 73-75]: dry powder mixing, melt mixing, surfactant-assisted mixing, electrostatic self-assembly, adsorption of polymers through  $\pi - \pi$  interactions, and *in situ* covalent polymerization. In addition, randomly aligned carbon nanotubes in polymer matrixes can be oriented by putting them under stress [5] (by extrusion or melt-fiber spinning), which further improves mechanical performance of the composite, along with its electrical and thermal conductivities, and also reduces the amount of carbon nanotubes needed. Non-covalent functionalization methods of CNTs with polymers preserve the molecular structure of CNTs, and also their mechanical and electronic properties. In contrast, covalent modification introduces 'defects' -  $sp^3$  hybridization, which affects the properties of carbon nanotubes, and hence requires precise control on the functionalization degree.

On the other hand, covalent modification of CNTs [76-79] can notably improve dispersion and interfacial interaction. Mild functionalization can be done as a prior step to polymerization, and covalent bonding of polymers can be achieved either by linking polymer chains to the nanotube (*grafting to*) or by growing polymer chains from the nanotube (*grafting from*). In this regard, some functionalization methods with polymers for SWNTs include: anionic polymerization initiated by carbanions [80], atomic-transfer radical polymerization (ATRP) [81], condensation and ring-opening-polymerization (ROP) [82], ring-opening metathesis polymerization (ROMP) [83], arylation [84], and

oxidative polymerization [85]. Functionalization of multi-walled carbon nanotubes is also a very important research field [3], and it includes practically the same methods than those used for SWNTs. Some work has also been done on nitrogen-doped MWNTs (CN<sub>x</sub>) [72], which do not require surface-modification procedures before polymerization due to the reactivity of nitrogen atoms and the interactions between CN<sub>x</sub> and the matrix [3]. Though each method has its own benefits, *grafting from* methods are nowadays some of the most important techniques for the synthesis of polymer-carbon nanotube nanocomposites, with precise control over the molecular weight and high grafting densities as well [86]. In contrast, *grafting to* procedures, which involve polymer preparation prior to bonding, offer precise control on the polymer's length and architecture, but functionalization densities can be low due to steric hindrance [87].

The synthesis of nanocomposites is strongly affected by the properties of carbon nanotubes (CNTs). In this regard, an important issue is the synthesis method for CNTs, which determines some of their physical properties, and has a strong impact on the reactivity of CNTs. For example [3], arc-grown CNTs are highly crystalline and relatively chemically inert, thus requiring activation procedures before polymerization to debundle them and to increase functionalization. On the other hand, pyrolytic CNTs are more reactive due to structural defects and kinks. Finally, it should be pointed out that many covalent functionalization methods require very controlled experimental conditions, like moisture-free reaction media. Carbon nanotubes are unique due to their outstanding and unique properties; nonetheless, graphene – an unwrapped carbon nanotube – and other related materials also show unique properties, some of them may be even more promising than those of carbon nanotubes, for certain applications.

In this work, we used the technique which is called nanotube salts, for the synthesis of composites from CNTs and the electronically conducting polymers polyaniline (PAni) and poly(2-aminobenzene sulfonic acid) (PoASA). In this method, previously used for the reductive functionalization of SWNTs [84, 88] and MWNTs [89, 90], CNTs acquire electrons and lithium cations from a liquid ammonia medium, thus forming salts. In our case, MWNTs salts were reacted with aniline and oASA. This method is further explained in chapter 2. Furthermore, in chapter 3 we see how the synthesis of MWNTs-PAni nanocomposites led us to a novel discovery: the unwrapping of MWNTs.

## 1.6 Novel carbon materials: graphene and graphene ribbons

Graphene is a 2D monolayer of carbon atoms, which was not thought to exist in the free state, due to its supposed instability in contrast to curved structures such as fullerenes and carbon nanotubes [11]. In graphene, carbon atoms are arranged in a honeycomb lattice that is made up of two equivalent carbon sublattices, whose energy bands intersect at the Fermi level near the edges of the Brillouin zone, in which electrons behave as massless Dirac fermions, thus leading to the predicted high electron mobilities ( $\sim 2 \times 10^5 \text{ cm}^2/(\text{V}\cdot\text{s})$ ) [91, 92], and making graphene a zero-gap semiconductor [93]. Moreover, other remarkable properties include high Young's modulus ( $\sim 1 \text{ TPa}$ ) [94], high fracture strength [94], thermal conductivity ( $\sim 5000 \text{ W}/(\text{m}\cdot\text{K})$ ) [95], high specific surface area (experimental values, 520–925  $\text{m}^2/\text{g}$ ) [15], ballistic transport [93], and quantum Hall effect at room temperature [93]. Furthermore, charge carriers follow relativistic mechanics, and are better described by the Dirac equation rather than by Schrödinger's [93]. Graphene and graphene ribbons can be obtained by several methods: by exfoliation of graphitic compounds [96-100], by decomposition of silicon carbide [101, 102], chemical vapor deposition [12, 103], organic synthesis [104], or annealing [105]. These methods are further explained in [chapter 3](#).

### 1.6.1 Importance of edges

A graphene nanoribbon (GNR) can be considered as an unrolled carbon nanotube, and can be described by a chiral vector with indices  $(n, m)$  [26]. Nonetheless, for GNRs the armchair/zigzag nomenclature refers to the direction of the edge, not to the chiral vector [106]. Finite graphite networks [107] with zigzag edges have special localized states at the Fermi level, but those with armchair edges have no such state. Depending on edge configuration, functionalization and doping, a GNR is predicted to be either semiconducting or metallic [108]. The edge state [107] originates from the topology of the  $\pi$  electron networks with a zigzag edge, and not from dangling bonds or bulk graphite. In GNRs, the parameters that control the properties of the edge state are [107]: the system size, defined by the ribbon width ( $M$ ), which denotes the system size (the

number of dimer lines for armchair ribbons and the number of zigzag lines for zigzag ribbons), and the edge shape, described as a mixture of zigzag and armchair sites. If a ribbon is solely limited by one or two edges, it is defined either as an armchair GNR or as a zigzag GNR [91]. Both examples are shown at figure 1.10.

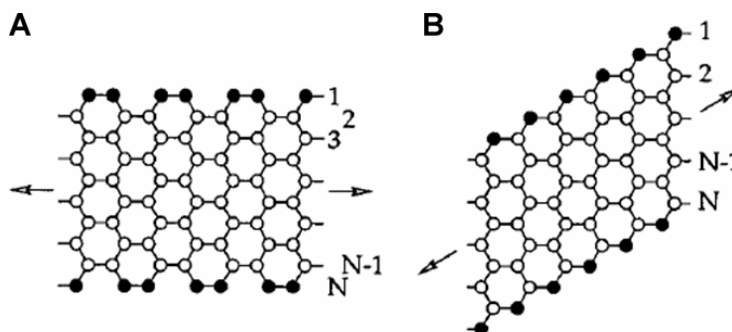


**Figure 1.10. Schematic representation of carbon nanoribbons.** (A) Armchair ( $N = 10$ ); (B) zigzag ( $N = 5$ ). Edge sites are indicated by solid circles on each side. Periodic boundary conditions are assumed for the edges. Arrows indicate the translational directions of the GNRs. Edge atoms are assumed to be hydrogen-functionalized with no contribution from dangling bonds to the electronic state near the Fermi level [107].

The edge shape [107] is defined by the atomic sites, i. e., the zigzag, armchair, and total edge sites. These sites give rise to the zigzag ratio  $r_{\text{zig}}$ , which is the number of zigzag sites relative to the total number of edge sites. The edge structure of a GNR can then be expressed as a permutation of  $a$  and  $z$ , which are armchair or zigzag atomic sites, respectively.

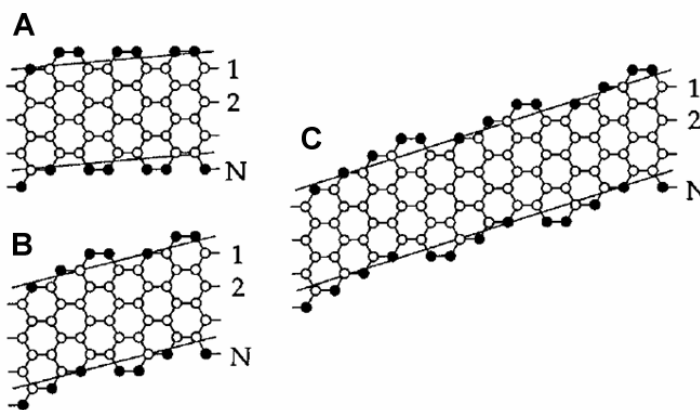


**Figure 1.11. Unit cells and edge vectors of carbon nanoribbons.** Edge sites are denoted by solid circles. Zigzag ratios and edge structure are: (A) 0.25,  $zaaa$ ; (B) 0.60,  $zzaza$ ; (C), 0.70,  $zzzazzazza$  [107].

For example, in figure 1.11A, there are one zigzag site and three armchair sites, with a total number of edges of 4. This gives us  $r_{\text{zig}} = 0.25$ , and an edge structure  $zaaa$ . Moreover, beside of the intrinsic properties of GNRs, the chemistry of their edges is an

important issue. Edges make GNRs [13, 108], carbon nanotubes [78, 109], and carbon nanofibers [110] more reactive and easier to functionalize than the relatively inert, inner  $sp^2$  graphitic network of these structures. A great amount of edges is relevant in applications such as: polymer composites, since they may allow improved interfacial interaction with the polymer matrix through anchoring of polymer chains, thus improving the properties of such composites; hydrogen storage and rechargeable batteries, because a high number of edges allow the easy insertion of several intercalant species and exfoliation (in MWNTs) [13], and drug delivery [109]. Edge functionalization could serve as a tool for modulation of the electronic properties of GNRs [108].

### **1.6.2 Applications of graphene and ribbons**

Due to its remarkable properties, graphene is attractive for applications such as: electromagnetic shielding [111, 112], composites [113, 114], field-effect transistors [115], catalysts [20, 21, 116, 117], and sensors [118, 119], single molecule electronics [120], hydrogen storage [121], rechargeable batteries [122], and high-density electrochemical capacitors [16]. Nonetheless, one of the driving forces that pushes research on graphene is the replacement of silicon in computer processors [123, 124]. According to Moore's law [125], the number of components in a silicon chip has doubled every 12 to 18 years since 1965, and it is thought to reach a limit due to miniaturization. If the gate dielectric thickness is below 2 nm, charge leakage occurs by quantum mechanical tunneling, thus causing problems related to off-state current, power consumption, heat, and dissipation of static power [115, 126]. These problems limit the speed and size of the transistors from which the processor is made up. In contrast, graphene behaves as a metal in which electrons move with a minimum resistance, thus making faster transistors. Furthermore, nano-scale size, graphene-based nanotransistors could make possible to increase the computing power of future processors [11]. To make such applications possible, scalable production methods are required. It is worth saying that the electronic properties will strongly depend on the synthesis method; for example, the Raman features used for the determination of the number of layers in microcleaved graphene are of no use in CVD-graphene.

In this work, we used multi-walled carbon nanotubes synthesized by chemical vapor deposition at 825 °C from a toluene/ferrocene mixture 97.5/2.5 wt %. The tubes were purified by a modified hydrothermal procedure, and, as we will further explain, used for the synthesis of carbon nanotubes nanocomposites by *in situ* polymerization of aniline and 2-aminobenzenesulfonic acid monomers by means of the nanotube salts method. During the synthesis of these composites we also found a striking discovery that was our motive force for a deep study on this phenomenon, which we also explain in chapter 3, and that led us to the production of a new material: ex-MWNTs, multi-layered carbon nanoribbons from MWNTs. It is noteworthy to mention that this finding was first published by our research group in the peer-reviewed journal *Nano Letters* (*Nano Lett.*, 2009, 9 (4), 1527-1533), a publication of the American Chemical Society (ISI impact factor 10.371). Further improvement on the production of ex-MWNTs, and deeper studies on their properties, will certainly open new research and application fields: terahertz-fast computer processors, rechargeable batteries, gas adsorption and storage, among others.



## References

- [1] M. S. Dresselhaus, G. Dresselhaus, A. Jorio. Unusual properties and structure of carbon nanotubes. *Annu. Rev. Mater. Res.* **34** (2004) 247-278.
- [2] R. H. Baughman, A. A. Zakhidov, W. A. de Heer. Carbon nanotubes - the route toward applications. *Science* **297** (2002) 787-792.
- [3] M. Terrones. Carbon nanotubes: synthesis and properties, electronic devices and other emerging applications. *Int. Mater. Rev.* **49** (2004) 325-377.
- [4] R. Khare, S. Bose. Carbon nanotube based composites - a review. *J. Miner. Mater. Charact. Eng.* **4** (2005) 31-46.
- [5] P. M. Ajayan, J. M. Tour. Nanotube composites. *Nature* **447** (2007) 1066-1068.
- [6] P. J. F. Harris. Carbon nanotube composites. *Int. Mater. Rev.* **49** (2004) 31-43.
- [7] B. P. Grady, A. Paul, J. E. Peters, W. T. Ford. Glass transition behavior of single-walled carbon nanotube-polystyrene composites. *Macromolecules* **42** (2009) 6152-6158.
- [8] A. G. MacDiarmid. "Synthetic metals": a novel role for organic polymers (nobel lecture). *Angew. Chem. Int. Ed.* **40** (2001) 2581-2590.
- [9] Y. Bar-Cohen. Electro-active polymers: current capabilities and challenges, in: Proceedings of the SPIE smart structures and materials symposium, *EAPAD Conference*, SPIE, 2002, 1-6.
- [10] M. Baibarac, P. Gómez-Romero. Nanocomposites based on conducting polymers and carbon nanotubes from fancy materials to functional applications. *J. Nanosci. Nanotech.* **6** (2006) 1-12.
- [11] K. S. Novoselov, A. K. Geim, S. V. Morozov, D. Jiang, Y. Zhang, S. V. Dubonos, I. V. Grigorieva, A. A. Firsov. Electric field effect in atomically thin carbon films. *Science* **306** (2004) 666-669.
- [12] J. Campos-Delgado, J. M. Romo-Herrera, X. Jia, D. A. Cullen, H. Muramatsu, Y. A. Kim, T. Hayashi, Z. Ren, D. J. Smith, Y. Okuno, T. Ohba, H. Kanoh, K. Kaneko, M. Endo, H. Terrones, M. S. Dresselhaus, M. Terrones. Bulk production of a new form of sp<sup>2</sup> carbon: crystalline graphene nanoribbons. *Nano Lett.* **8** (2008) 2773-2778.
- [13] A. Cano-Márquez, F. Rodríguez-Macías, J. Campos, C. Espinosa-González, F. Tristán, D. Ramírez-González, D. Cullen, D. Smith, M. Terrones, Y. Vega-Cantú. Ex-MWNTs: Graphene sheets and ribbons produced by lithium intercalation and exfoliation of carbon nanotubes. *Nano Lett.* **9** (2009) 1527-1533.
- [14] Y.-M. Lin, C. Dimitrakopoulos, K. A. Jenkins, D. B. Farmer, H.-Y. Chiu, A. Grill, Ph. Avouris. 100-GHz transistors from wafer-scale epitaxial graphene. *Science* **327** (2010) 662.
- [15] M. D. Stoller, S. Park, Y. Zhu, J. An, R. S. Ruoff. Graphene-based ultracapacitors. *Nano Lett.* **8** (2008) 3498-3502.
- [16] S. R. C. Vivekchand, C. S. Rout, K. S. Subrahmanyam, A. Govindaraj, C. N. R. Rao. Graphene-based electrochemical supercapacitors. *J. Chem. Sci.* **120** (2008) 9-13.

- [17] Z-S. Wu, W. Ren, L. Wen, L. Gao, J. Zhao, Z. Chen, G. Zhou, F. Li, H-M. Cheng. Graphene anchored with  $\text{Co}_3\text{O}_4$  nanoparticles as anode of lithium ion batteries with enhanced reversible capacity and cyclic performance. *ACS Nano* **4** (2010) 3187-3194.
- [18] S. Patchkovskii, J. S. Tse, S. N. Yurchenko, L. Zhechkov, T. Heine, G. Seifert. Graphene nanostructures as tunable storage media for molecular hydrogen. *P Natl. Acad. Sci. USA* **102** (2005) 10439-10444.
- [19] Layered graphene sheets could solve hydrogen storage issues. National Institute of Standards and Technology (NIST). Last access on: July 4, 2010. From: *ScienceDaily*, <http://www.sciencedaily.com/releases/2010/03/100317161952.htm>.
- [20] P. V. Kamat. Graphene-based nanoarchitectures. Anchoring semiconductor and metal nanoparticles on a two-dimensional carbon support. *J. Phys. Chem. Lett.* **1** (2010) 520-527.
- [21] B. Seger, P. V. Kamat. Electrocatalytically active graphene-platinum nanocomposites. Role of 2-D carbon support in PEM fuel cells. *J. Phys. Chem. C* **113** (2009) 7990-7995.
- [22] M. J. Allen, V. C. Tung, R. B. Kaner. Honeycomb carbon: a review of graphene. *Chem. Rev.* **110** (2010) 132-145.
- [23] M. A. Rafiee, J. Rafiee, Z. Wang, H. Song, Z-Z. Yu, N. Koratkar. Enhanced mechanical properties of nanocomposites at low graphene content. *ACS Nano* **3** (2009) 3884-3890.
- [24] H. W. Kroto, J. R. Heath, S. C. O'brien, R. F. Curl, R. E. Smalley.  $\text{C}_{60}$ : buckminsterfullerene. *Nature* **318** (1985) 162-163.
- [25] S. Iijima. Helical microtubules of graphitic carbon. *Nature* **354** (1991) 56-58.
- [26] S. Iijima, T. Ichihashi. Single-shell carbon nanotubes of 1-nm diameter. *Nature* **363** (1993) 603-605.
- [27] M. S. Dresselhaus, P. C. Eklund. Phonons in carbon nanotubes. *Adv. Phys.* **49** (2000) 705-814.
- [28] M. S. Dresselhaus, G. Dresselhaus, R. Saito. Physics of carbon nanotubes. *Carbon* **33** (1995) 883-891.
- [29] E. Flahaut, R. Bacsa, A. Peigney, C. Laurent. Gram-scale CCVD synthesis of double-walled carbon nanotubes. *Chem. Commun.* (2003) 1442-1443.
- [30] S. Iijima, P. M. Ajayan, T. Ichihashi. Growth model for carbon nanotubes. *Phys. Rev. Lett.* **69** (1992) 3100-3103.
- [31] M. Liu, J. M. Cowley. Structures of the helical carbon nanotubes. *Carbon* **32** (1994) 393-403.
- [32] H. Shiozawa, C. Kramberger, R. Pfeiffer, H. Kuzmany, T. Pichler, Z. Liu, K. Suenaga, H. Kataura, S. Ravi P. Silva. Catalyst and chirality dependent growth of carbon nanotubes determined through nano-test tube chemistry. *Adv. Mater.* **22** (2010) 3685-3689.
- [33] E. Cruz-Silva, F. López-Urías, E. Muñoz-Sandoval, B. G. Sumpter, H. Terrones, J-C. Charlier, V. Meunier, M. Terrones. Electronic transport and mechanical properties of phosphorus- and phosphorus-nitrogen-doped carbon nanotubes. *ACS Nano* **3** (2009) 1913-1921.
- [34] Y.-M. Choi, D.-S. Lee, R. Czerw, P.-W. Chiu, N. Grobert, M. Terrones, M. Reyes-Reyes, H. Terrones, J.-C. Charlier, P. M. Ajayan, S. Roth, D. L. Carroll, Y.-W. Park. Nonlinear behavior in

- the thermopower of doped carbon nanotubes due to strong, localized states. *Nano Lett.* **3** (2003) 839-842.
- [35] L. S. Panchakarla, A. Govindaraj, C. N. R. Rao. Nitrogen- and boron-doped double-walled carbon nanotubes. *ACS Nano* **1** (2007) 494-500.
- [36] F. Villalpando-Paez, A. Zamudio, A.L. Elias, H. Son, E.B. Barros, S.G. Chou, Y.A. Kim, H. Muramatsu, T. Hayashi, J. Kong, H. Terrones, G. Dresselhaus, M. Endo, M. Terrones, M.S. Dresselhaus. Synthesis and characterization of long strands of nitrogen-doped single-walled carbon nanotubes. *Chem. Phys. Lett* **424** (2006) 345-352.
- [37] B. G. Sumpter, V. Meunier, J. M. Romo-Herrera, E. Cruz-Silva, D. A. Cullen, H. Terrones, D. J. Smith, M. Terrones. Nitrogen-mediated carbon-nanotube growth: diameter reduction, metallicity, bundle dispersability, and bamboo-like structure formation. *ACS Nano* **1** (2007) 369-375.
- [38] S. H. Lim, H. I. Elim, X. Y. Gao, A. T. S. Wee, W. Ji, J. Y. Lee, J. Lin. Electronic and optical properties of nitrogen-doped multiwalled carbon nanotubes. *Phys. Rev. B* **73** (2006) 045402.
- [39] H. Jiang, D. Zhang, R. Wang. Silicon-doped carbon nanotubes: a potential resource for the detection of chlorophenols/chlorophenoxy radicals. *Nanotechnology* **20** (2009) 145501.
- [40] G. Guo, F. Wang, H. Sun, D. Zhang. Reactivity of silicon-doped carbon nanotubes toward small gaseous molecules in the atmosphere. *Int. J. Quantum Chem.* **108** (2008) 203-209.
- [41] D. J. Mann, M. D. Halls. Ab initio simulations of oxygen atom insertion and substitutional doping of carbon nanotubes. *J. Chem. Phys.* **116** (2002) 9014-9020.
- [42] P. A. Denis, R. Faccio, A. W. Mombru. Is it possible to dope single-walled carbon nanotubes and graphene with sulfur. *Chem. Phys. Chem.* **10** (2009) 715-722.
- [43] M. Terrones, A. Jorio, M. Endo, A. M. Rao, Y. A. Kim, T. Hayashi, H. Terrones, J.-C. Charlier, G. Dresselhaus, M. S. Dresselhaus. New direction in nanotube science. *Mater. Today* **7** (2004) 30-44.
- [44] H-S. Ahn, K-R. Lee, D-Y. Kim, S. Hanc. Field emission of doped carbon nanotubes. *Appl. Phys. Lett.* **88** (2006) 093122.
- [45] J.-C. Charlier, M. Terrones, M. Baxendale, V. Meunier, T. Zacharia, N. L. Rupesinghe, W. K. Hsu, N. Grobert, H. Terrones, G. A. J. Amaratunga. Enhanced electron field emission in B-doped carbon nanotubes. *Nano Lett.* **2** (2002) 1191-1195.
- [46] Y. Zhang, D. Zhang, C. Liu. Novel chemical sensor for cyanides: boron-doped carbon nanotubes. *J. Phys. Chem. B* **110** (2006) 4671-4674.
- [47] J. Kong, N. R. Franklin, C. Zhou, M. G. Chapline, S. Peng, K. Cho, H. Dai. Nanotube molecular wires as chemical sensors. *Science* **287** (2000) 622-625.
- [48] J. Li, G. Zhou, Y. Chen, B-L. Gu, W. Duan. Magnetism of C adatoms on BN nanostructures: implications for functional nanodevices. *J. Am. Chem. Soc.* **131** (2009) 1796-1801.
- [49] Y. Ma, P. O. Lehtinen, A. S. Foster, R. M. Nieminen. Hydrogen-induced magnetism in carbon nanotubes. *Phys. Rev. B* **72** (2005) 085451.
- [50] M. S. Ferreira, S. Sanvito. Contact-induced spin polarization in carbon nanotubes. *Phys. Rev. B* **69** (2004) 035407.

- [51] R. Kamalakaran, M. Terrones, T. Seeger, Ph. Kohler-Redlich, M. Rühle, Y. A. Kim, T. Hayashi, M. Endo. Synthesis of thick and crystalline nanotube arrays by spray pyrolysis. *Appl. Phys. Lett.* **77** (2000) 3385-3387.
- [52] M. Pinault, M. Mayne-L'Hermite, C. Reynaud, V. Pichot, P. Launois, D. Ballutaud. Growth of multiwalled carbon nanotubes during the initial stages of aerosol-assisted CCVD. *Carbon* **43** (2005) 2968-2976.
- [53] M. Mayne, N. Grobert, M. Terrones, R. Kamalakaran, M. Rühle, H. W. Kroto, D. R. M. Walton. Pyrolytic production of aligned carbon nanotubes from homogeneously dispersed benzene-based aerosols. *Chem. Phys. Lett* **338** (2001) 101-107.
- [54] W. Zhou, Z. Han, J. Wang, Y. Zhang, Z. Jin, X. Sun, Y. Zhang, C. Yan, Y. Li. Copper catalyzing growth of single-walled carbon nanotubes on substrates. *Nano Lett.* **6** (2006) 2987-2990.
- [55] N. Shah, Y. Wang, D. Panjala, G. P. Huffman. Production of hydrogen and carbon nanostructures by non-oxidative catalytic dehydrogenation of ethane and propane. *Energ. Fuel.* **18** (2004) 727-735.
- [56] X. Li, X. Tu, S. Zaric, K. Welsher, W. S. Seo, W. Zhao, H. Dai. Selective synthesis combined with chemical separation of single-walled carbon nanotubes for chirality selection. *J. Am. Chem. Soc.* **129** (2007) 15770-15771.
- [57] J. C. Charlier, H. Amara, Ph. Lambin. Catalytically assisted tip growth mechanism for single-wall carbon nanotubes. *ACS Nano* **1** (2007) 202-207.
- [58] Q. Fu, S. Huang, J. Liu. Chemical vapor depositions of single-walled carbon nanotubes catalyzed by uniform Fe<sub>2</sub>O<sub>3</sub> nanoclusters synthesized using diblock copolymer micelles. *J. Phys. Chem. B* **108** (2004) 6124-6129.
- [59] S. M. Bachilo, L. Balzano, J. E. Herrera, F. Pompeo, D. E. Resasco, R. B. Weisman. Narrow (n,m)-distribution of single-walled carbon nanotubes grown using a solid supported catalyst. *J. Am. Chem. Soc.* **125** (2003) 11186-11187.
- [60] H. M. Cheng, F. Li, G. Su, H. Y. Pan, L. L. He, X. Sun, M. S. Dresselhaus. Large-scale and low-cost synthesis of single-walled carbon nanotubes by the catalytic pyrolysis of hydrocarbons. *Appl. Phys. Lett.* **72** (1998) 3282-3284.
- [61] K. Hata, D. N. Futaba, K. Mizuno, T. Namai, M. Yumura, S. Iijima. Water-assisted highly efficient synthesis of impurity-free single-walled carbon nanotubes. *Science* **306** (2004) 1362-1364.
- [62] P. Ayala, A. Grüneis, T. Gemming, D. Grimm, C. Kramberger, M. H. Rummeli, Jr. F. L. Freire, H. Kuzmany, R. Pfeiffer, A. Barreiro, B. Büchner, T. Pichler. Tailoring n-doped single and double wall carbon nanotubes from a nondiluted carbon/nitrogen feedstock. *J. Phys. Chem. C* **111** (2007) 2879-2884.
- [63] S. Fan, M. G. Chapline, N. R. Franklin, T. W. Tombler, A. M. Cassell, H. Dai. Self-oriented regular arrays of carbon nanotubes and their field emission properties. *Science* **283** (1999) 512-514.
- [64] N. Grobert, W. K. Hsu, Y. Q. Zhu, J. P. Hare, H. W. Kroto, D. R. M. Walton, M. Terrones, H. Terrones, Ph. Redlich, M. Rühle, R. Escudero, F. Morales. Enhanced magnetic coercivities in Fe nanowires. *Appl. Phys. Lett.* **75** (1999) 3363-3365.
- [65] B. J. Hinds, N. Chopra, T. Rantell, R. Andrews, V. Gavalas, L. G. Bachas. Aligned multiwalled carbon nanotube membranes. *Science* **303** (2004) 62-65.

- [66] C. Wei, L. Dai, A. Roy, T. B. Tolle. Multifunctional chemical vapor sensors of aligned carbon nanotube and polymer composites. *J. Am. Chem. Soc.* **128** (2006) 1412-1413.
- [67] A. Oberlin, M. Endo, T. Koyama. Filamentous growth of carbon through benzene decomposition. *J. Cryst. Growth* **32** (1976) 335-349.
- [68] P. C. Eklund, J. M. Holden, R. A. Jishi. Vibrational modes of carbon nanotubes: spectroscopy and theory. *Carbon* **33** (1995) 959-972.
- [69] M. S. Dresselhaus, G. Dresselhaus, R. Saito, A. Jorio. Raman spectroscopy of carbon nanotubes. *Phys. Rep.* **409** (2005) 47-99.
- [70] S. B. Cronin, A. K. Swan, M. S. Ünlü, B. B. Goldberg, M. S. Dresselhaus, M. Tinkham. Measuring the uniaxial strain of individual single-wall carbon nanotubes: resonance Raman spectra of atomic-force-microscope modified single-wall nanotubes. *Phys. Rev. Lett.* **93** (2004) 167401.
- [71] A. C. Ferrari, J. C. Meyer, V. Scardaci, C. Casiraghi, M. Lazzeri, F. Mauri, S. Piscanec, D. Jiang, K. S. Novoselov, S. Roth, A. K. Geim. Raman spectrum of graphene and graphene layers. *Phys. Rev. Lett.* **97** (2006) 187401.
- [72] M. Terrones, A. G. Souza Filho, A. M. Rao. Doped carbon nanotubes: synthesis, characterization and applications. *Carbon Nanotubes*. A. Jorio, G. Dresselhaus and M. S. Dresselhaus (eds). Springer-Verlag Berlin Heidelberg: 2008; pp 531-566.
- [73] M. Moniruzzaman, K. I. Winey. Polymer nanocomposites containing carbon nanotubes. *Macromolecules* **39** (2006) 5194-5205.
- [74] C-Y. Hu, Y-J. Xu, S-W. Duo, R-F. Zhang, M-S. Li. Non-covalent functionalization of carbon nanotubes with surfactants and polymers. *J. Chin. Chem. Soc.* **56** (2009) 234-239.
- [75] K. Mylvaganam, L. C. Zhang. Fabrication and application of polymer composites comprising carbon nanotubes. *Recent Pat. Nanotechnol.* **1** (2007) 59-65.
- [76] B. Balasubramanian, M. Burghard. Chemically functionalized carbon nanotubes. *Small* **1** (2005) 180-192.
- [77] C. A. Dyke, J. M. Tour. Covalent functionalization of single-walled carbon nanotubes for materials applications. *J. Phys. Chem. A* **108** (2004) 11151-11159.
- [78] S. Banerjee, T. Hemraj-Benny, S. S. Wong. Covalent surface chemistry of single-walled carbon nanotubes. *Adv. Mater.* **17** (2005) 17-29.
- [79] A. Hirsch. Functionalization of single-walled carbon nanotubes. *Angew. Chem. Int. Ed.* **41** (2002) 1853-1859.
- [80] S. Chen, D. Chen, G. Wu. Grafting of poly(tBA) and ptBA-b-PMMA onto the surface of SWNTs using carbanions as the initiator. *Macromol. Rapid Commun.* **27** (2006) 882-887.
- [81] Z. Yao, N. Braidy, G. A. Botton, A. Adronov. Polymerization from the surface of single-walled carbon nanotubes - preparation and characterization of nanocomposites. *J. Am. Chem. Soc.* **125** (2003) 16015-16024.
- [82] F. Buffa, H. Hu, D. E. Resasco. Side-wall functionalization of single-walled carbon nanotubes with 4-hydroxymethylaniline followed by polymerization of  $\epsilon$ -caprolactone. *Macromolecules* **38** (2005) 8258-8263.

- [83] Y. Liu, A. Adronov. Preparation and utilization of catalyst-functionalized single-walled carbon nanotubes for ring-opening metathesis polymerization. *Macromolecules* **37** (2004) 4755-4760.
- [84] J. Chattopadhyay, A. K. Sadana, F. Liang, J. M. Beach, Y. Xiao, R. H. Hauge, W. E. Billups. Carbon nanotube salts. Arylation of single-wall carbon nanotubes. *Org. Lett.* **7** (2005) 4067-4069.
- [85] Y. Ma, W. Cheung, D. Wei, A. Bogozzi, P. L. Chiu, L. Wang, F. Pontoriero, R. Mendelsohn, H. He. Improved conductivity of carbon nanotube networks by in situ polymerization of a thin skin of conducting polymer. *ACS Nano* **2** (2008) 1197-1204.
- [86] M. Dehonor, K. Masenelli-Varlot, A. González-Montiel, C. Gauthier, J. Y. Cavallé, H. Terrones, M. Terrones. Nanotube brushes: polystyrene grafted covalently on CN<sub>x</sub> nanotubes by nitroxide-mediated radical polymerization. *Chem. Commun.* (2005) 5349-5351.
- [87] H. Li, F. Cheng, A. M. Duft, A. Adronov. Functionalization of single-walled carbon nanotubes with well-defined polystyrene by "click" coupling. *J. Am. Chem. Soc.* **127** (2005) 14518-14524.
- [88] F. Liang, J. M. Beach, K. Kobashi, A. K. Sadana, Y. I. Vega-Cantu, J. M. Tour, W. E. Billups. In situ polymerization initiated by single-walled carbon nanotube salts. *Chem. Mater.* **18** (2006) 4764-4767.
- [89] S. Pekker, J.-P. Salvetat, E. Jakab, J.-M. Bonard, L. Forró. Hydrogenation of carbon nanotubes and graphite in liquid ammonia. *J. Phys. Chem. B* **105** (2001) 7938-7943.
- [90] J. J. Stephenson, A. K. Sadana, A. L. Higginbotham, J. M. Tour. Highly functionalized and soluble multiwalled carbon nanotubes by reductive alkylation and arylation: the Billups reaction. *Chem. Mater.* **18** (2006) 4658-4661.
- [91] Y. H. Lu, R. Q. Wu, L. Shen, M. Yang, Z. D. Sha, Y. Q. Cai, P. M. He, Y. P. Feng. Effects of edge passivation by hydrogen on electronic structure of armchair graphene nanoribbon and band gap engineering. *Appl. Phys. Lett.* **94** (2009) 122111.
- [92] K.I. Bolotin, K. J. Sikes, Z. Jiang, M. Klima, G. Fudenberg, J. Hone, P. Kim, H.L. Stormer. Ultrahigh electron mobility in suspended graphene. *Solid State Commun.* **146** (2008) 351-355.
- [93] A. K. Geim, K. S. Novoselov. The rise of graphene. *Nature* **6** (2007) 183-191.
- [94] C. Lee, X. Wei, J. W. Kysar, J. Hone. Measurement of the elastic properties and intrinsic strength of monolayer graphene. *Science* **321** (2008) 385-388.
- [95] A. A. Balandin, S. Ghosh, W. Bao, I. Calizo, D. Teweldebrhan, F. Miao, C. N. Lau. Superior thermal conductivity of single-layer graphene. *Nano Lett.* **8** (2008) 902-907.
- [96] M. S. Dresselhaus, G. Dresselhaus. Intercalation compounds of graphite. *Adv. Phys.* **51** (2002) 1-186.
- [97] H. Shioyama. Cleavage of graphite to graphene. *J. Mater. Sci. Lett.* **20** (2001) 499-500.
- [98] S. Stankovich, R. D. Piner, X. Chen, N. Wu, S. T. Nguyen, R. S. Ruoff. Stable aqueous dispersions of graphitic nanoplatelets via the reduction of exfoliated graphite oxide in the presence of poly(sodium 4-styrenesulfonate). *J. Mater. Chem.* **16** (2006) 155-158.
- [99] L. M. Viculis, J. J. Mack, O. M. Mayer, H. T. Hahn, R. B. Kaner. Intercalation and exfoliation routes to graphite nanoplatelets. *J. Mater. Chem.* **15** (2005) 974-978.
- [100] D. D. L. Chung. Review graphite. *J. Mater. Sci.* **37** (2002) 1475-1489.

- [101] C. Berger, Z. Song, T. Li, X. Li, A. Y. Ogbazghi, R. Feng, Z. Dai, A. N. Marchenkov, E. H. Conrad, P. N. First, W. A. de Heer. Ultrathin epitaxial graphite: 2D electron gas properties and a route toward graphene-based nanoelectronics. *J. Phys. Chem. B* **108** (2004) 19912-19916.
- [102] H. Huang, W. Chen, S. Chen, A. T. S. Wee. Bottom-up growth of epitaxial graphene on 6H-SiC(0001). *ACS Nano* **2** (2008) 2513-2518.
- [103] A. Reina, X. Jia, J. Ho, D. Nezich, H. Son, V. Bulovic, M. S. Dresselhaus, J. Kong. Large area, few-layer graphene films on arbitrary substrates by chemical vapor deposition. *Nano Lett.* **9** (2009) 30-35.
- [104] X. Yang, X. Dou, A. Rouhanipour, L. Zhi, H. J. Räder, K. Müllen. Two-dimensional graphene nanoribbons. *J. Am. Chem. Soc.* **130** (2008) 4216-4217.
- [105] H. R. Gutiérrez, U. J. Kim, J. P. Kim, P. C. Eklund. Thermal conversion of bundled carbon nanotubes into graphitic ribbons. *Nano Lett.* **5** (2005) 2195-2201.
- [106] B. Obradovic, R. Kotlyar, F. Heinz, P. Matagne, T. Rakshit, M. D. Giles, M. A. Stettlera, D. E. Nikonov. Analysis of graphene nanoribbons as a channel material for field-effect transistors. *Appl. Phys. Lett.* **88** (2006) 142102.
- [107] K. Nakada, M. Fujita, G. Dresselhaus, M. S. Dresselhaus. Edge state in graphene ribbons: nanometer size effect and edge shape dependence. *Phys. Rev. B* **54** (1996) 17954-17961.
- [108] F. Cervantes-Sodi, G. Csányi, S. Piscanec, A. C. Ferrari. Edge-functionalized and substitutionally doped graphene nanoribbons: electronic and spin properties. *Phys. Rev. B* **77** (2008) 165427.
- [109] M. Prato, K. Kostarelos, A. Blanco. Functionalized carbon nanotubes in drug design and discovery. *Accounts Chem. Res.* **41** (2008) 60-68.
- [110] J. Huang, Y. Liu, T. You. Carbon nanofiber based electrochemical biosensors: a review. *Anal. Methods* (2010) 1-15.
- [111] J. Liang, Y. Wang, Y. Huang, Y. Ma, Z. Liu, J. Cai, C. Zhang, H. Gao, Y. Chen. Electromagnetic interference shielding of graphene/epoxy composites. *Carbon* **47** (2009)
- [112] D. D. L. Chung. Electromagnetic interference shielding effectiveness of carbon materials. *Carbon* **39** (2001) 279-285.
- [113] S. Stankovich, D. A. Dikin, G. H. B. Dommett, K. M. Kohlhaas, E. J. Zimney, E. A. Stach, R. D. Piner, S. T. Nguyen, R. S. Ruoff. Graphene-based composite materials. *Nature* **442** (2006) 282-286.
- [114] T. Ramanathan, A. A. Abdala, S. Stankovich, D. A. Dikin, M. Herrera-Alonso, R. D. Piner, D. H. Adamson, H. C. Schniepp, X. Chen, R. S. Ruoff, S. T. Nguyen, I. A. Aksay, R. K. Prud'homme, L. C. Brinson. Functionalized graphene sheets for polymer nanocomposites. *Nature Nanotechnol.* **3** (2008) 327-331.
- [115] M. Burghard, H. Klauk, K. Kern. Carbon-based field-effect-transistors for nanoelectronics. *Adv. Mater.* **21** (2009) 2586-2600.
- [116] E. Yoo, T. Okata, T. Akita, M. Kohyama, J. Nakamura, I. Honma. Enhanced electrocatalytic activity of Pt subnanoclusters on graphene nanosheet surface. *Nano Lett.* **9** (2009) 2255-2259.

- [117] G. M. Scheuermann, L. Rumi, P. Steurer, W. Bannwarth, R. Mülhaupt. Palladium nanoparticles on graphite oxide and its functionalized graphene derivatives as highly active catalysts for the Suzuki-Miyaura coupling reaction. *J. Am. Chem. Soc.* **131** (2009) 8262-8270.
- [118] J. D. Fowler, M. J. Allen, V. C. Tung, Y. Yang, R. B. Kaner, B. H. Weiller. Practical chemical sensors from chemically derived graphene. *ACS Nano* **3** (2009) 301-306.
- [119] F. Schedin, A.K. Geim, S. V. Morozov, E. W. Hill, P. Blake, M. I. Katsnelson, K. S. Novoselov. Detection of individual gas molecules adsorbed on graphene. *Nat. Mater.* **6** (2007) 652-655.
- [120] K. Müllen, J. P. Rabe. Nanographenes as active components of single-molecule electronics and how a scanning tunneling microscope puts them to work. *Accounts Chem. Res.* **41** (2008) 511-520.
- [121] A. K. Singh, M. A. Ribas, B. I. Yakobson. H-spillover through the catalyst saturation: an ab initio thermodynamics study. *ACS Nano* **3** (2009) 1657-1662.
- [122] E. Yoo, J. Kim, E. Hosono, H-S. Zhou, T. Kudo, I. Honma. Large reversible Li storage of graphene nanosheet families for use in rechargeable lithium ion batteries. *Nano Lett.* **8** (2008) 2277-2282.
- [123] N. L. Rangel, J. M. Seminario. Graphene terahertz generators for molecular circuits and sensors. *J. Phys. Chem. A* **112** (2008) 13699-13705.
- [124] Y-M. Lin, K. A. Jenkins, A. Valdes-Garcia, J. P. Small, D. B. Farmer, P. Avouris. Operation of graphene transistors at gigahertz frequencies. *Nano Lett.* **9** (2009) 422-426.
- [125] G. E. Moore. Cramming more components onto integrated circuits. *Electronics* **38** (1965) 114-117.
- [126] P. Zhao, J. Chauhan, J. Guo. Computational study of tunneling transistor based on graphene nanoribbon. *Nano Lett.* **9** (2009) 684-688.

# **Chapter 2 Nanocomposites from polyaniline (PAni), polypyrrole (PPy), and multi-walled carbon nanotubes (MWNTs)**

In the previous chapter we gave a general background on the properties and synthesis of carbon nanotubes and their polymer composites. Now, we remember some generalities about composites and introduce some conducting polymers, specifically, polyanilines and polypyrrole, in order to establish the importance of their composites with carbon nanotubes. Next, we explain some of the most relevant results on the characterization of composites from multi-walled carbon nanotubes, polyaniline, and sulfonated polyaniline.

## **2.1 Introduction**

Carbon materials have shown to be useful in the production of composites. In particular, carbon nanotubes (CNTs), due to their unique mechanical, thermal, electronic, and chemical properties, have paved the way to the synthesis and production of CNTs-polymer composites with improved properties and with a wide range of applications [1-5]. Functional composites derived from nanotubes and polymers are promising materials with superior properties that may become part of our daily lives, as integrating parts of practical devices such as cars, wearable electronics, flexible and electronic newspapers, intelligent buildings and other technologies to come. These composites usually present a synergistic effect derived from the properties of nanotubes and polymer, thus presenting properties that are not present in the individual components [1].

Due to properties [1] such as extremely high longitudinal elastic modulus (terapascal range), high thermal and electrical conductivity along the axial direction, low density, and high surface area, carbon nanotubes can compete with carbon or glass fibers, which are relatively large (micrometer-size diameters) and brittle, hence making nanotubes perfect candidates as fillers in polymer composites. For example, 10 nm-diameter nanotubes have an interfacial area almost 1000 times greater than that of 10  $\mu\text{m}$  fibers of the same volume. This may modify the properties of the polymer by affecting its chain entanglements, its morphology and its crystallinity. As a result, the composite can be much tougher and stronger than what would be expected from the polymer. Moreover, carbon nanotubes are flexible and can be easily bent, buckled, twisted, flattened or tangled without breaking, in contrast to carbon fibers; this is a direct consequence of the structure of nanotubes (a rolled graphene sheet into a seamless cylinder) and carbon fibers (randomly stacked graphene layers). Furthermore, nanotubes with high aspect ratios ( $\sim 10^4:1$ ) can form conductive paths throughout the matrix with just very small volume fractions of nanotubes, rendering the composite both strong and electrically conductive, and thus taking maximum advantage of their properties.

However, important problems arise when producing these composites, such as: poor interaction between CNTs and the polymer matrix, which results in lack of effective stress transfer and pull-out effects (sliding of CNTs from the polymer interface); bundling of CNTs, due to Van der Waals forces; and poor dispersion of CNTs in many solvents and polymers, which leads to heterogeneous dispersions. Examples of these are shown in [figure 2.1](#). Another problem is how to keep the alignment of CNTs (which can be achieved by extrusion techniques), since composites with aligned CNTs show improved mechanical properties in contrast to those with randomly oriented CNTs [1, 5]. Another issue is the high viscosity of polymer-CNTs mixtures due to the large surface area of CNTs [6], which makes extrusion difficult. These challenges have made CNTs-polymer composite molding and processing difficult.

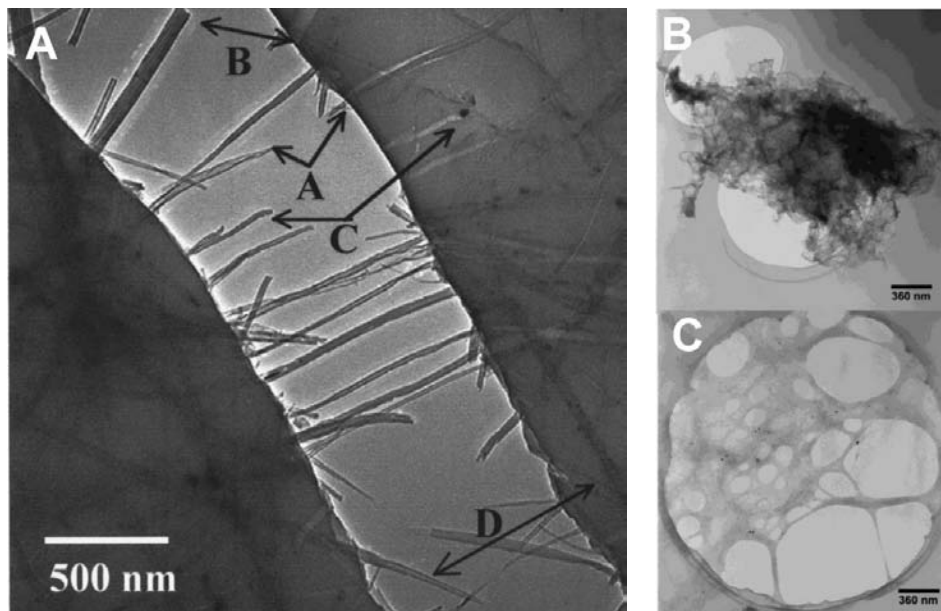


**Figure 2.1. Detrimental effects observed in carbon nanotube-polymer composites.** (A) MWNT/polystyrene composite fracture, in which some tubes are broken (A–B) but others are pulled-out (C–D); if this last effect predominates, the net effect will be a reduction in the interaction between the tubes and the polymer matrix [7]. (B–C) SWNTs/polymethylmetacrylate composite, showing (B) bundled SWNTs poorly dispersed in the PMMA matrix; in (C) though dispersion has improved, some tube aggregates are still present [8].

To overcome these issues, several approaches for the synthesis of composites have been performed [5], and can be classified as: physical (ball milling, mixing, electrostatic adsorption, non-covalent modification) and chemical (covalent functionalization). While physical methods allow the preservation of many of the properties of CNTs, the resulting composites most times lack of a strong interaction between the polymer matrix and CNTs. In contrast, although chemical methods (covalent functionalization) may alter some properties of CNTs through changes in hybridization (from  $sp^2$  to  $sp^3$ ), they allow researchers to tailor and custom the properties of CNTs-polymer nanocomposites.

Covalent functionalization approaches include *grafting to* and *grafting from* methods [9]. In *grafting to* methods, polymer chains are covalently linked to CNTs, thus allowing a precise control on the molecular weight of the polymer; nonetheless, once the first polymer chains are bonded to the tubes, steric hindrance limits the insertion of more polymer chains and thus limits the functionalization degree and the synthesis of CNTs embedded in a polymer matrix. On the other hand, *grafting from* procedures allow the synthesis of true CNTs-polymer nanocomposites, but sometimes without control on the functionalization degree.

In this thesis work, we used a *grafting from* approach, specifically a reductive alkylation method which is called the nanotube salts reaction. In this method, carbon nanotubes form highly reactive nanotube salts upon the adsorption of electrons and lithium ions from the liquid ammonia medium. The nanotube salts method has proven to be very effective for the functionalization of single-walled (SWNTs) and multi-walled carbon nanotubes (MWNTs) with vinylic monomers such as styrene [10] and acrylates [11]. In this chapter, we explain how we synthesized composites from MWNTs, polyaniline, sulfonated polyaniline and polypyrrole by means of the nanotube salts method. We chose aniline, a sulfonated aniline and pyrrole as monomers because of the unique electronic properties of their electronically conducting polymers (ECPs) [12-15], such as: doping, conductivity, electrocatalysis, and electrochromism, among others. Since these monomers possess conjugated bonds, their polymerization by the nanotube salts method should be possible, in a similar fashion to the polymerization of vinylic monomers. It is of interest to see what kind of changes might occur on the morphology and structure of carbon nanotubes after polymerization.

Thus, the original objective of this thesis was to functionalize MWNTs and nitrogen doped MWNTs (CN<sub>x</sub>) with these polymers by *in situ* polymerization with the nanotube salts method. Once this part of the research was completed, we would test this method with SWNTs and nitrogen-doped SWNTs. In addition, we would also synthesize composites from these tubes by means of other polymerization methods such as atomic-transfer radical polymerization (ATRP), nitroxide-mediated radical polymerization (NMRP), and the electrochemical methods cyclic voltammetry and chronoamperometry; and by using monomers and precursors such as 4-yodoaniline, 4,4'-sulfonylbenzoic acid, ethylene glycol and terephthalic acid. Finally, these alternative methods were going to be compared with the nanotube salts method.

## 2.2 Polyaniline (PAni), polypyrrole (PPy), and their composites with multi-walled carbon nanotubes (MWNTs)

Electronically conducting polymers (ECPs) are promising materials due to their optical and electronic properties, which makes possible their use in: electronic conduction [12], light-emitting diodes [16, 17], rechargeable batteries [18], sensors [19] [20], actuators [21], electronic devices [22], electromagnetic interference shielding (EMI shielding) [23], corrosion inhibition [24] and biomaterials [25]. Some of the most studied ECPs are polyacetylene, polythiophene, polypyrrole, and polyaniline, the last two being of interest for this thesis work.

### 2.2.1 Properties of electronically conducting polymers: PAni and PPy

Both polyaniline (PAni) and polypyrrole (PPy) share similar characteristics as: chemical and thermal stability, easy chemical or electrochemical synthesis, and doping processes which involve ion exchange. Doping occurs as a result of charge generation in the polymer, which requires the intake of counter-ions from the medium to balance the electrical charge. The doping process also changes the physical properties of the polymer, such as color (electrochromism) [22, 26, 27]. Figure 2.2 shows how the conductivity of PAni changes with the acidity of the solution.

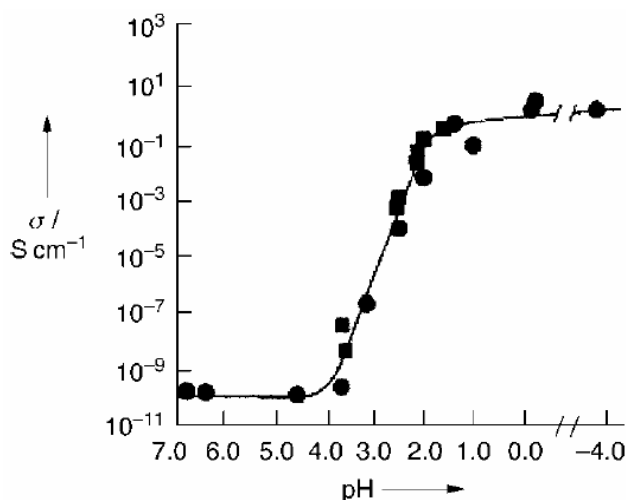


**Figure 2.2. Conductivity of emeraldine base as a function of the pH of the HCl dopant solution, as it undergoes protonic acid doping. Filled squares and circles represent two different series of experiments [12].**

On the other hand, the doping agent can also be bonded to the monomer (for example, carboxylic or sulfonic groups), in which case the synthesized polymer is a self-doped polymer. For example, the sulfonic acid group ( $-\text{SO}_3\text{H}$ ) [13] makes PANi self-doping, catalyzes its redox process, makes its conductivity independent of external protonation in a broad pH range ( $0 \leq \text{pH} \leq 7.5$ ), and localizes the electronic charge. Furthermore, the sulfonic acid group improves the solubility of PANi in aqueous solutions [13, 28] and its thermal stability [29], makes n-doping possible by redox reduction of the polymer [30] and eliminates the need of an electrolyte, which makes SPANi useful in rechargeable batteries.

Depending on the applied potential and/or the doping process, the obtained ECP can be either conducting or insulating. Figure 2.3 compares the conductivity of conducting polymers and other materials.

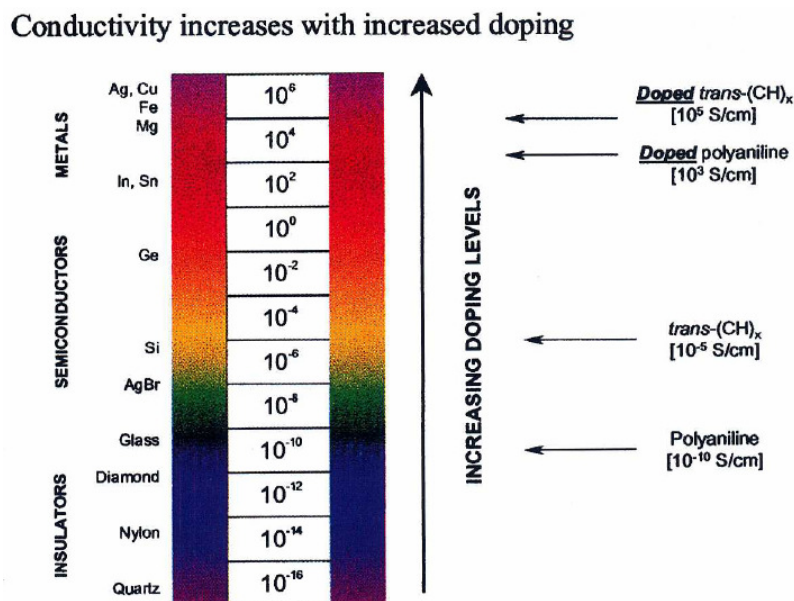
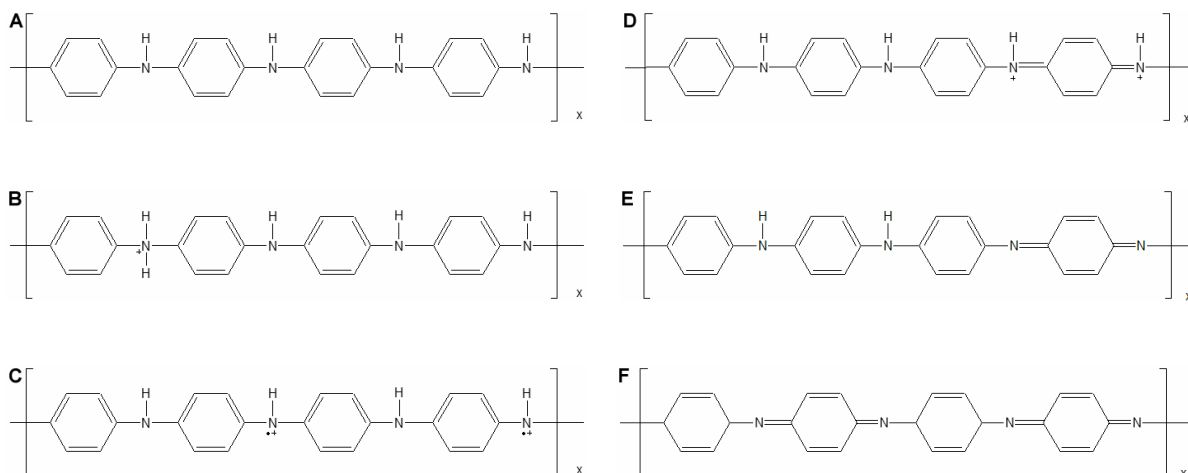


Figure 2.3. Conductivity comparison between electronic polymers and other materials [12].

In the particular case of PANi [14], doping also occurs by protonation of the amino group, which acts as a base. Hence, for PANi, conductivity depends not only on oxidation and anionic doping, but also on protonation. PANi possesses six main oxidation states [24], shown at figure 2.4.



**Figure 2.4. Main oxidation states of PANi.** (A) Fully reduced leucoemeraldine base; (B) protonated leucoemeraldine; (C) polaron of emeraldine salt; (D) bipolaron of emeraldine salt; (E) emeraldine base, partially oxidized; (F) fully oxidized pernigraniline. Leucoemeraldine, emeraldine base, and pernigraniline are insulating due to lack of anionic and protonic doping. Emeraldine salt, which is partially oxidized and doped both by protons and anions, represents the most conductive state [24].

Another characteristic of PPy and PANi is autocatalysis, that is, the oxidation potential of the synthesized polymer is lower than that of the monomer; hence, the polymer is also oxidized during electropolymerization. Both polymers are synthesized by chemical or electrochemical methods from acidic solutions of their corresponding monomers and an electrolyte. The main advantage of electrochemical methods is that they allow an easy and precise control on the electrical properties of these polymers by protonation and/or charge-transfer doping [12], as well as on the growth rate, and film thickness [31]; nevertheless, the properties of the resulting polymer are influenced by many variables such as solvent composition, monomer concentration, electrolyte concentration, applied potential, current density, preparation temperature, and the nature of the electrode material [31]. On the other hand, chemical methods allow the production of bulk quantities of material, in which the interaction with the medium is not limited to the electrode/electrolyte interface, as it occurs in electrochemical methods.

### 2.2.2 Nanocomposites from carbon nanotubes (CNTs), PANi, and PPy

Despite their remarkable electrical properties, ECPs are usually brittle, and their redox activity may decrease upon electrochemical cycling, thus limiting their possible application. Due to the outstanding mechanical and electronic properties of CNTs, and

the electronic properties of ECPs, nanocomposites generally show improved properties derived from the properties of each component [15, 32-37], thus making the synthesis of ECPs/CNTs composites a very attractive field, for example for the development of transistors and logic gates [38], sensors [39], and in electrocatalysis [39, 40]. These improvements are often due to charge transfer between polymer and CNTs, and to an increase in the load of CNTs [32, 34, 41, 42]; in addition, they occur with obvious changes in morphology and size, for example, polymer particles randomly mixed with the tubes, sometimes deposited over them; or as a uniform coating on the tubes; or even as a polymer matrix in which the tubes are fully immersed. Conversely, some properties may not be enhanced but depressed, such as: optical activity and electrical resistance [37], or thermal conductivity [43].

Raman spectra of MWNTs/polyaniline nanocomposites [33, 36, 40, 41, 44, 45] show main features from MWNTs at  $1585\text{ cm}^{-1}$  and  $1350\text{ cm}^{-1}$  corresponding to the G and D bands respectively, and several features from PANi at ca. 806, 1170, 1260, 1330, 1480, and  $1590\text{ cm}^{-1}$ , corresponding to: deformation of the benzenoid ring, C-H bending of the quinoid ring, C-H bending of the benzenoid ring, C-N<sup>+</sup> stretching, C=N and C-C stretching vibration of the quinoid ring, and C-C stretching vibration of the benzenoid ring, respectively. The  $1480\text{ cm}^{-1}$  and  $1590\text{ cm}^{-1}$  bands are of interest, since the intensity ratio is useful for the determination of the oxidation state of PANi: a more intense band at  $1480\text{ cm}^{-1}$  reveals that PANi is in its conducting state as emeraldine salt. Some typical bands shift to higher wavenumbers with increasing MWNTs content, showing constrained motion of PANi chains and thus, a strong interaction between quinoid rings of PANi and MWNTs. Figure 2.5A compares the Raman features for PANi, MWNTs, and their composites.

Structural characterization of polymers by means of X-ray diffraction (XRD) is not a common characterization method, since most polymers are amorphous materials presenting only small crystalline domains. Nonetheless, many researchers have reported XRD studies on PANi-MWNTs nanocomposites, which reveal characteristic features [41, 45, 46] for both components. CVD-grown MWNTs show significant signals at  $25.9^\circ$  and  $43^\circ$ , ascribed to the (002) and (111) planes of the graphite-like structure and the catalytic particles encapsulated inside MWNTs, respectively. On the other hand,

PAni displays various features at ca. 15°, 20°, 25°, 27°, and 30° associated to PAni in its emeraldine salt form, corresponding to the (011), (020), (200), (121), (022) planes [47]; the 15° and 25° peaks are ascribed to periodicity perpendicular to the polymer chain, and the 20° peak to periodicity parallel to the polymer chain [46]; an additional peak at 6.4° can be related to PAni chains organized into nanofibers or lamellae [37]. Some of these features are shown at figure 2.5B.

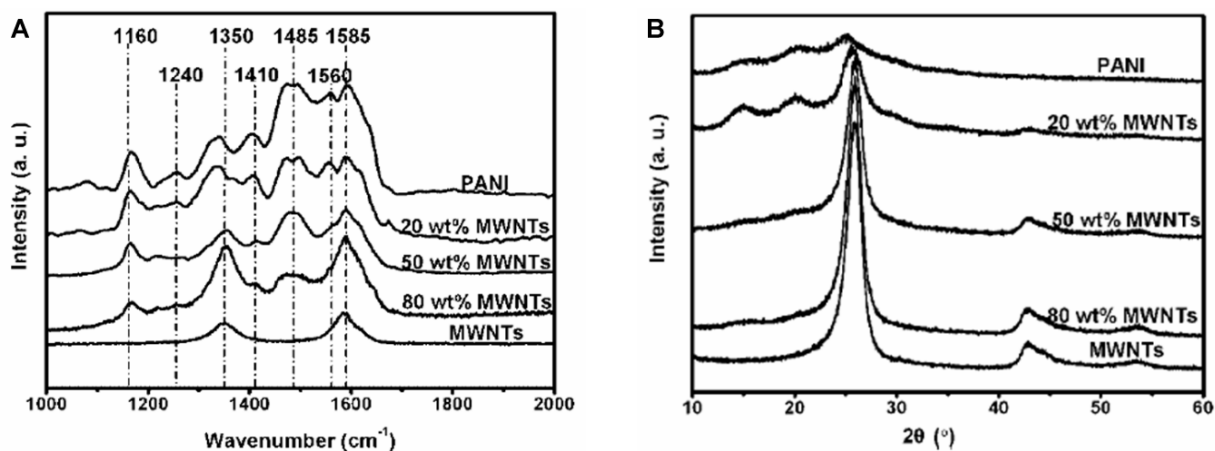


**Figure 2.5. Raman spectra and X-ray diffraction patterns for MWNTs, PANi, and their composites.** As the PANi content increases, both the characteristic Raman features (A) and diffraction peaks (B) for PANi become more evident [41].

We should emphasize that the properties of nanocomposites obtained from carbon nanotubes and electronically conducting polymers will strongly depend on the synthesis method, the type of tubes, and on the oxidation state and doping of ECPs. Understanding the properties of these composites is very important in order to get the most in their applications. Nevertheless, the synthesis method remains a critical issue for the production of engineered composites based on carbon nanotubes and conducting polymers.

### 2.2.3 Synthesis methods for nanocomposites derived from CNTs, PANi and PPy

In this regard, nanocomposites from CNTs, PANi and PPy are synthesized by several methods, which can be grouped as [15]: (i) direct mixing of the ECP with the CNTs [33, 42]; (ii) *in situ* chemical polymerization of the corresponding monomer in the

presence of CNTs [35, 36, 45-51], in which covalent bonding may occur; and (iii) electrochemical synthesis of ECP on a CNTs electrode [40, 52-54]. Covalent bonding includes some of the most versatile and widespread *grafting* methods. Though covalent functionalization alters the  $sp^2$  hybridization network in carbon nanotubes - and hence, it may also change some of their properties - it offers an efficient way in which better dispersion of CNTs in composites can be achieved, with strong interactions taking place between CNTs and the polymer matrix. At the beginning of this thesis work we used a recently developed *grafting from* technique, the nanotube salts method, to produce nanocomposites from MWNTs,  $CN_x$ , polyanilines and polypyrrole, because we considered this method to be a good alternative for the polymerization of aromatic monomers. In addition, we wished to combine the unique properties of each component and thus to obtain an outstanding material with enhanced electrical and mechanical properties.

#### **2.2.4 Nanocomposites from PANi, PPy, and MWNTs synthesized by the nanotube salts method**

*In situ* polymerization of pyrrole or anilines and carbon nanotubes by reductive alkylation had not been reported before this work. Reductive alkylation has been used in the reduction of amines [55] and aromatic compounds [56, 57], and it offers a simple, two-step functionalization method for graphite [58, 59], fullerenes [60], single-walled carbon nanotubes (SWNTs) [11, 59, 61-63], and multi-walled carbon nanotubes (MWNTs) [59, 64].

The nanotube-salts reaction occurs by a single-electron transfer mechanism [63], and is held in liquid ammonia. It is already known that liquid ammonia solutions can dissolve alkaline metals and solvate their valence electrons [65]. If an  $sp^2$ -hybridized carbon material such as graphite, buckyballs, or carbon nanotubes (CNTs) is added, it captures electrons from ammonia and acquires a negative charge, counter-balanced by alkali cations (lithium, for example), thus forming salts. It should be noted that the blue color of the reaction medium, associated to solvated electrons in liquid  $NH_3$ , disappears

and indicates charge transfer to the carbon material [61], unless excess alkali metal is used.

A general reaction scheme, exemplified for SWNTs, is depicted in figure 2.6. The experimental setup used in this thesis for the *in situ* synthesis of composites from multi-walled carbon nanotubes, polypyrrole and polyanilines is fully explained in the next section.

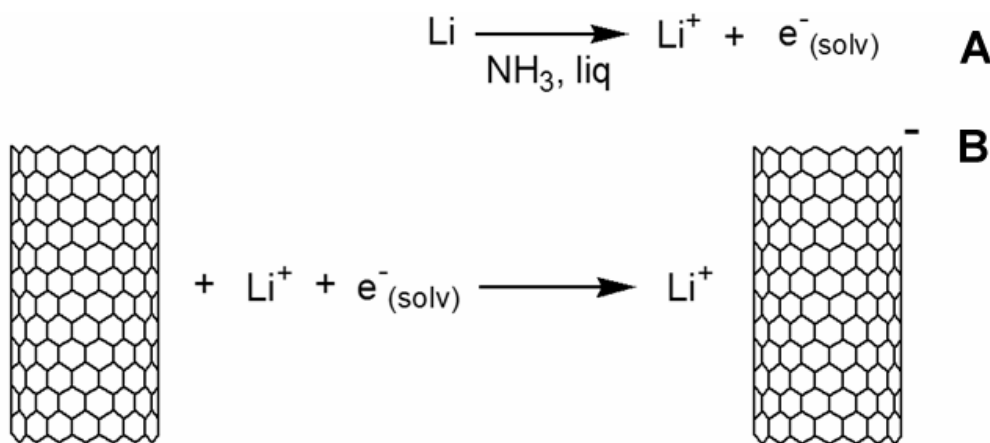


**Figure 2.6. Scheme for nanotube-lithium salt formation in liquid ammonia.** (A) Lithium is readily dissolved in liquid ammonia, leading to solvated electrons and lithium cations; (B) carbon nanotubes take electrons from ammonia, thus acquiring a negative charge which is counter-balanced by  $\text{Li}^+$ . Double bonds are omitted for clarity. For SWNTs, the formation of salts results in electrostatic repulsion and debundling of tubes; this can be followed by changes in the radial breathing modes (RBMs) of the Raman spectrum [11, 63, 66].

Nanotube salts are highly reactive towards alkyl halides, alkyl sulfides, and water. Great care should be taken when handling samples by keeping them under an inert atmosphere or in a dry, aprotic solvent. Other approaches for the formation of nanotube salts involve doping with lithium and sodium naphthalide radical ions, or metallic lithium and catalytic amounts of 4,4'-di-*tert*-butyl-biphenyl (DTBP) as electron carrier [67]. Nanotube salts form true thermodynamically stable solutions in polar organic solvents [66] such as sulfolane (4.2 mg/g), dimethyl sulfoxide (DMSO, 2 mg/g), tetrahydrofuran (THF), N-methyl formamide (NMF), etc. In addition, the nanotube salts method opens new ways to nanocomposite fibers, films synthesis, and controlled functionalization [68].

Figure 2.7 depicts summarizes some possible routes already reported on functionalization of carbon nanotubes by means of nanotube salts.

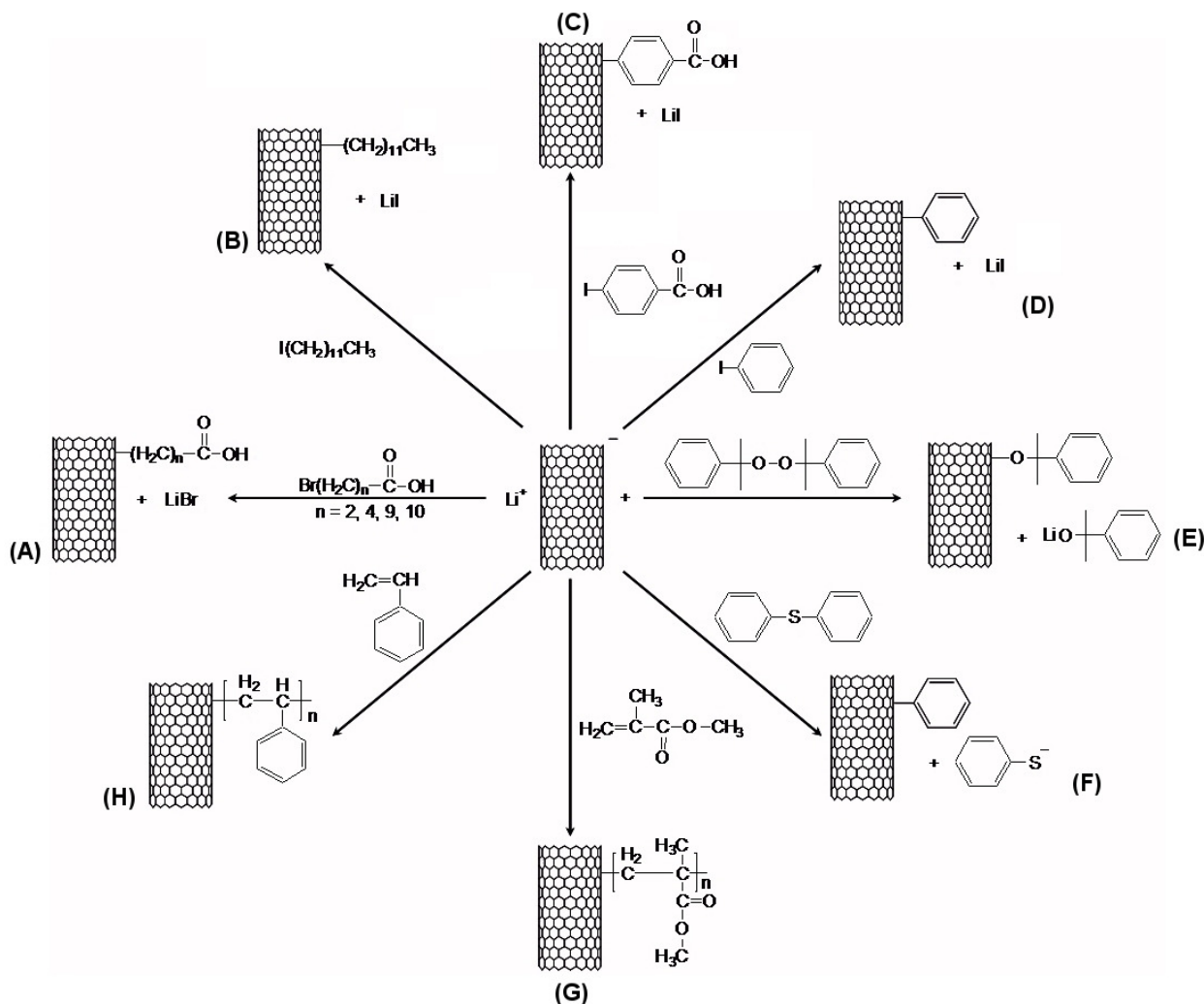


**Figure 2.7. Functionalization pathways for carbon nanotubes by the nanotube salts method.** The nanotube salts method allows modification of carbon nanotubes with several functional groups such as: **(A)** carboxylic acids [69]; **(B)** aliphatic chains [62]; **(C–F)** aryl groups [60, 63, 64, 70]; **(G)** poly(methyl methacrylate) [11]; **(H)** polystyrene [10]. The nanotube salts method is advantageous since the tubes do not require previous oxidation and functionalization occurs in a single step. Moreover, since electrostatic repulsion keeps nanotubes separated, it helps to improve the dispersion of the tubes in a polymer matrix.

## 2.3 Experimental procedure for the synthesis of composites from polyanilines (PANis), polypyrrole (PPy), and multi-walled carbon nanotubes (MWNTs)

### 2.3.1 Materials

Muti-walled carbon nanotubes (MWNTs) and nitrogen-doped multi-walled carbon nanotubes (CN<sub>x</sub>) used in this study were synthesized by a CVD process [71-73], from ultrasonically nebulized mixtures of ferrocene/benzylamine or ferrocene/toluene (catalyst:carbon source 2.5:97.5 wt%) for CN<sub>x</sub> and MWNTs, respectively. Synthesis was carried out in a quartz reactor placed in a tube furnace at 825–850 °C under flowing argon (2.5 L/min, Praxair, 99.998%) for 15 minutes. Ferrocene (Aldrich, 98+%), benzylamine (Aldrich, reagentplus, 99%), and toluene (anhydrous, 99.8%) were used as received. More details on this experimental procedure can be found at [section 1.3](#). Synthesized carbon nanotubes were purified by a modified hydrothermal procedure [74], which consisted in sonication for 4 hours in boiling water, followed by refluxing for 6 hours in 6 M HCl (Fermont, 37.2%). Purified carbon nanotubes were washed with distilled water and dried at 60 °C. Aniline (Aldrich, A.C.S. 99.5%) and pyrrole (Aldrich, 98%) were bi-distilled prior to use. Sulfonated aniline (2-aminobenzene sulfonic acid, oASA, Aldrich, 95%) and lithium (99% Li, “high sodium”, ~0.5% Na, reagent grade, Aldrich) were used as received. Ammonia gas (Praxair, 99.5%) was dried on KOH (Fermont, 87.4%) and CaCl<sub>2</sub> (Fermont, 98.7%) traps, using Drierite (Hammond Drierite Co., CaSO<sub>4</sub> > 98%, CoCl<sub>2</sub> < 2%) as indicator. Other materials used were methanol (CTR, 99.3%), ethanol (CTR), chloroform (CTR), hydrochloric acid (Fermont, 37.2%), nitrogen (Praxair, 99.9995%), acetone (CTR, 99.5%), and tetrahydrofuran (TEDIA, ACS grade) dried by reflux and distillation with LiAlH<sub>4</sub> (Aldrich, 95%).

### 2.3.2 Synthesis of nanocomposites

A flame-dried three-neck round-bottom flask was evacuated with argon for 5 minutes. Ammonia was then condensed into the flask by means of a cryogenic mixture of CaCl<sub>2</sub>,

acetone, and liquid nitrogen until ~125 mL to ~250 mL were obtained. In later experiments only acetone, liquid N<sub>2</sub>, and (occasionally) dry ice were used. Next, lithium, carbon nanotubes, and a monomer (pyrrole, aniline or sulfonated aniline) were added to the reactor while magnetically stirring the mixture and allowed to react for at least 5 hours or until full evaporation of NH<sub>3</sub>. Optionally, carbon nanotubes and/or the monomer were first dispersed by sonication or dissolution in dry THF. Unless otherwise specified, for MWNTs nanocomposites a 1:2:5 MWNTs:Li:monomer ratio was used. The reaction mixture was magnetically stirred up to full evaporation of NH<sub>3</sub>, which occurred after 5 to 12 hours (depending on weather). The experimental setup is depicted at [figure 2.8](#).

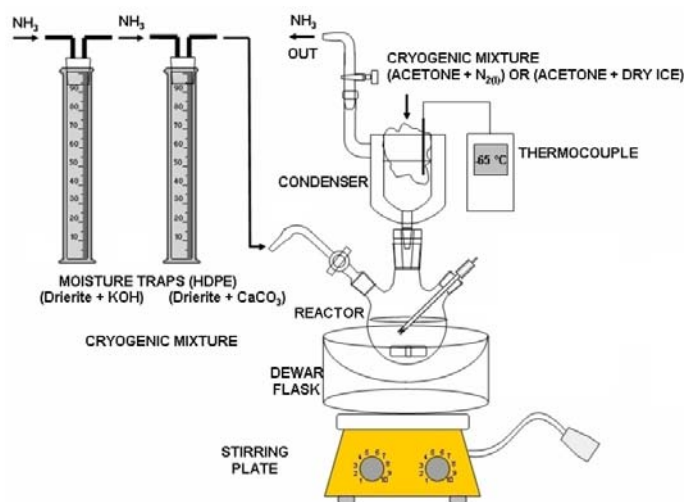


**Figure 2.8. Experimental setup for the synthesis of nanocomposites.** Ammonia is passed through moisture traps (left), and condensed by a cryogenic mixture (center, top) in a round flask (center, middle), to which metallic lithium, carbon nanotubes, and a monomer are added while stirring with an homogenizer or with magnetic stirring. Next, the mixture is magnetically stirred until NH<sub>3</sub> is fully evaporated.

Afterwards, the product was washed with methanol or ethanol (10 mL) and water (20 mL), followed by addition of 10% HCl (20 mL) and CHCl<sub>3</sub> (20 mL). The product was washed in a separatory funnel against HCl/CHCl<sub>3</sub>, and distilled H<sub>2</sub>O/CHCl<sub>3</sub>, 5 times each. A final wash with methanol or acetone was done while filtering through a 0.1 μm PTFE membrane, and then the nanocomposite was dried at 60 °C in a convection oven. In the next section, we show some of the most important results regarding the synthesis of these composites, focusing on the characterization by microscopy and spectroscopy.

## 2.4 Results and discussion

### 2.4.1 Morphology of nanocomposites from MWNTs and sulfonated PANi

Purification removes most amorphous carbon and also separates MWNTs, which helps their dispersion. However, [figure 2.9A](#) shows a mat of aligned, bundled MWNTs synthesized by CVD process, remaining after purification. Most tubes are straight, while some are undulated possibly due to the purification process, and show random particles possibly due to the iron catalyst and/or to amorphous carbon.

[Figure 2.9B](#) shows a composite from MWNTs and poly(2-aminobenzenesulfonic acid) (PoASA) (1:1 wt% MWNT:monomer ratio) in which MWNTs are entangled and disordered, with what we think are some PoASA spheres that appear occasionally and that are randomly placed, considering that the washing processes remove all of the unreacted monomer. These spheres melt, appear to degrade and then evaporate upon hitting them with the electron beam, which is an expected behavior consistent with polymer degradation under the e-beam [75, 76]. In [figure 2.9D](#) (1:4 wt% MWNTs:oASA ratio) MWNTs are bundled as if PoASA were coating the tubes, acting as a binder. Composites also present some areas in which MWNTs are poorly dispersed in the PoASA matrix as shown in [figures 2.9\(C and E\)](#), thus leading to heterogeneous composites; in others, MWNTs are well embedded in the polymer ([figure 2.9F](#)).

In addition, [figures 2.10\(A to E\)](#) also show that MWNTs are well embedded in a PoASA matrix; hence, excess monomer favors complete immersion of carbon nanotubes in the polymer matrix, though most of the oASA monomer is lost after reaction as free polymer or excess monomer, as could be seen during washing of nanocomposites. Wetting of MWNTs with polymer ([figure 2.10D](#)) indicates strong interactions between MWNTs and PoASA chains. We noticed that the polymer is swollen by the solvents used during washing, and once filtered as it dries it contracts and cracks naturally form. In these naturally occurring fractures nanotubes do not pull out from the matrix but break apart ([figure 2.10E](#)), which suggests the presence of covalent bonding between MWNTs and PoASA. On the other hand, very strong  $\pi - \pi$

interactions might also occur between the quinoid rings of PoASA and the phenyl rings of MWNTs [28].

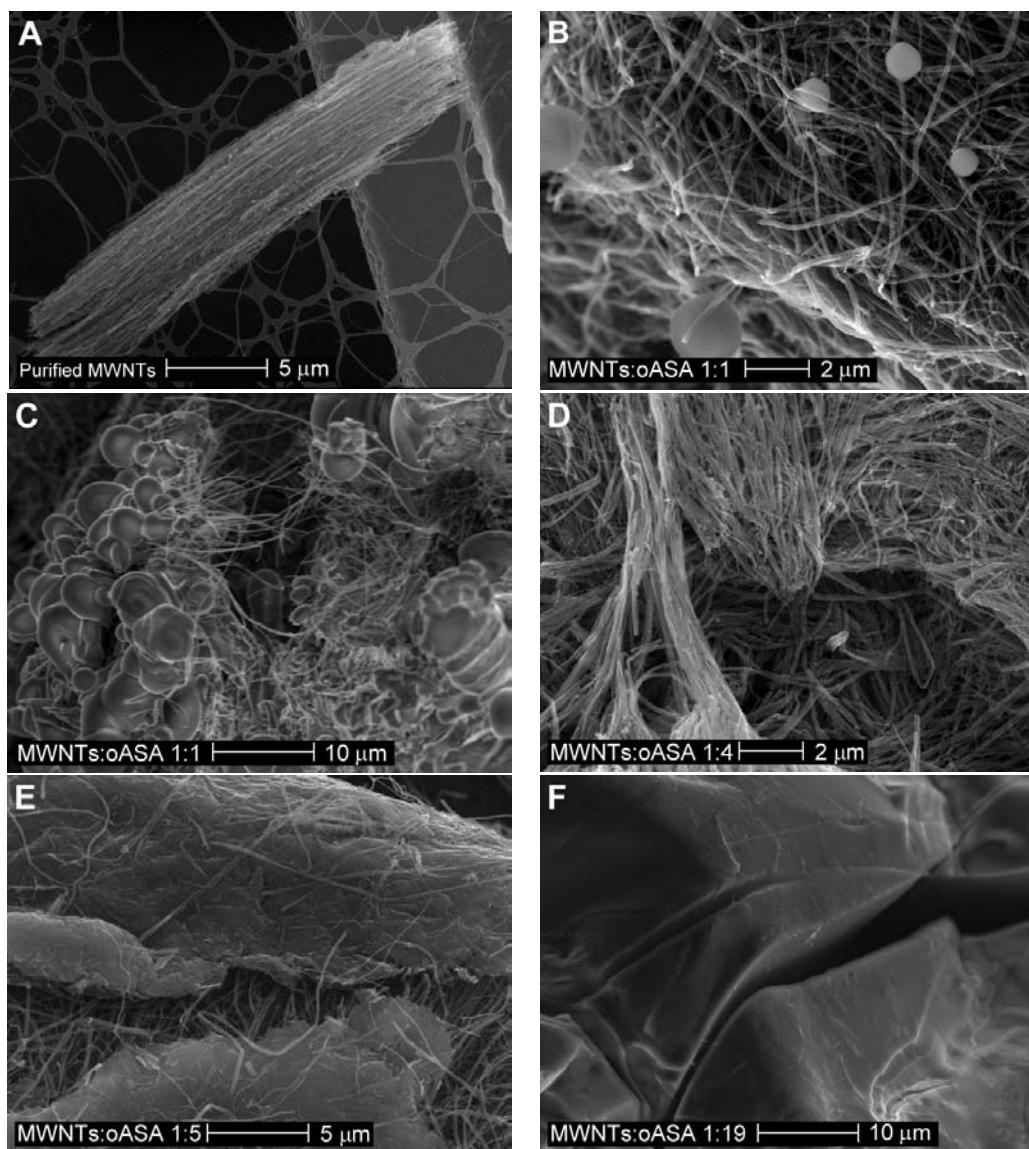


**Figure 2.9. SEM images of MWNTs and MWNTs/PoASA nanocomposites** showing different dispersions, obtained from different MWNTs:oASA ratios (wt./wt.). Purified MWNTs (**A**) are long ( $\sim 10\ \mu\text{m}$  length), bundled and aligned. MWNTs/PoASA nanocomposites (**B–F**) present different characteristics, for example, in (**B**) PoASA does not cover MWNTs, instead, it is present randomly as spheres of different size and some tubes present damage. Nanotubes may become bundled (**C**) due to the presence of a thin coating of PoASA that acts as a binder. In some cases, composites present poor dispersion as shown by the MWNTs partially covered at (**E**); in others, MWNTs are well embedded in the polymer (**F**). MWNT/PoASA (wt./wt.) ratios: (**B–C**) 332:1; (**D**) 26:1.

Moreover, the sulfonic acid group from PoASA could increase such interaction, due to its electron withdrawing nature. A problem that we found during the synthesis of

MWNTs/PoASA nanocomposites is that oASA is practically insoluble in a great variety of solvents, including tetrahydrofuran (THF) and  $\text{NH}_3$ ; this may also contribute to the heterogeneous distribution of PoASA on MWNTs.

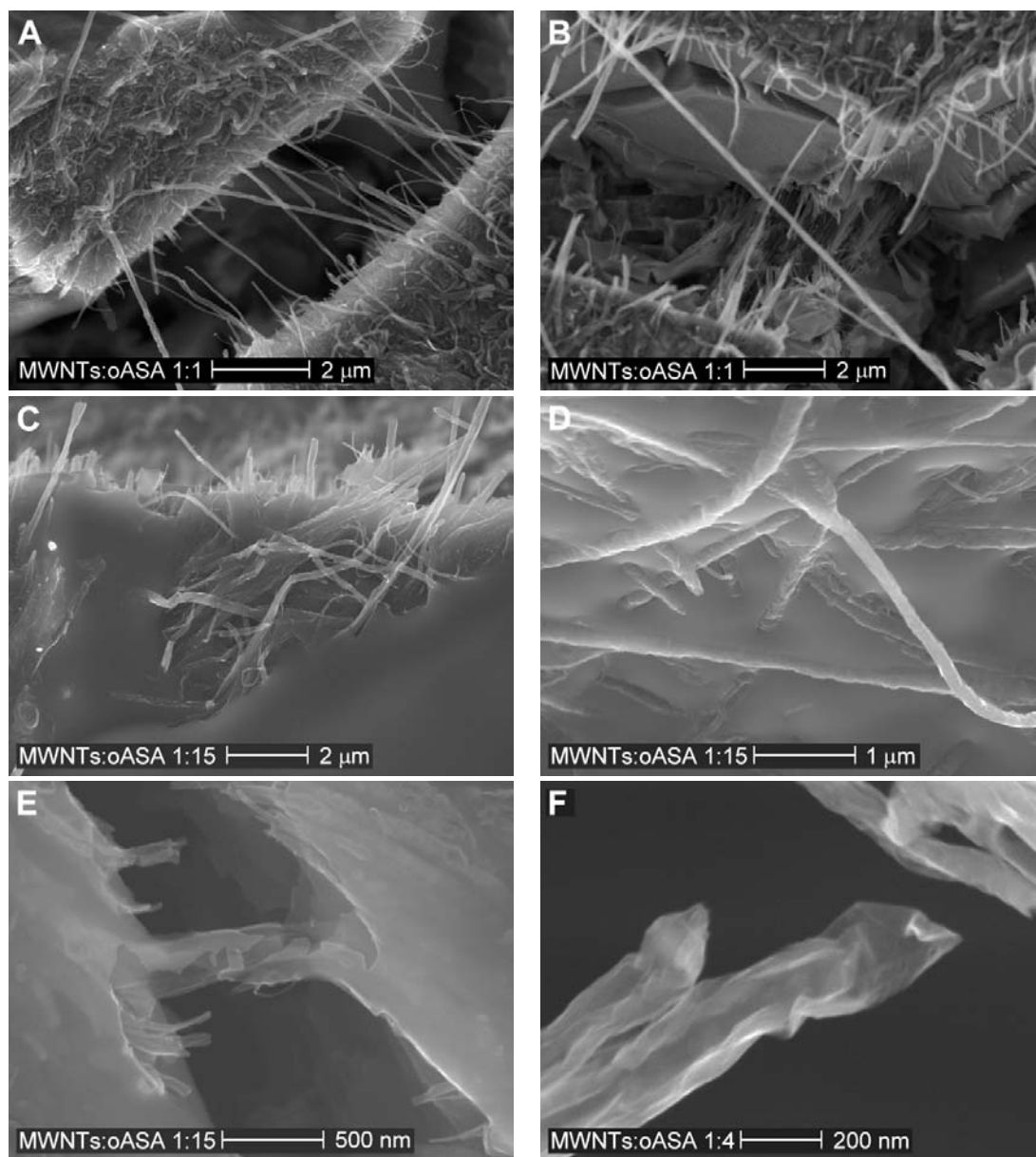


**Figure 2.10. SEM images of MWNTs/PoASA nanocomposites.** When excess monomer is used (**A – D**), MWNTs are fully embedded in the PoASA matrix. An important observation is that in some parts (**E**), the PoASA matrix shows broken MWNTs, with no sliding between the tubes and the PoASA, which suggests a very strong interaction between PoASA and MWNTs. In addition, some nanotube tips (**F**) seem to be opened, and ruffled or damaged. MWNT/PoASA (wt./wt.) ratios: (**A–B**) 332:1; (**F**) 26:1.

Finally, [figure 2.10F](#) (1:4 wt% MWNTs:oASA ratio) shows what seems to be MWNTs opened by their tips. The tubes look almost flat, showing a rugged and damaged surface;

such damage may be due to the nature of the reaction, since carbon nanotubes can be hydrogenated at some parts and hence present defects which give rise to damage [59]. This may happen if moisture enters the reaction system during evaporation of  $\text{NH}_3$ . The opening of MWNTs was an unexpected result which will be pursued in chapter 3.

#### 2.4.2 Morphology of nanocomposites from MWNTs and PANi

MWNTs/Polyaniline composites also show dispersion differences that lead to non-uniform composites (figures 2.11 A to C), in which MWNTs are poorly dispersed, and also to well-embedded MWNTs in the PANi matrix (figure 2.11D).

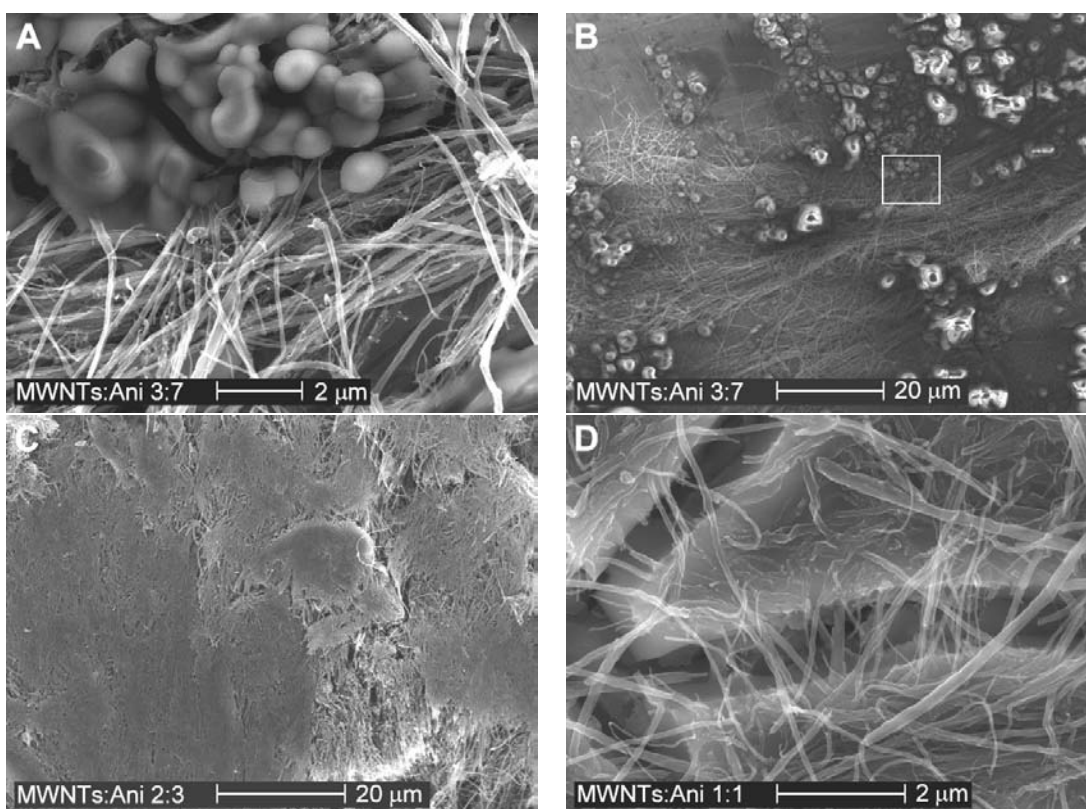


**Figure 2.11. SEM images of MWNT/PANI composites** showing different dispersions. (A – B) Non-homogeneous composites show PoASA agglomeration forming globular structures. (A) Is a zoomed in image of the rectangular area shown in (B). (C) Some areas of this composite are better coated than others, thus showing a heterogeneous distribution of PANi. (D) Fractured composite, showing that most tubes on the surface of the PANi matrix not immersed, in contrast to what tubes *in* the PANi matrix show. MWNT/PANI (wt./wt.) ratios: (A–B) 3:1; (C) 2:11; (D) 9:1.

Figure 2.12A (7:3 wt% MWNTs:Aniline ratio) shows a PANi matrix in which some tubes are partially embedded. A tube that seems to be separated from the PANi matrix

can also be seen, thus suggesting that interaction between MWNTs and PANi might be poor, in contrast to what was seen for MWNTs and PoASA. In addition, MWNTs (see arrow) may occasionally be fully opened longitudinally, at least in segments, in a similar fashion to what was observed in [figure 2.10F](#). [Figure 2.12B](#) (4:1 wt% MWNTs:Ani ratio) shows disordered and entangled MWNTs, which present some damage and are apparently coated by a PANi layer. [Figure 2.12C](#) (1:1 wt% MWNTs:Ani ratio) clearly shows that MWNTs are coated by PANi, which also forms spherical features that seem to protrude from the surface of MWNTs. Hence, the morphology of this composite is completely different to that presented by MWNT/PoASA composites. Occasionally, some tubes are opened at their tips (see arrow). Finally, [figure 2.12D](#) displays MWNTs fully embedded in a PANi matrix.

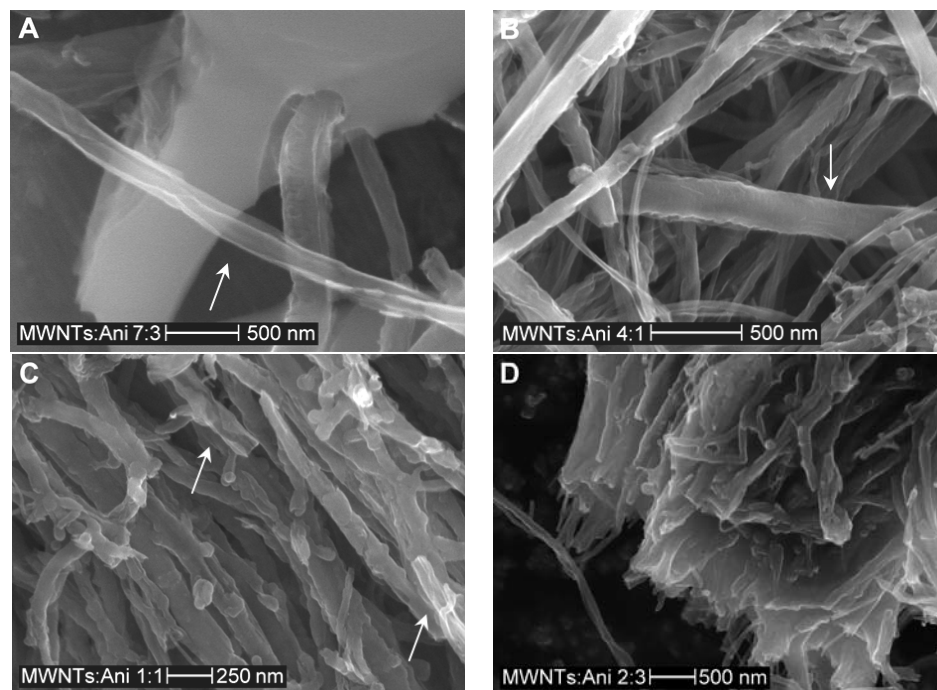


**Figure 2.12. SEM images of MWNT/PANI nanocomposites**, showing different features. **(A)** A MWNT opened longitudinally (see arrow). Second plane: a PANi matrix showing a MWNT separated from the matrix, suggesting poor interaction with PANi. The tube, which is about 300 nm wide, might be covered by a PANi layer. **(B)** MWNTs of different widths are observed, and some of them look damaged. Long tubes also present a ruffled surface, and might be coated by PANi. Note the width of the central tube (see arrow). Upon increasing the amount of PANi **(C, D)** we may presume that MWNTs are better coated by PANi. Furthermore, PANi forms quasi-spherical particles at some tips or protrude from the body of MWNTs. Some tubes (see arrows) show their tips opened. In **(D)** MWNTs are fully immersed in a PANi matrix. MWNT/PANI (wt./wt.) ratios: **(A)** 91:1; **(B)** 10:1; **(C)** 19:1; **(D)** 2:1.

We realized further studies on composites from MWNTs, polyaniline (PAni), and sulfonated polyaniline (PoASA). These materials are black, sticky, clustered flakes. Four-point conductivity measurements made with a home-built 4-point probe on some of these nanocomposites showed no clear trend of conductivity on MWNTs and polymer load, possibly due to the heterogeneous dispersion in all composites. It is expected that PAni and PoASA are in their non-conducting states with the polymerization conditions used, since oxidizing conditions (necessary to obtain the conducting form of PAni and PoASA) are not present in the nanotube salt reaction. It is worthy to say that HCl-doped PAni and MWNT:PAni nanocomposites (10 wt% MWNTs) [48] show conductivity values of 3.336 S/cm and 33.374 S/cm, respectively. Our nanocomposites show much lower values (see table 2.1), maybe also due to the lack at that time of the proper measurement equipment. Further studies are required to confirm the amount of polymer present (TGA), its oxidation state (XPS, UV-Vis), and its conductivity.

**Table 2.1. Conductivity for MWNTs/polyaniline nanocomposites** with different MWNTs:monomer ratios. Polyaniline monomers, 2-aminobenzenesulfonic acid and aniline, are abbreviated as oASA and aniline, respectively. Polymerization efficiency was calculated from weight measurements of composites, MWNTs, and monomers.

| Monomer | MWNTs:monomer | MWNTs<br>wt% | Polymer wt% | Polymerization |                 |
|---------|---------------|--------------|-------------|----------------|-----------------|
|         | (wt./wt.)     |              |             | Efficiency %   | $\sigma$ (S/cm) |
| oASA    | 2:3           | 60.6         | 39.4        | 65.2           | 0.0443          |
| oASA    | 7:3           | 92.6         | 7.4         | 24.6           | 1.8506          |
| oASA    | 4:1           | 95.7         | 4.3         | 22.4           | 4.7903          |
| Aniline | 4:1           | 90.8         | 9.2         | 48.7           | -               |
| Aniline | 3:7           | 76.5         | 23.5        | 33.5           | 0.4227          |
| Aniline | 3:2           | 87.6         | 12.4        | 29.2           | 1.6972          |

For comparison, “blank” experiments run without MWNTs (monomer, lithium, and NH<sub>3</sub> only) did not produce polymers; instead, a deep-brown solution was recovered after washing with HCl and chloroform. Though this solution was not characterized, it probably contained aniline oligomers and/or of excess of non-reacted monomer. This might be due to the intrinsic nature of the amino group in aniline, which behaves as electron donor (in contrast to oxidizing agents which induce polymerization), to the stability and/or poor reactivity of the monomer-derived species, and to the highly reductive character of the alkylation reaction. In contrast, some polymerization is obtained when

carbon nanotubes are present, that is, when nanotube salts (the polymerization initiator) are present.

On this basis [11, 63], a polymerization scheme may be proposed: (i) carbon nanotubes accept electrons, thus forming nanotube-salts; (ii) once monomer is added, electrons from the nanotube-salts interact with aniline monomers, thus forming reactive species which start polymerization of aniline. Nonetheless, and to properly establish a polymerization mechanism, a systematic characterization including X-ray Photoelectron Spectroscopy (XPS) and Nuclear Magnetic Resonance (NMR) is also suggested, which would give us more information about the types of bonding between MWNTs and aniline, and between aniline monomers as well.

### 2.4.3 Morphology of nanocomposites from $CN_x$ and PPy

At the beginning of this study we also performed only a few experiments on  $CN_x$ /PPy composites, since we decided to continue with MWNTs and then, after completing the whole picture of MWNTs composites, return to  $CN_x$  composites. Figure 2.13 shows representative examples of these composites. Figure 2.13A shows nitrogen-doped MWNTs ( $CN_x$ ) well coated by polypyrrole (PPy), much better than MWNTs by PoASA or PANi. This can be explained by the presence of dopant nitrogen atoms which make  $CN_x$  intrinsically more reactive in comparison to MWNTs [77], which facilitates covalent bonding to polypyrrole. Nevertheless, figure 2.13B shows poor dispersion of  $CN_x$  in PPy. This might be due to the fact that the homogenizer was not used for the synthesis of  $CN_x$ /PPy composites (these composites were synthesized during preliminary work), and to other factors such as that tubes were not purified, and sonication was not used for dispersion of the tubes. Despite the poor dispersion observed, figures 2.13(C, D) show that these composites display a much better coating of PPy on  $CN_x$ , less damaged tubes are seen but some tubes opened at their tips were observed (see arrow).

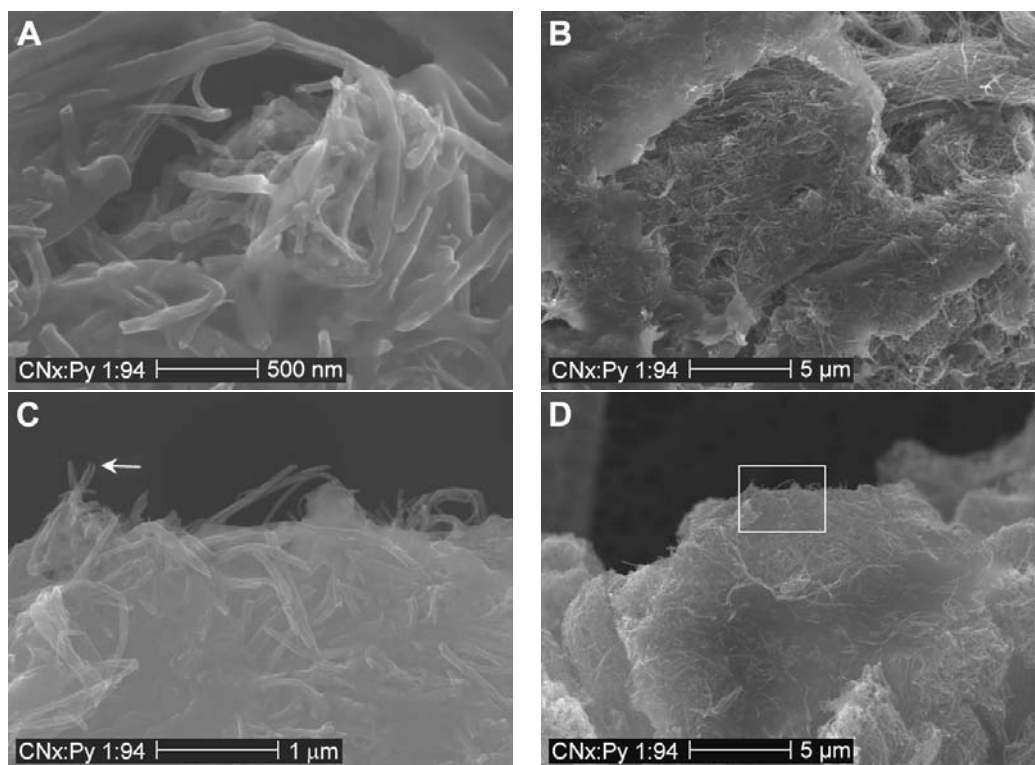


**Figure 2.13. SEM images of a nanocomposite from nitrogen-doped MWNTs ( $CN_x$ ) and PPy.** It is clear that  $CN_x$  are fully coated by PPy (**A**). Though in some areas good coverage of  $CN_x$  by PPy is obtained, in others it seems that  $CN_x$  are only bonded by PPy, thus leading to heterogeneous composites (**B**). Nevertheless, most  $CN_x$  are fully embedded in the PPy matrix (**C**), with only a few of them opened at their tips. (**D**) Is an image zoomed out from (**C**) (area marked in the rectangle), also showing that  $CN_x$  are fully embedded in a PPy matrix.

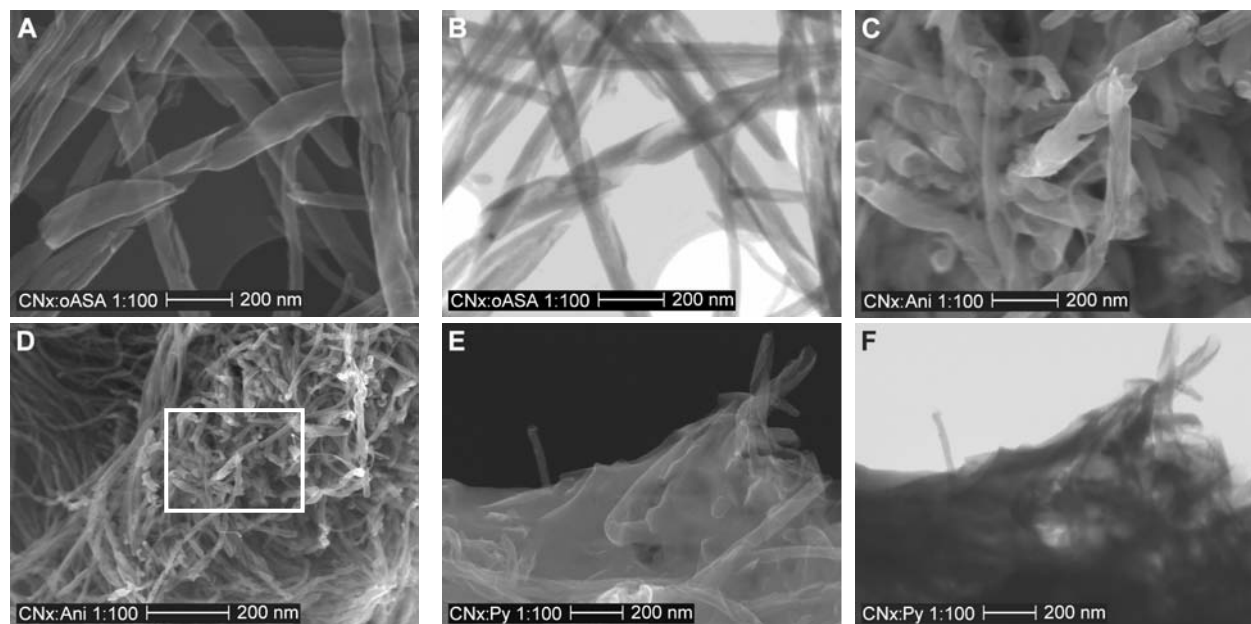


**Figure 2.14. SEM and STEM images of composites from  $CN_x$ , PoASA, PANi, and PPy.** (A–B) SEM and STEM images of opened  $CN_x$ . (C–D) Show features resembling cones; (D) is a zoomed out image of (C) (area enclosed in the rectangle). (E– F)  $CN_x$  fully immersed in PPy matrix, also showing opened tips.

We were also surprised to find (figure 2.14) that some tubes are opened helicoidally at their tips or body. It also seems that tubes are opened in segments, in agreement with their bamboo-like structure. Pyridinic sites and/or compartment unions could serve as starting points for unwrapping. CN<sub>x</sub> are opened (figures 2.14 A and B) at their tips or body either helicoidally (see tube at center) or almost longitudinally. Opened tubes present some damage. The opened regions can be more easily seen by STEM (figures 2.14 B and F), and may resemble cones (figures 2.14 C and D). Opened tips are also present in CN<sub>x</sub> fully immersed in a PPy matrix (figures 2.14 E and F).

#### 2.4.4 Spectroscopic studies on MWNTs/PAni nanocomposites

##### *Raman spectroscopy*

Raman spectra of MWNT/polyaniline nanocomposites (figure 2.15) show no similarities to those already reported in the literature (see section 2.2.2). Our results show two major features in purified MWNTs (figure 2.15A): the D (~1310 cm<sup>-1</sup>) and D' (~1630 cm<sup>-1</sup>) bands, which are due to “disorder” (sp<sup>3</sup> hybridized carbon) [78], and the G band (~1586 cm<sup>-1</sup>, sp<sup>2</sup> hybridized carbon), present with high intensity in crystalline samples and that comes accompanied by the D' band [79]. In composites (figures 2.15 B and C), the D and G features show a high I<sub>D</sub>/I<sub>G</sub> ratio (table 2.2) in comparison to purified MWNTs, and the intensity of the D' band increases, thus indicating that the amount of disorder increases. In addition, a small peak is observed from 1455 cm<sup>-1</sup> to 1468 cm<sup>-1</sup> in MWNT/PAni nanocomposites, and might be due either to C=N or C-C stretching of the benzenoid ring of polyaniline [36, 44].

No trend is observed and a high degree of disorder is present in all samples, probably due to defects and damage on the surface of MWNTs, and maybe to disorder of PAni chains. Moreover, the D peak presents a downshift in all nanocomposites, which strongly suggests that MWNTs are covalently functionalized [80], possibly by PAni chains and functional groups such as -OH or -H, which could have been introduced during the purification step of MWNTs and during the nanotube salts reaction,

respectively. The G peak increases in width, probably due to different functionalization degrees between nanotubes, that is, to the heterogeneity of composites.

Gao and co-workers [81] suggest that polyurea Raman signals in MWNTs-polyurea composites can be detected only if the polymer layer can absorb and reflect the whole excited energy; the presence of non-continuous polymer structures would make it difficult or even impossible for the polymer to completely absorb and reflect all the excited energy. In our composites, PANi barely covering MWNTs in heterogeneous composites would make it difficult for PANi to completely absorb and reflect all the excited energy, thus showing no signals in the Raman spectrum. The lack of Raman signals for conducting PANi in our composites can also be explained by the transparency of PANI, which supports the idea of PANi being in its non-conductive, reduced form (which is optically transparent). Finally, the very low relative amount of PANi in our composites (< 25%) can also explain why there were no PANi peaks.

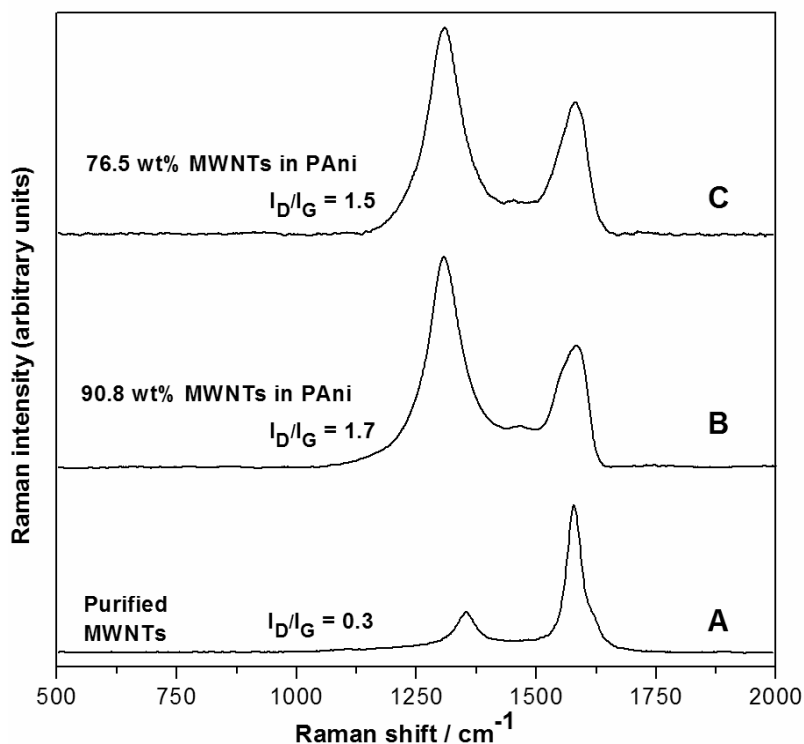


**Figure 2.15. Raman spectra of MWNTs and MWNTs/PANI nanocomposites** for different concentrations of MWNTs in PANi. (A) Purified MWNTs; (B) 90.8 wt% MWNTs composite (80:20 MWNTs:Ani nominal ratio); (C) 76.5 wt% MWNTs composite (30:70 MWNTs:Ani nominal ratio). Renishaw inVia microRaman system. Laser line: 514 nm; power: 1%; lens: 100x.

**Table 2.2. D and G Raman peak positions and relative intensities for MWNTs and MWNTs/PAni nanocomposites** obtained from different MWNTs:monomer ratios, showing high amount of disorder in all samples.

| Sample                 | D (cm <sup>-1</sup> ) | G (cm <sup>-1</sup> ) | I <sub>D</sub> /I <sub>G</sub> |
|------------------------|-----------------------|-----------------------|--------------------------------|
| Purified MWNTs         | 1357                  | 1582                  | 0.3                            |
| 95.7 wt% MWNTs in oASA | 1311                  | 1587                  | 1.7                            |
| 60.6 wt% MWNTs in oASA | 1316                  | 1587                  | 1.7                            |
| 87.6 wt% MWNTs in ANI  | 1323                  | 1590                  | 2.2                            |
| 76.5 wt% MWNTs in ANI  | 1310                  | 1588                  | 1.5                            |
| 90.8 wt% MWNTs in ANI  | 1306                  | 1582                  | 1.7                            |

### Fourier-Transform Infrared spectroscopy

Other interesting properties such as the oxidation state of PAni may be determined by Fourier-transformed infrared spectroscopy (FTIR). [Figure 2.16A](#) shows, for purified MWNTs, a characteristic C=C stretching band at ~1658 cm<sup>-1</sup>. [Figures 2.16\(B and C\)](#) show, for MWNTs/PAni composites, C=C stretching bands from quinoid (~1540 cm<sup>-1</sup>) and benzenoid (~1460 cm<sup>-1</sup>) rings [\[48\]](#). Nonetheless, the reported method completely differs from ours; hence, these bands cannot be assigned to the nanocomposites obtained by the nanotube salts method.

The peak at 719 cm<sup>-1</sup> might be ascribed to C-N=C bending of imine group [\[82\]](#), and the wide peak shown at ~1067 cm<sup>-1</sup> to 1122 cm<sup>-1</sup> may have weak contributions from PAni: deformation of benzenoid rings of polymeric chains (1018 cm<sup>-1</sup>); C-H bending, quinoid ring, and deformation of benzenoid ring (1101 cm<sup>-1</sup>); and a strong contribution from C=N asymmetric stretching [\[37, 41, 82\]](#) and C-H bending mode [\[82\]](#) of quinoid ring.

Other bands could belong to C-N<sup>+</sup> stretching in protonic acid doped PAni (1235 cm<sup>-1</sup>, doping could have occurred during washing with HCl), C-N stretching (secondary amine, 1296 cm<sup>-1</sup>) [\[33, 37, 41\]](#), and aromatic C-H symmetric (~2840 cm<sup>-1</sup>) and asymmetric (~2920 cm<sup>-1</sup>) stretching of polymerized benzenoid ring. The band at ~3400 cm<sup>-1</sup> due to N-H stretching of secondary amine present in emeraldine base PAni [\[82\]](#) is not observed, maybe because of the formation of quinone diimine from benzenoid structure, which is accompanied by loss of N-H bonds [\[83\]](#), or simply because PAni is present in our composites in small amounts (< 25%) and was synthesized by a different, non-oxidizing method. Complementary studies are needed (XPS), since it is difficult to assign the

above signals due to the small amount of polymer present at samples and to the synthesis method, which differs from common methods in that it does not involve oxidation of PANi, thus making it impossible to obtain its conducting form without further processing.

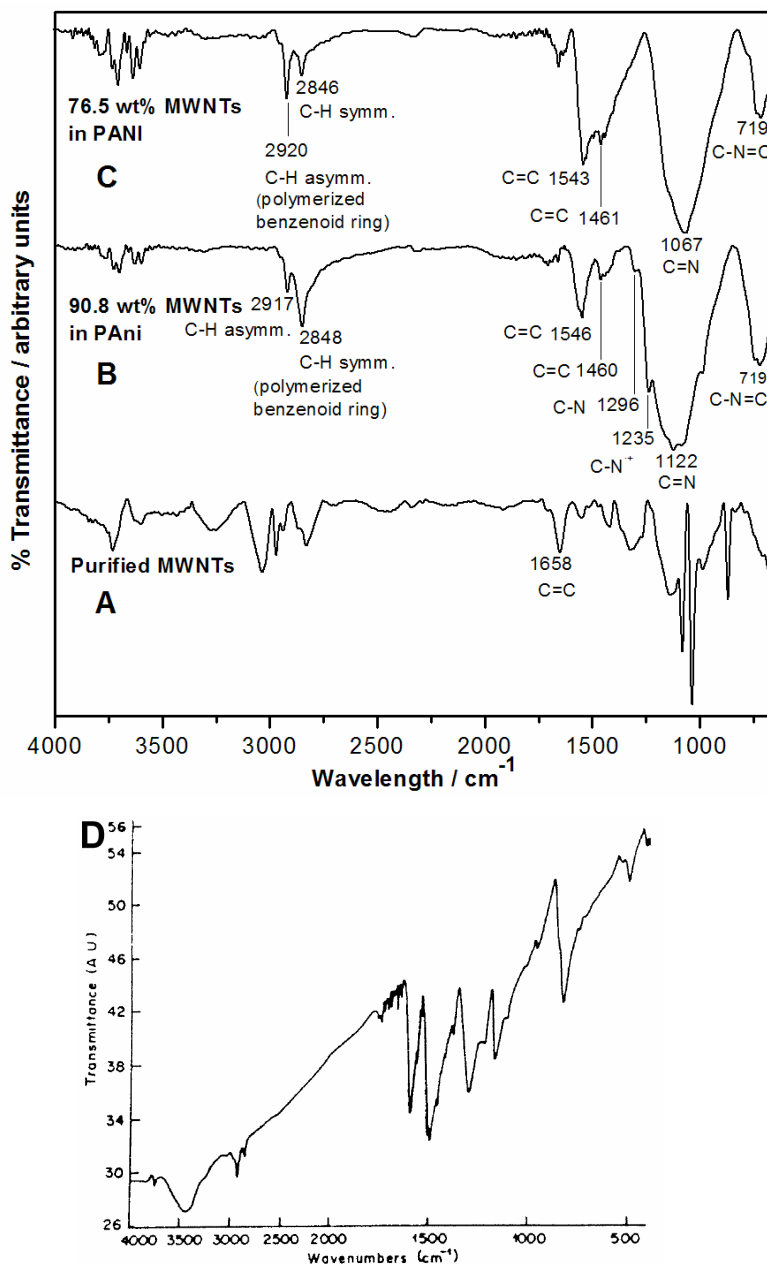


**Figure 2.16. FT-IR spectra for MWNTs and MWNTs/PAni nanocomposites** for different concentrations of MWNTs in PANi. **(A)** Purified MWNTs; **(B)** 90.8 wt% MWNTs composite (80:20 MWNTs:Ani nominal ratio); **(C)** 76.5 wt% MWNTs composite (30:70 MWNTs:Ani nominal ratio). Signals after 3500  $\text{cm}^{-1}$  can be regarded as noise. Spectra were obtained with a ThermoNicolet 6700 by ATR technique, with 1068 scans and a resolution of 8. **(D)** Emeraldine base PAni from reference [82].

### 2.4.5 X-Ray powder diffraction of MWNTs/PAni nanocomposites

We performed X-ray powder diffraction on some composites since it is a valuable tool for observing changes in solid, crystalline samples. In [figure 2.17A](#), purified MWNTs present a well defined, and sharp graphitic peak at  $26.5^\circ$  with an interlayer distance of  $\sim 3.42 \text{ \AA}$ , and a series of peaks (peak with highest intensity at  $44.08^\circ$ ) belonging to iron carbides.

For both MWNT/PAni composites, X-ray diffraction displays features which could not be ascribed to the conducting form of PAni, nor to  $\text{FeO}$ ,  $\text{Fe}_2\text{O}_3$ , or  $\text{Fe}_3\text{O}_4$  species, since they are absent or their amount is too low (diffractograms were visually compared with those at the International Centre for Diffraction Data – ICDD – database). Instead, in both composites, the broad peak observed from  $\sim 18^\circ$  to  $\sim 21.5^\circ$  ([figure 2.17 B and C](#)) may be due to insulating PAni [\[84\]](#).

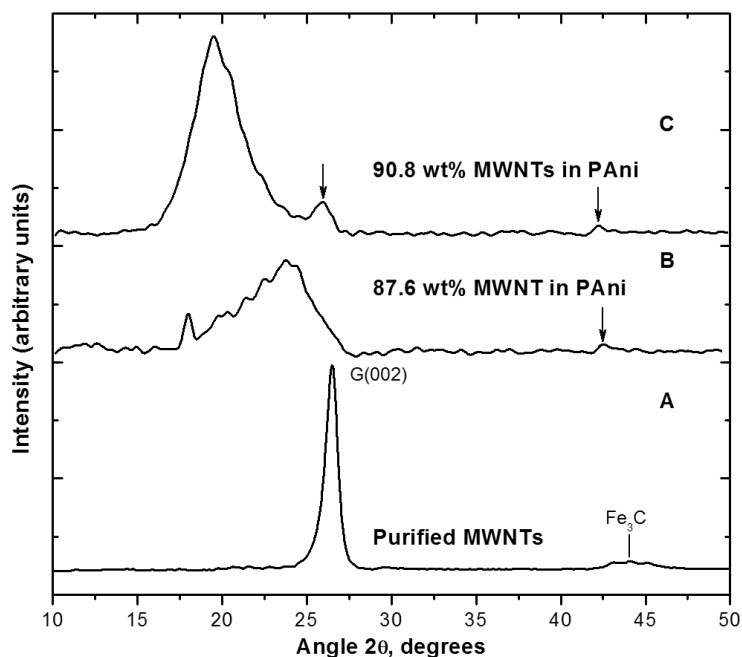


**Figure 2.17. Diffraction patterns for MWNTs and MWNTs/PAni nanocomposites** for different concentrations of MWNTs in PAni. **(A)** Purified MWNTs; **(B)** 87.6 wt% MWNTs composite (60:40 MWNTs:Ani nominal ratio); **(C)** 90.8 wt% MWNTs composite (80:20 MWNTs:Ani nominal ratio). Arrows show the location of the  $\text{Fe}_3\text{C}$  region.

However, for both composites no trend is observed in the amount of disorder. In the case of the 4:1 MWNTs:Ani composite (90.8 wt% MWNTs in PAni), a small graphitic peak at  $26.04^\circ$  (interlayer distance  $\sim 3.47 \text{ \AA}$ ) is observed; its presence should be due to the significant amount of MWNTs used for the synthesis of the composite. Note that in [\(B\)](#), such peak may be overlapped with the broad peak.

## 2.5 Conclusions

This study marks the first time that multi-walled carbon nanotubes (MWNTs and  $CN_x$ ) are modified with PANi and PPy by means of the nanotube salts method. There are still no other similar reported works. SEM images revealed poor dispersion of multi-walled carbon nanotubes within poly(2-aminobenzene sulfonic acid) (PoASA) and polyaniline (PANi) matrices, and also poor dispersion of polymer within MWNT bundles. To improve dispersion, we changed several variables such as: use of ultrahomogenization, dispersion of MWNTs by sonication in tetrahydrofuran, long reaction times, different addition order of reactants, and different MWNTs:monomer (wt.%) ratios. These changes (see appendix 3) were not effective to obtain a well dispersed composite and thus were not discussed.

In most cases, we found PoASA, PANi and PPy acting as binders with  $CN_x$  and MWNTs. In certain cases, when excess monomer was used in the reaction, fully embedded MWNTs in a polymer matrix were obtained. In all cases for MWNTs, heterogeneous dispersion of MWNTs was observed; in contrast,  $CN_x$  showed better dispersion in polypyrrole, probably due to the reactivity of nitrogen in both components. Originally, we wished to obtain nanocomposites with low MWNTs loads (0.1–1 wt%) and high polymerization efficiency (> 80%). However, this was not possible, since not all the excess monomer polymerized, probably due to the same reasons that did not produce polymer in blank experiments (lithium, ammonia, and aniline monomer without nanotubes): the intrinsic nature of the electron-donor amino group in aniline, the stability and/or poor reactivity of the species formed from monomers, and to the highly reductive character of the nanotube-salts reaction. These explanations still need further study to be confirmed.

Even when we used excess monomer we found regions rich in PoASA and PANi (MWNTs fully immersed in a polymer matrix), and zones in which polymer was scarce, showing that the polymerization conditions do not give a homogeneous composite. One way to improve dispersion could be by pre-dissolving MWNTs in aniline monomer [85] and by using cationic surfactants [36].

---

Due to the low quality of the MWNTs-PoASA and CN<sub>x</sub> composite samples, no further studies were performed. In particular, few experiments were done with CN<sub>x</sub> since further studies were to be performed only after completing research with MWNTs nanocomposites. Raman and FTIR spectroscopy suggest the existence of PANi in its non-conducting state, since no characteristic signals related to conducting PANi were observed or their contribution was small due to the low amount of polymer present in composites (< 25 wt% in most cases). Other works on the *in situ* polymerization of PANi and MWNTs have reported strong non-covalent interactions between phenyl and quinoid rings of MWNTs and PANi respectively; in this regard, further research would be needed in order to determine the type of interaction between MWNTs and polymer in our samples, for example, X-ray photoelectron spectroscopy (XPS). It is also desirable to perform a deeper study on the electronic properties (UV-Vis, XPS), conductivity, and morphology (HRTEM, AFM) of MWNTs functionalized with PPy, PANi, and PoASA.

The nanotube-salts method may not work properly for the development of homogeneous nanocomposites from multi-walled-carbon nanotubes and aromatic monomers with low loads of CNTs (less than 1%), but may be useful for the pre-functionalization of MWNTs with polyanilines or polypyrrole. Further grafting and/or modification of these conducting polymer-modified MWNTs with the same or other precursors of conducting polymers can be accomplished by a wide variety of methods, which are beyond this thesis. On the other hand, it seems that low loads of monomer lead to opening and damage in MWNTs, while high loads produce well-embedded MWNTs in a polymer matrix. The striking finding of opened tips and unfolding at MWNTs made us to think that this process could be directed towards the unzipping of MWNTs, and hence stimulated our research on this field, leaving behind the work on composites. This work on unzipping MWNTs is shown in the next chapter.



## References

- [1] P. M. Ajayan, J. M. Tour. Nanotube composites. *Nature* **447** (2007) 1066-1068.
- [2] M. Terrones. Carbon nanotubes: synthesis and properties, electronic devices and other emerging applications. *Int. Mater. Rev.* **49** (2004) 325-377.
- [3] R. Khare, S. Bose. Carbon nanotube based composites - a review. *J. Miner. Mater. Charact. Eng.* **4** (2005) 31-46.
- [4] R. H. Baughman, A. A. Zakhidov, W. A. de Heer. Carbon nanotubes - the route toward applications. *Science* **297** (2002) 787-792.
- [5] M. Moniruzzaman, K. I. Winey. Polymer nanocomposites containing carbon nanotubes. *Macromolecules* **39** (2006) 5194-5205.
- [6] R. Bacsa, C. Laurent, R. Morishima, H. Suzuki, M. Le Lay. Hydrogen storage in high surface area carbon nanotubes produced by catalytic chemical vapor deposition. *J. Phys. Chem. B* **108** (2004) 12718-12723.
- [7] D. Qian, E. C. Dickey, R. Andrews, T. Rantell. Load transfer and deformation mechanisms in carbon nanotube-polystyrene composites. *Appl. Phys. Lett.* **76** (2000) 2868-2870.
- [8] Z. Yao, N. Braid, G. A. Botton, A. Adronov. Polymerization from the surface of single-walled carbon nanotubes - preparation and characterization of nanocomposites. *J. Am. Chem. Soc.* **125** (2003) 16015-16024.
- [9] N. Tsubokawa. Preparation and properties of polymer-grafted carbon nanotubes and nanofibers. *Polym. J.* **37** (2005) 637-655.
- [10] C. G. Espinosa-González, J. Kaur, A. G. Cano-Márquez, F. J. Rodríguez-Macías, M. L. Shofner, Y. I. Vega-Cantú. Polystyrene-MWNT nanocomposites containing high load of polymer prepared via "nanotubes salts". *Manuscript in preparation* (2010)
- [11] F. Liang, J. M. Beach, K. Kobashi, A. K. Sadana, Y. I. Vega-Cantu, J. M. Tour, W. E. Billups. In situ polymerization initiated by single-walled carbon nanotube salts. *Chem. Mater.* **18** (2006) 4764-4767.
- [12] A. G. MacDiarmid. "Synthetic metals": a novel role for organic polymers (nobel lecture). *Angew. Chem. Int. Ed.* **40** (2001) 2581-2590.
- [13] J. Yue, Z. H. Wang, K. R. Cromack, A. J. Epstein, A. G. MacDiarmid. Effect of sulfonic acid group on polyaniline backbone. *J. Am. Chem. Soc.* **113** (1991) 2665-2671.
- [14] W. W. Focke, G. E. Wnek, Y. Wei. Influence of oxidation state, pH, and counterion on the conductivity of polyaniline. *J. Phys. Chem.* **91** (1987) 5813-5818.
- [15] M. Baibarac, P. Gómez-Romero. Nanocomposites based on conducting polymers and carbon nanotubes from fancy materials to functional applications. *J. Nanosci. Nanotech.* **6** (2006) 1-12.
- [16] R. J. Waltman, J. Bargon. Electrically conducting polymers: a review of the electropolymerization reaction, of the effects of chemical structure on polymer film properties, and of applications towards technology. *Can. J. Chem.* **64** (1986) 76-95.

- [17] G. Gustafsson, Y. Cao, G. M. Treacy, F. Klavetter, N. Colaneri, A. J. Heeger. Flexible light-emitting diodes made from soluble conducting polymers. *Nature* **357** (1992) 477-479.
- [18] M. G. Kanatzidis. Polymeric electrical conductors. *Chem. Eng. News December issue* (1990) 36-54.
- [19] M. Trojanowicz. Application of conducting polymers in chemical analysis. *Microchim. Acta* **143** (2003) 75-91.
- [20] H. Bai, G. Shi. Gas sensors based on conducting polymers. *Sensors* **7** (2007) 267-307.
- [21] *Electroactive polymers for robotic applications*. K. J. Kim and S. Tadokoro. Springer London: 2007.
- [22] A. A. Argun, P-H. Aubert, B. C. Thompson, I. Schwendeman, C. L. Gaupp, J. Hwang, N. J. Pinto, D. B. Tanner, A. G. MacDiarmid, J. R. Reynolds. Multicolored electrochromism in polymers: structures and devices. *Chem. Mater.* **16** (2004) 4401-4412.
- [23] Y. Wang, x. Jing. Intrinsically conducting polymers for electromagnetic interference shielding. *Polym. Adv. Technol.* **16** (2005) 344-351.
- [24] M. C. Bernard, S. Joiret, A. H-L. Goff, P. V. Phong. Protection of iron against corrosion using a polyaniline layer: I. Polyaniline electrodeposit. *J. Electrochem. Soc.* **148** (2001) B12-B16.
- [25] C. Ponce de León, S. A. Campbell, J. R. Smith, F. C. Walsh. Conducting polymer coatings in electrochemical technology Part 2 - Application areas. *T. I. Met. Finish.* (2008)
- [26] D. M. DeLongchamp, P. T. Hammond. Multiple-color electrochromism from layer-by-layer-assembled polyaniline/prussian blue nanocomposite thin films. *Chem. Mater.* **16** (2004) 4799-4805.
- [27] J. Yano. Electrochromism of polyaniline film incorporating a red quinone 1-amino-4-bromoanthraquinone-2-sulfonate. *J. Electrochem. Soc.* **144** (1997) 477-481.
- [28] H. Zhang, H. X. Li, H. M. Cheng. Water-soluble multiwalled carbon nanotubes functionalized with sulfonated polyaniline. *J. Phys. Chem. B* **110** (2006) 9095-9099.
- [29] C-C. Han, C-H. Lu, S-P. Hong, K-F. Yang. Highly conductive and thermally stable self-doping propylthiosulfonated polyanilines. *Macromolecules* **36** (2003) 7908-7915.
- [30] K. Krishnamoorthy, A. Q. Contractor, A. Kumar. Electrochemical synthesis of fully sulfonated n-dopable polyaniline: poly(metanillic acid). *Chem. Commun.* (2002) 240-241.
- [31] B. R. Saunders, R. J. Fleming, K. S. Murray. Recent advances in the physical and spectroscopic properties of polypyrrole films, particularly those containing transition-metal complexes as counteranions. *Chem. Mater.* **7** (1995) 1082-1094.
- [32] M. Cochet, W. K. Maser, A. M. Benito, M. A. Callejas, M. T. Martínez, J-M. Benoit, J. Schreiberb, O. Chauvet. Synthesis of a new polyaniline/nanotube composite: "in-situ" polymerisation and charge transfer through site-selective interaction. *Chem. Commun.* (2001) 1450-1451.
- [33] X-b. Yan, Z-j. Han, Y. Yang, B-k. Tay. Fabrication of carbon nanotube-polyaniline composites via electrostatic adsorption in aqueous colloids. *J. Phys. Chem. C* **111** (2007) 4125-4131.
- [34] M. Ginic-Markovic, J. G. Matison, R. Cervini, G. P. Simon, P. M. Fredericks. Synthesis of new polyaniline/nanotube composites using ultrasonically initiated emulsion polymerization. *Chem. Mater.* **18** (2006) 6258-6265.

- [35] B. Zhao, H. Hu, R. C. Haddon. Synthesis and properties of a water-soluble single-walled carbon nanotube-poly(*m*-aminobenzene sulfonic acid) graft copolymer. *Adv. Funct. Mater.* **14** (2004) 71-76.
- [36] X. Zhang, J. Zhang, R. Wang, Z. Liu. Cationic surfactant directed polyaniline/CNT nanocables: synthesis, characterization, and enhanced electrical properties. *Carbon* **42** (2004) 1455-1461.
- [37] R. Sainz, W. R. Small, N. A. Young, C. Vallés, A. M. Benito, W. K. Maser, M. in het Panhuis. Synthesis and properties of optically active polyaniline carbon nanotube composites. *Macromolecules* **39** (2006) 7324-7332.
- [38] M. Lefenfeld, G. Blanchet, J. A. Rogers. High-performance contacts in plastic transistors and logic gates that use printed electrodes of DNNSA-PANI doped with single-walled carbon nanotubes. *Adv. Mater.* **15** (2003) 1188-1191.
- [39] S. R. Ali, R. R. Parajuli, Y. Balogun, Y. Ma, H. He. A nonoxidative electrochemical sensor based on a self-doped polyaniline/carbon nanotube composite for sensitive and selective detection of the neurotransmitter dopamine: a review. *Sensors* **8** (2008) 8423-8452.
- [40] Z. Wang, J. Yuan, M. Li, D. Han, Y. Zhang, Y. Shen, L. Niu, A. Ivaska. Electropolymerization and catalysis of well-dispersed polyaniline/carbon nanotube/gold composite. *J. Electroanal. Chem.* **599** (2007) 121-126.
- [41] L. Li, Z-Y. Qin, X. Liang, Q-Q. Fan, Y-Q. Lu, W-H. Wu, M-F. Zhu. Facile fabrication of uniform core-shell structured carbon nanotube-polyaniline nanocomposites. *J. Phys. Chem. C* **113** (2009) 5502-5507.
- [42] W. R. Small, M. in het Panhuis. Inkjet printing of transparent, electrically conducting single-walled carbon-nanotube composites. *Small* **3** (2007) 1500-1503.
- [43] C. Meng, C. Liu, S. Fan. A promising approach to enhanced thermoelectric properties using carbon nanotube networks. *Adv. Mater.* **22** (2009) 535-539.
- [44] Z. Wei, M. Wan, T. Lin, L. Dai. Polyaniline nanotubes doped with sulfonated carbon nanotubes made via a self-assembly process. *Adv. Mater.* **15** (2003) 136-139.
- [45] T-M. Wu, Y-W. Lin, C-S. Liao. Preparation and characterization of polyaniline/multi-walled carbon nanotube composites. *Carbon* **43** (2005) 734-740.
- [46] T. Jeevananda, Siddaramaiah, N. H. Kim, S-B. Heo, J. H. Lee. Synthesis and characterization of polyaniline-multiwalled carbon nanotube nanocomposites in the presence of sodium dodecyl sulfate. *Polym. Adv. Technol.* **19** (2008) 1754-1762.
- [47] D. K. Kim, K. W. Oh, S. H. Kim. Synthesis of polyaniline/multiwall carbon nanotube composite via inverse emulsion polymerization. *J. Polym. Sci. Pol. Phys.* **46** (2008) 2255-2266.
- [48] H. Zengin, W. Zhou, J. Jin, R. Czerw, D. W. Smith, L. Echegoyen, D. L. Carrol, S. H. Foulger, H. Ballato. Carbon nanotube doped polyaniline. *Adv. Mater.* **14** (2002) 1480-1483.
- [49] Y. Ma, S. R. Ali, L. Wang, P. L. Chiu, R. Mendelsohn, H. He. In situ fabrication of a water-soluble, self-doped polyaniline nanocomposite: the unique role of DNA functionalized single-walled carbon nanotubes. *J. Am. Chem. Soc.* **128** (2006) 12064-12065.

- [50] E. Zelikman, R. Y. Suckeveriene, G. Mechrez, M. Narkis. Fabrication of composite polyaniline/CNT nanofibers using an ultrasonically assisted dynamic inverse emulsion polymerization technique. *Polym. Adv. Technol.* **21** (2010) 150-152.
- [51] T-M. Wu, S-J. Yen, E-C. Chen, R-K. Chiang. Synthesis, characterization, and properties of monodispersed magnetite coated multi-walled carbon nanotube/polypyrrole nanocomposites synthesized by in-situ chemical oxidative polymerization. *J. Polym. Sci. Pol. Phys.* **46** (2008) 727-733.
- [52] M. Baibarac, I. Baltog, C. Godon, S. Lefrant, O. Chauvet. Covalent functionalization of single-walled carbon nanotubes by aniline electrochemical polymerization. *Carbon* **42** (2004) 3143-3152.
- [53] E. Granot, B. Basnar, Z. Cheglakov, E. Katz, I. Willner. Enhanced bioelectrocatalysis using single-walled carbon nanotubes (SWCNTs)/polyaniline hybrid systems in thin-film and microrod structures associated with electrodes. *Electroanal.* **18** (2006) 26-34.
- [54] X-T. Zhang, W-H. Song. Electrochemical preparation and electrochemical behavior of polypyrrole/carbon nanotube composite films. *Front. Mater. Sci. China* **3** (2009) 194-200.
- [55] M. E. Garst, L. J. Dolby, S. Esfandiari, N. A. Fedoruk, N. C. Chamberlain, A. A. Avey. Reductions with lithium in low molecular weight amines and ethylenediamine. *J. Org. Chem.* **65** (2000) 7098-7104.
- [56] D. L. J. Clive, R. Sunasee. Formation of benzo-fused carbocycles by formal radical cyclization onto an aromatic ring. *Org. Lett.* **9** (2007) 2677-2680.
- [57] G. S. R. Subba Rao. Birch reduction and its application in the total synthesis of natural products. *Pure Appl. Chem.* **75** (2003) 1443-1451.
- [58] S. Chakraborty, W. Guo, R. H. Hauge, W. E. Billups. Reductive alkylation of fluorinated graphite. *Chem. Mater.* **20** (2008) 3134-3136.
- [59] S. Pekker, J.-P. Salvetat, E. Jakab, J.-M. Bonard, L. Forró. Hydrogenation of carbon nanotubes and graphite in liquid ammonia. *J. Phys. Chem. B* **105** (2001) 7938-7943.
- [60] A. Mukherjee, L. B. Alemany, J. Chattopadhyay, S. Chakraborty, W. Guo, S. M. Yates, W. E. Billups. Dodecylated large fullerenes: an unusual class of solids. *Chem. Mater.* **20** (2008) 5513-5521.
- [61] F. Liang, A. K. Sadana, A. Peera, J. Chattopadhyay, Z. Gu, R. H. Hauge, W. E. Billups. A convenient route to functionalized carbon nanotubes. *Nano Lett.* **4** (2004) 1257-1260.
- [62] F. Liang, L. B. Alemany, J. M. Beach, W. E. Billups. Structure analyses of dodecylated single-walled carbon nanotubes. *J. Am. Chem. Soc.* **127** (2005) 13941-13948.
- [63] J. Chattopadhyay, S. Chakraborty, A. Mukherjee, R. Wang, P. S. Engel, W. E. Billups. SET mechanism in the functionalization of single-walled carbon nanotubes. *J. Phys. Chem. C* **111** (2007) 17928-17932.
- [64] J. J. Stephenson, A. K. Sadana, A. L. Higginbotham, J. M. Tour. Highly functionalized and soluble multiwalled carbon nanotubes by reductive alkylation and arylation: the Billups reaction. *Chem. Mater.* **18** (2006) 4658-4661.
- [65] J. C. Thompson. Metal-nonmetal transition in metal-ammonia solutions. *Rev. Mod. Phys.* **40** (1968) 704-710.

- [66] A. Pénicaud, P. Poulin, A. Derré, E. Anglaret, P. Petit. Spontaneous dissolution of a single-wall carbon nanotube salt. *J. Am. Chem. Soc.* **127** (2005) 8-9.
- [67] A. García-Gallastegui, I. Obieta, I. Bustero, G. Imbuluzqueta, J. Arbiol, J. I. Miranda, J. M. Aizpuru. Reductive functionalization of single-walled carbon nanotubes with lithium metal catalyzed by electron carrier additives. *Chem. Mater.* **20** (2008) 4433-4438.
- [68] E. Anglaret, F. Dragin, A. Pénicaud, R. Martel. Raman studies of solutions of single-wall carbon nanotube salts. *J. Phys. Chem. B* **110** (2006) 3949-3954.
- [69] J. Chattopadhyay, F. J. Cortez, S. Chakraborty, N. K. H. Slater, W. E. Billups. Synthesis of water-soluble PEGylated single-walled carbon nanotubes. *Chem. Mater.* **18** (2006) 5864-5868.
- [70] J. Chattopadhyay, A. K. Sadana, F. Liang, J. M. Beach, Y. Xiao, R. H. Hauge, W. E. Billups. Carbon nanotube salts. Arylation of single-wall carbon nanotubes. *Org. Lett.* **7** (2005) 4067-4069.
- [71] R. Kamalakaran, M. Terrones, T. Seeger, Ph. Kohler-Redlich, M. Rühle, Y. A. Kim, T. Hayashi, M. Endo. Synthesis of thick and crystalline nanotube arrays by spray pyrolysis. *Appl. Phys. Lett.* **77** (2000) 3385-3387.
- [72] M. Pinault, M. Mayne-L'Hermite, C. Reynaud, V. Pichot, P. Launois, D. Ballutaud. Growth of multiwalled carbon nanotubes during the initial stages of aerosol-assisted CCVD. *Carbon* **43** (2005) 2968-2976.
- [73] M. Mayne, N. Grobert, M. Terrones, R. Kamalakaran, M. Rühle, H. W. Kroto, D. R. M. Walton. Pyrolytic production of aligned carbon nanotubes from homogeneously dispersed benzene-based aerosols. *Chem. Phys. Lett.* **338** (2001) 101-107.
- [74] E. R. Alvizo-Paez, J. M. Romo-Herrera, H. Terrones, M. Terrones, J. Ruiz-Garcia, J. L. Hernandez-Lopez. Soft purification of nitrogen-doped and undoped multi-wall carbon nanotubes. *Nanotechnology* **19** (2008) 155701-155710.
- [75] C. D. G. Minto, A. S. Vaughan. Electron irradiation and microstructure in polypyrrole. *J. Mater. Sci.* **30** (1995) 6028-6034.
- [76] S. Kumar, W. Wade Adams. Electron beam damage in high temperature polymers. *Polymer* **31** (1990) 15-19.
- [77] M. Dehonor, K. Masenelli-Varlot, A. González-Montiel, C. Gauthier, J. Y. Cavallé, H. Terrones, M. Terrones. Nanotube brushes: polystyrene grafted covalently on CN<sub>x</sub> nanotubes by nitroxide-mediated radical polymerization. *Chem. Commun.* (2005) 5349-5351.
- [78] W. Li, H. Zhang, C. Wang, Y. Zhang, L. Xu, K. Zhu, S. Xie. Raman characterization of aligned carbon nanotubes produced by thermal decomposition of hydrocarbon vapor. *Appl. Phys. Lett.* **70** (1997) 2684-2686.
- [79] J-h. Jeon, J-h. Lim, K-m. Kim. Hybrid nanocomposites of palladium nanoparticles having POSS and MWNTs via ionic interactions. *Macromol. Res.* **17** (2009) 987-994.
- [80] Y. Zhang, H. He, C. Gao, J. Wu. Covalent layer-by-layer functionalization of multiwalled carbon nanotubes by click chemistry. *Langmuir* **25** (2009) 5814-5824.
- [81] C. Gao, Y. Z. Jin, H. Kong, R. L. D. Whitby, S. F. A. Acquah, G. Y. Chen, H. Qian, A. Hartschuh, S. R. P. Silva, S. Henley, P. Fearon, H. W. Kroto, D. R. M. Walton. Polyurea-functionalized multiwalled carbon nanotubes: synthesis, morphology, and Raman spectroscopy. *J. Phys. Chem. B* **109** (2005) 11925-11932.

- 
- [82] M. Arora, V. Luthra, R. Singh, S. K. Gupta. Study of vibrational spectra of polyaniline doped with sulfuric acid and phosphoric acid. *Appl. Biochem. Biotech.* **96** (2001) 173-181.
- [83] Y. Furukawa, F. Ueda, Y. Hyodo, I. Harada, T. Nakajima, T. Kawagoe. Vibrational spectra and structure of polyaniline. *Macromolecules* **21** (1988) 1297-1305.
- [84] M. Deka, A.K. Nath, A. Kumar. Effect of dedoped (insulating) polyaniline nanofibers on the ionic transport and interfacial stability of poly(vinylidene fluoride-hexafluoropropylene) based composite polymer electrolyte membranes. *J. Membrane Sci.* **327** (2008) 188-194.
- [85] Y. Sun, S. R. Wilson, D. I. Schuster. High dissolution and strong light emission of carbon nanotubes in aromatic amine solvents. *J. Am. Chem. Soc.* **123** (2001) 5348-5349.

# Chapter 3 Nanoribbons and graphene generation from exfoliation of MWNTs

## 3.1 Introduction

Carbon is one of the most abundant elements in the universe. The chemistry of carbon is vast, allowing the synthesis of thousands of organic compounds, and is the basis for the existence of life (at least as we know it). Carbon [1] can be found in nature in its allotropic forms: diamond, graphite, fullerenes, nanotubes, and graphene. The term graphene appeared in 1987 [2] to describe single sheets of graphite, but the concept has already been around since 1947 [3]. Graphene [4], a two-dimensional crystal, which was supposed to be thermodynamically unstable, could not exist due to atomic displacement occasioned by thermal fluctuations and by the presence of defects that would make graphene unstable. This assumption was later supported by Mermin and by experimental observations. As a matter of fact, the melting temperature of thin films (in particular for metals and other 3D crystals) diminishes with decreasing thickness; as a result, films (with thickness of dozens of layers) become unstable and segregate into islands or decompose. Thin, 2D carbon films could only be obtained by aid of a support; on this respect, starting from the 1970s single layers of graphene were grown epitaxially on top of several materials [5]. Nonetheless, this epitaxial graphene showed altered electronic properties due to interaction of the  $\pi$  orbitals from the carbon network and the d orbitals of the substrate atoms. In an effort to obtain single graphene layers, graphitic sheets no less than 50 to 100 layers were obtained by mechanical exfoliation of graphite starting from 1990 [5].

It was not until 2004 that a research group led by A. K. Geim and K. Novoselov from Manchester University (UK) [6] successfully obtained graphene sheets up to several micrometers in size by mechanical exfoliation of highly oriented pyrolytic graphite (HOPG), in a process which was called micromechanical cleavage and that was done with a simple Scotch tape. After several separation steps the team obtained graphene

flakes on a SiO<sub>2</sub> substrate. This amazing discovery practically demolished what theory predicted. This is explained by the fact that atomic vibrations [1] are smaller than the interatomic distances, and coupling among bending and stretching modes can suppress other fluctuations; in addition, graphene has a low density of dislocations which is no match for the strong covalent bonding present in graphene. A little later, Berger and co-workers [7] synthesized high-quality graphene sheets by thermal decomposition of silicon carbide at high temperatures.

Graphene is a 2D, sp<sup>2</sup> honeycomb carbon lattice, and shows very interesting properties between traditional condensed-matter physics and the theory of relativistic electrons in vacuum (quantum electrodynamics) [8]. Due to the high quality of the carbon lattice, and the crystalline structure of graphene, electrons behave as massless Dirac fermions and move ballistically, that is, without scattering, for several hundreds of nanometers even at room temperature. This makes graphene suitable for the development of high-frequency transistors operating in the gigahertz range [9]. Moreover, though graphene has a zero band-gap which makes it a metallic conductor, its conductivity may be tuned up, thus making possible the creation of semiconducting devices. The lattice structure of graphene consists of two sublattices; in which the quantum-mechanical hopping between them forms two energy bands which intersect at the so called 'conical points (K and K') per Brillouin zone. Figure 3.1 depicts the lattice structure of graphene.

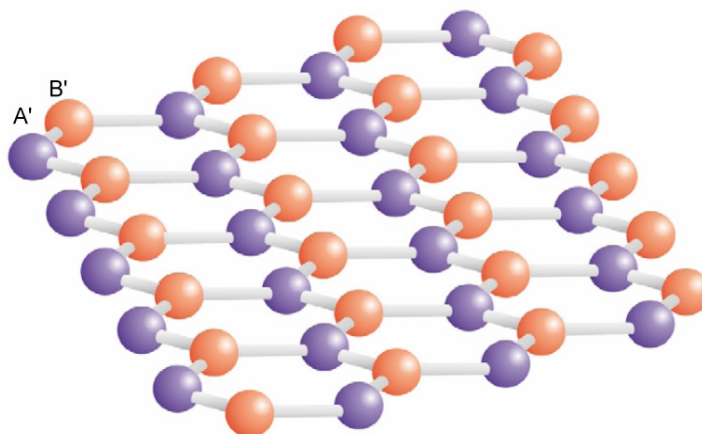


**Figure 3.1. Crystallographic structure of graphene.** Atoms from different sublattices are marked as A' and B', which repeat over the entire crystal [1].

### 3.1.1 Production methods for graphene and graphene ribbons

#### *Micromechanical cleavage / Exfoliation*

A very simple method consists of peeling off highly oriented pyrolytic graphite (HOPG) with Scotch tape [6]; graphene sheets can be further dispersed in acetone and placed on several substrates as shown at figure 3.2A. Figure 3.2B shows a graphene-based microdevice, and figure 3.2C shows its field-effect behavior, which is similar to that of ambipolar-field-effect semiconductors.

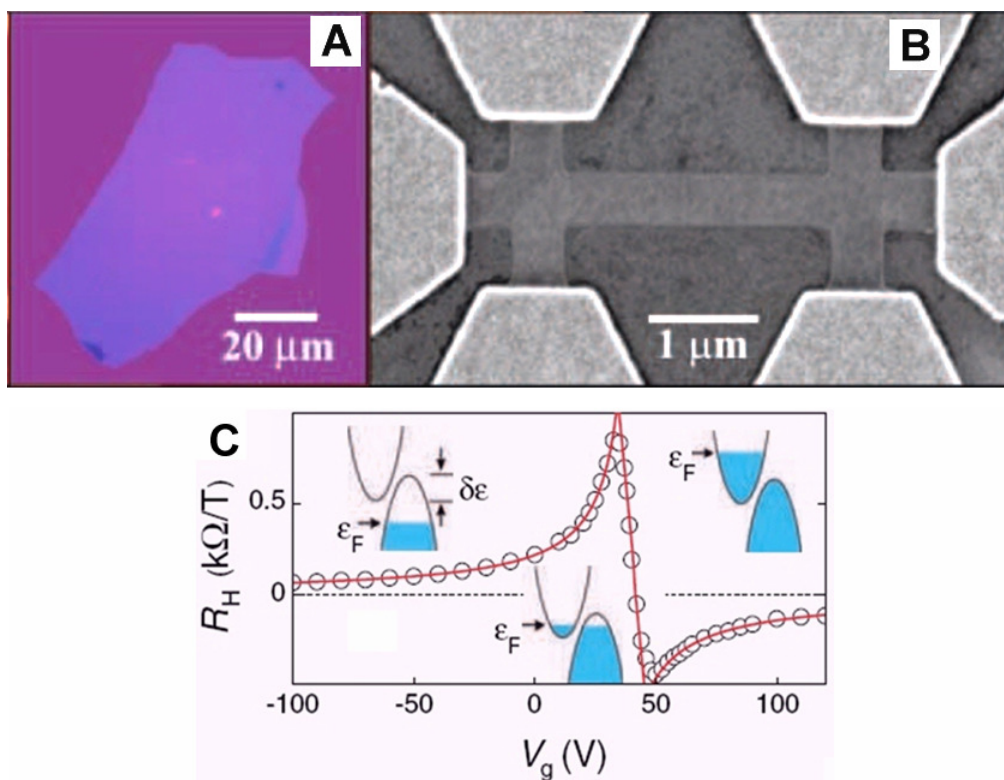


**Figure 3.2.** **A** graphene flake and a graphene-based FET device. **(A)** white light photograph of a graphene flake  $\sim 3$  nm width on a  $\text{SiO}_2$  substrate; **(B)** SEM image of a graphene-based microdevice; **(C)** Hall coefficient  $R_H$  as a function of  $V_g$  for a graphene layer at 5 K [6].

Microcleaved graphene presents intense Raman features: the G band ( $\sim 1580 \text{ cm}^{-1}$ ) and the G' band ( $\sim 2700 \text{ cm}^{-1}$ ). The line shape of the G' band may serve as a fingerprint for mono-, bi-, and few-layer graphene, as shown at figure 3.3 [10].

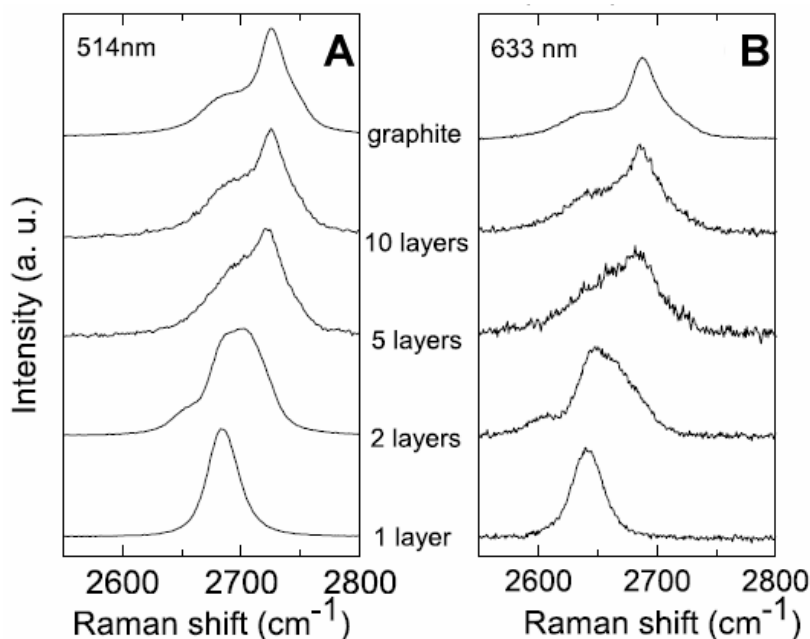


**Figure 3.3. Comparison of the G' Raman feature for graphite and graphene**, and evolution of the G' band with the number of layers [10].

### *Chemical oxidation and exfoliation of graphite*

Oxidation of graphite, followed by thermal shock or by dispersion in a proper solvent, is an inexpensive, long, and easy process by which individual graphene sheets or graphene flakes (up to grams) can be obtained. Graphite is usually oxidized by mixtures of strong acids and oxidants for several days [11]; afterwards, graphite is suddenly heated at high temperatures ( $\sim 1000$  °C) and exfoliated into graphene flakes. Other exfoliation methods involve intercalation of chemical species before thermal shock. As an example, intercalation of a mixture of sulfuric and nitric acids in graphite flakes [12] creates oxygen-bearing functional groups at their borders, kinks, and defects. An important point is that, upon functionalization, the  $sp^2$  network is disrupted, thus affecting the electrical properties of graphene. Thermal shock at high temperature ( $\sim 1000$  °C) evaporates intercalates and functional groups, which are suddenly expelled as gases, thus expanding and exfoliating the graphitic layers. Graphene flakes, obtained by this method, show capacitance values up to 117 F/g [13], higher than those presented by SWNTs and MWNTs, fast electrochemical redox response, and high surface area (up to  $\sim 920$  m<sup>2</sup>/g, determined by BET) as well; these properties make possible their use in

rechargeable batteries. Moreover, they also show [12] high on/off ratios ( $1 \times 10^5$ ) at room temperature, relatively high mobility of vacancies ( $200 \text{ cm}^2/\text{V}\cdot\text{s}$ ), and conductivity values [11] ranging from  $1 \times 10^3$  to  $2.3 \times 10^3 \text{ S/m}$  (bulk samples,  $0.3 \text{ g/cm}^3$ ).

An alternative to thermal shock is the dispersion of graphite oxide (GO) in a polar solvent. Due to the presence of oxygenated functional groups, graphite oxide (GO) exfoliates readily in a mixture of an organic solvent and water, from whence it can be spray-casted on a heated  $\text{SiO}_2$  substrate, and further reduced by hydrazine vapor [14]. Graphene obtained by this method can be dispersed in basic solutions from which conductive graphene films can be cast. Reduced GO shows a  $1 \times 10^4$  to  $1 \times 10^5$  fold increase in conductivity compared to that of parent GO [15]; individual graphene sheets from reduced GO have been used in the detection of gas molecules such as  $\text{NO}_2$  and  $\text{NH}_3$  [16], field-effect transistors with high switching speeds and high vacancies mobility have been built from exfoliated GO [12], and Schottky devices [14]. Furthermore, this method can be used to obtain uniform films of any desired coverage density, which show semiconducting behavior and a field effect response as well [14].

#### *Thermal decomposition*

Sublimation of silicon from silicon carbide leaves mono- or multilayer-graphene [17-19] known as epitaxially grown graphene (EG). Typically [18], a SiC substrate is annealed at high temperature ( $\sim 1000 \text{ }^\circ\text{C}$ ), which decomposes SiC and desorbs Si from the surface; thus forming a carbon layer. This layer, called carbon nanomesh, interfacial graphene, or carbon buffer layer, after further annealing at ultrahigh vacuum ( $P < 5 \times 10^{-9} \text{ mbar}$ ) produces monolayer ( $\sim 1200 \text{ }^\circ\text{C}$ , 2 min), bilayer ( $\sim 1250 \text{ }^\circ\text{C}$ , 2 min), or trilayer ( $> 1300 \text{ }^\circ\text{C}$ , 2 min) graphene on top of it, as depicted in figure 3.4.

In contrast to typical graphene, which is a zero-gap semiconductor, epitaxially grown graphene [20] presents a gap at the K point of the Brillouin zone, as demonstrated by angle-resolved photoemission spectroscopy (ARPES). This gap is probably due to breakage of the A-B sublattice symmetry, which leads to re-hybridization of the valence and conduction band states associated to the same Dirac point, thus resulting in a gap at the K point.

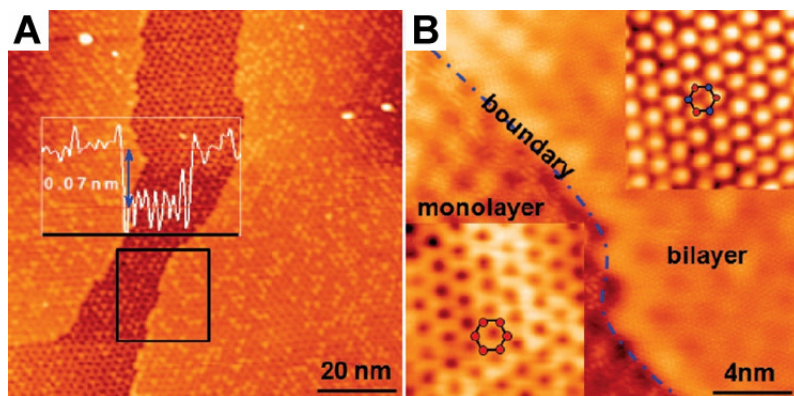


**Figure 3.4. STM images of epitaxial graphene on SiC(0001).** (A) STM image ( $100 \times 100 \text{ nm}^2$ ) of the monolayer (darker central region) and bilayer (lighter terraces aside) graphene. (B) High-resolution STM image ( $20 \times 20 \text{ nm}^2$ ) showing the coexistence of monolayer (lower left square) and bilayer (upper right zone) epitaxial graphene (EG). The hexagonal lattice is kept at the monolayer EG; while two inequivalent triangular lattices arise at the bilayer, showing AB stacking and a loss of lattice symmetry. Taken from [18].

In addition, EG is electron-doped, as revealed by the shifts of the Dirac point energy determined by ARPES; this shows that graphene may be a suitable semiconductor for nanoelectronics. The number of layers can be determined by multiple techniques. Raman spectroscopy allows the measurement of the full-width at half maximum (FWHM) of the G' (2D) peak [17], which may be helpful for layer number assignment. Auger spectroscopy, x-ray photoelectron spectroscopy (XPS), and ARPES measure the band structure along the  $k_z$  direction in the Brillouin point, which is directly related to the number of graphene layers [20]. An important fact is that the absence of  $\pi$  band dispersion along the  $k_z$  direction in two Brillouin zones indicates that the sample consists in single-layer graphene [20]. Epitaxial growth of graphene is still challenging. The tuning of the experimental conditions (e.g., annealing temperature, time, and vacuum pressure) remains as a critical task in order to precisely control the number of layers and the electronic properties of epitaxial graphene.

### *Chemical vapor deposition (CVD)*

CVD methods allow large-scale production of carbon nanotubes, carbon nanoribbons, and graphene [21-24]. Furthermore, in comparison to micromechanical cleavage, CVD methods allow the synthesis of large-area graphene [22]. Nucleation and growth of graphene monolayers is usually performed by exposure of a transition metal substrate (Pt [25], Ir [26], Ru [27], and Ni [28]) to a hydrocarbon gas under low pressure

or ultra-high-vacuum (UHV) conditions, thus making this method expensive. In contrast, graphene can be obtained at ambient pressure [22] on a polycrystalline Ni/SiO<sub>2</sub>/Si substrate at high temperature (900–1000 °C) under a mixture of flowing CH<sub>4</sub> (5–25 cm<sup>3</sup>/min) and H<sub>2</sub> (1500 cm<sup>3</sup>/min), which is injected for 5–10 min.

Mono, bi, and tri-layer of continuous, conducting graphene films were grown by this method, being the area of the film limited to the Ni substrate. Raman spectra of 1, 2, and 3 graphene layers show characteristic features (figure 3.5) such as: a very low-intensity D band (~1350 cm<sup>-1</sup>), and the symmetry-allowed graphite band or G band (~1580 cm<sup>-1</sup>). In addition, 1 layer graphene is characterized by a very sharp line width (30 cm<sup>-1</sup>) and a single Lorentzian profile of the G' band, (~2700 cm<sup>-1</sup>). The shape of the G' peak is useful in the determination of the number of layers. Since the G' band is similar in 1-L and 3-L graphene, the intensity ratio of the G and G' bands ( $I_G/I_{G'}$ ) correlates better with the number of layers in CVD graphene [22].

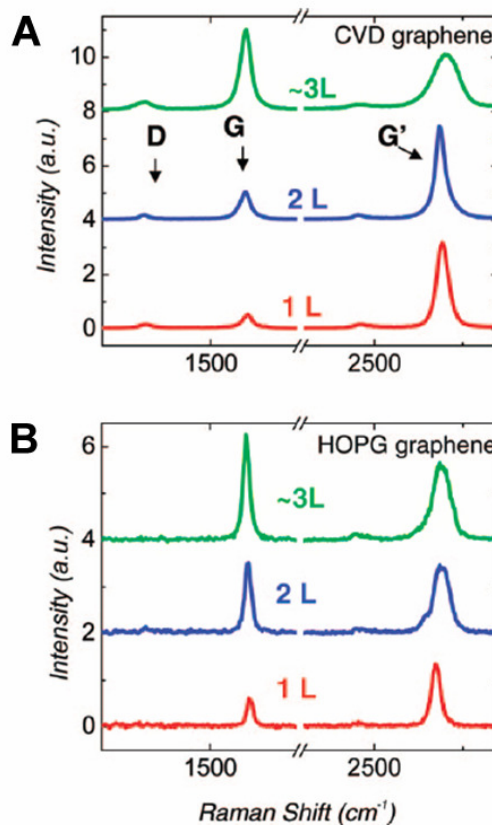


**Figure 3.5. Raman spectra of CVD-grown graphene films on Ni/SiO<sub>2</sub>/Si.** 1, 2, and 3 layers of: (A) CVD-graphene; (B) HOPG-graphene obtained by microcleavage and added for comparison.  $\lambda = 532$  nm. In HOPG, the G' line shape is a good measure of the numbers of layers [22].

Highly crystalline, graphite-like structure multi-layered carbon nanoribbons (figure 3.6) have also been synthesized by CVD [29], showing ABAB stacking and strong Raman features at 1355 cm<sup>-1</sup> (D band) and 1584 cm<sup>-1</sup> (G band); the high intensity of the D band is caused by ripples and edges present in carbon nanoribbons. This is supported by XPS analysis, which confirms the presence of sp<sup>2</sup> and sp<sup>3</sup> bonding in a 1:1 ratio. These ribbons show metal-like, ohmic I-V behavior.

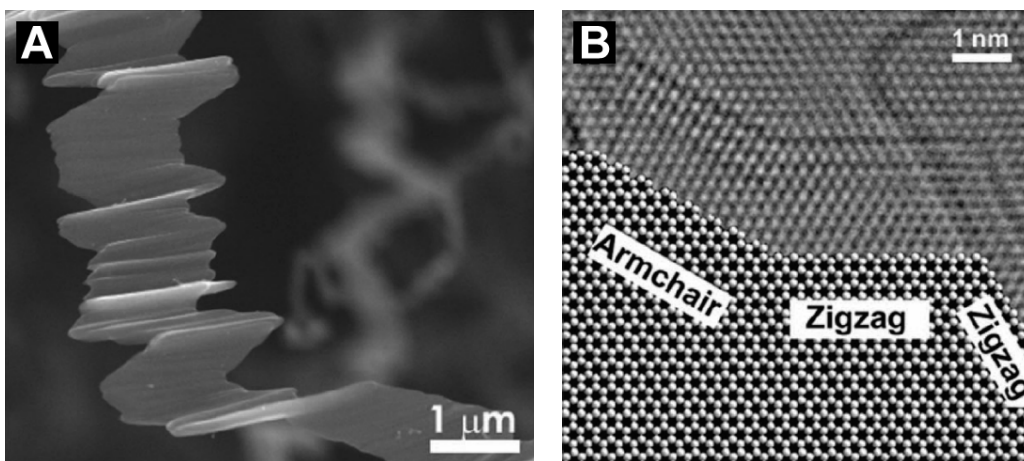


**Figure 3.6. CVD-grown graphene nanoribbons.** (A) SEM image, showing the characteristic rippled appearance of the ribbons obtained by JRCd. (B) HRTEM image showing the presence of zigzag and armchair edges after Joule heating of a ribbon; note that the lower region is a schematic of the hexagonal structure [29].

### Annealing of Carbon Nanotubes

Multi-shell, graphitic nanoribbons (GNRs) have been obtained [30] after heating arc-discharge SWNTs at high temperatures ( $> 1800$  °C). Bundled SWNTs coalesced into GNRs (figure 3.7); SWNTs samples showed dominant features at  $1353\text{ cm}^{-1}$  and  $1582\text{ cm}^{-1}$  (D and G bands, respectively), the intense D band being assigned to the finite width of GNRs, and a shoulder at  $\sim 1570\text{ cm}^{-1}$  that seems to be derived from the  $1582\text{ cm}^{-1}$  interlayer modes of graphite and that is due to the cylindrical symmetry of small-diameter CNTs.

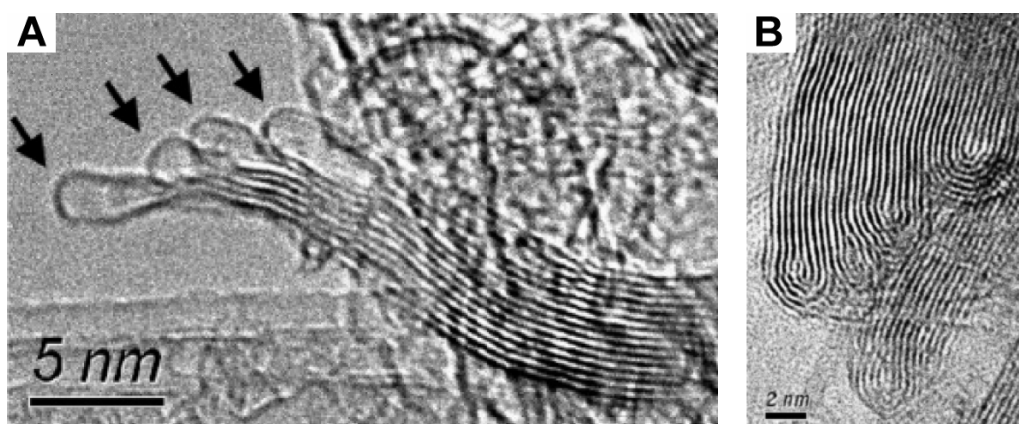


**Figure 3.7. Multilayered, graphitic carbon nanoribbons from coalesced SWNTs.** (A) GNRs obtained from coalescence and collapse of arc-discharge SWNTs at  $1800$  °C; (B) another type of GNRs, formed after bundling of SWNTs into MWNTs and further collapse after annealing at  $2200$  °C [30].

## Organic synthesis

Carbon chemistry has become a valuable and elegant tool as a bottom-up approach for the synthesis of GNRs from phenylene [31] or naphthalene [32] derivatives as building blocks. For example, the Suzuki-Miyaura coupling of 1,4-diiodo-2,3,5,6-tetraphenylbenzene and 4-bromophenyl-boronic acid [31], after further reaction with *n*-butyl-lithium and 2-isopropoxy-4,4,5,5-tetramethyl-[1,3,2]dioxaborolane and polymerization and reduction of the resulting product, led to the successful synthesis of polyphenylenes, as observed in figure 3.8.

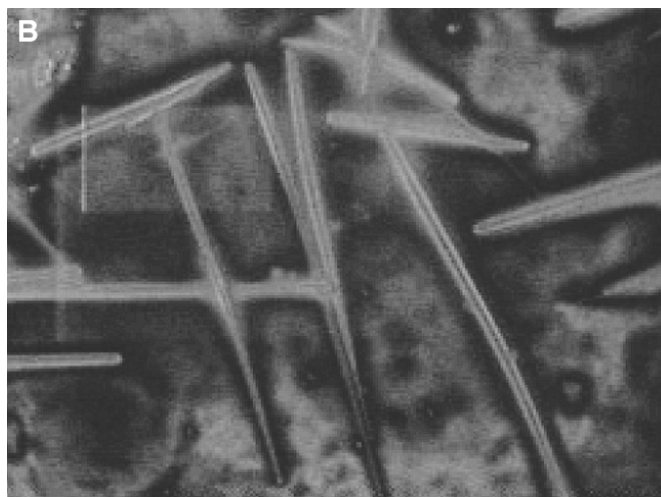
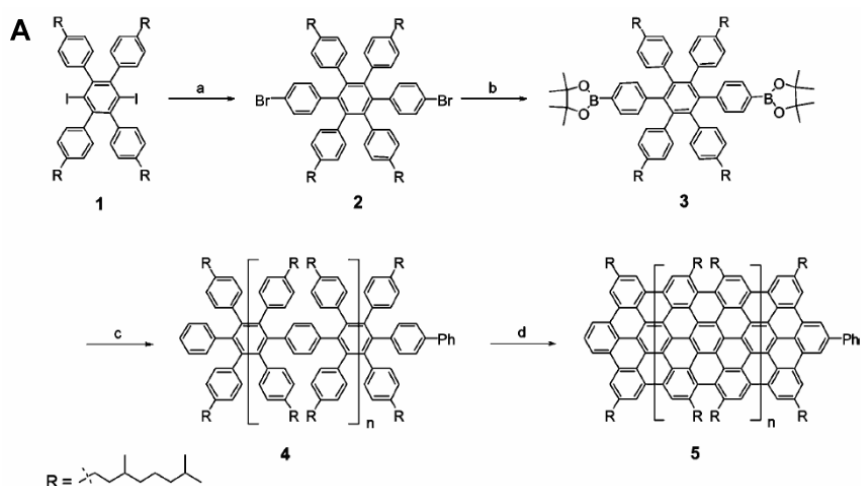


**Figure 3.8. Suzuki-Miyaura coupling leading to carbon nanoribbons.** 1, coupling of 1,4-diiodo-2,3,5,6-tetraphenylbenzene and 4-bromophenyl-boronic acid; 2, reaction with *n*-butyl-lithium, followed by reaction with 2-isopropoxy-4,4,5,5-tetramethyl-[1,3,2]dioxaborolane, and polymerization of (3) and (1), thus obtaining polyphenylenes (4) which were further reduced by FeCl<sub>3</sub>. Reaction efficiency was ~37%. Polyphenylene nanoribbons (100–200 nm wide, 5 μm long) were dispersible in organic solvents [31].

By using Wittig reactions followed by stilbene-like photocyclizations as the main steps of synthesis, Mallory *et al.* [33] produced polycyclic aromatic compounds called *n*-phenacenes, for which the number of phenyl rings is associated to a specific wavelength at UV spectra. In a more complete study [34], GNRs were synthesized from polyphenylenes by repeated Diels-Alder cycloaddition of 1,4-bis(2,4,5-triphenylcyclopentadienone-3-yl)benzene and diethynylterphenyl in good yield. Raman spectra, which resembles to that of disordered graphite, showed important features at  $1322\text{ cm}^{-1}$  (D band), and  $1603\text{ cm}^{-1}$  (G band); thus suggesting the presence of disorder, i. e., of structural defects and small conjugated domains with finite size. For a more detailed and recent review on the synthesis of GNRs, the reader can refer to [35].

Graphene snares many of the remarkable properties of carbon nanotubes, but can be produced by low-cost scalable methods. On this respect, exfoliation of graphite intercalated compounds [36-40] and Si sublimation from SiC substrates [7, 17-19] are some of the most promising methods for the obtention of graphene in bulk quantities at a relatively low cost. This would bring into reality appliances such as “smart clothing”, quantum computers, faster computer chips, biotech drugs, better batteries for electric cars, electronic and flexible newspapers, building-integrated photovoltaics [41]. Many of these applications are being developed with vast funding in research centers around the globe; for example, Lin and co-workers at the IBM T. J. Watson Research Center (Yorktown Heights, NY 10598, USA) have recently built a 100 Ghz graphene-based computer processor [9] from wafer-scale epitaxial graphene, thus demonstrating the high potential of graphene for electronics. Moreover, according to ISI Web of Knowledge, the number of publications has almost doubled in the last two years (2008–2010), with a total of more than 6500 research papers published in a 5-year timespan (search term: graphene). It seems that graphene may become a new milestone of nanotechnology.

### 3.1.2 Graphene nanoribbons from multi-walled carbon nanotubes: the nanotubes salt method

In this chapter we present the main results concerning a singular phenomenon from which we talked in chapter 2: the unfolding of multi-walled carbon nanotubes into carbon nanoribbons during the synthesis of composites. This unexpected result consisted in the opening of some tubes either at the tips or at some segments after purification of composites; thus, we decided to study this phenomenon. In this chapter, we present a novel, efficient method for the synthesis of carbon nanoribbons by unfolding MWNTs. In this method, MWNTs are opened at their tips and are intercalated with ionic lithium and ammonia, which allows the unzipping of MWNTs into carbon nanoribbons and stacked sheets. One of the main features of these unwrapped MWNTs or ex-MWNTs is the large number of exposed edges that can be functionalized and that are susceptible of further chemical modification, hence making this material attractive for different applications. Furthermore, ex-MWNTs can be functionalized in the same way that carbon nanotubes [42-46], and improve their dispersion in a wide variety of solvents and polymers, thus easing their potential applications. In addition, characterization of the morphology and of some vibrational and structural properties of these ex-MWNTs allowed us to propose a mechanism for the exfoliation of MWNTs.

We should note that exfoliation is commonly understood as the separation of bundled single-walled carbon nanotubes in individual carbon nanotubes; in contrast, in this thesis we define the term *exfoliation* as the unfolding or the separation of graphitic sheets in tubes, since it occurs by a breakage and separation of layers, as will be discussed below.

Our interest in the exfoliation phenomenon arose from the direct observation by electron microscopy of opened MWNTs during the synthesis of nanocomposites from *in situ* polymerization of anilines and pyrrole. After washing nanocomposites with hydrochloric and nitric acids, we found by SEM and TEM several tubes damaged, while others appeared partially exfoliated or unfolded, as shown at figures 3.9 and 3.10.

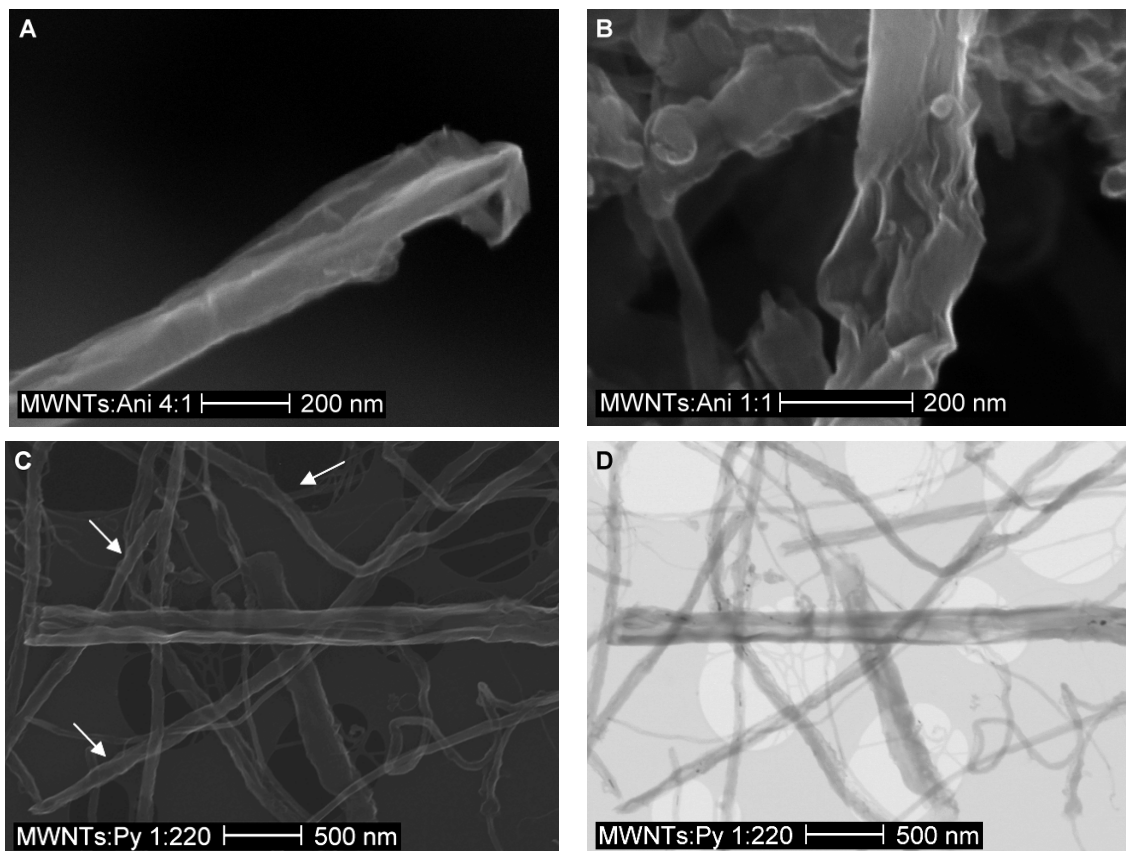


**Figure 3.9. SEM/STEM images of exfoliated MWNTs after washing MWNTs/PAni and MWNTs/PPy nanocomposites with acids:** (A) A partially opened tip of a MWNT, note the damage imparted to the tube. (B) A segment of a MWNT opened in the middle. (C) MWNTs showing varying widths, many of them are damaged and some are opened (see arrows). Note the big tube (middle) that seems to be fully opened. (D) STEM image of (C), which shows the opened tubes in better detail.

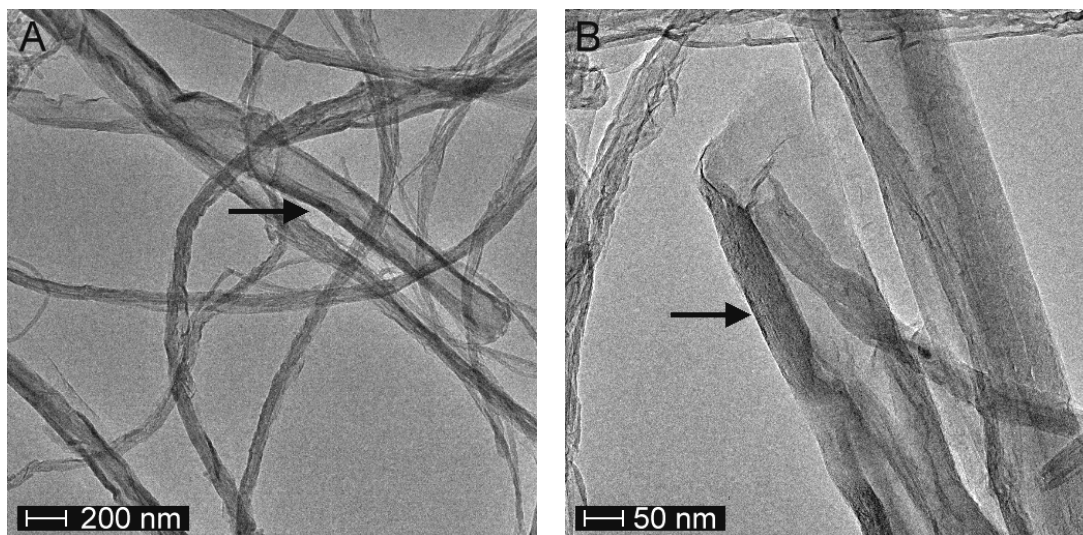


**Figure 3.10. TEM images of exfoliated MWNTs** (see arrows) after washing MWNTs-polyaniline nanocomposites with HCl. (A) Shows tubes with different width, all of them show damage, others show partial opening, and a few ones are completely opened (at least, in a segment, see arrow). (B) Ex-MWNTs displaying more clearly their ribbon-like morphology (see arrow). Adapted from [47].

We considered that this was due to intercalation. However, this phenomenon had not been reported; some authors [48] have only found that the diameter of MWNTs enlarges by a factor of two over the original value, after the electrochemical intercalation and de-intercalation of lithium with propylene carbonate as an electrolyte; this suggests that the walls may be ruptured [49, 50]. Meier *et al.* found that nitrogen-doped MWNTs ( $\text{CN}_x$ ) subjected to Birch reduction conditions led to fractured  $\text{CN}_x$ . In both cases tubes remained in a concentric arrangement and unwrapping was not reported, showing only detachment of some graphitic material or breakage of tube walls (figures 3.11A and B).

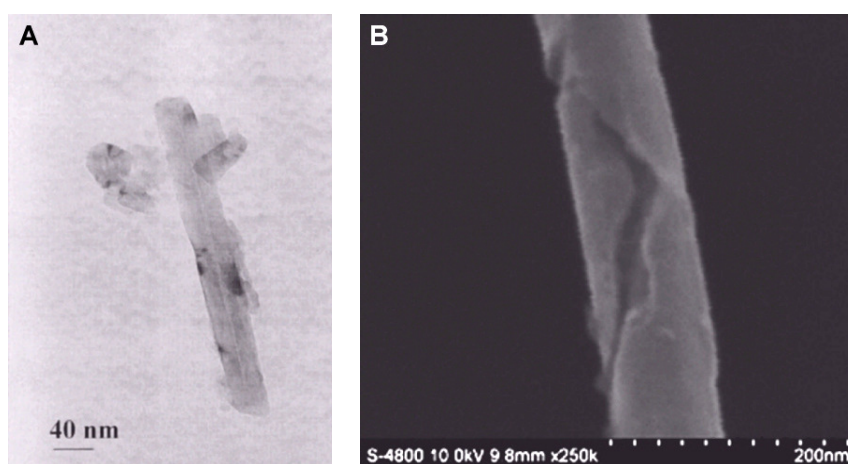


**Figure 3.11. Partial exfoliation and breakage in MWNTs and  $\text{CN}_x$ .** (A) MWNTs showing detachment of graphitic material and expansion after lithium intercalation in a carbonate-based solvent mixture [50]. (B) Nitrogen-doped MWNTs ( $\text{CN}_x$ ) displaying breakage of tube walls after Birch reduction [48].

Intercalation changes the interplanar distance between graphitic cylinders. Depending on the experimental conditions and the nature of the intercalants, the interlayer distance may vary considerably. For example, intercalation of lithium in graphite changes the interlayer distance from 3.35 Å to 3.70 Å [51], while simultaneous intercalation of Li and  $\text{NH}_3$  in graphite leads to an interlayer distance of 6.62 Å [52]. To the best of our knowledge, no research has been reported on the co-intercalation of Li and  $\text{NH}_3$  in MWNTs and the production of carbon nanoribbons from unzipping intercalated MWNTs. Arc-grown MWNTs hydrogenated in Li- $\text{NH}_3$  medium [53] showed only ruffled concentric cylinders, but no exfoliation was observed probably because the tubes are highly crystalline and have their ends closed, thus avoiding intercalation. A more detailed introduction to the intercalation in graphite can be found in [appendix A.2](#).

## 3.2 Experimental procedure for the synthesis of exfoliated multi-walled carbon nanotubes (ex-MWNTs)

### 3.2.1 Materials

For a full description of materials, please refer to [section 2.3](#). Originally, CVD-grown MWNTs (~400  $\mu\text{m}$  to 500  $\mu\text{m}$  long, see [section 1.3](#) for the synthesis procedure) were purified by a modified hydrothermal procedure [\[54\]](#). In further experiments we also cut and purified MWNTs with a modification of the method of Liu *et al.* [\[55\]](#). In this method acids cut MWNTs into shorter tubes and also remove their caps, thus facilitating intercalation of Li and  $\text{NH}_3$ . MWNTs were cut and opened at their ends by sonication (0.1 mg/mL) in a mixture of  $\text{HNO}_3\text{:H}_2\text{SO}_4$  3:1 for ~30 hours. Cut MWNTs were filtered (PTFE 0.22  $\mu\text{m}$ , Sartorius) and washed with methanol and water. MWNTs were separated from undesired carbon and organic materials (such as humic acids) either by sonication in 0.1 M NaOH for 30 minutes or magnetic stirring for 12 hours, followed by washing with distilled water.

### 3.2.2 Nanoribbons and graphene generation from lithium-ammonia intercalation and exfoliation in MWNTs

A procedure similar to that used for the synthesis of composites in chapter 2 was followed, except that no monomers were used, and the volume of condensed  $\text{NH}_3$  was not less than 250 mL. Purified MWNTs (~25 mg) were dispersed by sonication in dry tetrahydrofuran (~50 mL), followed by addition to liquid  $\text{NH}_3$ . Li was then added in a 10:1 ratio Li/C (w/w). The reactor was kept cold with an acetone-dry ice (~ -77  $^\circ\text{C}$ ) or acetone-liquid  $\text{N}_2$  bath (~ -94.7  $^\circ\text{C}$ ). Intercalation was allowed to proceed for several hours; and then allowed to heat to ambient temperature to evaporate  $\text{NH}_3$  (~ 5 to 20 hours). After full evaporation of  $\text{NH}_3$ , a 10% HCl solution was carefully added under inert atmosphere to the reactor (since the excess Li reaction with acid is highly exothermic), then the mixture was magnetically stirred for several minutes, after which the product

was recovered by microfiltration (Millipore, PTFE, 0.45  $\mu\text{m}$  pores) and dried in a gravity oven at 100  $^{\circ}\text{C}$  (Lindberg/Blue M, GO1390A-1) for one to two hours, and cooled in a desiccator (anhydrous  $\text{CaCl}_2$  was used as desiccant). The experimental setup is shown at [figure 3.12](#).

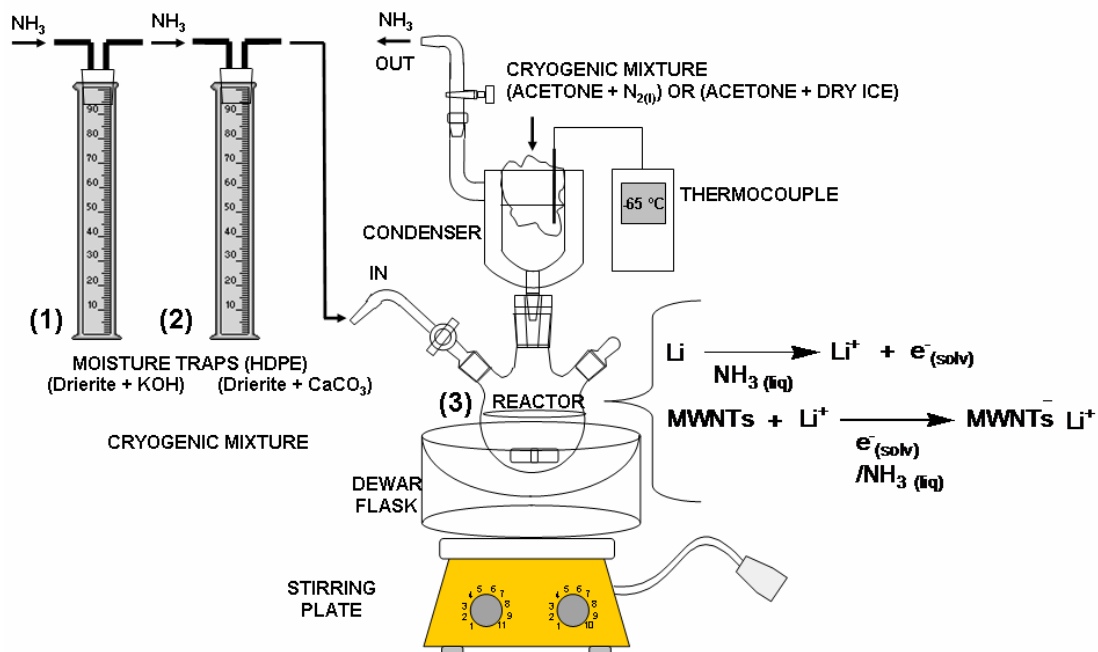


**Figure 3.12.** Experimental setup for lithium-ammonia intercalation in MWNTs.

In addition, samples were abruptly heated at 1000  $^{\circ}\text{C}$ ; each sample was introduced in a quartz tube (45.75" L x 1.25" O.D.) under flowing argon, and the assembly was then introduced in a tube furnace (Barnstead|Thermolyne 21100) for one or several minutes ([see figure 3.13](#)). Care was taken to put the sample in the hottest zone of the furnace with aid of measuring tape and a thermocouple thermometer. The full set of experimental conditions used in the exfoliation of MWNTs for all experiments can be found in [appendix A.3](#).

Scanning transmission electron microscopy (STEM, images taken in a FEI XL-30 SFEG) was used as a key tool to compare the efficiency of the different intercalation and exfoliation procedures. Samples were sonicated for  $\sim 30$  s to 2 min in ethanol or methanol, and one to three drops of the obtained suspension were placed on lacey-carbon TEM grids.

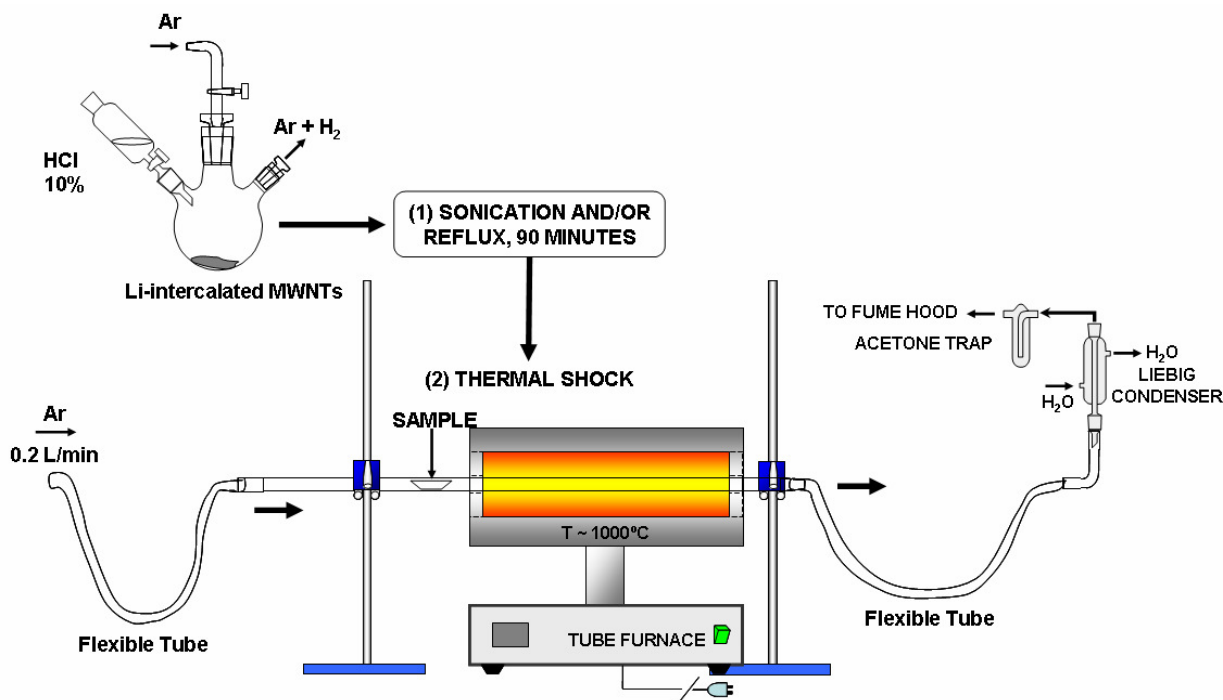


**Figure 3.13. Exfoliation of lithium-intercalated MWNTs.** The excess Li is removed by careful addition of 10% HCl under inert atmosphere, and refluxed for several minutes. Next, the dry product is placed in a ceramic boat and put in a quartz tube. The tube is suddenly inserted in a tube furnace at 1000 °C for one or several minutes.

According to the extent damage and exfoliation present in samples, tubes were classified as: intact, damaged (only outer walls were exfoliated or ruffled), partially exfoliated (open tube ends or opened segments were present), and ex-MWNTs (tubes completely unwrapped along their main axis); as shown in [figure 3.14](#). At least 40 nanotubes were classified and counted to estimate the efficiency of each treatment. Statistics was done by opening SEM images (preferably, at high resolution) with Image Pro Plus V 4.5 (Media Cybernetics) and by visually counting intact, damaged, partially exfoliated tubes or ex-MWNTs; counts were input in a spreadsheet and their relative amounts calculated. Measurements were done using the scale bar in each image for calibration. In most cases, several images were needed to complete counting. Further characterization was done by transmission electron microscopy (JEOL 4000, with the help of Jessica Campos, David Smith and David Cullen at Arizona State University), atomic force microscopy (AFM, JEOL JSPM 5200, tapping mode), micro-Raman spectroscopy (InVia Renishaw, 514 nm, 1% power), X-Ray powder diffraction (XRD Bruker D8 Advance), and thermogravimetric analysis (Thermo-Cahn VersaTherm).

## 3.3 Results and discussion

### 3.3.1 Morphology

#### *Electron Microscopy techniques*

Figure 3.14 shows scanning electron microscope images of intact, damaged, partially exfoliated, and completely unwrapped tubes obtained after exfoliation. Where more exfoliation was apparent, about 100 nanotubes or more were counted to estimate more accurately the extent of exfoliation.

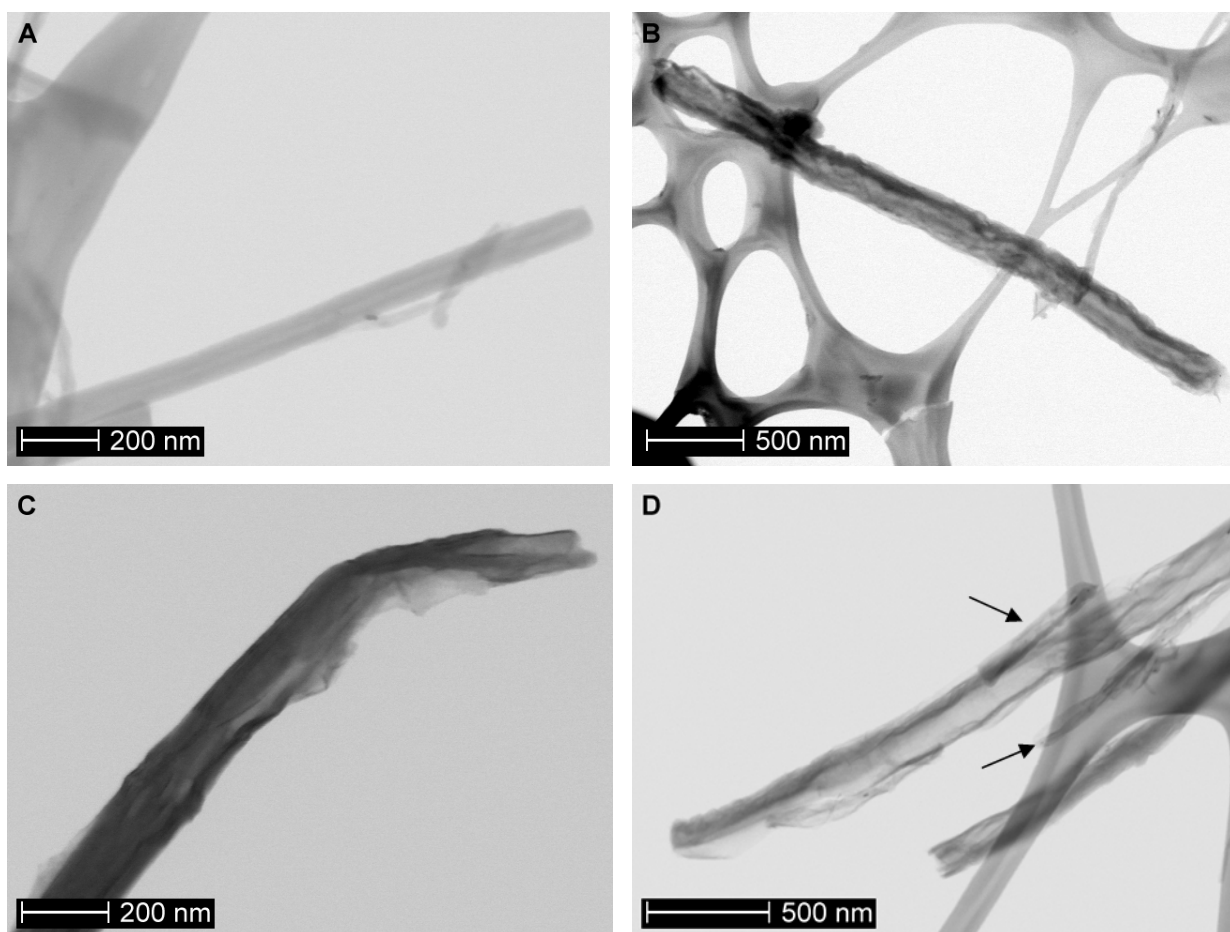


**Figure 3.14. STEM micrographs after lithium intercalation and exfoliation in MWNTs.** (A) A tube showing no damage, walls remain intact. (B) A damaged tube, note how the outer walls seem to be rippled and wavy. (C) A tube end partially exfoliated; the tube also shows some damage. (D) Ex-MWNTs, nanotubes completely unzipped along their whole length; image modified from [47].

Figure 3.14A shows an intact tube. Note that the outer walls look intact and no damage is seen. Figure 3.14B shows a representative of a “damaged” tube where the walls are rippled, even fragmented, but the tube does not open. Other MWNTs are opened partially at the tips or in segments, such as the one presented at figure 3.14C. In contrast, figure 3.14D displays tubes opened in a ribbon-like fashion and showing some damage at their edges and walls. In addition, it seems that smaller tube fragments may detach from larger tubes. Figure 3.14D shows that the width of these unwrapped MWNTs can reach up to 100 nm or more, with an almost-flat appearance.

The original exfoliation procedure using purified MWNTs and acids produced only a small amount of unwrapped MWNTs (ex-MWNTs, ~0–5%), and a large amount (~3–60%) of partially exfoliated, damaged (~20–55%), and intact (~0–50%) tubes. Exfoliation may occur as an effect of lithium intercalation within the concentric graphitic layers, followed by unwrapping of MWNTs upon reaction of lithium with the 10% (v/v) HCl solution used to remove residual Li. Preliminary results [56] showed that low amounts of Li led to a lower exfoliation degree. In subsequent experiments we always used a 10:1 Li/C ratio (w/w) to ensure full intercalation and thus enhance exfoliation and opening of MWNTs.

Sonication in dry THF to disperse MWNTs, and soft acid treatments to induce defects in the walls before reaction did not increase the amount of exfoliated MWNTs.

Refluxing in 10% HCl for 2 h was more effective for exfoliating MWNTs than room-temperature magnetic stirring, sonication in a bath (~60 °C) was equally effective, and refluxing after sonication was moderately more effective. Alkali metal-THF ternary graphite intercalation compounds (GICs) have been reported [36]. Adding THF after reaction with Li-NH<sub>3</sub>, allowing NH<sub>3</sub> to evaporate, and leaving the nanotube salts in THF at room temperature in a closed container under magnetic stirring for 1 week did not increase the amount of ex-MWNTs. This suggests that neither further intercalation of Li nor formation of a ternary Li-THF compound occur under these conditions. The use of HNO<sub>3</sub> and H<sub>2</sub>SO<sub>4</sub> instead of HCl does not produce more unwrapped tubes, but increases damage due to oxidation. Ultrahomogenization during addition of reactants also induces damage to MWNTs.

By using purified MWNTs (~50–100  $\mu\text{m}$  long, without cutting) on the experiments described, ~50% of the tubes were partially exfoliated (unwrapping running up from 2–3  $\mu\text{m}$  from the tip), ~20% were intact, and almost no ex-MWNTs were observed. [Figures 3.14C](#), [3.15](#) and [3.16](#) depict clear examples of partial unwrapping.

The volume of  $\text{NH}_3$  could also be a very important factor, since the highest amount of ex-MWNTs was obtained with the following  $\text{NH}_3/\text{Li}/\text{C}$  ratios: 14:5:1 (65%), 10:5.6:1 (50%), and 33:1:2 (43%); on this basis, a 10:1 ratio  $\text{NH}_3/\text{C}$  (v/w) was used (~10 mL of  $\text{NH}_3$  per mg of MWNTs).

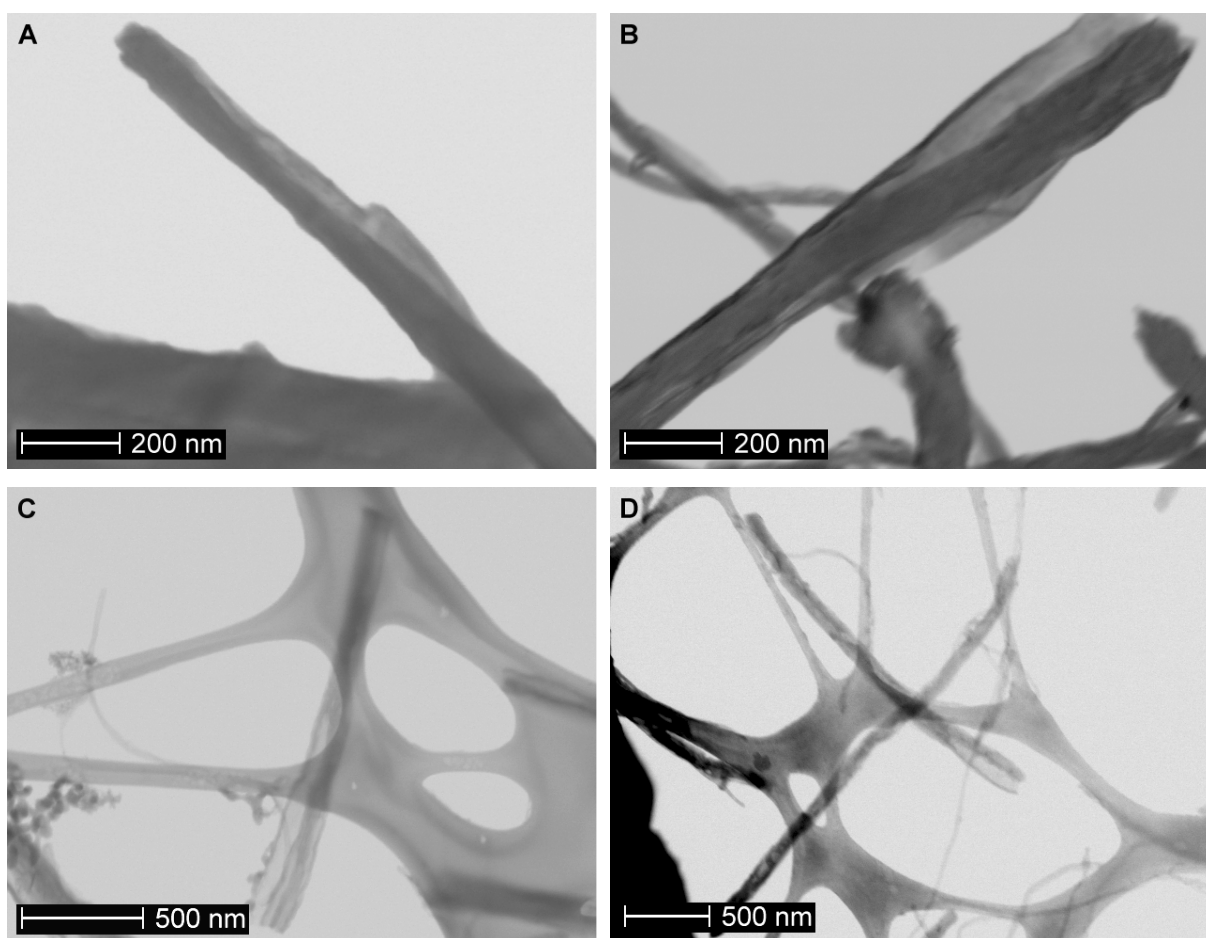


**Figure 3.15. STEM micrographs of partially unwrapped MWNTs**, obtained by reaction of intercalated lithium with acids. **(A)** A MWNT apparently showing unwrapping in a tip. **(B)** A MWNT partially exfoliated tip segment, it seems that the tube has been halved; note the damage on the outer walls, denoted by the wavy aspect. Exfoliation runs ~600 nm from the tip to the center of the tube. **(C)** A short MWNT (~1.5  $\mu\text{m}$  long) partially unwrapped standing on a lacey carbon/Formvar support (from a copper grid); the exfoliated segment is ~700 nm. Accompanying material at left may be derived either from the intercalation reaction and/or the exfoliation process. **(D)** Two crossed damaged and partially unwrapped MWNTs, along with non-exfoliated tubes of small diameter and some material produced during exfoliation.

TEM images also reveal that during exfoliation, MWNTs are opened in a zipper-like fashion, as shown at [figure 3.16](#). Such opening in many cases seems to extend in the direction of the basal plane.

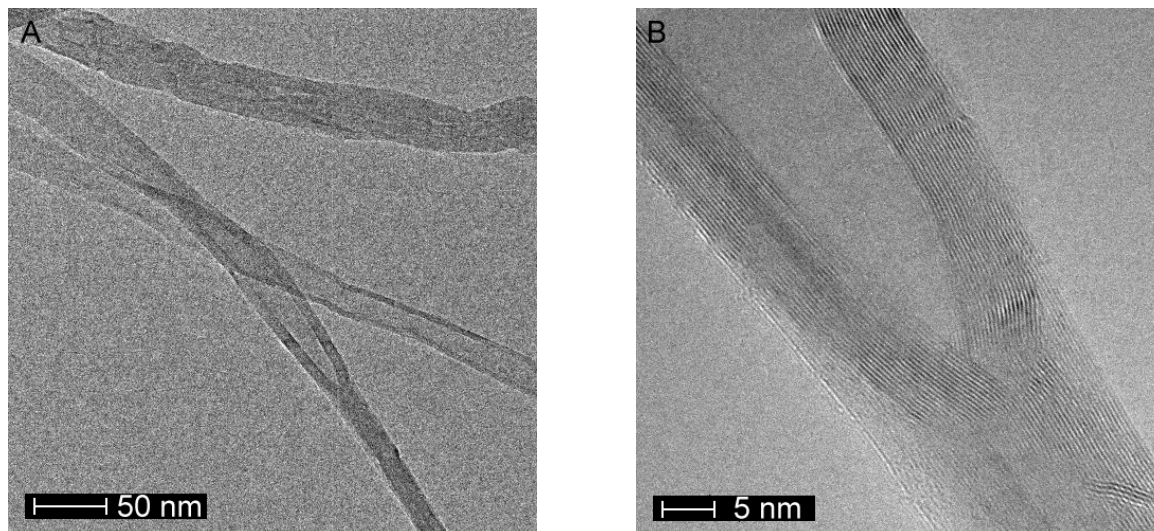


**Figure 3.16. TEM images of partially exfoliated MWNTs**, showing how exfoliation occurs after exposing Li-intercalated MWNTs to HCl. **(A)** MWNTs unfolding into carbon nanoribbons; **(B)** detailed view of a MWNT in the process of unwrapping [\[47\]](#).

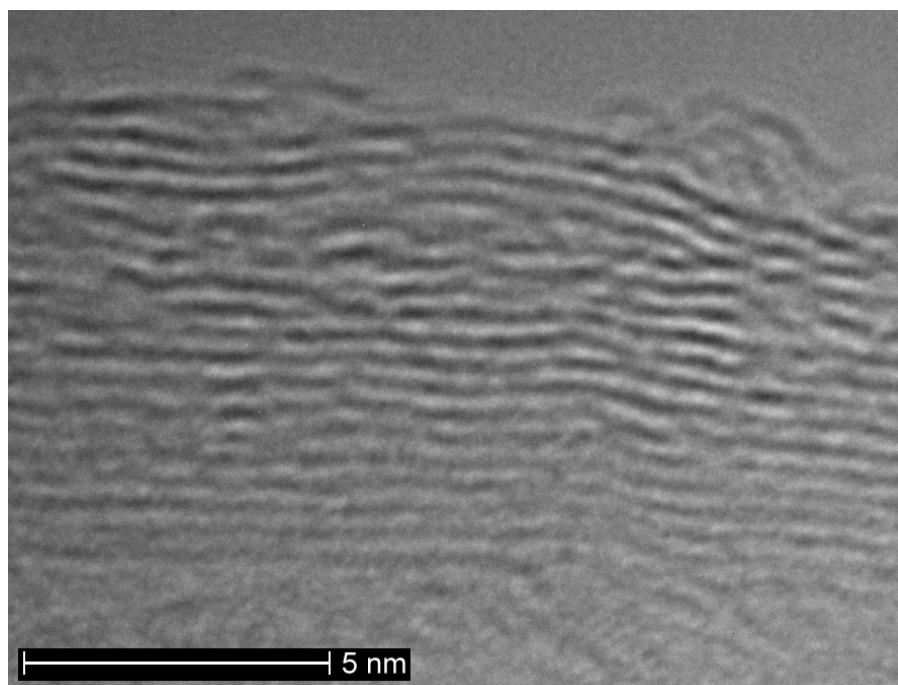


**Figure 3.17. Interlayer distances in a MWNT after Li intercalation and acid treatment.** Non-statistical measurement of interlayer distance was done randomly in this zone with aid of Image Pro Plus V. 4.5. Note how the interlayer distance and the disorder on graphitic walls increase when going from the inner layers (low region) to the outer shells (up). The interlayer distance may vary from  $\sim 3.5$  Å to  $\sim 5.2$  Å.

We noticed that the interlayer distance changes after lithium intercalation, as demonstrated in [figure 3.17](#). Note that the interlayer distance increases when going from the inner cores to the external shells, though it varies within graphitic sheets. Damage also increases, as can be seen in the irregular appearance and the broken graphitic walls (outermost layers). Small distance changes, such as intercalation of Li alone, cannot produce significant stress on the graphitic walls; in contrast, huge changes, such as those expected from co-intercalation of Li and  $\text{NH}_3$ , may induce extreme stress that may break nanotubes within concentric layers, which may lead to fracture and breakage of the tube walls and hence to unwrapping of the tubes. The expanded interlayer distance allows the access of intercalants and the further strong, exothermal reaction of acids with lithium and  $\text{NH}_3$ , thus contributing to the exfoliation of tubes.

We also found that by removing the caps of MWNTs by sonication in a strong acid mixture ( $\text{HNO}_3\text{:H}_2\text{SO}_4$  3:1) we ensure that we have open ends in MWNTs and an easy intercalation of lithium through the open ends. We had previously found that unwrapping runs from 2–3  $\mu\text{m}$  from the tip. Hence, by this sonication process we also aimed to obtain short tubes; cut nanotubes showed a wide distribution of lengths; most nanotubes were < 2  $\mu\text{m}$  long, and some MWNTs longer than 5  $\mu\text{m}$  remained. Hence, cutting of MWNTs contributed to exfoliation in a great extent, as observed in [figures 3.14D](#) and [3.18A](#). This cutting process also induces damage to nanotubes, but the process alone does not open or unwrap nanotubes, as can be seen in [figures 3.18B](#) and [3.18C](#).

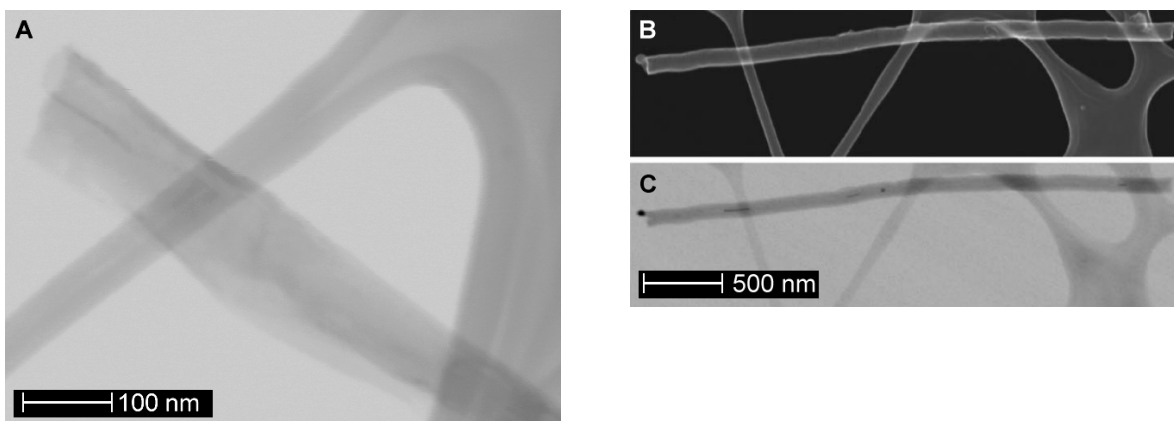


**Figure 3.18. STEM micrographs after lithium intercalation and exfoliation in MWNTs. (A)** An ex-MWNT, note the increment in width after exfoliation and the curved and almost planar structure (compare with the tube at [figure 3.14A](#)). **(B, C)** These images show that oxidative cutting damages the surface of MWNTs, but this treatment does not unfold MWNTs [\[47\]](#).

After Li intercalation and sonication in HCl, ~50% of these shortened tubes were partially exfoliated, ~25% were fully unwrapped, and a few percent of intact MWNTs remained.

It is known that intercalated compounds of graphite can be exfoliated when exposed to thermal treatments [40]. After sudden heating in a furnace at 1000 °C under flowing argon for 1 min, samples showed a higher amount of ex-MWNTs. Repeating this process four more times produced better exfoliation than a single thermal shock.

Alkali metal-ammonia ternary GICs have also been reported [36]. After performing this process in cut MWNTs, previously exposed for several hours to liquid NH<sub>3</sub> without Li, we did not observe either intercalation or exfoliation; tubes look practically the same as before being exposed to liquid NH<sub>3</sub>, as depicted in figure 3.19.

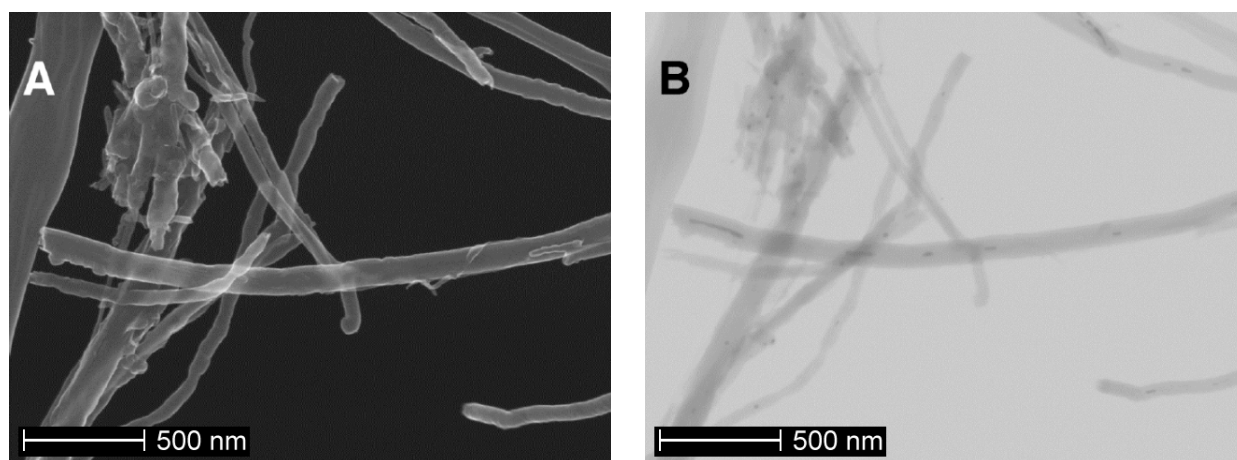


**Figure 3.19. Cut MWNTs after exposing to liquid NH<sub>3</sub> without lithium.** (A) SEM and (B) STEM images show that the tubes look practically the same as those obtained from oxidative cutting. Walls present certain damage and some encapsulated catalyst particles can still be seen [47].

This shows that a ternary Li-NH<sub>3</sub> intercalation compound should be formed among the concentric cylinders of cut MWNTs; this intercalation compound should produce a significant number of unwrapped MWNTs. After performing the thermal procedure on Li-NH<sub>3</sub> intercalated, short MWNTs, the resulting material consists of ~50% ex-MWNTs, ~25% partially exfoliated nanotubes, and a few percent of intact tubes. Note the drastically increased width in MWNTs after this thermal treatment, as shown at the histograms of figure 3.20.

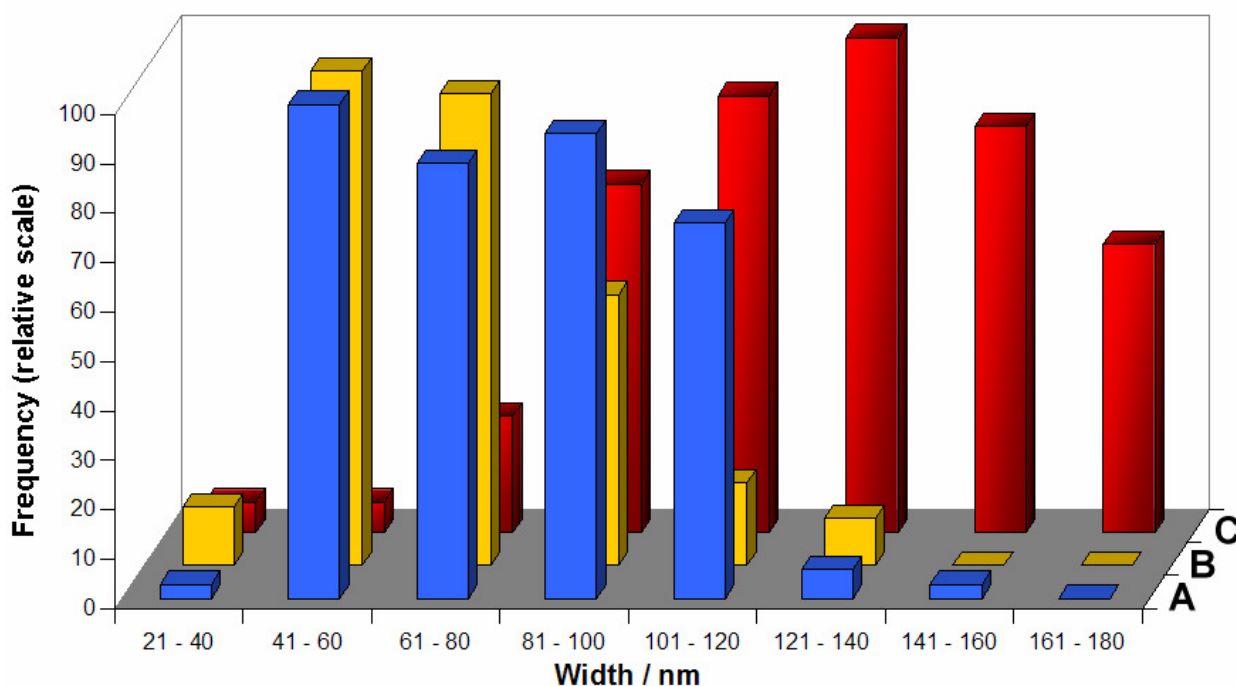


**Figure 3.20. Width distribution for MWNTs.** (A) Non-purified MWNTs; (B) cut MWNTs; (C) unwrapped MWNTs or ex-MWNTs, exfoliation was performed by acid reflux and thermal shock at 1000 °C; in this case counting was done on three different experiments with stoichiometries  $\text{NH}_3\text{:Li:MWNTs}$  7:10:1, 35:20:1, and 10:10:10. For (A) and (B) 121 tubes were counted, and 37 for (C). Mean width values are: (A) 80 nm, (B) 71 nm, and (C) 128 nm. Note how the width distribution in (A) and (B) lie around 40–120 nm, while that for (C) lies between 80–180 nm, thus demonstrating the huge increase in width present in ex-MWNTs.

Repeating intercalation and exfoliation for a second time with this product resulted in a moderate increase in the total amount of ex-MWNTs (~55–60%). This suggests that once exfoliation occurs and the initial order is lost, further intercalation mostly occurs in undamaged portions of the tubes. Partially open nanotubes and ex-MWNTs may be further exfoliated during the second treatment, but non-exfoliated tubes cannot be opened in a greater extent because they are already damaged. Nanotube length is also another important factor, since the longest tubes remained partially exfoliated after a second treatment. [Figure 3.21](#) shows more clear examples of ex-MWNTs.

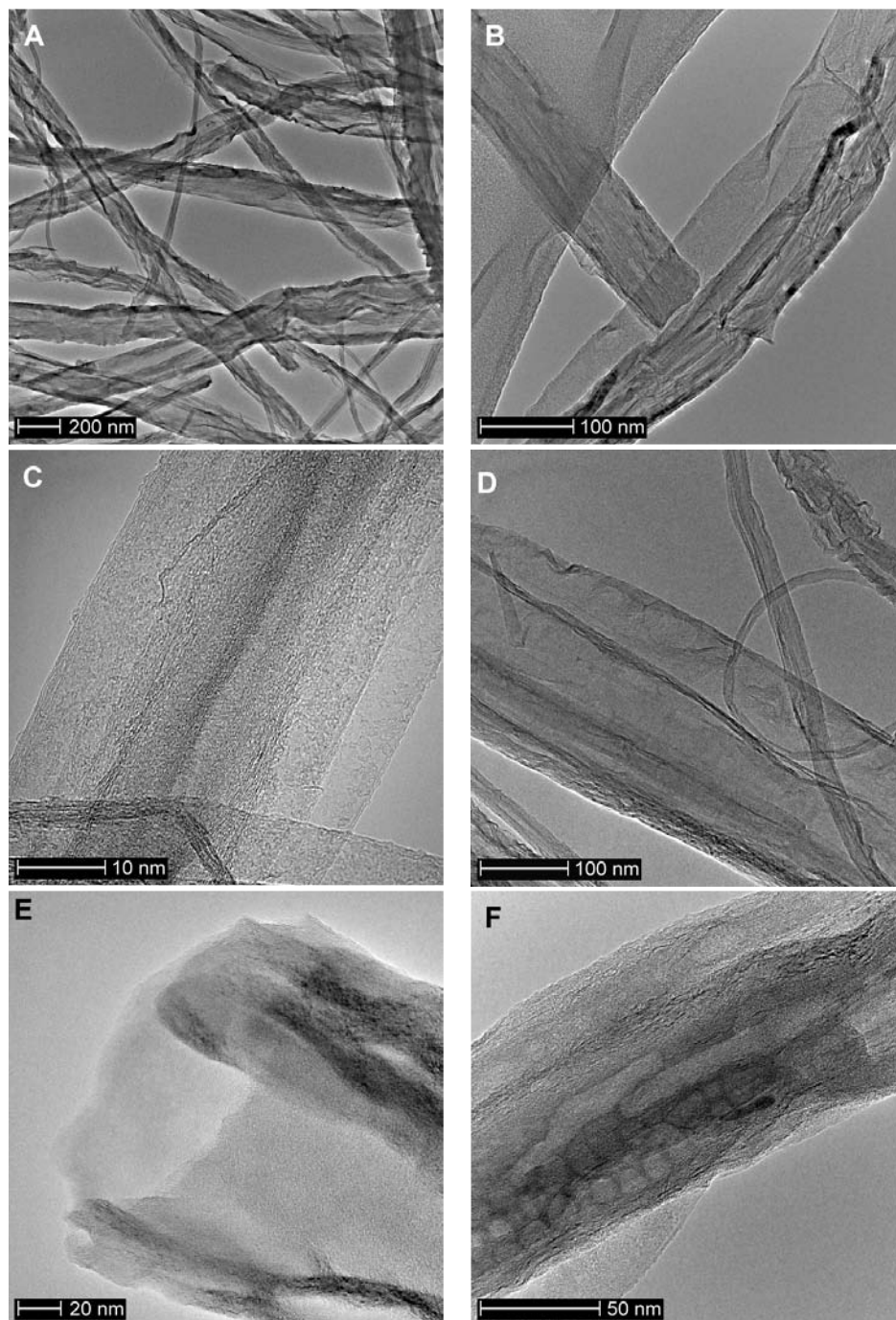


**Figure 3.21. TEM images of exfoliated MWNTs.** (A) Several unwrapped MWNTs showing a ribbon-like appearance; most of these carbon nanoribbons show damage. (B) An opened MWNT and a curved ex-MWNT, showing that these ribbons are composed of stacked graphitic sheets, which may vary in number. (C) A ribbon segment showing stacked sheets with well defined, straight edges. (D) A ribbon composed of several stacked layers, displaying damage at edges; other materials are a partially exfoliated MWNT, a looped and damaged tube, and an opened tube segment showing great damage. (E) Open end of an unwrapped MWNT, showing both several and a few stacked, concentric layers. (F) Ex-MWNTs showing a porous morphology resembling “lacey carbon”. Some of these examples were found when synthesizing composites from MWNTs and polyanilines (A, C, D, E), while others were obtained after sonication in 60% HCl and thermal shock at 1000 °C (B, F).

The nanotubes are, in most cases, opened longitudinally and ex-MWNTs consist of several stacked graphitic shells, from a few ones to hundreds of them, held by Van der Waals forces. [Figure 3.21A](#) shows an example of several ex-MWNTs resembling graphene nanoribbons (GNRs), which also show damage at edges. [Figure 3.21B](#) also depicts clear examples of unwrapped MWNTs formed by stacked graphene layers: a flattened, straight tube, and a bent and curved one from which a graphitic sheet protrudes. These sheets may be formed by a few or several graphene layers, as shown in [figure 3.21C](#) and [figure 3.21D](#), respectively. [Figure 3.21D](#) also shows GNRs damaged and rippled at edges, probably as a result of the chemical treatment, and partially exfoliated tubes as well. [Figure 3.21E](#) shows in more detail the open end of an ex-MWNT; note that exfoliated walls may be composed of a few or several walls. [Figure 3.21F](#) depicts unwrapped MWNTs with porous aspect, due to detachment of graphene segments maybe during the intercalation reaction and/or the acid exfoliation process; these porous MWNTs resemble lacey carbon.

### ***Atomic Force Microscopy***

SEM and TEM give a good idea of the morphology of ex-MWNTs and how exfoliation occurs by just interpreting two-dimensional images. Nonetheless, some important aspects of ex-MWNTs are difficult to observe and determine, such as the height of unfolded graphene sheets in ex-MWNTs, thus requiring of a technique that allows three-dimensional imaging of the morphological features of ex-MWNTs. Hence, we obtained AFM images from samples sonicated in ethanol and placed on freshly cleaved highly oriented pyrolytic graphite (HOPG) substrates by using a micropipette tip (one to three fine drops). AFM images were processed by means of WinSPM DPS Version 2.02 from JEOL, Ltd. [Figure 3.22A](#) shows an almost flat and layered topography, and interesting features such as steps. These steps are more evident in [figures 3.22\(C to H\)](#), which correspond to a few tens and up to hundreds of graphene sheets. Note, however, that since we did not calibrate the Z measurement in the AFM, heights might be over estimated, as shown in several reports of GNRs synthesis [\[57-59\]](#). Thus, the number of graphene layers may actually not reach hundreds of sheets.

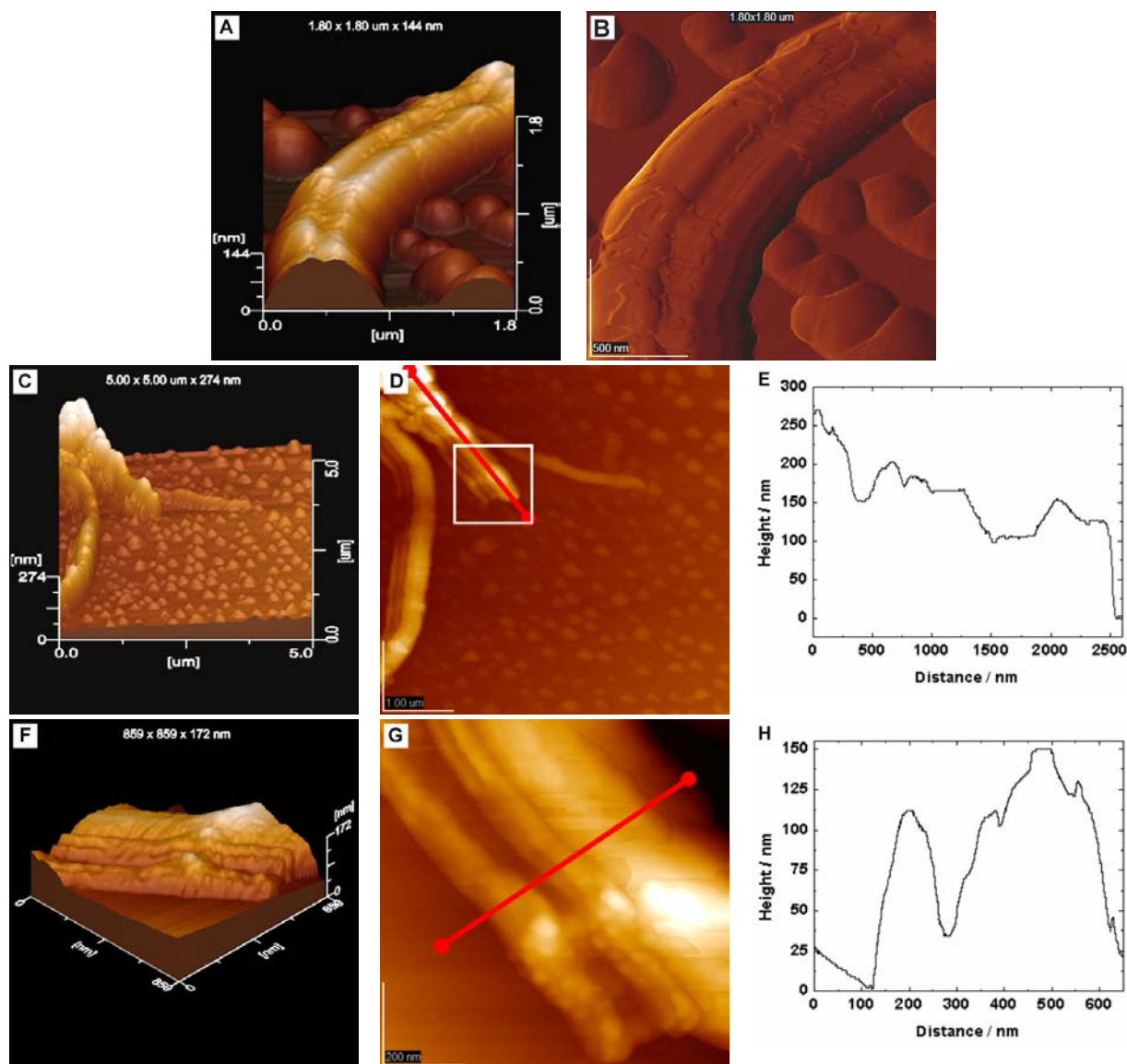


**Figure 3.22.** AFM images of an ex-MWNT and graphitic platelets over HOPG. (A) 3D topography image showing an ex-MWNT, as well as interesting features such as steps and spherical particles that accompany ex-MWNTs; (B) root mean square (RMS) image showing the roughness of the ex-MWNT shown in (A), and also how it is covered by features such as steps. These steps are composed of tens to hundreds of graphene sheets, as seen in the following examples. (C) 3D topography images and line profile of ex-MWNTs showing a stepped surface. The longitudinal profile analysis from the squared area at (D), reveals that the number of layers varies between  $\sim 290$ – $460$ , as shown in (E). (F to H) topography images of an ex-MWNT and transversal profile analysis; in this case the number of layers (94–124) corresponds to  $\sim 325$ – $430$  nm. The calculus was made considering an interplanar distance of  $3.45 \text{ \AA}$ , which corresponds to one graphene layer.

Graphene flakes are also usually seen at the surface of ex-MWNTs; an example of this is shown at [figure 3.22B](#), in which the heights of these partial walls correspond to 10–20 graphene layers, as calculated by profile analysis with WinSPM and shown at [figure 3.23](#).

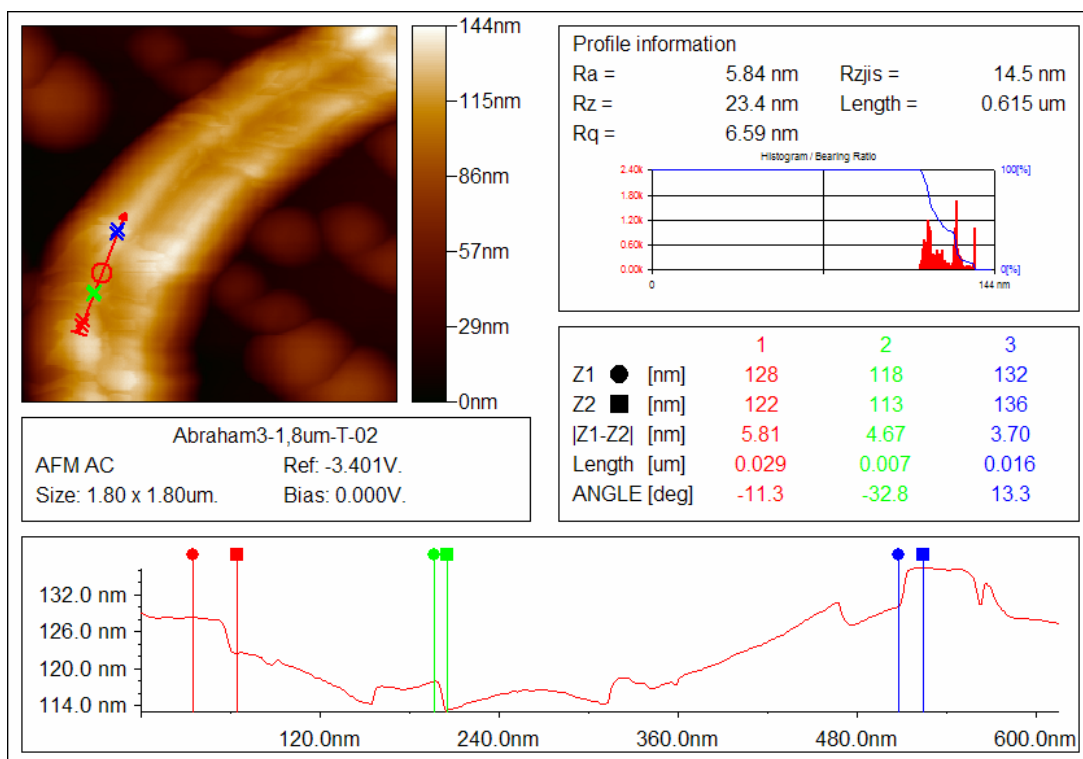


**Figure 3.23. Profile analysis of the surface of an ex-MWNT**, as obtained from WinSPM. Markers (1, 2, 3) are used to delimit steps and to measure their height, indicated by the  $|Z1-Z2|$  distance. According to profile analysis, graphene flakes are composed of 17, 13, and 11 graphene sheets.

In some cases, it is possible to observe voids on these layers of the same type as the porous features shown in [figure 3.21F](#); these features are due to detachment of graphene pieces from wall defects due to sonication [60]. These graphene pieces are irregular, possibly due to the random nature of wall defects, which cannot be controlled yet by our method. Along with ex-MWNTs, it is usual to find several spherical nanoparticles when placing samples on HOPG substrates, similar to those synthesized by Chakraborty *et al.* [61] by reductive alkylation of fluorinated graphite. We thought that these nanoparticles were due to undesired organics such as humic acids, and that would be removed by exposing cut MWNTs to alkaline solutions (1 M NaOH or 1 M KOH) [55]. Nevertheless, nanoparticles still appeared after this alkaline treatment.

Phase imaging at [figure 3.24](#) shows very little contrast among hemispherical nanoparticles, ex-MWNTs, and the HOPG substrate, thus indicating that these materials are similar. Hence, these nanoparticles should be graphite platelets which aggregate as the solvent evaporates, possibly functionalized at edges and formed from smaller particles and graphene sheets. These smaller particles originate from exfoliation of small pieces such as those from the holes, and from flakes detached from outer graphitic layers ([figure 3.22B](#)), and from pieces derived from tips and edges of nanotubes.

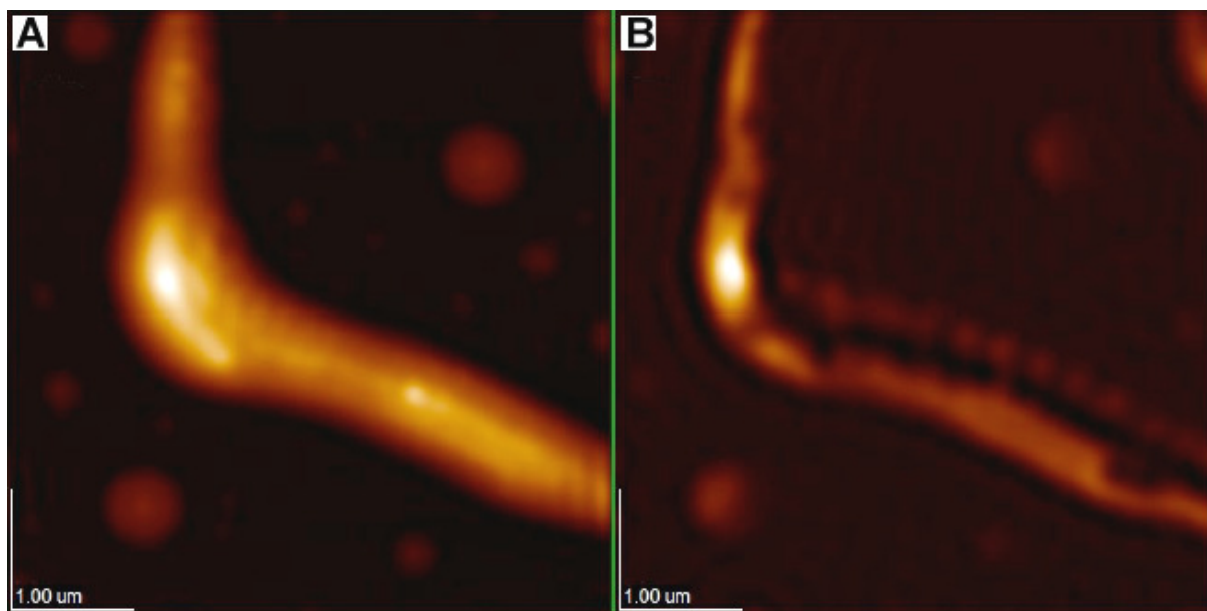


**Figure 3.24. Phase comparison of graphitic materials by AFM.** (A) Topography image of an ex-MWNT and the graphene platelets produced during the process; (B) phase image. Note the small difference in contrast in (B) between ex-MWNT, graphitic nanoplatelets, and HOPG, which indicates similar surface properties and hence suggests that they are made of the same material [47].

### 3.3.2 Spectroscopic studies on ex-MWNTs

#### *Raman spectroscopy*

Raman spectroscopy ([figure 3.25](#)), for several types of MWNTs show first-order features [62, 63]: the G or graphitic band ( $1540\text{ cm}^{-1}$ ) and the D band ( $1330\text{ cm}^{-1}$ ). The intensity of these features depends on the phonon energy and on the incident laser energy [64]. As expected, the  $I_{\text{D}}/I_{\text{G}}$  ratio ([table 3.1](#)) is small for non-purified MWNTs ([figure 3.25A](#)), purified MWNTs ([figure 3.25B](#)) and for cut MWNTs ([figure 3.25C](#))

( $I_D/I_G = 0.5, 0.2$  and  $0.3$  respectively), showing a high graphitization degree as well as a relatively low amount of surface defects and amorphous carbon.

After exposition to liquid  $\text{NH}_3$  (figure 3.25D), the main Raman features for cut MWNTs show no shifts, which would imply that ammonia by itself does not intercalate among graphitic walls, but co-intercalates with lithium as a  $\text{Li-NH}_3$  complex.

Ex-MWNTs obtained ( $\text{NH}_3:\text{Li}:\text{MWNTs}$  6:10:1 stoichiometry during the nanotube salts reaction) by acid treatment (figure 3.25E), show an increase in the intensity of the D band ( $I_D/I_G = 1.2$ ), since it is due to the induced disorder, defects, and functional groups ( $-\text{OH}$ ,  $-\text{COOH}$ ,  $-\text{CO}$ ) generated during lithium intercalation and the exothermic reaction of acid and  $\text{H}_2\text{O}$  with Li. In addition, the G band decreases, also due to the increase in disorder.

In contrast, after thermal shock at  $1000\text{ }^\circ\text{C}$  (figure 3.25F), ex-MWNTs behave similar to non-purified and cut MWNTs ( $I_D/I_G = 0.7$ ). This fact suggests that the thermal shock induces graphitization, eliminates functional groups, and anneals defects at edges.

**Table 3.1. Characteristic Raman bands and shifts for different types of MWNTs. (A)** As-synthesized; **(B)** purified; **(C)** cut; **(D)** cut and exposed to  $\text{NH}_3$ ; **(E)** ex-MWNTs, exfoliation by 60%  $\text{HNO}_3$ ; **(F)** ex-MWNTs, exfoliation by 60%  $\text{HNO}_3$  and thermal shock.

| MWNTs | D / $\text{cm}^{-1}$ | $\Delta\text{D}$ / $\text{cm}^{-1}$ | G / $\text{cm}^{-1}$ | $\Delta\text{G}$ / $\text{cm}^{-1}$ | $I_D/I_G$ | G' / $\text{cm}^{-1}$ | D+G / $\text{cm}^{-1}$ |
|-------|----------------------|-------------------------------------|----------------------|-------------------------------------|-----------|-----------------------|------------------------|
| A     | 1335.5               | 0.0                                 | 1584.2               | 0.0                                 | 0.5       | 2665.6                | 2930.9                 |
| B     | 1356.7               | 21.2                                | 1582.0               | 2.2                                 | 0.2       | 2708.0                | 2950.8                 |
| C     | 1359.1               | 23.6                                | 1584.3               | 0.1                                 | 0.3       | 2707.4                | 2959.0                 |
| D     | 1356.6               | 21.2                                | 1586.4               | 2.2                                 | 0.7       | 2705.4                | 2947.0                 |
| E     | 1334.9               | 0.5                                 | 1590.7               | 6.5                                 | 1.2       | 2680.6                | 2911.7                 |
| F     | 1356.4               | 21.0                                | 1586.2               | 2.0                                 | 0.7       | 2707.8                | 2959.3                 |

In addition, the  $\text{D}_2$  mode (or  $\text{D}'$  band,  $1610\text{ cm}^{-1}$ ) is caused by structural defects [65] and disorder that result from functionalization [66], and is a distinctive feature of graphitic carbons. It is present as a shoulder at  $\sim 1615\text{ cm}^{-1}$ , and is more evident for cut MWNTs due to functionalization with  $-\text{OH}$ ,  $-\text{COOH}$ , and  $-\text{CO}$ . Moreover, a small peak appears after acid and thermal treatments at  $\sim 1480\text{ cm}^{-1}$ ; we previously stated in chapter 2 that this peak would be due to polyaniline, but this feature also appears in ex-MWNTs.

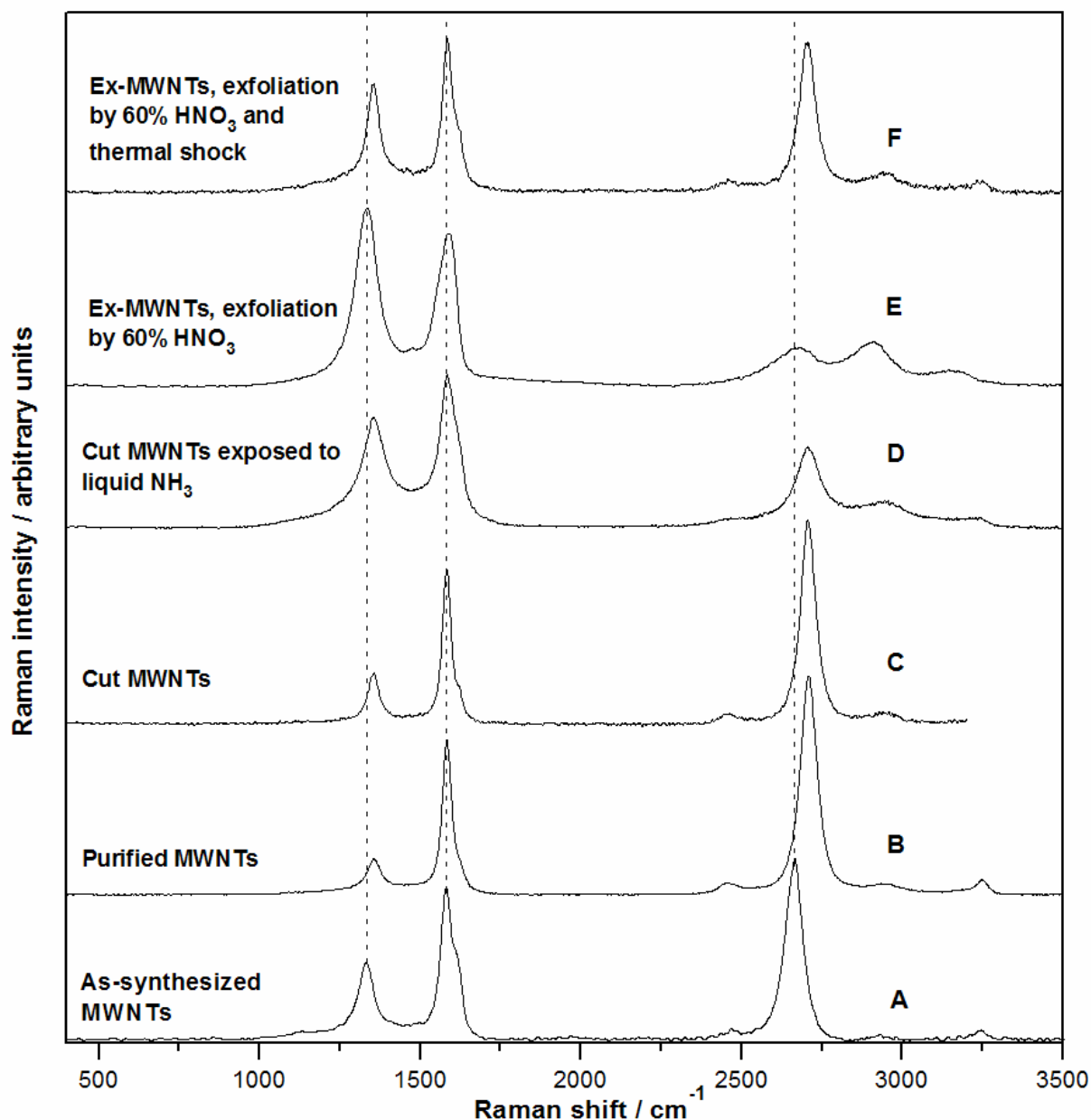


**Figure 3.25. Raman spectra for different types of MWNTs.** (A) MWNTs as synthesized by CVD process; (B) purified MWNTs; (C) MWNTs after sonication for 30 hours in  $\text{HNO}_3:\text{H}_2\text{SO}_4$  3:1 mixture; (D) cut MWNTs after being exposed to liquid  $\text{NH}_3$ ; (E) ex-MWNTs obtained exfoliation with 60%  $\text{HNO}_3$ ; (F)  $\text{HNO}_3$  exfoliated material after thermal treatments.

The G' band is a second-order process activated by double resonance (DR) processes. Figures 3.25 (A, B, C and F) show the characteristic shape of the G' band found in turbostratic carbons, that is, in multilayered materials. The G' band feature is also present in high-quality samples, and its intensity can be comparable to that of the G

band [64]. The shift and the intensity increase of the G' band in cut MWNTs may also be due to less amorphous carbon present in the sample, despite more surface defects might be present because of covalent functionalization with –COOH and –OH groups on walls and edges due to the oxidizing acid treatment during the cutting process.

In contrast, after exposition of cut MWNTs to liquid NH<sub>3</sub> the intensity of the G' band decreases, maybe due to reaction with the –COOH functional groups and hence to loss of the initial structural order.

For Li-NH<sub>3</sub> intercalated samples, the observed shifts in the G' band may be due to the presence of the intercalants [50, 67]. After thermal shock, loss of functional groups and annealing take place, thus inducing order in ex-MWNTs, which is denoted by a marked increase of the intensity of the G' band, similar to that of present in graphene [10]; and a new shift suggests that either no intercalated Li-NH<sub>3</sub> is present or its amount is too small. Moreover, the G' band changes from a one peak to a two peak feature, which can be associated to the degree of graphitization of the sample and may be related to the stacking order occurring along the c axis [68]. Other second order modes are located at 2480 cm<sup>-1</sup>, 2950, and 3250 cm<sup>-1</sup>, and correspond to overtones of the D, D+G and G bands [15, 68]. In this regard, the overtone at ~2480 cm<sup>-1</sup>, either vanishing or combining with the G' band in ex-MWNTs exfoliated by acid may be due to increase in disorder.

### **Fourier-Transform Infrared spectroscopy**

FT-IR spectroscopy done on various samples, revealed characteristic features of aromatic carbon structures (figure 3.26). MWNTs display a characteristic aromatic C=C stretching band at ~1650 – 1670 cm<sup>-1</sup> [69]. The bands in the range 2850–3030 cm<sup>-1</sup> are usually assigned to sp<sup>2</sup> C-H and/or sp<sup>3</sup> C-H stretching, along with the bands at 1430 cm<sup>-1</sup> (CH<sub>2</sub>, CH<sub>3</sub> deformation) and 670 – 690 C-H deformation (figures 3.26 B to E); the observed peaks in as-synthesized MWNTs (figure 3.26A) may also be due to contamination from the spectrometer. Other bands of interest could be assigned according to the theoretical IR structure of SWNTs [70]: 1st order A<sub>2</sub> (669–683 cm<sup>-1</sup>, and

$\sim 880\text{ cm}^{-1}$ ); 2nd order  $2E_9$ ,  $2E_{19}$ , and  $2E_{10}$  ( $\sim 1090\text{ cm}^{-1}$ ); and 2nd order  $2E_{12}$ ,  $2E_6$ , and  $2E_9$  ( $\sim 1430\text{ cm}^{-1}$ ).

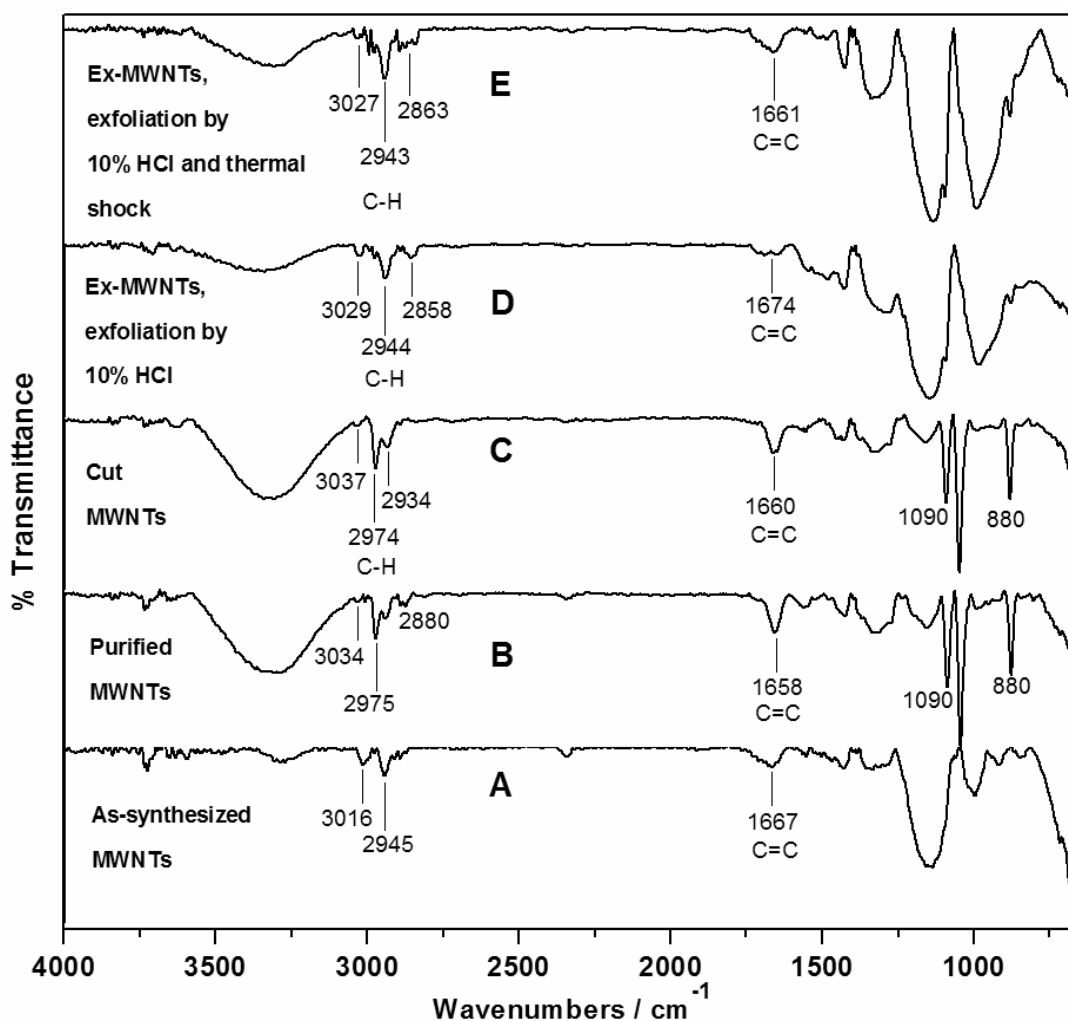


**Figure 3.26. FT-IR spectra for different types of MWNTs.** Characteristic absorption bands for aromatic C-H stretching are found at  $2889\text{--}2982\text{ cm}^{-1}$ , which appear not only in MWNTs but also in ex-MWNTs due to the nature of ex-MWNTs. The band at  $2900\text{--}3300\text{ cm}^{-1}$  may be due to  $\text{H}_2\text{O}$  adsorbed on the sample, and the band at  $2345\text{ cm}^{-1}$  is due to  $\text{CO}_2$  from the surrounding atmosphere. Spectra were obtained with a ThermoNicolet 6700 by ATR technique, with 200 scans (response was the similar to that from 1068 scans) and a resolution of 8.

On the other hand, we observe signals possibly related to  $-\text{COOH}$ ,  $-\text{OH}$ , or adsorbed water (figures 3.26B and C). Even though we observe these signals and MWNTs are surely functionalized, the amount of functional groups may be too low to be detected by FT-IR, and hence a more sensitive technique such as XPS is required for a more detailed study.

### 3.3.3 X-Ray powder diffraction

The crystallographic features for different types of MWNTs are shown in [figure 3.27](#), whereas important crystallographic data are displayed in [table 3.2](#). Diffraction patterns were first normalized, taking the (110) peak ( $\alpha$ -Fe,  $\sim 43^\circ$ ) of non-purified (as synthesized) MWNTs as the standard intensity. The relative intensity of (002) is obtained by comparing the intensity of the (002) peak at each diffraction pattern against that from purified MWNTs, and is a qualitative measure of the crystalline character of MWNTs.

As-synthesized MWNTs ([figure 3.27A](#)) show a peak at  $26^\circ$ , whose low intensity may be due to amorphous carbon present in the sample. The intensity of the  $26^\circ$  peak increases after purification ([figure 3.27B](#)) and cutting ([figure 3.27C](#)) of MWNTs (R. I. = 2.45), due to the removal of amorphous carbon and other impurities; thus showing the sample a more crystalline character. We considered the possibility of intercalation of ammonia by itself. After exposing cut MWNTs only to liquid ammonia ([figure 3.27D](#)), no important shifts were observed, thus demonstrating that  $\text{NH}_3$  does not intercalate alone or results in exfoliation. Only a decrease in the  $26^\circ$  peak intensity and a small shift were observed, possibly as a result of reaction of ammonia with the acidic functional groups present in the sample.

Intercalated and HCl treated samples ([figure 3.27E](#)) show disorder since the (002) peak depletes. A signal located at  $19.1^\circ$  appears, with an average interlayer spacing of  $4.69 \text{ \AA}$ , which is much larger than that of the Li graphite intercalation compound, thus indicating that some Li- $\text{NH}_3$  complex may remain between graphene layers. Exfoliated layers may also contribute to this broad peak.

After thermal treatment ([figure 3.27F](#)) of acid-treated samples, the remaining intercalants are expelled, thus completing exfoliation and unwrapping. Interestingly, the graphitic (002) peak reappears at  $3.45 \text{ \AA}$ , showing that exfoliated layers can undergo recrystallization. The width of the (002) peak is due to a distribution of interlayer spacings, since we can suppose that an intercalation gradient should exist, i.e., the interlayer distance should decrease when going from the outermost shell to the core of the nanotubes, as seen in [figure 3.17](#). This distribution is qualitatively measured by the full-width at half maximum value (FWHM), which can be calculated by hand from the

diffractograms. The remaining shoulder at  $21.36^\circ$  in ex-MWNTs represents an interlayer distance of  $4.21 \text{ \AA}$  and corresponds to exfoliated and disordered walls and also to disordered and coalesced graphene sheets.

Finally, the region around  $43^\circ$  corresponds to iron carbides (see arrows). These peaks shift, probably due to phase changes and formation of other species like iron oxides. Nevertheless, the observed changes cannot be ascribed to crystallographic data from the ICDD database, maybe due to experimental limitations, like the small amount of iron species in our samples.

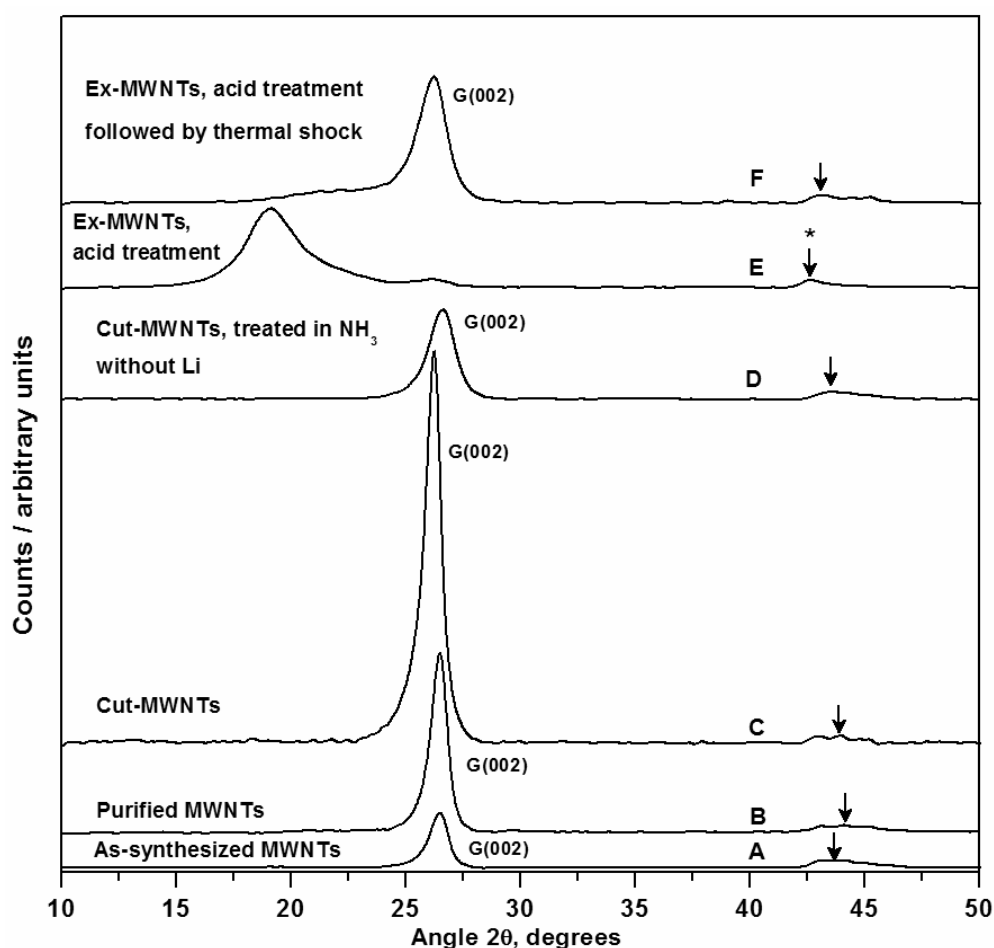


**Figure 3.27. Diffraction patterns for different types of MWNTs.** As-synthesized MWNTs show a characteristic (002) diffraction peak at  $26.5^\circ$ ; its intensity is small due to the presence of amorphous carbon and other impurities. After purification and cutting of MWNTs, the intensity of the (002) peak increases due to removal of such impurities, as denoted by the high and sharp peak at  $26.2^\circ$ . After being exposed to ammonia, the intensity of the (002) peak decreases and a small shift is observed. Ex-MWNTs obtained by reflux in acid show a great loss of order, as depicted by the depleted peak at  $26^\circ$ , and by the appearance of a wide diffraction peak at  $19.1^\circ$ . Thermal shock completes exfoliation and unwrapping. The reappearance of the (002) peak at  $3.45 \text{ \AA}$  indicates that ex-MWNTs undergo recrystallization.

**Table 3.2. Interplanar distance, crystallite size, and relative (002) intensities for MWNTs.** \*Note how the interplanar distance changes dramatically for ex-MWNTs obtained by acid. The reported value does not correspond to the (002) peak of graphite (which appears depleted at 26.1°); it was added for comparison.

| MWNTs  | $d_{002}$ (Å) | FWHM   | R. I. |
|--|---------------|--------|-------|
| Non-purified                                       | 3.42          | 0.9890 | 0.38  |
| Purified   | 3.42          | 0.8242 | 1     |
| Cut (30 h sonication)                              | 3.45          | 0.8242 | 2.45  |
| Cut and exposed to $\text{NH}_3$                   | 3.40          | 1.3187 | 0.56  |
| * Ex-MWNTs, exfoliation by 10% HCl                 | 4.69          | 2.5824 | 0.49  |
| Ex-MWNTs, exfoliation by 10% HCl and thermal shock | 3.45          | 1.3736 | 0.77  |

### 3.3.4 Reactivity of carbon structures towards oxidation. Thermogravimetric analysis

Thermogravimetric analysis was useful to determine the reactivity of exfoliated MWNTs upon oxidation (figure 3.28). TGA analyses on non-purified and purified MWNTs were also performed as a comparison. The highest residual mass ( $R_M$ ) (figure 3.28A, inset) is obtained from non-purified MWNTs, since this sample contains the highest amount of catalyst iron particles. The small differences in  $R_M$  between purified, cut, and ex-MWNTs can be due to width distribution, MWNTs fragments, loss of functional groups, and small amounts of remaining intercalated lithium species.

From TGA curves (figure 3.28A), the reactivity of ex-MWNTs towards oxidation is higher than the one observed for purified and non-purified MWNTs, as noted in a 64 °C decrease of the onset temperature of ex-MWNTs (figure 3.28B) when compared to purified MWNTs, due to the presence of exposed and functionalized edges. On the other hand, cut MWNTs are much more reactive, possibly due to defects, edges, functional groups produced during the cutting process, and remaining small oxidized carbon materials; moreover, cut MWNTs are not annealed, in contrast to ex-MWNTs.

In addition, in all cases DTG curves exhibit a shoulder or a peak at  $T_{\text{ONSET}}$ , which is due to amorphous carbon [71, 72] in non-purified MWNTs. Purified MWNTs may contain some remains of amorphous carbon and may also be functionalized with –OH, and –COOH groups as a result of the purification process. Cut-MWNTs show a high peak, which is due to short tubes or fragments of tubes obtained as a result of the cutting

process. Ex-MWNTs show a shoulder caused by remaining defects, different widths in ex-MWNTs, and graphene platelets.

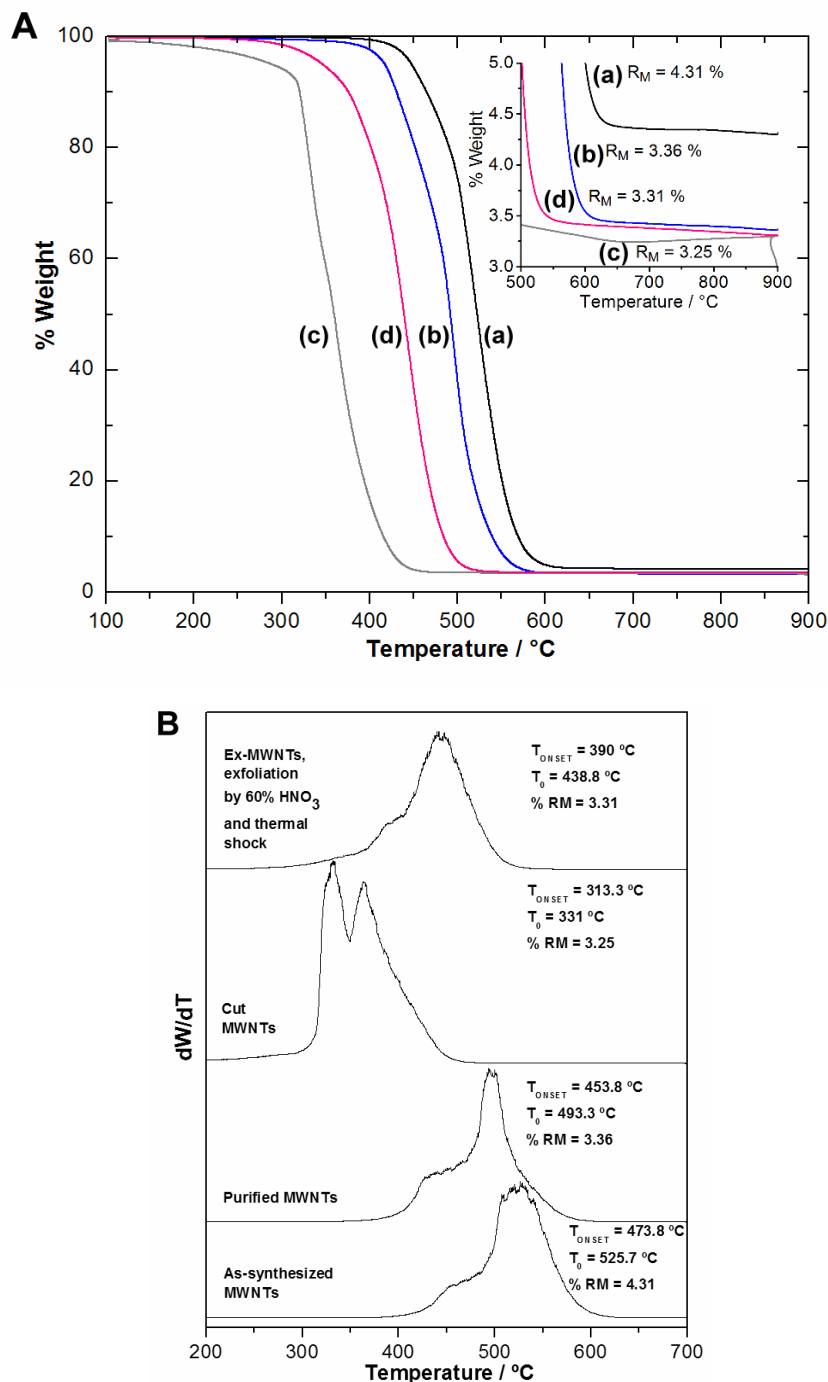


**Figure 3.28. Thermogravimetric measurements on MWNTs. (A)** TGA curves: (a) as-synthesized MWNTs; (b) purified MWNTs; (c) cut-MWNTs; (d) ex-MWNTs exfoliated by acid and thermal shock. **(B)** Differential thermograms for MWNTs: contributions to the temperature with the fastest oxidation rate ( $T_0$ ) may arise from impurities, amorphous carbon, catalyst, structural defects, functional groups, and width distribution.

### 3.4 Mechanism for unzipping of MWNTs

The characterization of ex-MWNTs allows us to propose a mechanism for exfoliation of unwrapping of lithium intercalated MWNTs, as schematized in [figure 3.29](#).

Cut MWNTs are suspended in THF and added to liquid  $\text{NH}_3$  (10 mL/mg), followed by addition of Li (10:1 ratio Li/C w/w) under magnetic stirring. The open ends facilitate intercalation of ammonia-solvated lithium ([figure 3.29A](#)) in between graphitic walls as a result of electrostatic attraction between negatively charged MWNTs and Li cations. Structural defects on the opened tips serve as initial points for unwrapping, and ease the insertion of Li- $\text{NH}_3$  complex ([figure 3.29A](#)), whose nature should be similar to that of  $\text{K}(\text{NH}_3)_4^+$  units [73, 74]. Defects on the walls, induced by cutting in a strong acid mixture, facilitate intercalation and unwrapping and act as starting points for the detachment of graphene pieces. In this initial unwrapping, the newly formed edges could react or be functionalized with hydrogen or amino groups.

When the reaction product (Li- $\text{NH}_3$  intercalated MWNTs) is exposed to 10% HCl, the acid reacts with lithium and neutralizes  $\text{NH}_3$ ; the exothermic reaction results in exfoliation, which further opens the nanotubes ([figure 3.29B](#)). In this process, oxygenated groups may be formed.

When these samples are placed in a ceramic boat inside a quartz tube and suddenly heated under flowing argon at 1000 °C, the remaining intercalants, possibly a combination of Li- $\text{NH}_3$  complexes and other Li intercalation compounds, are suddenly removed, thus leading to full unwrapping of many MWNTs ([figure 3.29B](#)). Functional groups could also be expelled as gases that may expand fast; nonetheless, since most of these groups must be on the surface, they should not contribute significantly to exfoliation.

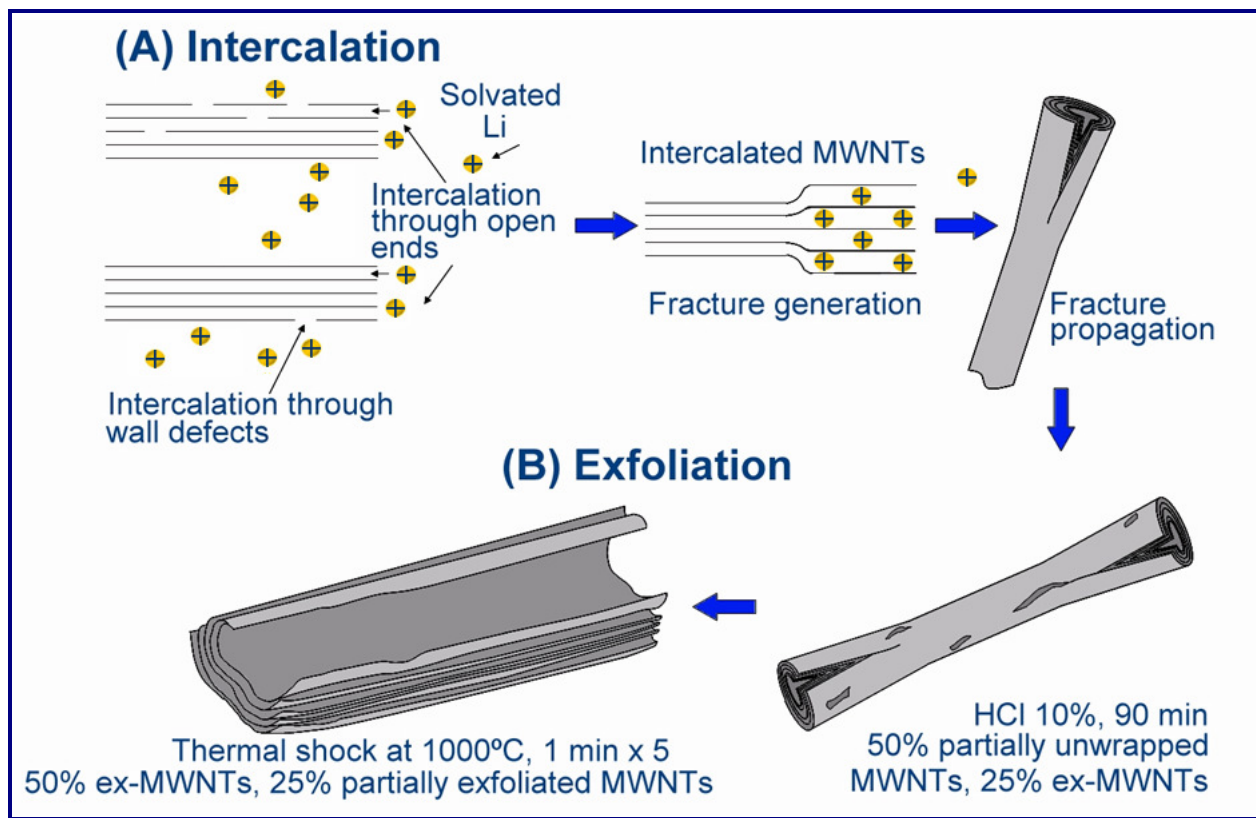


**Figure 3.29. Intercalation mechanism in MWNTs and their exfoliation.** Solvated Li is represented by spheres. **(A)** Li-NH<sub>3</sub> complex intercalation occurs among the concentric graphene cylinders. Open ends ease the intercalation of ammonia-solvated lithium among graphitic walls, which occurs as a result of electrostatic attraction between negatively charged MWNTs and Li cations. Structural defects on the opened tips act as starting points for unwrapping and ease intercalation of the Li-NH<sub>3</sub> complex. Fracture generation is represented for a half of a tube section. **(B)** Defects on the walls induced by cutting in a strong acid mixture, facilitate intercalation and unwrapping and act as starting points for the detachment of graphene pieces. In this initial unwrapping, the newly formed edges should react or be functionalized with hydrogen or amino groups. Next, upon exposition of intercalated MWNTs to acid, the strong exothermic reaction between lithium, NH<sub>3</sub>, and acid results in exfoliation. Finally, sudden heating expels the remaining intercalants, thus completely unwrapping many MWNTs.

### 3.5 Other methods for obtention of GNRs from CNTs

Following our pioneering work, alternative routes for making GNRs from MWNTs have appeared. These methods include chemical oxidation [75], argon plasma etching [76], metal particle-assisted unzipping [77], and electrical current-induced unwrapping [78].

Oxidative cutting [75] of CVD MWNTs produced GNRs by suspending MWNTs in concentrated  $\text{H}_2\text{SO}_4$ , followed by treatment with 500 wt%  $\text{KMnO}_4$  for 1 h at room temperature, and 1 h at 55 – 70 °C. MWNTs showed an increase in width from 40–80 to > 100 nm. GNRs showed ohmic behavior after annealing under  $\text{H}_2$ , and bilayered GNRs showed FET-like behavior. Despite the high yield (80–100 %), this method does not work well with laser-oven-produced MWNTs, and has little control on the structure of the edges of GNRs. Due to defects, these GNRs showed an intense D band; hence, their electronic characteristics might be inferior to those of wide, mechanically peeled sheets of graphene.

Argon plasma etching [76] allowed the obtention of GNRs with quality similar to that of lithographically patterned GNRs and similar electron mobility (~10 times lower than that from large 2D graphene sheets). In this method, MWNTs were fixed in a thin layer of PMMA (polymethyl methacrylate); the modified film was then exposed to a 10-W argon plasma for several times, which vaporized the surface of MWNTs not covered by PMMA. GNRs were recovered by dissolving the polymer with acetone vapor, followed by a thermal treatment to remove residual PMMA. GNRs obtained by this method showed graphene-like I-V behavior, excellent flexibility in comparison to MWNTs, and controlled structure and quality (uniform edges and width, low intensity of the Raman D band). This approach is also compatible with semiconductor processing and elaboration of GNR arrays for electronics. Nonetheless, it is difficult to reproduce it at large scale, and the yield is limited by the diameter distribution (dispersion) of starting MWNTs, which also affects the width and number of layers in GNRs.

Cobalt and nickel nanoparticles are known to cut graphite through catalytic hydrogenation. In this regard, Elías [77] and coworkers cut MWNTs and  $\text{CN}_x$  in zigzag or armchair directions, depending on the particle size. Co and Ni particles were grown by

sonication of CNTs in a  $\text{CoCl}_2$  3 wt% solution in methanol, followed by dropping a 30 mL aliquot on a clean Si wafer, drying at room temperature, and thermal treatment at 500 °C for 1 hour to allow proper nucleation of the metal particles on CNTs. Alternatively, Ni nanoparticles were deposited on the surface of CNTs by sputtering. Catalytic hydrogenation either of MWNTs or  $\text{CN}_x$  was carried out by thermal treatment at 850 °C for 30 min under an  $\text{Ar}/\text{H}_2$  flux (90:10 v/v). Most tubes were either cut, partially open, or open along the axis thus forming GNRs. Partially opened tubes (GNRs with tube ends) might show magnetoresistive properties [79]. This simple, non-aggressive approach allowed the obtention of GNRs with cleaner edges. Nevertheless, since the concentric carbon shells in MWNTs possess different chiralities, catalyst particles can cut MWNTs in different directions, not only along the tube axis; defects could also alter the cutting direction. Work has still to be done to reach full control on the cutting process and to increase the yield (5 % of fully opened tubes with Co particles).

GNRs can also be obtained by applying an electric current to a MWNT fixed onto a substrate [78]. By using a proper bias control, part of the MWNT is damaged due to the asymmetric contact between the tip of the MWNT and the electrodes, and the remaining MWNT is separated from its sheath by sliding. These flexible GNRs showed ohmic behavior and stood large currents without failure. Despite this method offers the possibility to study the electrical properties of GNRs in a TEM, it does not allow the large-scale production of GNRs.

Despite the simplicity of these methods, most of them offer very low yields. By improving the characteristics of the starting materials (MWNTs) used in the nanotube salts reaction and by optimizing the experimental conditions, the yield of GNRs obtained by the nanotube salts reaction can certainly be increased to a large scale. Moreover, even that we cannot control yet the shape of borders, the high number of edges can be exploited for a variety of applications like polymer composites, rechargeable batteries, hydrogen adsorption, etc.

## 3.6 Other layered carbon materials

As an extension to the exfoliation study on MWNTs, the lithium intercalation and exfoliation procedures were applied to graphene nanoribbons (GNRs) supplied by Ph. D. student Jessica Campos Delgado at IPICYT. This study was motivated by the results obtained in exfoliation of MWNTs. GNRs were synthesized by a common CVD process from pyrolysis of a ferrocene-thiophene-ethanol mixture 1:0.095:100 (g/mL/mL) at 950 °C under argon flux (0.8 L/min) [29] (see [table A.3.2](#) for experimental conditions).

### 3.6.1 Morphology

[Figure 3.30 \(A to D\)](#) show typical SEM/STEM micrographs of GNRs. After applying the exfoliation procedure used for MWNTs, carbon layers up to 4  $\mu\text{m}$  long are obtained as the one depicted at [figure 3.31 \(A and B\)](#).

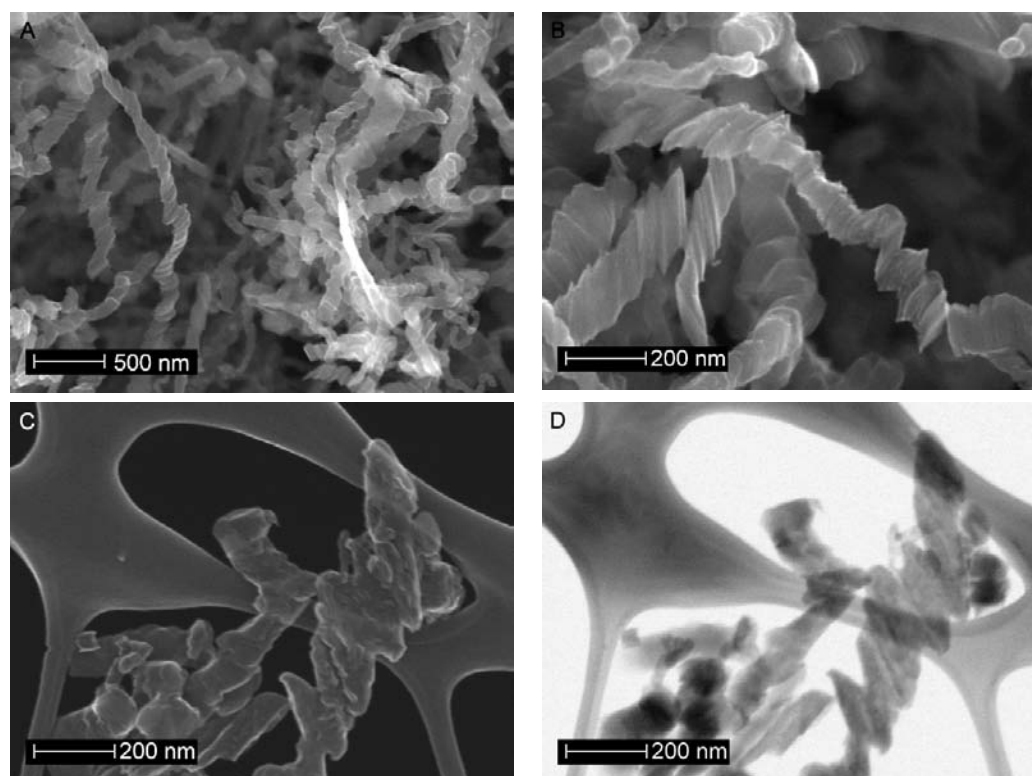


**Figure 3.30. SEM/STEM micrographs of non-intercalated pristine graphene nanoribbons. (A, B) GNRs with no intercalation or exfoliation procedures applied. (C, D) Lithium-intercalated GNRs after sonication and reflux in 10% HCl for 90 minutes at each step; nanoribbons show certain damage. Images A and B taken by J. R. Campos Delgado.**

A probable mechanism of formation of these graphene plates is the coalescence of graphene nanoribbons upon thermal shock (figure 3.31, C and D). It should be stressed that thermal shock of non-intercalated graphene nanoribbons only results in their partial agglomeration or in plates with an irregular morphology (figure 3.31, E and F).

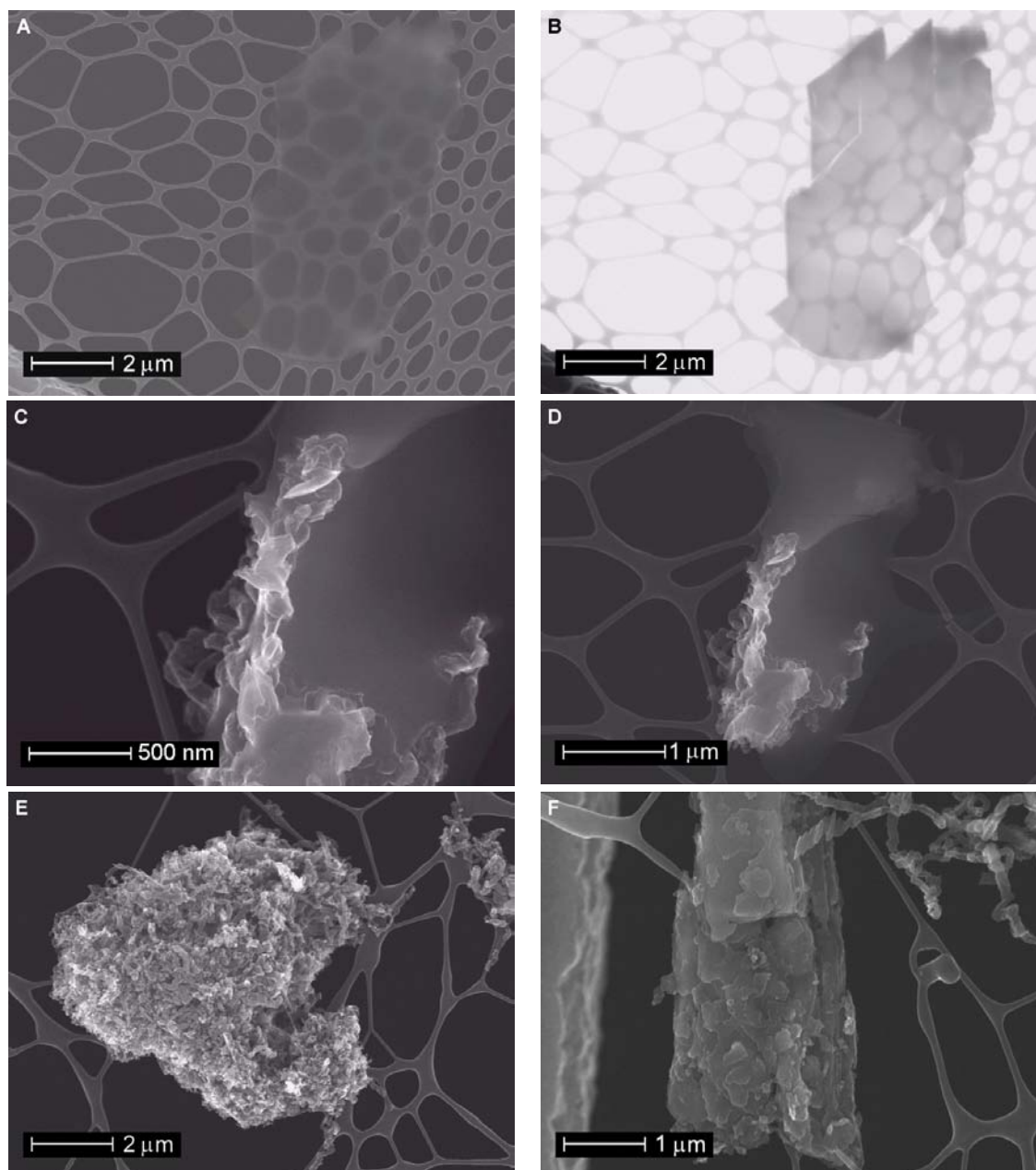


**Figure 3.31. SEM/STEM micrographs of graphene nanoribbons after Li intercalation and thermal treatments. (A to D)** Lithium-intercalated graphene nanoribbons after thermal shock at 1000 °C, note the uniform topography of the obtained stacked graphene at (A) and (B), and the coalescence of nanoribbons at (C) and (D). Irregular agglomerations observed after thermal shock at 1000 °C of non-intercalated graphene nanoribbons, which denotes the importance of intercalated lithium.

### 3.6.2 Raman spectroscopy

Raman spectra of MWNTs and pristine graphene nanoribbons show similar vibrational modes on their first and second order characteristics. Figure 3.32 and table 3.3 display the most important features for these carbon materials. The  $I_D/I_G$  ratio and the low intensity of the  $G'$  band show that pristine GNRs are disordered. Nonetheless, after lithium intercalation and a sudden 1-minute thermal shock at 1000 °C, only a small and wide band appears at 1560  $\text{cm}^{-1}$ , probably as a result of mixing of the D and G bands. Additional sharp peaks are observed at 157, 194, 1089, and 2300  $\text{cm}^{-1}$ , which might be due to cosmic noise.

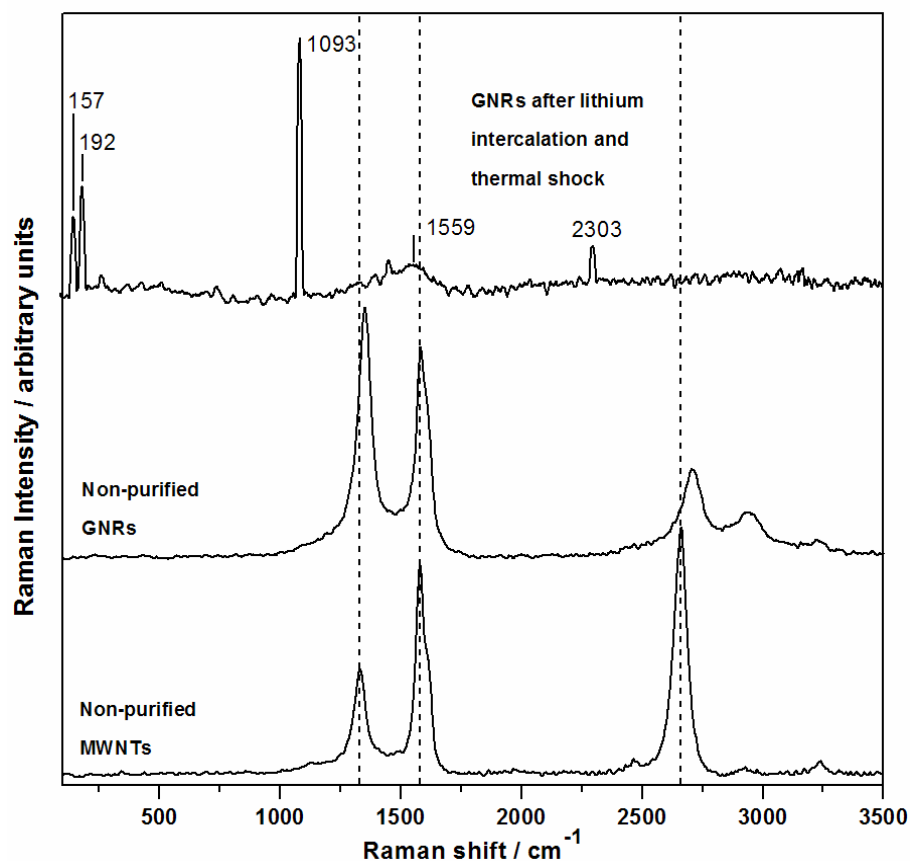


**Figure 3.32. Raman spectra of MWNTs and GNRs.** As-synthesized MWNTs show characteristic D, G, and  $G'$  features. These are practically the same in as-synthesized GNRs, and show disorder. In contrast, GNRs after lithium and thermal treatments show very different features which cannot be ascribed as in the previous examples. GNRs were intercalated with lithium (stoichiometry  $\text{NH}_3:\text{Li}:\text{CNR}$  28:10:1) and later suddenly heated at 1000 °C for one minute. The spectrum of GNRs treated by thermal shock is not normalized; only spectra from as-synthesized MWNTs and pristine GNRs are normalized relative to the G peak.

**Table 3.3. Characteristic Raman bands and shifts for MWNTs and CNRs.** Shifts are due to differences in electronic properties.

| Sample             | D / cm <sup>-1</sup> | ΔD / cm <sup>-1</sup> | G / cm <sup>-1</sup> | ΔG / cm <sup>-1</sup> | I <sub>D</sub> /I <sub>G</sub> | G' / cm <sup>-1</sup> | D+G / cm <sup>-1</sup> |
|--------------------|----------------------|-----------------------|----------------------|-----------------------|--------------------------------|-----------------------|------------------------|
| Non-purified MWNTs | 1335                 | 0.0                   | 1584                 | 0.0                   | 0.5                            | 2665                  | 2931                   |
| Non-purified NRs   | 1353                 | 18.0                  | 1583                 | -0.8                  | 1.2                            | 2709                  | 2923                   |

It is worthy to say that the Raman spectrum of GNRs after lithium and thermal treatments resembles to that of graphene [10]. On the other hand, and to the best of our knowledge, no research has been done on lithium intercalation and thermal shock of these GNRs. Further studies are required; not only to understand the electronic properties of these GNRs, but also to understand what is happening when GNRs are exposed to lithium in liquid ammonia, and during the thermal treatment. Further studies will surely give new light into novel materials and research paths.

### 3.7 Conclusions

For the first time, we have obtained carbon nanoribbons from unwrapping MWNTs, adding up a significant contribution to the state-of-the-art in the synthesis of novel nanostructures. Only after the publication of this work, other researchers have also reported the obtention of carbon nanoribbons from MWNTs [75-78].

Characterization allowed us to establish an unwrapping mechanism for MWNTs. Lithium and ammonia intercalate through graphitic walls and defects, creating stress among graphitic walls. Defects act as starting points for unwrapping and fracture generation. Li-intercalated MWNTs unwrap due to the strong exothermal reaction between Li and acids, and to the vaporization of the remaining intercalants after thermal shock. In addition, ex-MWNTs obtained by acid treatment show a high loss of order, and huge interlayer distances in comparison to as-synthesized MWNTs. In contrast, after thermal shock ex-MWNTs display recrystallization and high order. In addition, we found that by cutting MWNTs in a strong acid mixture, shortened MWNTs show better exfoliation after lithium intercalation due to their relatively short size (since exfoliation occurs within a 0.5 to 1  $\mu\text{m}$  range), and to their open ends, which allow a better intercalation of Li-NH<sub>3</sub> complex. Furthermore, using a 10:10:1 ratio (v/w/w) of NH<sub>3</sub>, lithium, and MWNTs, was the best for an optimum exfoliation. Moreover, from experiments run on MWNT samples without lithium, we found that lithium should intercalate through graphitic walls and defects along with ammonia as a Li-NH<sub>3</sub> complex, while NH<sub>3</sub> does not intercalate alone.

We have developed an original method in which intercalation and exfoliation are used for making a novel graphene nanoribbon-like material: ex-MWNTs. This method could be industrially scaled, hence making it less expensive and easier to produce large amounts of ex-MWNTs. Other materials produced are stacked graphene sheets, and nanoplatelets. Statistical counting showed that the yields of nanoribbon production are as high as 50%, and may be increased by further improvements in the intercalation and exfoliation procedures. Moreover, further characterization is needed to understand the nature of the intercalants at different stages in the process. The quality and characteristics of the starting material should be improved, for example, dimensions.

If monodisperse MWNTs are used from the beginning, it is expected that the obtained GNRs will be uniform in width and length. This could lead us to better control on the production and dimensions of nanoribbons, graphene flakes, and platelets. By taking advantage of their high amount of edges, ex-MWNTs could then be tested in field-effect transistors, rechargeable batteries, sensors, hydrogen storage devices, polymer nanocomposites, etc. The production method used for ex-MWNTs can be extended to other systems, to explore new routes for the synthesis of new materials.

## References

- [1] M. I. Katsnelson. Graphene: carbon in two dimensions. *Mater. Today* **10** (2007) 20-26.
- [2] S. Mouras, A. Hamm, D. Djurado, J.-C. Cousseins. Synthesis of first stage graphite intercalation compounds with fluorides. *Rev. Chim. Miner.* **24** (1987) 572-582.
- [3] P. R. Wallace. The band theory of graphite. *Phys. REv.* **71** (1947) 622-634.
- [4] A. K. Geim, K. S. Novoselov. The rise of graphene. *Nat. Mater.* **6** (2007) 183-191.
- [5] C. Oshima, A. Nagashima. Ultra-thin epitaxial films of graphite and hexagonal boron nitride on solid surfaces. *J. Phys. Cond. Mat.* **9** (1997) 1-20.
- [6] K. S. Novoselov, A. K. Geim, S. V. Morozow, D. Jiang, Y. Zhang, S. V. Dubonos, I. V. Grigorieva, A. A. Firsov. Electric field effect in atomically thin carbon films. *Science* **306** (2004) 666-669.
- [7] C. Berger, Z. Song, T. Li, X. Li, A. Y. Ogbazghi, R. Feng, Z. Dai, A. N. Marchenkov, E. H. Conrad, P. N. First, W. A. de Heer. Ultrathin epitaxial graphite: 2D electron gas properties and a route toward graphene-based nanoelectronics. *J. Phys. Chem. B* **108** (2004) 19912-19916.
- [8] Graphene calling. *Nat. Mater.* **6** (2007) 169.
- [9] Y.-M. Lin, C. Dimitrakopoulos, K. A. Jenkins, D. B. Farmer, H.-Y. Chiu, A. Grill, Ph. Avouris. 100-Ghz transistors from wafer-scale epitaxial graphene. *Science* **327** (2010) 662.
- [10] A. C. Ferrari, J. C. Meyer, V. Scardaci, C. Casiraghi, M. Lazzeri, F. Mauri, S. Piscanec, D. Jiang, K. S. Novoselov, S. Roth, A. K. Geim. Raman spectrum of graphene and graphene layers. *Phys. Rev. Lett.* **97** (2006) 187401.
- [11] H. C. Schniepp, J.-L. Li, M. J. McAllister, H. Sai, M. Herrera-Alonso, D. H. Adamson, R. K. Prud'homme, R. Car, D. A. Saville, I. A. Aksay. Functionalized single graphene sheets derived from splitting graphite oxide. *J. Phys. Chem. B* **110** (2006) 8535-8539.
- [12] X. Li, X. Wang, L. Zhang, S. Lee, H. Dai. Chemically derived, ultrasmooth graphene nanoribbon semiconductors. *Science* **319** (2008) 1229-1232.
- [13] S. R. C. Vivekchand, C. S. Rout, K. S. Subrahmanyam, A. Govindaraj, C. N. R. Rao. Graphene-based electrochemical supercapacitors. *J. Chem. Sci.* **120** (2008) 9-13.
- [14] S. Gilje, S. Han, M. Wang, K. L. Wang, R. B. Kaner. A chemical route to graphene for device applications. *Nano Lett.* **7** (2007) 3394-3398.
- [15] G. Wang, J. Yang, J. Park, X. Gou, B. Wang, H. Liu, J. Yao. Facile synthesis and characterization of graphene nanosheets. *J. Phys. Chem. C* **112** (2008) 8192-8195.
- [16] J. D. Fowler, M. J. Allen, V. C. Tung, Y. Yang, R. B. Kaner, B. H. Weiller. Practical chemical sensors from chemically derived graphene. *ACS Nano* **3** (2009) 301-306.
- [17] D. S. Lee, C. Riedl, B. Krauss, K. von Klitzing, U. Starke, J. H. Smet. Raman spectra of epitaxial graphene on SiC and of epitaxial graphene transferred to SiO<sub>2</sub>. *Nano Lett.* **8** (2008) 4320-4325.
- [18] H. Huang, W. Chen, S. Chen, A. T. S. Wee. Bottom-up growth of epitaxial graphene on 6H-SiC(0001). *ACS Nano* **2** (2008) 2513-2518.

- [19] Y. Q. Wu, P. D. Ye, M. A. Capano, Y. Xuan, Y. Sui, M. Qi, J. A. Cooper, T. Shen, D. Pandey, G. Prakash, R. Reifengerger. Top-gated graphene field-effect-transistors formed by decomposition of SiC. *Appl. Phys. Lett.* **92** (2008) 092102.
- [20] S.Y. Zhou, D. A. Siegela, A. V. Fedorovc, A. Lanzara. Departure from the conical dispersion in epitaxial graphene. *Physica E* **40** (2008) 2642–2647.
- [21] P. R. Somani, S. P. Somani, M. Umeno. Planer nano-graphenes from camphor by CVD. *Chem. Phys. Lett.* **430** (2006) 56-59.
- [22] A. Reina, X. Jia, J. Ho, D. Nezich, H. Son, V. Bulovic, M. S. Dresselhaus, J. Kong. Large area, few-layer graphene films on arbitrary substrates by chemical vapor deposition. *Nano Lett.* **9** (2009) 30-35.
- [23] A. Ismach, C. Druzgalski, S. Penwell, A. Schwartzberg, M. Zheng, A. Javey, J. Bokor, Y. Zhang. Direct chemical vapor deposition of graphene on dielectric surfaces. *Nano Lett.* **10** (2010) 1542-1548.
- [24] A. N. Obraztsov. Chemical vapour deposition: making graphene on a large scale. *Nat. Nanotechnol.* **4** (2009) 212-213.
- [25] H. Ueta, M. Saida, C. Nakai, Y. Yamada, M. Sasaki, S. Yamamoto. Highly oriented monolayer graphite formation on Pt(111) by a supersonic methane beam. *Surf. Sci.* **560** (2004) 183.
- [26] J. Coraux, A. T. N'Diaye, C. Busse, T. Michely. Structural coherency of graphene on Ir(111). *Nano Lett.* **8** (2008) 565-570.
- [27] A. L. Vázquez de Parga, F. Calleja, B. Borca, M. C. G. Passeggi, J. J. Hinarejos, F. Guinea, R. Miranda. Periodically rippled graphene: growth and spatially resolved electronic structure. *Phys. Rev. Lett.* **100** (2008) 056807.
- [28] A. G. Starodubov, M. A. Medvetskiĭ, A. M. Shikin, V. K. Adamchuk. Intercalation of silver atoms under a graphite monolayer on Ni(111). *Phys. Solid State* **46** (2004) 1341-1348.
- [29] J. Campos-Delgado, J. M. Romo-Herrera, X. Jia, D. A. Cullen, H. Muramatsu, Y. A. Kim, T. Hayashi, Z. Ren, D. J. Smith, Y. Okuno, T. Ohba, H. Kanoh, K. Kaneko, M. Endo, H. Terrones, M. S. Dresselhaus, M. Terrones. Bulk production of a new form of sp<sup>2</sup> carbon: Crystalline graphene nanoribbons. *Nano Lett.* **8** (2008) 2773-2778.
- [30] H. R. Gutiérrez, U. J. Kim, J. P. Kim, P. C. Eklund. Thermal conversion of bundled carbon nanotubes into graphitic ribbons. *Nano Lett.* **5** (2005) 2195-2201.
- [31] X. Yang, X. Dou, A. Rouhanipour, L. Zhi, H. J. Räder, K. Müllen. Two-dimensional graphene nanoribbons. *J. Am. Chem. Soc.* **130** (2008) 4216-4217.
- [32] Y. Li, Z. Wang. Bis-N-annulated quaterrylene: An approach to processable graphene nanoribbons. *Org. Lett.* **11** (2009) 1385-1387.
- [33] F. B. Mallory, K. E. Butler, A. C. Evans, E. J. Brondyke, C. W. Mallory, C. Yang, A. Ellenstein. Phenacenes: a family of graphite ribbons. 2. Syntheses of some [7]phenacenes and an [11]phenacene by Stilbene-like photocyclizations. *J. Am. Chem. Soc.* **119** (1997) 2119-2124.
- [34] J. Wu, L. Gherghel, M. D. Watson, J. Li, Z. Wang, C. D. Simpson, U. Kolb, K. Müllen. From branched polyphenylenes to graphite ribbons. *Macromolecules* **36** (2003) 7082-7089.

- [35] M. Terrones, A. R. Botello-Méndez, J. Campos-Delgado, F. López-Urías, Y. I. Vega-Cantú, F. J. Rodríguez-Macías, A. L. Elías, E. Muñoz-Sandoval, A. G. Cano-Márquez, J-C. Charlier, H. Terrones. Graphene and graphite nanoribbons: morphology, properties, synthesis, defects and applications. *Nanotoday* **5** (2010) 351-372.
- [36] M. S. Dresselhaus, G. Dresselhaus. Intercalation compounds of graphite. *Adv. Phys.* **51** (2002) 1-186.
- [37] H. Shioyama. Cleavage of graphite to graphene. *J. Mater. Sci. Lett.* **20** (2001) 499-500.
- [38] L. M. Viculis, J. J. Mack, O. M. Mayer, H. T. Hahn, R. B. Kaner. Intercalation and exfoliation routes to graphite nanoplatelets. *J. Mater. Chem.* **15** (2005) 974-978.
- [39] S. Stankovich, R. D. Piner, X. Chen, N. Wu, S. T. Nguyen, R. S. Ruoff. Stable aqueous dispersions of graphitic nanoplatelets via the reduction of exfoliated graphite oxide in the presence of poly(sodium 4-styrenesulfonate). *J. Mater. Chem.* **16** (2006) 155-158.
- [40] D. D. L. Chung. Exfoliation of graphite. *J. Mater. Sci.* **22** (1987) 4190-4198.
- [41] Rejuvenating Moore's law with nanotechnology. J. Wolfe. Forbes, June 05, 2007. Last access on: April 13, 2010. From: <http://www.forbes.com/>.
- [42] B. Balasubramanian, M. Burghard. Chemically functionalized carbon nanotubes. *Small* **1** (2005) 180-192.
- [43] A. Hirsch. Functionalization of single-walled carbon nanotubes. *Angew. Chem. Int. Ed.* **41** (2002) 1853-1859.
- [44] D. Tasis, N. Tagmatarchis, A. Bianco, M. Prato. Chemistry of carbon nanotubes. *Chem. Rev.* **106** (2006) 1105-1136.
- [45] S. Banerjee, T. Hemraj-Benny, S. S. Wong. Covalent surface chemistry of single-walled carbon nanotubes. *Adv. Mater.* **17** (2005) 17-29.
- [46] C. A. Dyke, J. M. Tour. Covalent functionalization of single-walled carbon nanotubes for materials applications. *J. Phys. Chem. A* **108** (2004) 11151-11159.
- [47] A. Cano-Márquez, F. Rodríguez-Macías, J. Campos, C. Espinosa-González, F. Tristán, D. Ramírez-González, D. Cullen, D. Smith, M. Terrones, Y. Vega-Cantú. Ex-MWNTs: Graphene sheets and ribbons produced by lithium Intercalation and exfoliation of carbon nanotubes. *Nano Lett.* **9** (2009) 1527-1533.
- [48] M. S. Meier, R. Andrews, D. Jacques, K. B. Cassityab, D. Qian. Tearing open nitrogen-doped multiwalled carbon nanotubes. *J. Mater. Chem.* **18** (2008) 4143-4145.
- [49] J. Zhou, C. Booker, R. Li, X. Zhou, T-K. Sham, X. Sun, Z. Ding. An electrochemical avenue to blue luminescent nanocrystals from multiwalled carbon nanotubes (MWCNTs). *J. Am. Chem. Soc.* **129** (2007) 744-745.
- [50] G. Maurin, Ch. Bousquet, F. Henn, P. Bernier, R. Almaira, B. Simon. Electrochemical lithium intercalation into multiwall carbon nanotubes: A micro-Raman study. *Solid State Ionics* **136-137** (2000) 1295-1299.
- [51] N. A. W. Holzwarth, S. G. Louie, S. Rabi. Lithium-intercalated graphite: self-consistent electronic structure for stages one, two, and three. *Phys. Rev. B* **28** (1983) 1013-1025.

- [52] T. Enoki, M. Suzuki, M. Endo. *Graphite intercalation compounds and applications*. Oxford University Press: New York, 2003.
- [53] S. Pekker, J.-P. Salvetat, E. Jakab, J.-M. Bonard, L. Forr. Hydrogenation of carbon nanotubes and graphite in liquid ammonia. *J. Phys. Chem. B* **105** (2001) 7938-7943.
- [54] E. R. Alvizo-Paez, J. M. Romo-Herrera, H. Terrones, M. Terrones, J. Ruiz-Garcia, J. L. Hernandez-Lopez. Soft purification of nitrogen-doped and undoped multi-wall carbon nanotubes. *Nanotechnology* **19** (2008) 155701-155710.
- [55] J. Liu, A. G. Rinzler, H. Dai, J. H. Hafner, R. K. Bradley, P. J. Boul, A. Lu, T. Iverson, K. Shelimov, C. B. Huffman, F. Rodriguez-Macias, Y-S. Shon, T. Randall Lee, D. T. Colbert, R. E. Smalley. Fullerene pipes. *Science* **280** (1998) 1253-1256.
- [56] A. Cano-Márquez, F. Rodríguez-Macías, M. Terrones, Y. Vega-Cantú. (2008). Unpublished results.
- [57] P. Nemes-Incze, Z. Osváth, K. Kamarás, L.P. Biró. Anomalies in thickness measurements of graphene and few layer graphite crystals by tapping mode atomic force microscopy. *Carbon* **46** (2008) 1435-1442.
- [58] C. H. Lui, L. Liu, K. F. Mak, G. W. Flynn, T. F. Heinz. Ultraflat graphene. *Nature* **462** (2009) 339-341.
- [59] H. S. Skulason, P. E. Gaskell, T. Szkopek. Optical reflection and transmission properties of exfoliated graphite from a graphene monolayer to several hundred graphene layers. *Nanotechnology* **21** (2010) 295709.
- [60] K. L. Lu, R. M. Lago, Y. K. Chen, M. L. H. Green, P. J. F. Harris, S. C. Tsang. Mechanical damage of carbon nanotubes by ultrasound. *Carbon* **34** (1996) 814-816.
- [61] S. Chakraborty, W. Guo, R. H. Hauge, W. E. Billups. Reductive alkylation of fluorinated graphite. *Chem. Mater.* **20** (2008) 3134-3136.
- [62] H. Hiura, T.W. Ebbesen, K. Tanigaki, H. Takahashi. Raman studies of carbon nanotubes. *Chem. Phys. Lett.* **202** (1993) 509-512.
- [63] F. Tuinstra, J. L. Koenig. Raman spectrum of graphite. *J. Chem. Phys.* **53** (1970) 1126-1130.
- [64] M. S. Dresselhaus, G. Dresselhaus, R. Saito, A. Jorio. Raman spectroscopy of carbon nanotubes. *Phys. Rep.* **409** (2005) 47-99.
- [65] G. Maurin, F. Henn, B. Simon, J. F. Colomer, J. B. Nagy. Lithium doping of multiwalled carbon nanotubes produced by catalytic decomposition. *Nano Lett.* **1** (2001) 75-79.
- [66] Y. Zhang, H. He, C. Gao, J. Wu. Covalent layer-by-layer functionalization of multiwalled carbon nanotubes by click chemistry. *Langmuir* **25** (2009) 5814-5824.
- [67] M. Inaba, H. Yoshida, Z. Ogumi, T. Abe, Y. Mizutani, M. Asano. In situ Raman study on electrochemical Li intercalation into graphite. *J. Electrochem. Soc.* **142** (1995) 20-26.
- [68] M. A. Pimenta, G. Dresselhaus, M. S. Dresselhaus, L. G. Cancado, A. Jorio, R. Saito. Studying disorder in graphite-based systems by Raman spectroscopy. *Phys. Chem. Chem. Phys.* **9** (2007) 1276-1291.

- [69] Characteristic IR band positions. ALS Infrared Beamlines. Last access on: Jul 3, 2010. From: <http://infrared.als.lbl.gov/content/web-links/60-ir-band-positions>.
- [70] U. J. Kim, X. M. Liu, C. A. Furtado, G. Chen, R. Saito, J. Jiang, M. S. Dresselhaus, P. C. Eklund. Infrared-active vibrational modes of single-walled carbon nanotubes. *Phys. Rev. Lett.* **95** (2005) 157402.
- [71] B. P. Ramesh, W.J. Blau, P.K. Tyagi, D.S. Misra, N. Ali, J. Gracio, G. Cabral, E. Titus. Thermogravimetric analysis of cobalt-filled carbon nanotubes deposited by chemical vapour deposition. *Thin Solid Films* **494** (2006) 128-132.
- [72] E. Titus, N. Ali, G. Cabral, J. Gracio, P. Ramesh Babu, M.J. Jackson. Chemically functionalized carbon nanotubes and their characterization using thermogravimetric analysis, Fourier transform infrared, and Raman spectroscopy. *J. Mater. Eng. Perform.* **15** (2006) 182-186.
- [73] H. Zabel, D. A. Neumann. Neutron scattering studies of potassium-ammonia layers in graphite. *Can. J. Chem.* **66** (1988) 666-671.
- [74] X. W. Qian, S. A. Solin. Staging properties of potassium-ammonia ternary graphite intercalation compounds at high ammonia pressure. *Phys. Rev. B* **39** (1989) 8707-8714.
- [75] D. V. Kosynkin, A. L. Higginbotham, A. Sinitskii, J. R. Lomeda, A. Dimiev, B. K. Price, J. M. Tour. Longitudinal unzipping of carbon nanotubes to form graphene nanoribbons. *Nature* **458** (2009) 872-876.
- [76] L. Jiao, L. Zhang, X. Wang, G. Diankov, H. Dai. Narrow graphene nanoribbons from carbon nanotubes. *Nature* **458** (2009) 877-880.
- [77] A. L. Elías, A. R. Botello-Méndez, D. Meneses-Rodríguez, V. J. González, D. Ramírez-González, L. Ci, E. Muñoz-Sandoval, P. M. Ajayan, H. Terrones, M. Terrones. Longitudinal cutting of pure and doped carbon nanotubes to form graphitic nanoribbons using metal clusters as nanoscalpels. *Nano Lett.* **10** (2009) 366-372.
- [78] K. Kim, A. Sussman, A. Zettl. Graphene nanoribbons obtained by electrically unwrapping carbon nanotubes. *ACS Nano* **4** (2010) 1362-1366.
- [79] H. Santos, L. Chico, L. Brey. Carbon nanoelectronics: unzipping tubes into graphene ribbons. *Phys. Rev. Lett.* **103** (2009) 086801.



## Chapter 4 Conclusions, perspectives, and future work

### 4.1 Conclusions

The unique electronic and physical properties of carbon nanotubes (CNTs) may vary as a function of the synthesis method and its experimental conditions. The properties of CNTs are determined by the way the hexagonal carbon lattice is oriented, defects (vacancies, disclinations, etc.), diameter, and number of walls; hence, full control over these factors remains as a major challenge. Once these and other factors are managed, at least in a certain extent, large-scale tailored synthesis of CNTs will certainly be achieved, along with their potential applications. From all the synthesis methods, CVD and arc-discharge offer relatively cheap alternatives for large-scale synthesis of CNTs. Nevertheless, more work is needed for the synthesis methods to obtain CNTs with tailored characteristics, and to scale their production. Nowadays, CNTs are a huge research topic, especially in the field of CNTs-polymer composites.

Synthesis methods for composites vary, and they consist in physical procedures such as mixing and self-assembly, or in chemical methods involving covalent bonding. The first methods allow the synthesis of nanocomposites without significantly altering the properties of CNTs, while the second ones are aimed to obtain strong interactions between the nanotubes and the polymer matrix. Furthermore, covalent bonding methods may allow precise control and tuning of the properties of nanocomposites without notably altering those of the original CNTs.

The original purpose of this thesis research was to produce composites from multi-walled carbon nanotubes (MWNTs), nitrogen-doped MWNTs (CN<sub>x</sub>), and the electronically conducting polymers (ECPs) polyaniline (PAni), poly(2-aminobenzene sulfonic acid) (PoASA, a sulfonated polyaniline) and polypyrrole (PPy), in a single step by means of an *in situ* polymerization method. The objective was achieved, we showed it was possible to synthesize these composites from MWNTs, or nitrogen-doped MWNTs (CN<sub>x</sub>), with PAni, PoASA, and PPy. This *in situ* polymerization was via a reductive

alkylation method which is called the 'nanotube salts' reaction. Since these salts are highly reactive towards several vinylic monomers, we decided to use this method with anilines and pyrrole, which are aromatic monomers.

Nevertheless, in most samples we found heterogeneous dispersion of MWNTs within PoASA and PANi matrices, which was more evident with monomer loads < 50 wt%. In addition, it was not possible to obtain composites with low MWNTs loads (< 1 wt%). Interaction between MWNTs and sulfonated PANi (PoASA) is strong, probably due to the sulfonated groups which withdraw the electronic density from the polymer chain, thus creating partially positive charges in the PoASA skeleton, which might be attracted by MWNTs. No pull-out effects were seen in fractures that occur when the composite dried; instead, MWNTs break and remain in the PoASA matrix. Moreover, composites are highly disordered, as shown by Raman and X-Ray diffraction. It was neither possible to control the oxidation state nor to accurately determine the conductivity of composites. Although we showed that the nanotube salts method can produce CNT composites with PANi and PPy, we found that it was not a convenient method, due to problems with dispersion and homogeneity.

However, we observed an interesting phenomenon not previously reported in composites that led to a new and interesting research path: the opening of CNTs into multi-walled carbon nanoribbons or ex-MWNTs. We found these nanoribbons mainly in composites obtained with low loads of monomer (< 50 wt%). We thus decided to explore this path; ex-MWNTs were obtained by the same method used for composite synthesis but without adding monomers.

Lithium and ammonia intercalate through tube ends and wall defects. Ex-MWNTs are produced when intercalated MWNTs are exposed to acids and then abruptly heated to high temperatures. As a result, the exothermic reaction of lithium and lithium-ammonia complexes with acids generates stress and fractures, and expels intercalants through tube defects, thus opening or unwrapping the tubes. The use of high temperatures in addition to acids was a key factor to obtain fully unwrapped MWNTs, since high temperatures force the ejection of remaining intercalants, thus opening more tubes. Other important conditions that helped us to improve the intercalation and exfoliation processes were: a 10:10:1 v/w/w NH<sub>3</sub>:Li:CNTs ratio, high NH<sub>3</sub> volumes

(20:1 v/w NH<sub>3</sub>:CNTs ratio) were preferred, and cutting MWNTs in strong acid mixtures, which allowed better lithium intercalation.

We successfully produced ex-MWNTs with yields as high as 50%. Characterization allowed us to understand better the formation of ex-MWNTs. SEM and TEM micrographs show that after exfoliation, ex-MWNTs are wider (~120–140 nm) than MWNTs and are composed of several graphitic sheets. AFM confirmed this and revealed interesting features such as steps composed of several graphitic layers, graphene flakes on the surface of ex-MWNTs, and graphitic nanoplatelets that originated from ex-MWNTs. TGA analysis showed that ex-MWNTs are more reactive towards oxidation than MWNTs, probably due to the presence of edges. Ex-MWNTs obtained by acid treatment show loss of order, with interlayer spacings ~1.5 times higher than those presented by as-synthesized MWNTs. Interestingly, after thermal shock ex-MWNTs are re-crystallized, ordered, and with interlayer spacings close to those shown by MWNTs.

It is important to note that this was a pioneering and novel work on graphene nanoribbons (GNRs) from MWNTs, and only after its publication other research groups also announced the production of GNRs from other methods. Our research was published in the peer-review journal *Nano Letters* (DOI: 10.1021/nl803585s, impact factor 10.371).

## 4.2 Perspectives and future work

### *Nanocomposites from Carbon Nanotubes and Conducting Polymers*

It would be interesting to obtain composites with low loads of MWNTs (<1%). To do so, dispersion of CNTs in polyaniline or polypyrrole matrices should be improved, and the reaction equilibrium could be directed towards full polymerization of the monomers. It would be interesting to determine the type of interaction of bonding between carbon nanotubes and the conducting polymers, which could be achieved with aid of x-ray photoelectron spectroscopy (XPS). Moreover, composites would reveal interesting electrochemical properties such as doping, charge capacity and electrocatalytic activity.

In addition, electrochemical techniques such as cyclic voltammetry could be used to tune the oxidation state of the conducting polymers, and hence, the electronic properties of the composite. A potential application of these composites could be the making of precision actuators and biochemical sensors.

#### *Ex-MWNTs: properties and applications*

We successfully obtained carbon nanoribbons from MWNTs. Nonetheless, further understanding of the exfoliation mechanism is required; in this regard, theoretical calculations could cast more light into this. Further characterization could also contribute to a better understanding on the properties of ex-MWNTs. It would be interesting to know if single and bulk ex-MWNTs are as conductive as graphene sheets produced by other methods. XPS would tell us the relative amount of  $sp^3$  and  $sp^2$  bonding. By means of micro-Raman spectroscopy on single ex-MWNTs we could see if the electronic properties change when moving from the center to the edges of ex-MWNTs. It would also be interesting to see how the magnetic properties of ex-MWNTs (if there are any) differ from those of MWNTs, or graphene nanoribbons.

Moreover, the possible research paths and applications of ex-MWNTs are numerous. This unique finding has opened numerous new and active fields of research and application which not only will cast valuable basic knowledge, but that may also contribute to solve important problems.

For example, by means of micromanipulation we could build FETs and Schottky diodes with single ex-MWNTs, and determine their performance as building blocks for computer processors. Deposition of particles from metals such as Au or Pd on ex-MWNTs would be useful in the making of catalysts. The large amount of edges and surface area would let us to explore the intercalation of other chemical species beyond Li and  $NH_3$ , and applications such as gas adsorption, rechargeable batteries, and polymer composites. Functionalization of edges also may enable new applications of GNRs such as in sensors and controlled drug delivery. Single sheets from ex-MWNTs could also help in human DNA sequencing.

Improving the efficiency of rechargeable batteries, catalysts in fuel cells, and super-capacitors for electric vehicles will be a small but important step towards reduction of greenhouse gases, particularly important in under-developed or industrialized nations. Water requirements for human activities rise as the world population increases, making research on water purification technologies unavoidable, in which GNRs could play an important role. Graphene is capable of absorbing a wide range of light frequencies, representing a less toxic and cheaper alternative for harvesting solar energy. Graphene sheets from GNRs can also be used in thin transparent electrodes for organic light-emitting diodes (OLEDs), with a performance and efficiency comparable to that of indium-tin-oxide transparent anodes, but potentially giving more freedom for device design and use, for example in flexible electronic displays. The extension of the method used for production of ex-MWNTs to other systems may lead to new materials, as seen in section 3.6.

Research on graphene and graphene nanoribbons is an exploding new field of research. The ex-MWNTs method for obtention of GNRs stands as an important contribution in the field. We envision that ex-MWNTs may be suitable for many applications being developed for GNRs.



# Appendices



# Appendix A.1 Properties and synthesis of carbon nanotubes

## A.1.1 Summary of properties

Table A.1. Most significant properties of carbon nanotubes and related materials.

| Property                    | Symbol     | Formula / Value(s)   | Reference(s) |
|-----------------------------|------------|--|--------------|
| Carbon-carbon bond distance | $a_{C-C}$  | 1.421 Å (graphite).  | [1]          |
| Unit vectors                | $a_1, a_2$ | $a_1 = \left(\frac{\sqrt{3}}{2}, \frac{1}{2}\right)a$ ; $a_2 = \left(\frac{\sqrt{3}}{2}, -\frac{1}{2}\right)a$   | [1]          |
| Reciprocal vectors          | $b_1, b_2$ | $b_1 = \left(\frac{1}{\sqrt{3}}, 1\right) \cdot \frac{2\pi}{a}$ ; $b_2 = \left(\frac{1}{\sqrt{3}}, -1\right) \cdot \frac{2\pi}{a}$   | [1]          |
| Unit vector length          |            | $\sqrt{3}a_{C-C} = 2.46 \text{ Å}$   | [1]          |
| Interlayer distance         |            | 3.355 Å (graphite).<br>3.335 Å (graphite).<br>3.42 Å (as synthesized CVD-MWNTs).   | [2]<br>[3]   |
| Chiral vector               | $C_h$      | $C_h = na_1 + ma_2 = (n, m)$ ; $n, m$ : integers.  | [1]          |
| Chiral angle                | $\theta$   | $\text{Sin } \theta = \frac{\sqrt{3}m}{2\sqrt{n^2 + nm + m^2}}$ ; $0 \leq \theta \leq 30^\circ$<br>$\text{Cos } \theta = \frac{2n + m}{2\sqrt{n^2 + nm + m^2}}$ ;<br>$\text{Tan } \theta = \frac{\sqrt{3}m}{2n + m}$ | [1]          |
| Nanotube diameter           | $d_t$      | $d_t = \frac{L}{\pi} = \frac{\sqrt{n^2 + nm + m^2}}{\pi} a$  | [1]          |
| Nanotube perimeter          | $L$        | $L =  C_h  = a\sqrt{n^2 + nm + m^2}$ ; $0 \leq  m  \leq n$   | [1]          |
| Lattice parameter           |            |  |              |
| Hybridization               |            | $sp^2$ ; $sp^3$ arises upon functionalization or defect creation.  |              |
| Aromaticity                 | $K$        | $K = 2^{(m+1)}$ , for $(n,0)_m$ zigzag nanotubes where $m$ equals to the number of hexagons which form a row perpendicular to the tube axis.   | [4]          |

Table A.1. Most significant properties of carbon nanotubes and related materials (continued).

| Property             | Symbol           | Formula / Value(s)   | Reference(s) |
|----------------------|------------------|--|--------------|
| Density of states    | $N$              | $N(E_F) = \frac{8}{\sqrt{3}\pi a  t }$   | [1]          |
| Energy gap           | $E_g$            | $E_g = \frac{ t  \cdot a_{C-C}}{d_t}$  | [1]          |
| Resistance           | $R$              | 100 k $\Omega$ , single MWNT at 4.2 K, two-terminal and four-point configurations. | [5]          |
|                      |                  | 200 k $\Omega$ , metallic SWNTs junction.  | [6]          |
|                      |                  | 500 k $\Omega$ , semiconducting SWNTs junction.                                    |              |
|                      |                  | 10 M $\Omega$ , semiconducting-metallic SWNTs (Schottky barrier).                  |              |
| Young's modulus      | $E$              | 1 TPa (SWNT).  | [7]          |
|                      |                  | 320 GPa to 1470 GPa (SWNTs ropes perimeter).                                       |              |
|                      |                  | 270 GPa to 950 GPa (MWNTs, outer layer).<br>200 GPa to 4000 GPa (MWNTs, axial).    | [8]          |
| Tensile strength     | $\sigma_s$       | 170 Mpa (SWNT, theoretical).   | [9]          |
|                      |                  | 13 GPa to 52 GPa (SWNTs ropes).  | [7]          |
|                      |                  | 11 GPa to 63 GPa (MWNTs, outer shell).   | [8]          |
| Stress               | $\sigma$         | 5.3 GPa (single SWNT).   | [10]         |
| Thermal conductance  | $G$              | $1.6 \times 10^{-7}$ W/K (MWNT)  | [11]         |
| Thermal conductivity | $\lambda$ or $k$ | 37000 W/m K at 100 K, and 6600 W/m K at 300 K for a (10, 10) SWNT (predicted).     | [12]         |
|                      |                  | 3000 W/m K at 300 K (single MWNT)  | [11]         |
| Thermoelectric power | $S$              | 40 $\mu$ V/K at 300 K (single SWNT or mat)   | [13]         |
|                      |                  | 80 $\mu$ V/K at 300 K (metallic & doped MWNT)                                      | [11]         |
| Density              | $\rho$           | 1.3 g/mL   | [14]         |

## A.1.2 Other synthesis methods for carbon nanotubes

### *Electric arc discharge*

Electric arc discharge is a simple and traditional method for synthesis of fullerenes and carbon nanotubes [15-17]. The experimental setup is shown at figure A.1.1.

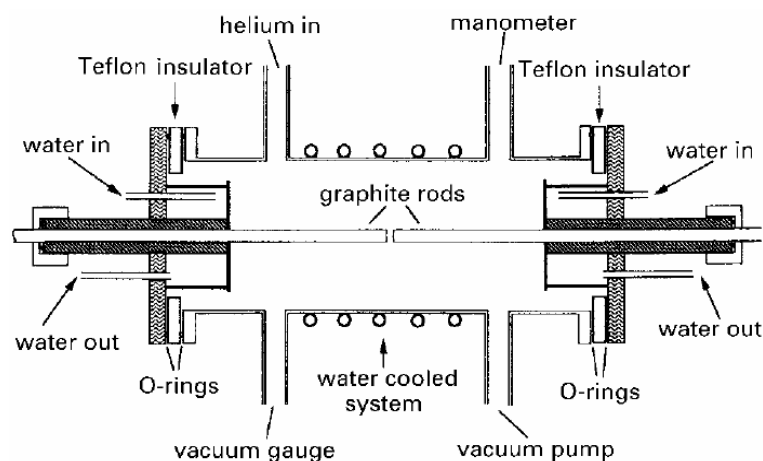


**Figure A.1.1. Cross-sectional view of a carbon arc generator** used for the synthesis of carbon nanotubes [16].

A gas (Ar, He, or H<sub>2</sub>) flows at constant pressure (~100 to 2500) torr through the reaction chamber. A bias voltage of 15 V to 35 V and a dc electric current of 50 A to 120 A are applied across two high-purity, water-cooled carbon rod electrodes (~5 mm d. for the anode, and ~20 mm d. for the cathode) separated by a 1 mm gap. The magnitude of the applied current depends on experimental variables such as gas pressure, the size of the electrodes and their separation. As the carbon anode (positive electrode) is consumed, a motor-driven mechanism keeps the electrodes at a constant distance. A macroscopic carbon deposit forms at the cathode (negative electrode), comprised of aligned carbon nanotubes (parallel to the electric current) and polyhedral particles at the core and a hard, grey shell on the periphery. Addition of a transition metal (a catalyst) to the anode allows the synthesis of SWNTs [16, 18]. Typical catalysts are Fe, Ni, Co, and their mixtures [15, 16] in various atomic percentages. In this regard, SWNTs have been successfully obtained by using mixtures of 4.2 at. % Ni, and 1 at. %

Y [18] placed in a drilled hole in the cathode under a ~500 torr helium atmosphere. Mixtures of SWNTs and MWNTs have been synthesized by using a composite graphite anode containing 8.6 wt % Ni and Co (1:1 Ni/Co); the SWNTs bundles are deposited only at the inner walls of the arc chamber whereas the MWNTs are found at the cathode deposit [17]. In addition, sulfur [19] has also been used along with catalyst metals, promoting nanotube growth and broadening the diameter distribution. On the other hand, it has been found that Cu, depending on the experimental conditions, may either hinder or enhance the catalytic action of Co [20, 21]. Depending on the experimental conditions, the soot will be primarily comprised of fullerenes, SWNTs or MWNTs, with minor quantities of amorphous carbon and particles. Furthermore, the melting point of metals, their vapor pressure and their affinity towards carbon have an important effect on the amount of produced SWNTs [22], for example, Ti impedes the formation of SWNTs due to its strong affinity towards carbon [20]. SWNTs (~1 nm d.) have been synthesized under a methane, argon and iron vapor mixture [15]. MWNTs have also been obtained in high yields by replacing helium by hydrogen [23]. A typical example of an arc-grown MWNT is shown at figure A.1.2.

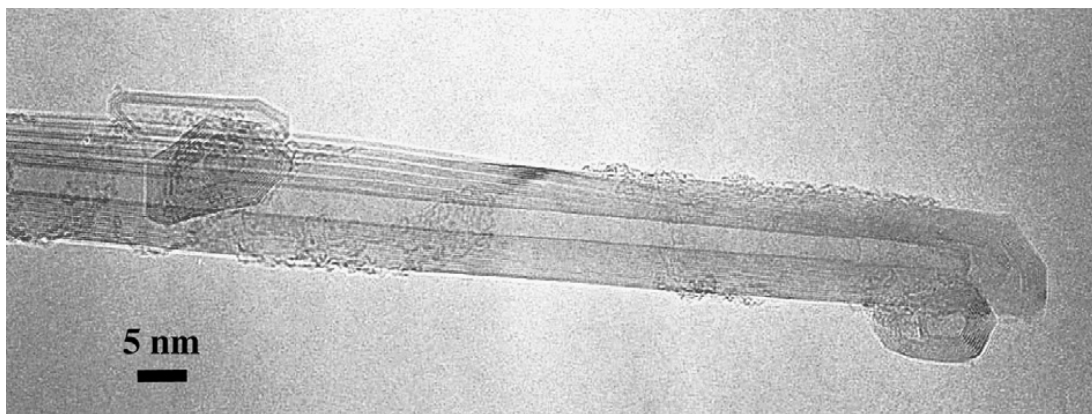


**Figure A.1.2. TEM micrograph of an arc-grown MWNT** with its characteristic needle-like end, obtained at the cathode deposit. Anode: graphite-Ni/Co composite (1:1 Ni/Co, 8.6 wt % each). Cathode: high density graphite (99.9% purity). Pressure: 600 torr He, dc voltage: ~20–25 V, current ~100–120 A, gap: ~1–2 mm [17].

Although being an easy, cheap, and scalable process (a Krätschmer reactor can surpass 100 mg/min of soot containing SWNTs [24]), arc-discharge synthesis of SWNTs presents fluctuations in the arc due to temperature gradients which provoke an irregular

and fast conductive flow, which carries the reactants out of the high temperature region in  $< 100$  ms, shortens the residence time for nanotube growth, and ultimately decreases the control over the experimental conditions [25]. In this regard, Alford *et al.* [25], have attempted the use of microgravity conditions to improve the synthesis, but the required time to establish the optimum experimental conditions for extended nanotube growth is larger than the duration of the free fall of the reactor, which makes it necessary to carry out these experiments at outer space.

### Laser ablation

Historically, this method is important since it was first used for the synthesis of fullerenes [26] and high-purity SWNTs [27]. A schematic is shown at figure A.1.3.

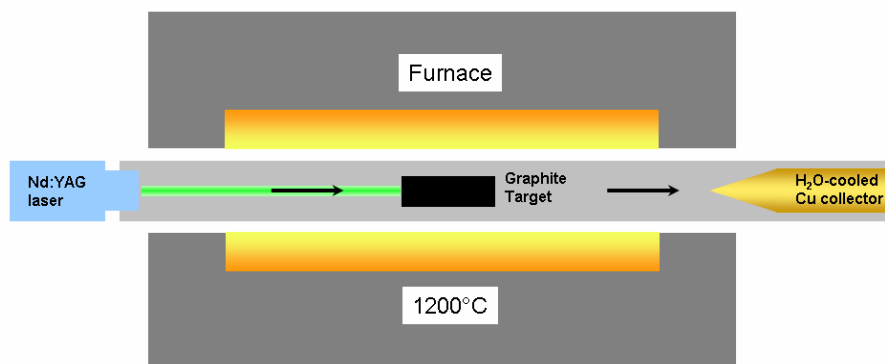


**Figure A.1.3. Experimental setup for production of carbon nanotubes by laser ablation.** Carbon nanotubes deposit on a Cu collector [16, 28].

A laser beam hits a graphite target placed within a quartz tube at high temperature (1200 °C) under flowing gas (argon or nitrogen), thus producing a very hot plasma plume (2700 to 3700) °C, in which carbon species and catalyst (if used) are vaporized. As the plume expands and cools down to 1200 °C, the dissociated carbon species react and may produce fullerenes [26], SWNTs [16, 27, 29] and MWNTs [16, 28, 30] as main products, as exemplified in figure A.1.4.

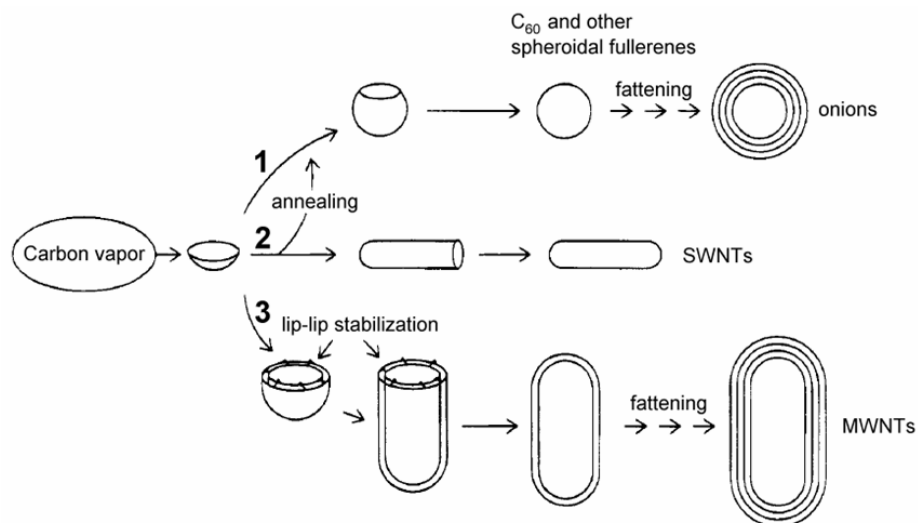


**Figure A.1.4. Fullerene branching paths.** An initial graphitic flake containing at least one pentagon forms in the condensing vapor. **(1)** Annealing at high temperature leads to closed fullerene; further nucleation produces “onions”. **(3)** High carbon density may nucleate a second open layer, which grows much faster. When the edges of both layers reach each other before closing, ad-atoms stabilize the open conformation, and carbon adds to the open edges to form the nanotube. Additional layers grow and anneal on the underlying nanotube template. Growth terminates when the adsorption energy of atoms and small clusters, falls below the thermal energy of the adsorbate. **(2)** Without spot-welds to stabilize the open structure, rapid annealing to fullerenes prohibits the formation of single-walled nanotubes [28].

MWNTs can be obtained at pressures of ~500 torr. MWNT can be 300 nm and up to several micrometers long, and may be comprised of up to 30 graphitic layers, as displayed in figure A.1.5. The making of MWNTs may be explained by stabilization of the inner graphitic layer by bridging ad-atoms, thus prolonging the lifetime of the open structure. MWNTs nucleation and growth increase with carbon density at the beginning of the process; this occurs when the laser spot is reduced. The addition of carbon to the open edges lengthens the nanotubes before annealing closes the tubes [28].

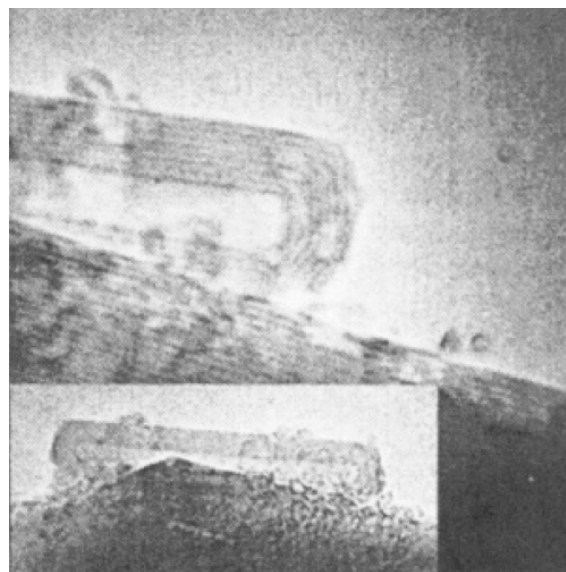


**Figure A.1.5. TEM images of laser-ablation-grown MWNTs.** The number of layers varied from 4 to 24, while the inner diameters range from 1.5 to 3.5 nm [28].

Similarly to the arc discharge process, the use of a metal catalyst in the target (binary mixtures of Fe, Pt, Co, or Ni improve the yield), previously mixed with graphite, die cast and machined, produces SWNTs. When the laser strikes the target, C<sub>3</sub>, C<sub>2</sub>, and C species are produced, along with vaporized catalysts atoms and small clusters. Once the vapor leaves the surface, carbon species coalesce and form larger molecules and fullerenes. Catalyst metals also form clusters at a lower rate. The catalyst particles absorb and/or adsorb low-molecular weight carbon species, i. e., C<sub>2</sub>, and may attach to fullerenes or graphene sheets thus preventing their closure. Then, a nanotube may grow from the carbon dissolved in or adsorbed on the catalyst. It is expected that nanotubes grow at the beginning of plume evolution, and it is stopped by carbon coating of the catalyst particles. Growth may also be limited by poisoning of the catalyst particles or their solidification after having increased their size sufficiently. If the target is placed in an inner tube, carbon clusters, catalysts, and fullerenes accumulated in it may dissociate, forming an additional feedstock for carbon nanotube growth and reducing the amount of amorphous carbon present, thereby producing very pure SWNTs [29].

### **Solar energy**

An alternative method for synthesis of MWNTs (with a minor amount of SWNTs) involves direct vaporization of a graphite rod by focused solar light under nitrogen atmosphere [31]. The experimental setup is depicted at [figure A.1.6](#). Under nitrogen atmosphere, catalyst particles (< 30 nm d.) contribute to the formation of bamboo-shaped MWNTs (15–50 nm d., doping level ≤ 11 at. % with Ni catalyst, [figure A.1.7A](#)), while smaller ones promote the formation of small bundles of SWNTs (0.9 nm d., [figure A.1.7B](#)). In contrast, when using argon catalyst particles are greater in size (< 80 nm d.), and large bundles of SWNTs (1.2–1.5 nm d.) are observed. In addition, nanotubes samples contain catalyst particles embedded in amorphous carbon, carbon vesicles and amorphous carbon. Though this method presents itself as a cheap, environmental low-impact alternative, improvements are required in order to obtain high yields, compete with other methods such as CVD or arc-discharge, and make this method of commercial significance.

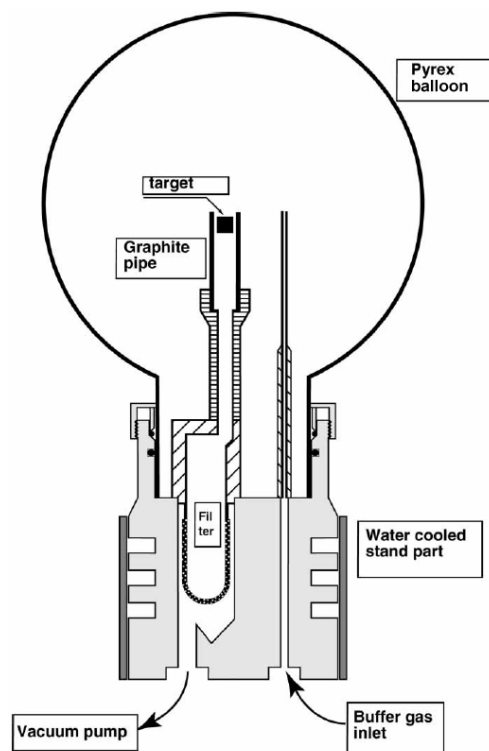


**Figure A.1.6. Schematic of a solar reactor for synthesis of carbon nanotubes.** A Pyrex water-cooled spherical chamber encloses a graphite rod (target) made of a mixture of graphite and a catalyst (4 at. % Ni or 2 at. % Ni and Co), which is located at the center of the chamber. The reactor is evacuated with either argon or nitrogen ( $P = 450 \text{ hPa}$  to  $550 \text{ hPa}$ , flow rate:  $0.2 \text{ m}^3/\text{h}$ ), obtaining in the last case nitrogen-doped nanotubes. Peak solar flux at the focus:  $1600 \text{ kW}/\text{m}^2$ . Samples are collected at the graphite pipe [31].

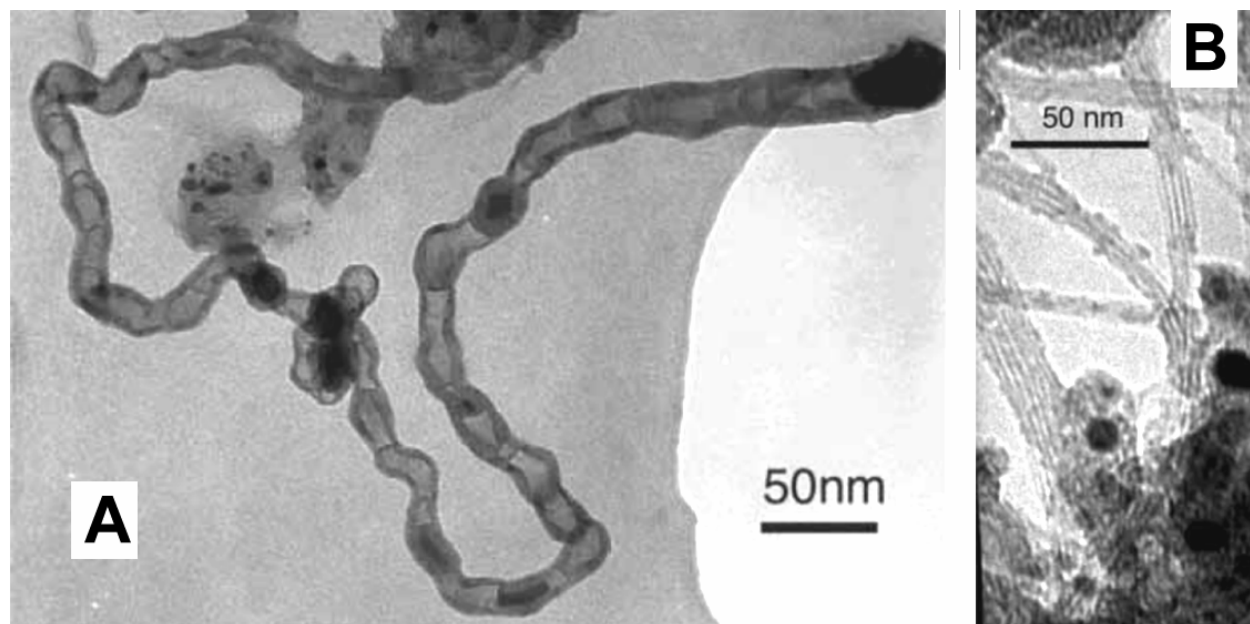


**Figure A.1.7. Carbon nanotubes synthesized by solar energy.** (A) Nitrogen-doped MWNTs showing a compartmentalized structure and encapsulated catalyst particles. (B) Bundles of SWNTs grown from catalyst particles [31].

### Natural lava as supporting catalyst

Another uncommon procedure involves the use of volcanic lava as supporting catalyst for carbon nanotube synthesis [32]. Lava from Mt. Edna contains 11 wt %  $\text{Fe}_2\text{O}_3$  and 48 wt %  $\text{SiO}_2$ , and is first grounded in a mortar and reduced with flowing hydrogen (50 mL/min) in a vertical quartz reactor at 700 °C for 2 h. Next, an ethylene/ $\text{H}_2$  flow (200 mL/min, 1:1 wt % ethylene/ $\text{H}_2$  ratio) is kept for 2 h at 700 °C. Synthesized carbon nanotubes (<10 nm d., [figure A.1.8](#)) show characteristic Raman bands at  $1350\text{ cm}^{-1}$  and  $1560\text{ cm}^{-1}$ . This method, upon better control of experimental conditions, may represent a non-expensive alternative to large-scale production of carbon nanostructures.

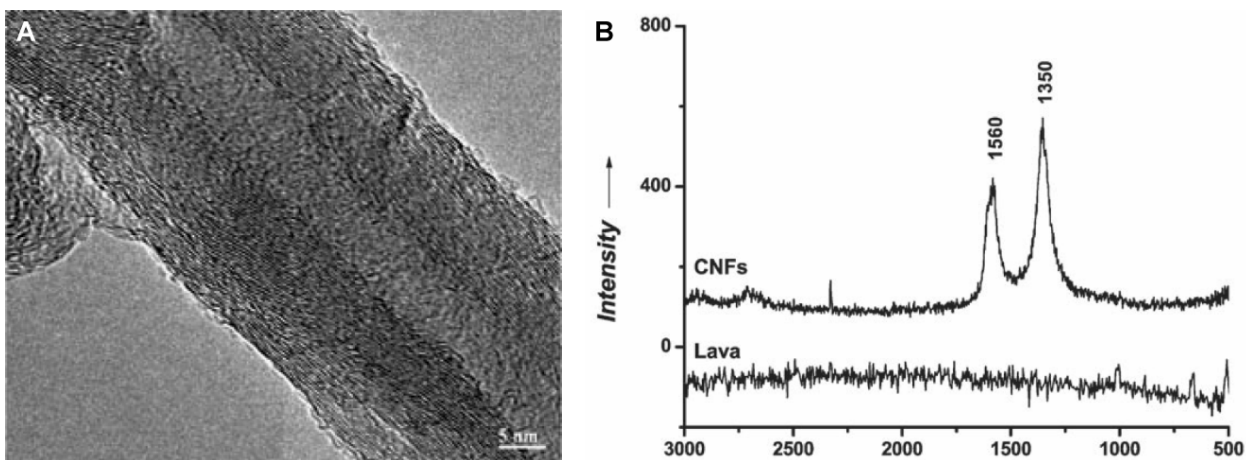


**Figure A.1.8. MWNTs grown on lava.** (A) TEM micrograph of a carbon nanotube showing parallel multi-walled structure, grown on ground lava stones powder after decomposition of ethylene. Scale bar: 5 nm. (B) Raman spectra of lava stones before and after CVD, covered with carbon nanotubes and nanofibers [32].



## References

- [1] M. S. Dresselhaus, G. Dresselhaus, R. Saito. Physics of carbon nanotubes. *Carbon* **33** (1995) 883-891.
- [2] M. K. Song, S. D. Hong, K. T. No. The structure of lithium intercalated graphite using an effective atomic charge of lithium. *J. Electrochem. Soc.* **148** (2001) A1159-A1163.
- [3] G. Gao, T. Cagin, W. A. Goddard. Energetics, structure, mechanical and vibrational properties of single walled carbon nanotubes (SWNT), in: *Fifth Foresight Conference on Molecular Nanotechnology*, Palo Alto, CA, USA, November 5-8, 1997. Foresight Institute.
- [4] I. Lukovits, F. H. Kármán, P. M. Nagy, E. Kálmán. Aromaticity of carbon nanotubes. *Croat. Chem. Acta* **80** (2007) 233-237.
- [5] M. Ahlskog, R. J. M. Vullers, E. Seynaeve, C. Van Haesendonck, A. Fonseca, J. B. Nagy. Conductivity measurement of catalytically synthesized carbon nanotubes. *Science and applications of nanotubes*. D. Tománek and R. J. Enbody (eds). Kluwer Academic Publishers: New York, 2000; pp 349-354.
- [6] M. E. Itkis, F. Borondics, A. Yu, R. C. Haddon. Thermal conductivity measurements of semitransparent single-walled carbon nanotube films by a bolometric technique. *Nano Lett.* **7** (2007) 900-904.
- [7] M-F. Yu, B. S. Files, S. Arepalli, R. S. Ruoff. Tensile loading of ropes of single wall carbon nanotubes and their mechanical properties. *Phys. Rev. Lett.* **84** (2000) 5552-5555.
- [8] M-F. Yu, O. Lourie, M. J. Dyer, K. Moloni, T. F. Kelly, R. S. Ruoff. Strength and breaking mechanism of multiwalled carbon nanotubes under tensile load. *Science* **287** (2000) 637-640.
- [9] C. M. Evans, B. J. Landi, R. Raffaele, I. Krainsky, S. Bailey, G. Landis. Thermoelectric and thermionic emission properties of carbon nanotubes, in: *2nd International Energy Conversion Engineering Conference*, Providence, Rhode Island, August. 16-19, 2004. American Institute of Aeronautics and Astronautics, 5589.
- [10] S. B. Cronin, A. K. Swan, M. S. Ünlü, B. B. Goldberg, M. S. Dresselhaus, M. Tinkham. Measuring the uniaxial strain of individual single-wall carbon nanotubes: resonance Raman spectra of atomic-force-microscope modified single-wall nanotubes. *Phys. Rev. Lett.* **93** (2004) 167401.
- [11] P. Kim, L. Shi, A. Majumdar, P. L. McEuen. Thermal transport measurements of individual multiwalled nanotubes. *Phys. Rev. Lett.* **87** (2001) 215502.
- [12] S. Berber, Y-K. Kwon, D. Tománek. Unusually high thermal conductivity of carbon nanotubes. *Phys. Rev. Lett.* **84** (2000) 4613-4616.
- [13] C. Yu, L. Shi, Z. Yao, D. Li, A. Majumdar. Thermal conductance and thermopower of an individual single-wall carbon nanotube. *Nano Lett.* **5** (2005) 1842-1846.
- [14] N. M. Pugno. Macroscopic invisible cables. *Microsyst. Technol.* **15** (2009) 175-180.
- [15] S. Iijima, T. Ichihashi. Single-shell carbon nanotubes of 1-nm diameter. *Nature* **363** (1993) 603-605.
- [16] M. Terrones. Carbon nanotubes: synthesis and properties, electronic devices and other emerging applications. *Int. Mater. Rev.* **49** (2004) 325-377.

- [17] R.B. Mathur, S. Seth, C. Lal, R. Rao, B.P. Singh, T.L. Dhami, A.M. Rao. Co-synthesis, purification and characterization of single- and multi-walled carbon nanotubes using the electric arc method. *Carbon* **45** (2007) 132-140.
- [18] C. Journet, W. K. Maser, P. Bernier, A. Loiseau, M. Lamyde la Chapelle, S. Lefrant, P. Deniard, R. Leek, J. E. Fischer. Large-scale production of single-walled carbon nanotubes by the electric-arc technique. *Nature* **388** (1997) 756-758.
- [19] M. Haluška, V. Skákalová, D. Carroll, S. Roth. The influence of sulfur promoter on the production of SWCNTs by the arc-discharge process, in: AIP Conference Proceedings, *Electronic Properties of Novel Nanostructures*, American Institute of Physics, New York, 2005, 87-91.
- [20] S. Seraphin, D. Zhou. Single-walled carbon nanotubes produced at high yield by mixed catalysts. *Appl. Phys. Lett.* **64** (1994) 2087-2089.
- [21] A. Chambers, N. M. Rodriguez, R. T. K. Baker. Modification of the catalytic behavior of cobalt by the addition of copper. *J. Phys. Chem.* **99** (1995) 10581-10589.
- [22] W.K. Maser, J.M. Lambert, P.M. Ajayan, O. Stephan, P. Bernier. Role of Y-Ni-B mixtures in the formation of carbon nanotubes and encapsulation into carbon clusters. *Synthetic. Met.* **77** (1996) 243-247.
- [23] S. Bandow, S. Asaka, X. Zhao, Y. Ando. Purification and magnetic properties of carbon nanotubes. *Appl. Phys. A* **67** (1998) 23-27.
- [24] B. Hornbostel, M. Haluska, J. Cech, U. Dettlaff, S. Roth. Arc discharge and laser ablation synthesis of singlewalled carbon nanotubes. *Carbon nanotubes: from basic research to nanotechnology*. V. N. Popov and P. Lambin (eds). Springer: Dordrecht, The Netherlands, 2006; pp 1-18.
- [25] J. M. Alford, G. R. Mason, D. A. Feikema. Free fall plasma-arc reactor for synthesis of carbon nanotubes in microgravity. *Rev. Sci. Instrum.* **77** (2006) 074101.
- [26] H. W. Kroto, J. R. Heath, S. C. O'brien, R. F. Curl, R. E. Smalley. C<sub>60</sub>: buckminsterfullerene. *Nature* **318** (1985) 162-163.
- [27] A. Thess, R. Lee, P. Nikolaev, H. Dai, P. Petit, J. Robert, C. Xu, Y. H. Lee, S. G. Kim, A. G. Rinzler, D. T. Colbert, G. E. Scuseria, D. Tománek, J. E. Fischer, R. E. Smalley. Crystalline ropes of metallic carbon nanotubes. *Science* **273** (1996) 483-487.
- [28] T. Guo, P. Nikolaev, A. G. Rinzler, D. Tománek, D. T. Colbert, R. E. Smalley. Self-assembly of tubular fullerenes. *J. Phys. Chem.* **99** (1995) 10694-10697.
- [29] C.D. Scott, S. Arepalli, P. Nikolaev, R. E. Smalley. Growth mechanisms for single-wall carbon nanotubes in a laser-ablation process. *Appl. Phys. A* **72** (2001) 573-580.
- [30] J. Sabbaghzadeh, P. Jafarkhani, S. Dadras, M. J. Torkamany. Synthesis of multi-wall carbon nanotubes by copper vapor laser. *Appl. Phys. A* **94** (2009) 293-297.
- [31] D. Luxembourg, G. Flamant, D. Laplaze, J. L. Sauvajol, S. Enouz, A. Loiseau. Nitrogen-doped carbon nanotubes produced by solar energy. *Fuller. Nanotub. Car. N* **15** (2007) 257-266.
- [32] D. S. Su, X-W. Chen. Natural lavas as catalysts for efficient production of carbon nanotubes and nanofibers. *Angew. Chem. Int. Ed.* **46** (2007) 1823-1824.

## Appendix A.2 Graphite intercalation compounds (GICs)

### A.2.1 Introduction

Intercalation in graphite is not a new phenomenon. In 1841, Schafhäütl observed a great absorption of acids by graphite. In 1932, the structures of some alkali metal-intercalated compounds were elucidated by X-Ray diffraction. Afterwards, in the 1940's and 1950's more detailed studies were performed. The importance of research in intercalated graphitic materials arises not only from the understanding their electronic and vibrational properties, but also from their possible applications, e.g., rechargeable batteries, catalysts, electronic devices, etc. [1, 2].

Graphene is a monolayer of carbon atoms arranged in a 2D honeycomb lattice, and may be considered as the building block of 0D structures such as fullerenes, 1D carbon nanotubes, and 3D graphite [3]. It was thought that graphene should not exist due in part to the works of Landau, Peierls, and Mermin, which stated that thermal fluctuations in 2D crystal lattices would displace atoms in the interatomic distance range. Experiments, performed on non-mesoporous crystals, supported such theories [3]. It was not until 2004 that graphene was discovered [4] by means of simple Scotch-tape mechanical peeling, thus making such theories to collapse.

Graphite [5] is a 3D array of AB stacked, quasi-infinite planes (each called *graphene*) of  $sp^2$  carbon atoms arranged in a hexagonal pattern. Each carbon atom has one  $2s$  orbital and three  $2p$  orbitals which upon hybridization give rise to 3 coplanar  $sp^2$  orbitals and one  $p_z$  orbital perpendicular to the plane. The  $sp^2$  orbitals, with dihedral angles equal to  $120^\circ$ , bind (through  $\sigma$  or sigma bond) to another set of three carbon atoms. The remaining  $p$  orbital binds to another  $p$  orbital, forming a  $\pi$  bond and giving rise to electronic resonance. The  $\pi$  band, close to the Fermi energy level, primarily contributes to graphite's electronic properties. The bond length between vicinal carbon atoms is  $1.421 \text{ \AA}$ , and the interplanar distance is  $3.354 \text{ \AA}$ . When moving from a single, 2D graphene plane to the 3D array of graphite, the number of bonding and antibonding

$\sigma$  and  $\pi$  bands increases. Overlapping of  $\pi$  bands at the Fermi level generates a density of states different from that of 2D graphene (whose value equals zero at the Fermi level). This makes a difference between the semi-metallic and the semi-conducting properties of 3D graphite and 2D graphene, respectively [6]. Graphite is an anisotropic material, since its mechanic and electronic properties are different in the basal plane (parallel) and out of the plane (perpendicular) directions, as a result of the type of predominant interaction (conjugated  $\pi$  orbitals in the plane and among planes). The weak interplanar interaction among planes is responsible for the slipping of graphene flakes, and for the greasy feeling of graphite at the touch, and also for the use of graphite as a lubricant. It also makes possible the intercalation, through diffusion, of several species among graphitic planes, i.e., *electron-donors*, such as alkali metals and lanthanides, and *electron-acceptors*, such as halogens, acids and other electrophilic molecules [1, 2, 5].

During the intercalation process several species may be intercalated, leading to the formation of binary, ternary or quaternary intercalated compounds: acids ( $\text{H}_2\text{SO}_4$ ,  $\text{HNO}_3$ ), alkali metals (Na, K, Li, Ca, Rb, or Cs), salts ( $\text{CoCl}_2$ ,  $\text{FeCl}_3$ ), ammonia, or organic solvents (tetrahydrofuran, carbonates), etc. Co-intercalated species will contribute to the spacing among graphitic layers [2]. Typical intercalation procedures include [2, 7-11]: simple mixing of graphite with fused alkali metals or salts, two-zone vapor transport technique (bulb method), electrochemical intercalation from solutions, sonication, or mixing of the graphitic material with a solution of the alkali metal in liquid ammonia. Due to the reactive nature of the intercalants, all reactions should take place under inert atmosphere, i. e., argon or nitrogen. The choice of the intercalation method will strongly depend on the chemical and physical properties of the intercalants and the graphitic hosting material.

Graphite intercalated compounds (GICs) may be defined by the *intercalation number* ( $n$ ), which refers to the number of carbon layers among the closest intercalant layers [1, 2, 12]. The intercalation number is not a fixed chemical property of GICs, but a physical consequence of the energy and entropy balance of the interacting intercalated layers [12]. GICs possess several stoichiometries, e.g.,  $\text{LiC}_{27}$ ,  $\text{LiC}_{18}$  or  $\text{LiC}_6$ , in which GICs with lower subindex number have a greater amount of intercalant. As an example, the intercalation of lithium in graphite is schematized at figure A.2.1.

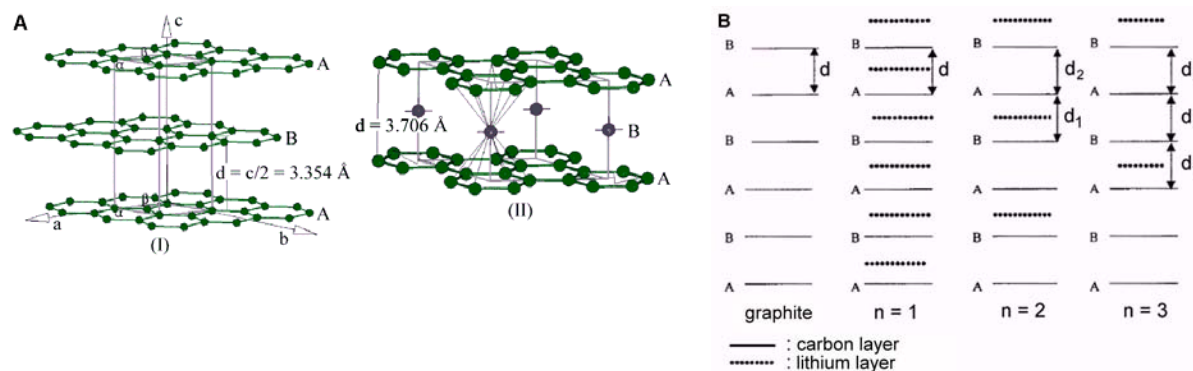


**Figure A.2.1. Lithium intercalation in graphite.** (A) (I) Simplified crystalline hexagonal structure of graphite showing the AB stacking and the unit cell, and (II) structure of a GIC with  $\text{LiC}_6$  stoichiometry ( $n=1$ ) and stacking sequence ABA, where B corresponds to the lithium intercalated layer [13]. (B) Intercalation scheme in graphite, where  $d$  corresponds to the average interplanar distance of graphite,  $d_1$ , with intercalated lithium;  $d_2$ , without intercalated lithium and alternated with  $d_1$  [12].

Non-intercalated graphite [12] (figure A.2.1AI) shows carbon layers alternated through a  $c$  axis, and shifted in the basal plane direction (AB stacking). Once intercalation occurs, graphitic planes align each other (AA stacking) due to interaction of carbon atoms with the intercalant (figure A.2.1AII). Intercalant layers may be alternated with 1, 2, 3 or more graphitic layers, giving rise to the mentioned intercalation number (figure A.2.1AB). The interplanar distance ( $d_{002}$ ) will depend on the amount of intercalant, i.e., on the stoichiometry, and will increase with the amount of intercalant. It should be pointed out that the interplanar distance is a pondered average distance from all the values present at the unit cell, which vary according to the intercalation number. The enthalpy of formation of GICs will also be a function of such stoichiometry. For example, it has been calculated [14] from experimental data an  $E_F$  value of  $-17 \text{ kJ/mol}$  for  $\text{LiC}_{12}$  ( $n=2$ ) and of  $-11 \text{ kJ/mol}$  for  $\text{LiC}_6$  ( $n=1$ ), which indicates a greater repulsion among lithium atoms for  $n=1$ , and that  $\text{LiC}_{12}$  is energetically more stable than  $\text{LiC}_6$ . The increased negative value may be due to the fact that graphite networks with higher number of benzene rings are more stable due to resonance, thus accepting fewer electrons than a network with a lower number of benzene rings. GICs are classified according to their electronic properties and structural arrangements defined by the type of intercalant. The electronic interaction between carbon and intercalant, although having a covalent and metallic character, is primarily ionic such as in the case of alkali metals [1].

## A.2.2 Ternary and higher order GICs

Ternary GICs with the general formula  $KC_{24}(NH_3)_x$  were first prepared in 1954. One of the early jobs [15] on ternary intercalation compounds reports the suppression of diamagnetism in graphite upon sodium intercalation (3 wt%), attributed to the formation of a ternary lamellar compound with chemisorbed. Several studies on these compounds have revealed key features, such as the presence of these compounds as monolayers in graphite, conductivity, structural changes, and the type of rotation of intercalated ammonia molecules. It has also been found that stoichiometry affects conductivity, for example, potassium-ammonia GICs show a transition from metal to non metal when the ammonia fraction increases from  $x = 4$  to  $x = 4.5$  [16]. Binary compounds exposed to hydrogen may change their structure to a ternary GIC. The introduced hydrogen behaves as an electron acceptor, e. g., in  $C_8K$ . As a result, the 1s band becomes partially filled upon accepting charge from the potassium 4s band and the graphitic  $\pi^*$  band, and electronic features such as Hall effect and transverse magnetoresistance arise [17]. Total charge transfer from alkali metals to graphite occurs in binary compounds. In contrast, in ternary GICs, upon introduction of a more electronegative intercalant, charge transfer is not complete, as has been predicted by first-principles density-functional theory studies on  $\beta$ - $K_4SC_{12}$  [18], and confirmed in  $KHgC_x$  compounds by measuring core electron binding energies in  $KHgC_8$  and  $KHgC_4$  [19], which suggest increasing occupancy of K valence orbitals or of hybridized valence states with significant K character. Lithium may also be co-intercalated with calcium [20] by mixing their liquid alloy with pyrographite at  $< 350$  °C; an important parameter is the alloy composition, if too much lithium is used, only a binary GIC will be obtained.  $Ta_2S_2C$  can be obtained [8] from mixing stoichiometric amounts of each element followed by a several-days long heating process in a sealed silica tube under vacuum at high temperatures; the resulting intercalated product is composed of stacked layers of S-Ta-C-Ta-S. Ternary intercalation compounds obtained from mixing graphite with fluoride and fluoride compounds [21] such as  $AsF_5$ ,  $BF_3$ ,  $PF_5$  resulted in graphite salts  $C_8AsF_6$ ,  $C_8BF_4$ ,  $C_{12}PF_6$ , which were used as anion-exchange resins highly resistant towards strong acids and oxidizers.

Binary GICs may be turned into ternary GICs upon exposition to a co-intercalating solvent, such as THF. In this way,  $\text{Cs}(\text{THF})_{1.3}\text{C}_{24}$  and  $\text{K}(\text{THF})_{2.5}\text{C}_{24}$  ternary compounds (figure A.2.2) have been synthesized [22]. Moreover, electrochemical co-intercalation of solvents such as propylene carbonate [23] as co-intercalant with lithium can be detected by Raman spectroscopy, which shows a characteristic doublet close to -

the G band, and a change from doublet to singlet for the G' band, which denotes a change in stacking [24].

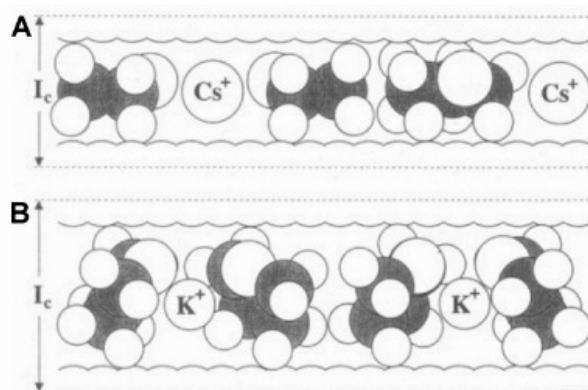


**Figure A.2.2. Proposed schematic for  $\text{Cs}(\text{THF})_{1.2}\text{C}_{24}$  and  $\text{K}(\text{THF})_{2.5}\text{C}_{24}$  in accordance to simulations of proton NMR spectra. The distance between intercalant layers, determined by X-ray diffraction, is (A) 7.1 Å and (B) 8.9 Å [22].**

### A.2.3 The intercalation of ammonia

The first works on ammonia co-intercalation were performed by Rüdorff and co-workers [2]. Research on ammonia intercalation has focused on studies of intercalated ammonia layers [25], calculus of properties [16], intercalation of ammonia under harsh conditions such as high pressures [26]. To intercalate ammonia in graphite it is necessary to create hydrogen bonds between the carbon atoms and the ammonia molecules. One approach consists in exposing exfoliated graphite oxide (4.92 Å) to ammonia [27, 28]. Epoxy and hydroxyl functional groups generated at the basal plane and carboxylic acid groups at the borders allow the absorption of dry ammonia (2.9 Å), which is enhanced by the presence of moisture on the surface of GO. On the other hand, if water (2.8 Å) is present in the challenge gas, it will be preferentially absorbed through competition with  $\text{NH}_3$  for active sites. Intercalation of ammonia may be confirmed by FT-IR spectroscopy, which shows: N-H stretching ( $1000\text{ cm}^{-1}$ ), adsorption or ammonia/intercalation ( $600\text{-}1700\text{ cm}^{-1}$ ), and  $\text{NH}_4^+$  ( $3000\text{-}3300\text{ cm}^{-1}$  and  $1300\text{ cm}^{-1}$ ).

## A.2.4 Characterization techniques for GICs

Characterization of GICs [2] includes methods such as visual inspection of color, weight uptake, chemical analysis, electron microscopy, and diffraction measurements. Sample color observed by visual inspection gives qualitative information on the stage: stage 1 alkali metal compounds show a yellow, gold or red color; stage 2 compounds, steel blue; stage 3, dark blue; higher stages, graphite-metallic. In addition, we can determine by direct chemical analysis the chemical formula for the intercalation compounds, and gravimetric measurements also give information about the sample stage if the chemical formula of the compound is known and stoichiometry is assumed. Nonetheless, these methods are qualitative because of sample inhomogeneity, the presence of intercalate vacancies and the preferential accumulation of intercalants near to crystal defects.

On the other hand, electron microscopy techniques and x-ray diffraction are key tools [2] for the study of GICs. Transmission electron microscopy (TEM) provides information on the structure of the intercalated compound, gives direct evidence of defects, dislocations, exfoliation in graphitic layers, and allows the measurement of interlayer expansion. Additional information can be obtained through scanning electron microscopy (SEM) and scanning transmission electron microscopy (STEM); for example, microcrack formation as a result of intercalation, and important structural changes in multi-walled carbon nanotubes such as exfoliation [9] as a result of expulsion of intercalants. X-ray diffraction studies [2] give information about the stage index, stage fidelity, and in-plane order. Stage fidelity occurs when there are no satellite diffraction peaks due to admixed stages, and by accurate distinction between stages  $n$  and  $n + 1$ . Moreover, sharp diffraction peaks at large diffraction angles evidences that samples are single staged, and not an average over a distribution of stages. The opposite happens when stage infidelity appears. For example, a mixed stage sample contains macroscopic regions that show stage  $n$  and other regions with stages  $n + 1$  or  $n - 1$ . Some reflections may be broadened relative to those from a single-staged sample; others can be identified with each constituent of the sample, while others are shifted due to unresolved components. In the case of randomly staged materials, various stages will be present in

the random arrangement of regions. Only dominant stages will show well-defined diffraction patterns but with reflections showing extensive line broadening. Analysis of the intensity of the (00l) reflections can also approximately determine the stage number, by relating the square root of the observed intensities to the magnitude of the structure factor. Since the structure factor determines the relative intensity of the (00l) reflections, the index l of the reflection with maximum peak intensity (00l̂) approximately determines the stage number.

Other characterization methods have become useful for the study of lithium intercalated graphitic compounds, starting from the introduction of lithium-ion rechargeable batteries in 1990 by Sony [29]. These methods, which are often combined [24, 30], include: Raman spectroscopy [2], nuclear magnetic resonance [22], x-ray photoelectron spectroscopy (XPS) [31-33]. Electrochemical methods such as cyclic voltammetry and electrochemical impedance spectroscopy allow the determination of capacity [10, 30, 34-36], the study of kinetics during lithium intercalation [37, 38]. When tracing of very small amounts of intercalated lithium is needed, other techniques used in the detection of lithium are: lithium nuclear magnetic resonance (<sup>7</sup>Li NMR) [39], near-edge x-ray absorption fine structure (NEXAFS, also called x-Ray absorption near-edge structure or XANES) [40], electron-energy loss spectroscopy (EELS) [41, 42], electron spin resonance (ESR) [43, 44], and Auger electron spectroscopy (AES) [45, 46]. Additionally, changes caused by intercalants may be followed by dilatometric techniques in order to discern between solvated and unsolvated lithium intercalation and deintercalation in graphite, and to have a better knowledge on the expansion/contraction mechanism of graphite when used as anode in lithium-ion batteries [47].



## References

- [1] J. E. Fischer, T. E. Thompson. Graphite intercalation compounds. *Phys. Today* **31** (1978) 36-45.
- [2] M. S. Dresselhaus, G. Dresselhaus. Intercalation compounds of graphite. *Adv. Phys.* **51** (2002) 1-186.
- [3] A. K. Geim, K. S. Novoselov. The rise of graphene. *Nat. Mater.* **6** (2007) 183-191.
- [4] K. S. Novoselov, A. K. Geim, S. V. Morozov, D. Jiang, Y. Zhang, S. V. Dubonos, I. V. Grigorieva, A. A. Firsov. Electric field effect in atomically thin carbon films. *Science* **306** (2004) 666-669.
- [5] D. D. L. Chung. Review graphite. *J. Mater. Sci.* **37** (2002) 1475-1489.
- [6] M. Caragiu, S. Finberg. Alkali metal adsorption on graphite: A review. *J. Phys.: Condens. Matter* **17** (2005) R995-R1024.
- [7] A. K. Ibrahim, G. O. Zimmerman. Magnetic properties of graphite intercalation compounds. *Phys. Rev. B* **35** (1987) 1860-1868.
- [8] R. Brec, J. Ritsma, G. Ouvrard, J. Rouxel. Alkali metal intercalates of  $Ta_2S_2C$ . *Inorg. Chem.* **16** (1977) 660-665.
- [9] A. Cano-Márquez, F. Rodríguez-Macías, J. Campos, C. Espinosa-González, F. Tristán, D. Ramírez-González, D. Cullen, D. Smith, M. Terrones, Y. Vega-Cantú. Ex-MWNTs: Graphene sheets and ribbons produced by lithium Intercalation and exfoliation of carbon nanotubes. *Nano Lett.* **9** (2009) 1527-1533.
- [10] G. Maurin, Ch. Bousquet, F. Henn, P. Bernier, R. Almaira, B. Simon. Electrochemical lithium intercalation into multiwall carbon nanotubes: a micro-Raman study. *Solid State Ionics* **136-137** (2000) 1295-1299.
- [11] J. E. Jones, M. C. Cheshire, D. J. Casadonte Jr., C. C. Phifer. Facile sonochemical synthesis of graphite intercalation compounds. *Org. Lett.* **6** (2004) 1915-1917.
- [12] M. K. Song, S. D. Hong, K. T. No. The structure of lithium intercalated graphite using an effective atomic charge of lithium. *J. Electrochem. Soc.* **148** (2001) A1159-A1163.
- [13] K. R. Kganyago, P. E. Ngoepe. Structural and electronic properties of lithium intercalated graphite  $LiC_6$ . *Phys. Rev. B* (2003) 205111.
- [14] Y. Reynier, R. Yazami, B. Fultz. The entropy and enthalpy of lithium intercalation into graphite. *J. Power Sources* **119-121** (2003) 850-855.
- [15] W. C. Sleppy. Reaction of sodium with graphite at 400°. *Inorg. Chem.* **5** (1966) 2021-2023.
- [16] L. Bernasconi, P. A. Madden. Structure and short timescale ion dynamics of potassium-ammonia graphite intercalation compounds. *Phys. Chem. B* **106** (2002) 1161-1172.
- [17] K. Nakazawa, K. Suzuki, T. Enoki. Hall effect in potassium-hydrogen-graphite intercalation compounds and their conduction mechanism. *Phys. Rev. B* **46** (1992) 16106-16114.
- [18] A. Rodríguez-Forteza, C. Rovira, P. Ordejón, C. Héroid, P. Lagrange, E. Canadell. Electronic Structure and Charge Transfer in the Ternary Intercalated Graphite  $\beta$ - $KS_{0.25}C_3$ . *Inorg. Chem.* **45** (2006) 9387-9393.

- [19] S. B. DiCenzo, P. A. Rosenthal. Valence bands of  $\text{KHgC}_4$  and  $\text{KHgC}_8$ . *Phys. Rev. B* **34** (1986) 3620-3624.
- [20] S. Pruvost, C. Hérold, A. Hérold, P. Lagrange. Co-intercalation into graphite of lithium and sodium with an alkaline earth metal. *Carbon* **42** (2004) 1825-1831.
- [21] K. O. Christe, R. D. Wilson. Anion exchange in tetrafluoroammonium salts using graphite salts as an oxidizer and acid-resistant anion-exchange medium. *Inorg. Chem.* **28** (1989) 4175-4177.
- [22] C. Schmidt, M. E. Rosen, D. F. Caplan, A. Pines, M. F. Quinton. Orientation and motion of tetrahydrofuran in graphite intercalation compounds: Proton NMR studies of  $\text{Cs}(\text{THF})_{1.3}\text{C}_{24}$  and  $\text{K}(\text{THF})_{2.5}\text{C}_{24}$ . *J. Phys. Chem.* **99** (1995) 10565-10572.
- [23] J. O. Besenhard, M. Winter, J. Yang, W. Biberacher. Filming mechanism of lithium-carbon anodes in organic and inorganic electrolytes. *J. Power Sources* **54** (1995) 228-231.
- [24] H-L. Zhang, C-H. Sun, F. Li, C. Liu, J. Tan, H-M. Cheng. New insight into the interaction between propylene carbonate-based electrolytes and graphite anode material for lithium ion batteries. *J. Phys. Chem. C* **111** (2007) 4740-4748.
- [25] X. W. Qian, D. R. Stump, S. A. Solin. Structural properties of potassium-ammonia liquids in graphite. *Phys. Rev. B* **33** (1986) 5756-5769.
- [26] X. W. Qian, S. A. Solin. Staging properties of potassium-ammonia ternary graphite intercalation compounds at high ammonia pressure. *Phys. Rev. B* **39** (1989) 8707-8714.
- [27] M. Seredych, T. J. Bandosz. Mechanism of ammonia retention on graphite oxides: Role of surface chemistry and structure. *J. Phys. Chem. C* **111** (2007) 15596-15604.
- [28] M. Seredych, T. J. Bandosz. Removal of ammonia by graphite oxide via its intercalation and reactive adsorption. *Carbon* **45** (2007) 2130-2132.
- [29] B. Scrosati. Challenge of portable power. *Nature* **373** (1995) 557-558.
- [30] M. Wang, Z. H. Li, G. T. Wu. Electrochemical lithium insertion properties of carbon nanotubes produced by catalytic pyrolysis of acetylene. *Russ. J. Electrochem.* **41** (2005) 946-949.
- [31] K. Kanamura, S. Shiraishi, H. Takezawa, Z. Takehara. XPS analysis of the surface of a carbon electrode intercalated by lithium ions. *Chem. Mater.* **9** (1997) 1797-1804.
- [32] V. Z. Mordkovich. Synthesis and XPS investigation of superdense lithium-graphite intercalation compound,  $\text{LiC}_2$ . *Synthetic Met.* **80** (1996) 243-247.
- [33] H. Momose, H. Honbo, S. Takeuchi, K. Nishimura, T. Horiba, Y. Muranaka, Y. Kozono, H. Miyadera. X-ray photoelectron spectroscopy analyses of lithium intercalation and alloying reactions on graphite electrodes. *J. Power Sources* **68** (1997) 208-211.
- [34] H. Zheng, K. Jiang, T. Abe, Z. Ogumi. Electrochemical intercalation of lithium into a natural graphite anode in quaternary ammonium-based ionic liquid electrolytes. *Carbon* **44** (2006) 203-210.
- [35] K. Hanai, Y. Liu, T. Matsumura, N. Imanishi, A. Hirano, Y. Takeda. Electrochemical behavior of the composite anodes consisting of carbonaceous materials and lithium transition-metal nitrides for lithium-ion batteries. *Solid State Ionics* **179** (2008) 1725-1730.

- [36] L. Ke-zhi, X. Yan-hui, W. Xiao-lin, L. Guo-hua. Electrochemical intercalation of lithium into raw and mild oxide-treated carbon nanotubes prepared by CVD. *J. Wuhan Univ. Technol.* **19** (2004) 21-25.
- [37] M. M. Kamisah, H. Siti Munirah, M. S. Mansor. Electrochemical impedance study of lithium-ion insertion into rice husk carbon. *Ionics* **13** (2007) 223-225.
- [38] Y. NuLi, J. Yang, Z. Jiang. Intercalation of lithium ions into bulk and powder highly oriented pyrolytic graphite. *J. Phys. Chem. Solids* **67** (2006) 882-886.
- [39] S. Łoś, M. Letellier, P. Azaïs, L. Duclaux. Li doped carbons (activated microporous carbons and graphite): Characterisation by resonance spectroscopies (ESR and  $^7\text{Li}$  NMR) and their potentiality for hydrogen adsorption. *J. Phys. Chem. Solids* **67** (2006) 1182-1185.
- [40] A. Braun, H. Wang, J. Shim, S. S. Lee, E. J. Cairns. Lithium K(1s) synchrotron NEXAFS spectra of lithium-ion battery cathode, anode and electrolyte materials. *J. Power Sources* **170** (2007) 173-178.
- [41] A. Naji, P. Thomas, J. Ghanbaja, D. Billaud. Identification by TEM and EELS of the products formed at the surface of a carbon electrode during its reduction in  $\text{MClO}_4\text{-EC}$  and  $\text{MBF}_4\text{-EC}$  electrolytes (M=Li, Na). *Micron* **31** (2000) 401-409.
- [42] A. Naji, P. Willmann, D. Billaud. Electrochemical intercalation of lithium into graphite: Influence of the solvent composition and of the nature of the lithium salt. *Carbon* **36** (1998) 1347-1352.
- [43] T. Takenobu, T. Muro, Y. Iwasa, T. Mitani. Antiferromagnetism and phase diagram in ammoniated alkali fulleride salts. *Phys. Rev. Lett.* **85** (2000) 381-384.
- [44] Y. Matsumura, S. Wang, Y. Nakagawa, C. Yamaguchi. An electron-spin resonance study of lithium charged carbon electrodes. *Synthetic Met.* **85** (1997) 1411-1412.
- [45] Z. P. Hu, A. Ignatiev. Lithium adsorption on the graphite (0001) surface. *Phys. Rev. B* **30** (1984) 4856-4859.
- [46] J. S. Murday, B. I. Dunlap. Carbon KVV Auger line shapes of graphite and stage-one cesium and lithium intercalated graphite. *Phys. Rev. B* **24** (1981) 4764-4770.
- [47] M. Winter, G. H. Wrodnigg, J. O. Besenhard, W. Biberacher, P. Novák. Dilatometric investigations of graphite electrodes in nonaqueous lithium battery electrolytes. *J. Electrochem. Soc.* **147** (2000) 2427-2431.



## **Appendix A.3 Experimental conditions and exfoliation data**



Table A.3.1. Experimental conditions for composites.

| Experiment       |  |   |
|------------------|--|---|
| Code             | Reaction   | Notes   |
| CNx-PoASA-SN-01  | CN <sub>x</sub> = 10 mg<br>Li = 200 mg<br>oASA = 1115.3 mg<br>V <sub>NH<sub>3</sub></sub> = 125 mL * | Addition: (1) Li, (2) oASA, (3) oASA. oASA monomer (a dust) was heated at 60 °C in a gravity oven prior to use. After reaction, water, ethanol and 10% HCl were carefully added.<br>* Approximate volume, for experiments 1 to 10.  |
| CNx-PoASA-SN-02  | CN <sub>x</sub> = 11.5 mg<br>Li = 231 mg<br>oASA = 1115.3 mg   | Pyrrole was bi-distilled prior to use.  |
| CNx-PPy-SN-03    | CN <sub>x</sub> = 11.5 mg<br>Li = 231 mg<br>Py = 1.2 mL ≈ 1159.2 mg                                  |   |
| CNx-PAni-SN-04   | CN <sub>x</sub> = 11.5 mg<br>Li = 230 mg<br>Ani = 1.2 mL ≈ 1225.2 mg                                 |   |
| MWNT-PPy-05      | MWNTs = 46.1 mg<br>Li = 923 mg<br>Py = 4.8 mL ≈ 4636.8 mg  |   |
| MWNT-PAni-06     | MWNTs = 47.2 mg<br>Li = 933.1 mg<br>Ani = ?  |   |
| CNx-PoASA-07     | CN <sub>x</sub> = 46 mg<br>Li = 920 mg<br>oASA = 4410 mg   |   |
| MWNT-PoASA-08    | MWNTs = 54.7 mg<br>Li = 901.6 mg<br>V <sub>THF</sub> = 140 mL<br>oASA = ?                            | MWNTs and oASA were dried in gravity oven prior to use. Addition: (1) NH <sub>3</sub> , (2) MWNTs dispersed in 30 mL of dry THF by sonication for 25 min, (3) Li, (4) oASA, 5 min homogenization. Magnetic stirring for 5 min and addition of 40 mL of THF  |
| MWNT-PoASA-09    | MWNTs = 45.1 mg<br>Li = 914 mg<br>oASA = 4045.4 mg   | MWNTs were neither dried nor dispersed prior to addition. MWNTs were added in 4 portions, at 1 – 2 min intervals. Homogenization for 5 min, then it was stopped and followed by magnetic stirring. Argon flux was kept for 15 min more, NH <sub>3</sub> was then allowed to evaporate.                  |
| MWNT-PoASA-SN-10 | MWNTs = 51 mg<br>Li = 100 mg<br>oASA = 114.4 mg  | Addition: (1) MWNTs, (2) oASA, (3) Lithium. Homogenization, slow NH <sub>3</sub> evaporation under magnetic stirring.<br>Washing: 5 times with distilled H <sub>2</sub> O and 10% HCl, filtering & washing with CH <sub>3</sub> OH.   |
| MWNT-PoASA-SN-11 | MWNTs = 50.4 mg<br>Li = 108.2 mg<br>oASA = 253 mg  | Addition: (1) MWNTs, (2) lithium. Homogenization, followed by addition of THF (250 mL) to replace NH <sub>3</sub> . Magnetic stirring for 14 h, addition of oASA, T = 50°C, 1 h reaction time.  |
| MWNT-PoASA-SN-12 | MWNTs = 40 mg<br>Li = 103.1 mg<br>oASA = 253.3 mg  | Addition: (1) lithium under magnetic stirring, (2) oASA, (3) MWNTs (sonicated). Reaction time: 4 h 45 min.<br>Washing: CH <sub>3</sub> OH, 5% HCl; filtering and washing with CH <sub>3</sub> CH <sub>2</sub> OH.   |
| MWNT-SN-13       | MWNTs = 53.1 mg<br>Li = 104.1 mg<br>V <sub>THF</sub> = 180 mL  | Addition: (1) MWNTs, (2) lithium. Homogenization: 6 min. Reaction time: 20 h 45 min.<br>Washing: 4 times with CH <sub>3</sub> OH and 5% HCl; filtering and washing with CH <sub>3</sub> OH.   |
| MWNT-PoASA-SN-14 | MWNTs = 50.1 mg<br>Li = 104.1 mg<br>oASA = ? mg  | Addition: (1) MWNTs, 5 min homogenization, (2) lithium, 4 min homogenization, (3) THF. Magnetic stirring for 28 h. Sonication of salts for 5 min, followed by slow addition to reactor loaded with oASA. 5 min homogenization, magnetic stirring for 12 h.<br>Washing: 7 times with CH <sub>3</sub> OH. |
| MWNT-PoASA-SN-15 | MWNTs = 53.2 mg<br>Li = 105 mg<br>oASA = 250 mg  | Addition: (1) MWNTs, 5 min homogenization, (2) lithium, 5 min homogenization. Magnetic stirring, addition of oASA, 5 min homogenization. Slow evaporation.<br>Filtering and washing with CH <sub>3</sub> OH.  |
| MWNT-SN-16       | Li = 105 mg<br>oASA = 250 mg   | Blank experiment. Lithium addition followed by oASA, 5 min homogenization, ammonia was replaced by THF.   |
| MWNT-PoASA-SN-17 | MWNTs = 51.1 mg<br>Li = 127.3 mg<br>oASA = 259.1 mg  | Repetition of exp 15, purified MWNTs. THF = 130 mL. Addition order: MWNTs, Li, homog. (5 min), magnetic stirring, monomer, homog. (5 min), THF, magnetic stirring.<br>Washing: CH <sub>3</sub> OH and 5% HCl, final wash (when filtering) with methanol and acetone.                                    |

Table A.3.1. Experimental conditions for composites (continued).

| Experiment       |   |  |
|------------------|---|--|
| Code             | Reaction  | Notes  |
| MWNT-PoASA-SN-18 | MWNTs = 52.6 mg<br>Li = 102 mg<br>oASA = 254.9 mg<br>V <sub>THF</sub> = 220 mL                                | Addition: (1) MWNTs, 5 min homogenization, (2) lithium, 5 min homogenization, (3) THF as replacement for NH <sub>3</sub> . Magnetic stirring for 16 h.<br>Next day nanotube salts were sonicated for 5 min, and then added under homogenization (total time: 17 min) to a reactor loaded with oASA (previously homogenized for 5 min). Magnetic stirring for 12 h. |
| MWNT-PoASA-SN-19 | MWNTs = 53.1 mg<br>Li = 519.4 mg<br>oASA = 1000.4 mg  | Addition: (1) MWNTs, 6 min homogenization, (2) lithium, (3) oASA, 5 min homogenization. Magnetic stirring up to full evaporation of NH <sub>3</sub> . Washed 14 times.   |
| MWNT-PoASA-SN-20 | MWNTs = 50.1 mg<br>Li = 500 mg<br>oASA = 754.3 mg<br>V <sub>THF</sub> = 120 mL                                | Nanotube salts, after 1 day, were sonicated for 5 min, then added to a reactor with oASA under magnetic stirring. Reaction time: 3 h.<br>Washing: CHCl <sub>3</sub> , HCl.   |
| MWNT-PoASA-SN-21 | MWNTs = 31.8 mg, purified<br>Li = 236.4 mg<br>oASA = 225.43 mg<br>V <sub>THF</sub> = 120 mL                   | Addition: (1) MWNTs, 5 min homogenization, (2) lithium, (3) oASA (previously sonicated for 3 min in dry THF), 5 min homogenization. Magnetic stirring for 1 day.<br>Washing: 5 to 7 times with toluene and 0.5 M or 5 % HCl 1:1 (30 to 50 mL). SAME CONDITIONS FOR EXPERIMENTS 21 – 37   |
| MWNT-PoASA-SN-22 | MWNTs = 25.7 mg<br>Li = 228 mg<br>oASA = 100 mg   | Organic phase acquired brownish color maybe due to oligomers.  |
| MWNT-PoASA-SN-23 | MWNTs = 30.4 mg<br>Li = 227.8 mg<br>oASA = 26.4 mg  | Left overnight for full evaporation of NH <sub>3</sub> . Washed 4 times.   |
| MWNT-PoASA-SN-24 | MWNTs:oASA 50:50 (wt./wt.)<br>MWNTs = 29.5 mg<br>Li = 233 mg<br>oASA = 27 mg<br>V <sub>THF</sub> = 120 mL     | Addition: (1) Li, 3 min homogenization, (2) MWNTs, 5 min homogenization, (3) THF, magnetic stirring overnight. Next day: addition of nanotube salts to oASA (previously dispersed in THF) under homogenization. Reaction time: 4 h, 20 min.<br>First washing: aqueous phase slightly colored green. Organic phase: gray.   |
| MWNT-PoASA-SN-25 | MWNTs:oASA 30:70 (wt./wt.)<br>MWNTs = 27.2 mg<br>Li = 228.3 mg<br>oASA = 59.2 mg<br>V <sub>THF</sub> = 130 mL |  |
| MWNT-PoASA-SN-26 | MWNTs:oASA 60:40 (wt./wt.)<br>MWNTs = 26.4 mg<br>Li = 229.9 mg<br>oASA = 16.8 mg<br>V <sub>THF</sub> = 130 mL |  |
| MWNT-PoASA-SN-27 | MWNTs:oASA 80:20 (wt./wt.)<br>MWNTs = 28.6 mg<br>Li = 228.0 mg<br>oASA = 6.9 mg<br>V <sub>THF</sub> = 100 mL  |  |
| MWNT-PoASA-SN-28 | MWNTs:oASA 70:30 (wt./wt.)<br>MWNTs = 27.7 mg<br>Li = 229.1 mg<br>oASA = 11.8 mg<br>V <sub>THF</sub> = 125 mL |  |
| MWNT-PoASA-SN-29 | MWNTs:oASA 90:10 (wt./wt.)<br>MWNTs = 25.7 mg<br>Li = 229.1 mg<br>oASA = 3 mg<br>V <sub>THF</sub> = 50 mL     |  |
| MWNT-PoASA-SN-30 | MWNTs:oASA 40:60 (wt./wt.)<br>MWNTs = 25.1 mg<br>Li = 229.2 mg<br>oASA = 38.3 mg<br>V <sub>THF</sub> = 120 mL |  |

Table A.3.1. Experimental conditions for composites (continued).

| Experiment      |   |          |                              |
|-----------------|---|----------|------------------------------|
| Code            | Reaction  |          | Notes                        |
| MWNT-PAni-SN-31 | MWNTs:aniline<br>(wt./wt.)<br>MWNTs = 25.4 mg<br>Li = 227 mg<br>Ani = 20 g                                | 0.1:99.9 | Excess aniline monomer used. |
| MWNT-PAni-SN-32 | MWNTs:aniline 50:50 (wt./wt.)<br>MWNTs = 26.7 mg<br>Li = 225 mg<br>Ani = 25.4 g                           |          | Excess aniline monomer used. |
| MWNT-PAni-SN-33 | MWNTs:aniline 70:30 (wt./wt.)<br>MWNTs = 27.2 mg<br>Li = 226 mg<br>Ani = 12.2 mg                          |          |                              |
| MWNT-PAni-SN-34 | MWNTs:aniline 60:40 (wt./wt.)<br>MWNTs = 25.5 mg<br>Li = 227.5 mg<br>Ani = 18.7 mg                        |          |                              |
| MWNT-PAni-SN-35 | MWNTs:aniline 40:60 (wt./wt.)<br>MWNTs = 26.1 mg<br>Li = 228.2 mg<br>Ani = 38.2 mg<br>Composite = 39.2 mg |          |                              |
| MWNT-PAni-SN-36 | MWNTs:aniline 30:70 (wt./wt.)<br>MWNTs = 25.1 mg<br>Li = 227.2 mg<br>Ani = 58.8 mg<br>Composite = 32.8 mg |          |                              |
| MWNT-PAni-SN-37 | MWNTs:aniline 80:20 (wt./wt.)<br>MWNTs = 26.8 mg<br>Li = 226.8 mg<br>Ani = 6.2 mg<br>Composite = 29.5 mg  |          |                              |

**Table A.3.2. Experimental conditions for exfoliation of MWNTs**, summarized in the code name for each experiment.

| Experiment |   |  |   |
|------------|---|--|---|
| No.        | Code  | Intercalation  | Exfoliation   |
| 1          | EXNTs-p_S_THF_120m-N*L*M*_8_10_1-R_HCl30_120m           | Sonication of purified MWNTs for 180 min in 100 mL of dry THF (0.261 mg/mL, ultrasonic tip VCX-500, 6 sec sonication, 3 seconds pause) under N <sub>2</sub> . Addition of metallic Li. Deep blue color in medium, no bronze phase observed. Vigorous magnetic stirring (no. 7, Barnstead), Sonication of MWNTs in THF for 6 min (ultrasonic bath). Addition of MWNTs under N <sub>2</sub> atmosphere. Condensation of ca. 50 mL of NH <sub>3</sub> . Magnetic stirring up to next day without Dewar.<br><b>NH<sub>3</sub>:Li:MWNTs</b> 7.7:9.7:1<br><b>mL:mg:mg</b> 200:254.7:26.1 | Addition of ca. 30 mL of H <sub>2</sub> O to deactivate remaining metallic lithium. Slow addition of 100 mL of 30% HCl under N <sub>2</sub> , followed by 2 hs reflux (30 mL H <sub>2</sub> O + 100 mL 30% HCl, 120 min reflux.) Product washed 5 times with CHCl <sub>3</sub> :5% HCl 1:5, and 3 times with H <sub>2</sub> O until neutral pH was obtained. Wet sample weight (WW) = 31.3 mg, down to 30.5 mg (mass loss due to handling). Dry sample weight (DW) = 30.2 mg. |
| 2          | EXNTs-p-S_THF_120m-N*L*M*_8_10.5_1-S_HCl30_120m         | Same procedure as in experiment 1.<br><b>NH<sub>3</sub>:Li:MWNTs</b> 8:10.5:1<br><b>mL:mg:mg</b> 200:264.9:25.1  | Reactor set in ultrasonic bath, addition of 100 mL of 30% HCl under N <sub>2</sub> (atmosphere kept for 30 min). Sonication (since beginning of HCl addition) for 120 min in 100 mL of 30% HCl. H <sub>2</sub> O added after 85 min of sonication to lower MWNTs from the wall. Same washing procedure as in experiment 1. 8-day stay in desiccator.<br>WW = 28.5 mg, DW = 28.3 mg.   |
| 3          | EXNTs-p-N*L*M*_7_10_2-S_HCl30_120m                      | Sonication used to re-disperse the MWNTs. Condensation of 180 mL of NH <sub>3</sub> . Addition of Li. Condensation continued. Sonication of MWNTs in 50 mL of dry THF for 10 min, followed by addition to reactor. Overnight magnetic stirring in Dewar flask up to next day. Bronze phase observed.<br><b>NH<sub>3</sub>:Li:MWNTs</b> 7.2:10.2:1<br><b>mL:mg:mg</b> 180:255.6:25  | Reactor set in ultrasonic bath, addition of 100 mL of 30% HCl under N <sub>2</sub> . Addition of 50 mL of 5% HCl to lower MWNTs from the wall. Sonication for 120 min. Same washing procedure as in experiment 1. DW = 28.6 mg.   |
| 4          | EXNTs-S+R_HNO3H2SO4_120m-N*L*M*_1_5.4_10-S+R_HCl30_120m | Sonication for 120 min in 154 mL of HNO <sub>3</sub> :H <sub>2</sub> SO <sub>4</sub> 3:1 (0.195 mg/mL). Reflux for 120 min in the same medium. MWNTs washed against H <sub>2</sub> O and dried. Addition order not reported.<br><b>NH<sub>3</sub>:Li:MWNTs</b> 7:10.2:1<br><b>mL:mg:mg</b> 200:308.4:30  | Sonication and reflux for 120 min (each) in 100 mL of 37.5% HCl (not reported). DW = 39 mg.   |
| 5          | CNx-p-S_THF_20m-N*L*C*_4_21_1-S+R_HCl38_120m            | Sonication of purified CN <sub>x</sub> for 20 min in 50 mL of dry THF before addition. First lithium addition after NH <sub>3</sub> condensation (260.4 mg), then CN <sub>x</sub> were added. Addition of the rest of Li after 5 min. Bronze phase observed in small amount. High-speed vigorous magnetic stirring (no. 10). Left in slow magnetic stirring (no. 5). After 5 min 265.7 mg of Li were added.<br><b>NH<sub>3</sub>:Li:CN<sub>x</sub></b> 3.9:20.6:1<br><b>mL:mg:mg</b> 100:526.1:25.5  | Lithium deactivated by 37.5% HCl added under N <sub>2</sub> flux; MWNTs were lowered from the wall with H <sub>2</sub> O. Sonication and reflux for 120 min (each) in 100 mL of 37.5% HCl. After reflux media showed an orange-brown tone. Same washing procedure as in experiment 1. W = 27.8 mg.  |
| 6          | CNx-p-S_THF_120m-N*L*C*_5_21_1-R_HCl38_120m             | Sonication of purified CN <sub>x</sub> for 120 min in 50 mL of dry THF before addition. Gradual lithium addition. High-speed vigorous magnetic stirring (no. 10). Left in slow magnetic stirring (no. 5).<br><b>NH<sub>3</sub>:Li:CN<sub>x</sub></b> 4.7:20.8:1<br><b>mL:mg:mg</b> 120:531:25  | Lithium deactivated by 37.5% HCl added under N <sub>2</sub> flux; MWNTs were lowered from the wall with H <sub>2</sub> O. Reflux for 120 min in 100 mL of 37.5% HCl. After 105 min CN <sub>x</sub> form aggregates. Same washing procedure as in experiment 1. W = 29.2 mg.   |

**Table A.3.2. Experimental conditions for exfoliation of MWNTs (continued)**, summarized in the code name for each experiment.

| Experiment |   |   |  |
|------------|---|---|--|
| No.        | Code  | Intercalation   | Exfoliation  |
| 7          | CNx-p-S_THF_120-<br>S_N*L^C-4_20_1-<br>S+R_HCl38_120&210m                       | Sonication of purified CN <sub>x</sub> for 120 min in 50 mL of dry THF before addition. CN <sub>x</sub> were added after 3 h of Li addition (NH <sub>3</sub> volume was kept constant by continuous condensation).<br><b>NH<sub>3</sub>:Li:CN<sub>x</sub></b> 3.9:19.7:1<br><b>mL:mg:mg</b> 100:503.3:25.6  | Sonication and reflux for 120 and 210 min (respectively) in 100 mL of 37.5% HCl. Same washing procedure as in experiment 1.                              |
| 8A         | EXNTs-r4ms-<br>S_HNO3_120m-<br>N*L*M_10_10_1-<br>S+R_HCl37_15+120m              | Non-purified 4 min CVD synthesis MWNTs, sonicated in 100 mL of concentrated HNO <sub>3</sub> for 30 min; next, reflux was started but was stopped because of quick exothermic decomposition. Reactor allowed to cool down. Sonication performed for 90 min. MWNTs washed with CHCl <sub>3</sub> /H <sub>2</sub> O, then twice with 1 M NaOH (100 and 150 mL). Alkaline phase: Deep green at first wash. Addition order not specified.<br><b>NH<sub>3</sub>:Li:MWNTs</b> 10.1:10.4:1<br><b>mL:mg:mg</b> 250:257:24.8       | Sonication and reflux for 15 and 120 min (respectively) in 100 mL of 37.2% HCl. Product washed with CHCl <sub>3</sub> /H <sub>2</sub> O.<br>W = 25.3 mg. |
| 8B         | EXNTs-r4ms-<br>S_HNO3_120m-<br>N*L*M_10_10_1-<br>S+R_HCl37_15+120m-<br>TT_30m   |   | Sonication and reflux (specified above), sudden thermal treatment at 950 °C for 30 min.  |
| 9A         | EXNTs-Cp12hs-<br>N*M*L_8_10.5_1-<br>S+R_HCl37_15+120m                           | Sonication of MWNTs (200 mg) for 12 hs in HNO <sub>3</sub> :H <sub>2</sub> SO <sub>4</sub> 3:1, taken to separatory funnel and filtered. Sonicated in H <sub>2</sub> O for 30 min. pH = 5. Filtration and washing with 100 mL of 1 M NaOH. Alkaline phase: Yellow. Sonication in 100 mL of the same solution for 10 min, followed by filtration and washing with H <sub>2</sub> O until neutral pH. Very fine material in filtered solution.<br><b>NH<sub>3</sub>:Li:MWNTs</b> 8:10.5:1<br><b>mL:mg:mg</b> 250:317.3:30.3 | Same as in experiment 8.<br>W = 35.9 mg  |
| 9B         | EXNTs-Cp12hs-<br>N*M*L_8_10.5_1-<br>S+R_HCl37_15+120m-<br>TT_30m                |   | W = 26.6 mg (after thermal shock)  |
| 10A        | EXNTs-r2ms-<br>R_6M_HCl_120m-<br>N*M*L_41_38_1-<br>S+R_HCl37_15+120m            | Non-purified MWNTs, synthesized by 30 seconds followed by pause and 90 seconds more (2 min synthesis). Reflux in 150 to 1650 mL of 6 M HCl for 120 min.<br><b>NH<sub>3</sub>:Li:MWNTs</b> 41:37.9:1<br><b>mL:mg:mg</b> 250:231:6.1  | Same as in experiment 8. W = 8.4 mg  |
| 10B        | EXNTs-r2ms-<br>R_6M_HCl_120m-<br>N*M*L_41_38_1-<br>S+R_HCl37_15+120m-<br>TT_30m |   | W = 25.9 mg after thermal shock.   |

**Table A.3.2. Experimental conditions for exfoliation of MWNTs (continued)**, summarized in the code name for each experiment.

| Experiment |  |   |  |
|------------|--|---|--|
| No.        | Code   | Intercalation   | Exfoliation  |
| 11A        | EXNTs-<br>r2ms_6M_H2SO4_120m-<br>N*L*M_5_10_1-<br>S+R_HCl37_120m                                   | Non-purified MWNTs, 2 min synthesis, sonicated in acetone for 6 min and refluxed in 180 mL of 6 M H <sub>2</sub> SO <sub>4</sub> for 120 min.<br>MWNTs were washed with H <sub>2</sub> O until neutral pH, then with 100 mL of 1 M NaOH.<br>MWNTs washed with H <sub>2</sub> O to neutral pH.<br><b>NH<sub>3</sub>:Li:MWNTs</b> 5:10:1<br><b>mL:mg:mg</b> 250:501.2:50  | Not reported. May be the same as in experiment 8. W = 56.3 mg.   |
| 11B        | EXNTs-<br>r2ms_6M_H2SO4_120m-<br>N*L*M_5_10_1-<br>S+R_HCl37_120m-<br>TT_30m                        |   | W = 22.9 mg after thermal shock.   |
| 12         | EXNTs-<4mm-<br>N*L*M_12_10_1-<br>S+R_HCl135+128m   | Sonication of MWNTs < 4 mm length in 25 mL dry THF. MWNTs sonicated in 20 mL of dry THF before addition.<br>Lithium added after condensation of 50 mL of NH <sub>3</sub> . Moderate magnetic stirring (no. 6). Condensation of 210 mL of NH <sub>3</sub> .<br>Addition of MWNTs, followed by 60 mL of dry THF.<br><b>NH<sub>3</sub>:Li:MWNTs</b> 12.1:10:1<br><b>mL:mg:mg</b> 210:173.2:17.3                    | Sonication and reflux for 135 and 128 min each in 100 mL of 5% HCl.<br>W = 39 mg.  |
| 13         | EXNTs-S_THF_5m-<br>N*L*M_10_14_1-<br>S+R_HCl30_120m  | MWNTs sonicated in 20 mL of dry THF (5 min approx.)<br>Addition of Li, followed by MWNTs addition after 30 min of magnetic stirring. THF volume completed to 100 mL (blue color faded away).<br><b>NH<sub>3</sub>:Li:MWNTs</b> 9.8:13.9:1<br><b>mL:mg:mg</b> 200:285:20.5   | Sonication for 120 min and reflux for 60 or 120 mL in 100 mL of 30% HCl.<br>W = 18 mg.   |
| 14         | EXNTs-2ND-E12-<br>S_THF_4m-<br>N*L*M_5_10_1-<br>S+R_HCl30_255+120m-<br>MS+S_1M_NaOH_37.5h<br>s+50m | Non-exfoliated product from experiment 12, sonicated in dry THF for 4 min.<br>Second intercalation reaction, non-exfoliated product from experiment 12.<br>Lithium addition under vigorous magnetic stirring (#8-10). After 5 min MWNTs were added, plus 10 mL of dry THF. Bronze color. Left under soft magnetic stirring (#5).<br><b>NH<sub>3</sub>:Li:MWNTs</b> 5.2:10.2:1<br><b>mL:mg:mg</b> 200:390.6:38.4 | Sonication (255 min) and reflux (120 min) in 100 mL of 30% HCl, followed by dilution with H <sub>2</sub> O and filtration.<br>Resuspended in acetone/ and 100 mL of 1 M NaOH, magnetic stirring for 37.5 hs followed by 50 min sonication.<br>W = 40.5 mg.   |
| 15A        | EXNT-Cp28hs-<br>S_THF_15m-<br>N*L*M*_7_10_1-<br>S_HNO360+1M_NaOH_60m                               | Sonication of purified, 15 min synthesis MWNTs for 28 hs 38 min in HNO <sub>3</sub> :H <sub>2</sub> SO <sub>4</sub> 3:1, 1 mg/mL. Sonication of cut MWNTs in 50 mL of dry THF for 15 min (1 mg/mL).<br>Addition of (1) Li, (2) MWNTs. High-speed vigorous magnetic stirring (no. 10).<br>Bronze phase observed next day.<br><b>NH<sub>3</sub>:Li:MWNTs</b> 6.9:10:1<br><b>mL:mg:mg</b> 350:505.5:50.8           | 60% HNO <sub>3</sub> added, sonication started. Strong decomposition observed, sonication stopped until decomposition ceased. Sonication for 60 min in 60% HNO <sub>3</sub> . Product diluted with H <sub>2</sub> O, filtered, washed and sonicated in acetone and 50 mL 1 M NaOH for 60 min. Filtered and washed with methanol. W = 26.6 mg (it may be assumed that the rest was lost during HNO <sub>3</sub> treatment). |

**Table A.3.2. Experimental conditions for exfoliation of MWNTs (continued),** summarized in the code name for each experiment.

| Experiment |   |   |  |
|------------|---|---|--|
| No.        | Code  | Before Intercalation / Li intercalation   | Exfoliation  |
| 15B        | EXNT-Cp28hs-S_THF_15m-N*L*M*7_10_1-S_HNO360+1M_NaOH_60m-TT_1m | Same as in 15A  | W = 14.2 mg after 1 min sudden thermal treatment at 1000 °C.   |
| 16A        | EXNT-Cp24hs-S_THF_30m-N*L*M_6_10_1-1WK-S_HNO3_60_120m         | <p>Sonication of purified, 15 min synthesis MWNTs for 24 hs in HNO<sub>3</sub>:H<sub>2</sub>SO<sub>4</sub> 3:1 24 hs (2 mg/mL). MWNTs sonicated in 100 mL of dry THF for 30 min before addition.</p> <p>Slow addition of Li. Vigorous magnetic stirring activated. Next, drop-wise addition of MWNTs suspended in 100 mL of dry THF. Deep blue color remains. Addition of 100 mL more of dry THF. Left for 1 week under vigorous magnetic stirring.</p> <p><b>NH<sub>3</sub>:Li:MWNTs</b> 6:10:1<br/><b>mL:mg:mg</b> 300:500:49.8</p> | <p>Addition of 100 mL of 60% HNO<sub>3</sub> under argon. Sonication started after 15 min. Argon flux stopped after 20 min.</p> <p>Sonication for 90 - 120 min in 100 mL of 60% HNO<sub>3</sub>. W = 54.3 mg.</p>  |
| 16B        | EXNT-Cp24hs-S_THF_30m-N*L*M_6_10_1-1WK-S_HNO3_60_120m-TT_1m   |   | W = 15 mg after 1 min sudden thermal treatment at 1000 °C  |
| 17A        | EXNT-2ND-N*L*M_35_20_1-HNO3:H2SO4_3:1-90m                     | <p>Product from experiment 16, sonicated in 20 mL of dry THF for 5 min. Second intercalation reaction. 100 mL dry THF added to reactor.</p> <p><b>NH<sub>3</sub>:Li:MWNTs</b> 35:20:1:1<br/><b>mL:mg:mg</b> 700:402:20</p>  | <p>Slow and paused addition of 100 mL of concentrated HNO<sub>3</sub>:H<sub>2</sub>SO<sub>4</sub> 3:1 previously ice-cooled acid mixture under argon flux; reactor set in a cool water bath. Strong decomposition of HNO<sub>3</sub> when taking reactor out from bath. Reactor put in bath. More HNO<sub>3</sub> decomposition when using acetone for transferring reactor's content. 100 mL of distilled H<sub>2</sub>O added. Decomposition continued upon sonication. Sonication stopped. Color changed from dark-orange to green. Sonication continued. The ex-MWNTs form a sticky slurry. Ex-MWNTs could only be dispersed in CHCl<sub>3</sub>.</p> <p>Sonication for 90 min (total time) in HNO<sub>3</sub>:H<sub>2</sub>SO<sub>4</sub>. Product filtered and washed with methanol, resuspended and left overnight under magnetic stirring in a mixture of methanol, acetone and 100 mL of 1 M NaOH.</p> <p>Product filtered and washed with distilled H<sub>2</sub>O up to neutral pH. W = 20.4 mg.</p> <p>1 min sudden thermal treatment at 1000 °C</p> |
| 17B        | EXNT-2ND-N*L*M_35_20_1-HNO3:H2SO4_3:1-90m-TT_1m               |   |  |
| 18A1       | EXNTs-Cr28hs-N*L*M_9_9_1-S_HCl10_120m                         | <p>Non-purified MWNTs 15 min synthesis. Sonicated for 28 hs in HNO<sub>3</sub>:H<sub>2</sub>SO<sub>4</sub> 3:1 (0.1 mg/mL), and for 90 min in 1 M NaOH.</p> <p>Li was added after NH<sub>3</sub> condensation (500 mL). Volume kept constant for 1 hour by addition of liquid N<sub>2</sub> to condenser. MWNTs added. Magnetic stirring in Dewar.</p> <p><b>NH<sub>3</sub>:Li:MWNTs</b> 9.4:9.4:1<br/><b>mL:mg:mg</b> 500:500.5:53.1</p>   | <p>Sonication for 120 min of part A in 10% HCl. Product divided in 2 parts (A2, A3, ca. 80 mL).</p>  |

**Table A.3.2. Experimental conditions for exfoliation of MWNTs (continued)**, summarized in the code name for each experiment.

| Experiment |  |  |   |
|------------|--|--|---|
| No.        | Code   | Before Intercalation / Li intercalation  | Exfoliation   |
| 18A2       | EXNTs-Cr28hs-<br>N*L*M_9_9_1-<br>S+R_HCl10_120m+110<br>m     |  | Reflux for 110 min (sonication 120 min and reflux 110m in 10% HCl sample 18A2).   |
| 18A3       | EXNTs-Cr28hs-<br>N*L*M_10_10_1-<br>S_HCl10_120m-TT_1m        | Same as in 18A1  | Thermal shock, 1 min at 1000 °C (sonication for 120 min in 10% HCl, followed by 1 min thermal treatment).   |
| 18A4       | EXNT-Cr28hs-<br>N*L*M_9_9_1-<br>S+R_HCl10_120+110m-<br>TT_1m |  | Thermal shock, 1 min at 1000 °C on sample 18A2 (sonication for 120 min, reflux for 110 min, and thermal treatment for 1 min)  |
| 18B1       | EXNT-Cr28hs-<br>N*L*M_9_9_1-<br>R_HCl10_105m                 |  | Reflux for 105 min of part B.   |
| 18B2       | EXNT-Cr28hs-<br>N*L*M_9_9_1-<br>R_HCl10_105m-TT_1m           |  | Product from B1 was thermally shocked for 1 min at 1000 °C.   |
| 18C        | EXNT-Cr28hs-NOTHF-<br>N*L*M_10_10_1-<br>TT_2mx3              |  | Thermal shock, 2 min at 1000 °C, 3 times on the remaining 25% of the reaction product (2 min x 3 because of the remaining lithium oxide, TT_2mx3).<br>After thermal shock, sample 18C was slightly smashed in agata mortar and dispersed in 100 mL of 10% HCl to dissolve remaining oxide.<br>Sonication of the mixture for 15 min, followed by filtration and rinsing with H <sub>2</sub> O until neutral pH was obtained. Product dried with acetone, put into an oven, and left in desiccator. |
| 19A        | BLANK-Cr28hs-<br>N*M_11_1                                    | This experiment is aimed to determine if NH <sub>3</sub> intercalates by itself.<br>Non-purified MWNTs 15 min synthesis sonicated for 29 hs 34 min in HNO <sub>3</sub> :H <sub>2</sub> SO <sub>4</sub> 3:1, (0.1 mg/mL), and for 90 min in 1 M NaOH.<br>Soft magnetic stirring (no. 5). Condensed NH <sub>3</sub> phase remained for 19 hs (ca. 150 mL). | No exfoliation performed. W = 28.9 mg.  |
| 19B        | BLANK-Cr28hs-<br>N*M_11_1-R_HCl_10-<br>90m-TT_1m             |  | 90 min reflux in 10% HCl & 1 min thermal shock at 1000 °C.  |
| 19C        | BLANK-Cr28hs-<br>N*M_11_1-TT_1m                              | <b>NH<sub>3</sub>:Li</b> 11.3:1<br><b>mL:mg:mg</b> 800:70.6  | Only 1 min thermal shock at 1000 °C.<br>W = 27.2 mg   |
| 20A        | N*L*CNR_28_10_1  | Lithium intercalation in carbon nanoribbons.<br>Addition order not specified.  | No procedures performed.  |
| 20B        | N*L*CNR_28_10_1-<br>S_HCl_10_115m                            | <b>NH<sub>3</sub>:Li:CNR</b> 28:10.3:1<br><b>mL:mg:mg</b> 700:257.3:25   | Sonication for 115 min in 10% HCl.  |
| 20C        | N*L*CNR_28_10_1-<br>S+R_HCl_10_115+90m                       |  | Sonication for 115 min in 10% HCl and reflux for 90 min en 10% HCl.   |
| 20D        | NR-CNR*L*N_1_10_28-<br>TT_1m                                 |  | Sudden thermal treatment, 1 min at 1000 °C.   |
| 21         | EXNTs-Cr28hs-<br>N*L*M_6_4_1-<br>R_HCl10_120m-<br>TT_1mx5    | MWNTs and Li gradually added in combination, watching for fading of blue color. Color remains when MWNTs:Li 1:5.<br><b>NH<sub>3</sub>:Li:MWNTs</b> 5.6:4.3:1<br><b>mL:mg:mg</b> 700:537:125.5  | Reflux in 10% HCl for 120 min, filtered and left in acetone. Product filtered and rinsed with H <sub>2</sub> O until neutral pH was obtained. Product dried.<br>Redispersed by sonication (30 min?) in 200 mL of KOH (pH 11 solution) before centrifugation. Product rinsed with H <sub>2</sub> O up to pH = 7 and dried. Sudden thermal treatment, 1 min at 1000 °C, five times.   |

Table A.3.2. Experimental conditions for exfoliation of MWNTs (continued), summarized in the code name for each experiment.

| Experiment |  |  |  |
|------------|--|--|--|
| No.        | Code   | Before Intercalation / Li intercalation  | Exfoliation  |
| 22         | EXNTs-2ND-N*L*M_14_5_1-R_HCl10_90m-TT_1mx5                   | Second intercalation. Fine powdered MWNTs, product from experiment 21. Simultaneous addition and homogenization of MWNTs. Lithium addition after 30 min.<br><b>NH<sub>3</sub>:Li:MWNTs</b> 13.7:5.1:1<br><b>mL:mg:mg</b> 350:129.8:25.5  | Reflux in 10% HCl for 90 min, followed by sudden thermal treatment, 1 minute at 1000 °C, five times.                           |
| 23         | EXNTs-Cr28hs-N*L*M_14_6_1-R_HCl09_107m-TT_1mx5               | Non-purified MWNTs 15 min synthesis, 28 hs sonication in concentrated HNO <sub>3</sub> :H <sub>2</sub> SO <sub>4</sub> 3:1 (0.5 mg/mL). Fine powdered MWNTs in agata mortar. Lithium addition after condensation of 250 mL NH <sub>3</sub> . Homogenization for 17 min. MWNTs addition after full condensation. Homogenization continued for 17 more min.<br><b>NH<sub>3</sub>:Li:MWNTs</b> 14.3:5.6:1<br><b>mL:mg:mg</b> 350:138:24.5 | Reflux in 9.25% HCl for 107 min, followed by sudden thermal treatment, 1 minute at 1000 °C, five times.                        |
| 24A        | EXNTs-Cr28hs-N*L*M_16_12_1-R_HCl10_90m                       | Non-purified MWNTs 15 min synthesis, 28 hs sonication in concentrated HNO <sub>3</sub> :H <sub>2</sub> SO <sub>4</sub> 3:1 (0.5 mg/mL) Addition of: (1) Lithium, (2) MWNTs (after 10 min of soft magnetic stirring).<br><b>NH<sub>3</sub>:Li:MWNTs</b> 15.8:11.7:1<br><b>mL:mg:mg</b> 700:519.5:44.2   | 90 min reflux in 10% HCl.  |
| 24B        | EXNTs-Cr28hs-N*L*M_16_12_1-R_HNO315_90m                      |  | 90 min reflux in 15% HNO <sub>3</sub> . Product filtered, washed and suspended in 1 M KOH.                                     |
| 24C        | EXNTs-Cr28hs-N*L*M_16_12_1-R_1M_NaOH_90m-R_HCl10_90m-TT_1mx5 |  | 90 min reflux in 1 M NaOH. Product centrifuged. 90 min reflux in 10% HCl, then thermal shock, 1 minute at 1000 °C, five times. |
| 25         | CN <sub>x</sub> -Cp51hs-N*L*C_31.7_5_1-R_HCl10_120m-TT_1mx5  | Purified CN <sub>x</sub> 15 min synthesis, sonicated for 50 hs 40 min in HNO <sub>3</sub> :H <sub>2</sub> SO <sub>4</sub> 3:1 (0.11 mg/mL). Li addition followed by 15 min vigorous magnetic stirring. Addition of CN <sub>x</sub> .<br><b>NH<sub>3</sub>:Li:CN<sub>x</sub></b> 31.7:5:1<br><b>mL:mg:mg</b> 700:110.2:22.1   | 120 min reflux in 10% HCl followed by thermal shock 1 min at 1000 °C, five times.  |
| 26         | EXNTs-Cr28hs-N*L*M_33_1_2-R_HCl09_90m-TT_1mx5                | Non-purified MWNTs 15 min synthesis, 28 hs sonication in concentrated HNO <sub>3</sub> :H <sub>2</sub> SO <sub>4</sub> 3:1 (0.5 mg/mL). Fine powdered MWNTs. Addition of 23.4 mg of Li. Blue color faded after 16 min of vigorous magnetic stirring. 18.7 mg of Li added. Blue color did not fade. Addition of MWNTs under argon flux.<br><b>NH<sub>3</sub>:Li:MWNTs</b> 33.2:1.1:2<br><b>mL:mg:mg</b> 700:23.4:42.1                   | Reflux in 10% HCl for 90 min, followed by sudden thermal treatment, 1 min at 1000 °C, five times.                              |
| 27A        | EXNTs-Cr30hs-N*L*M_63_3_5                                    | Non-purified MWNTs 15 min synthesis, 30 hs sonication in concentrated HNO <sub>3</sub> :H <sub>2</sub> SO <sub>4</sub> 3:1<br><b>NH<sub>3</sub>:Li:MWNTs</b> 63.2:3.1:5<br><b>mL:mg:mg</b> 670:32.8:53   | Reaction product (slurry) taken directly from the reactor in capillary tubes, and sealed with vacuum grease.                   |

**Table A.3.2. Experimental conditions for exfoliation of MWNTs (continued)**, summarized in the code name for each experiment.

| Experiment |  |  |  |
|------------|--|--|--|
| No.        | Code   | Before Intercalation / Li intercalation  | Exfoliation  |
| 27B        | EXNTs-Cr30hs-<br>N*L*M_63_3_5-<br>S_HCl_10_90m               | Same as in 27A   | Sonication in 100 mL of 10% HCl for 92 min.  |
| 27C        | EXNTs-Cr30hs-<br>N*L*M_63_3_5-<br>S+R_HCl_10_90m             |  | Sonication & reflux in 100 mL of 10% HCl for 92 and 93 min respectively.                             |
| 27D        | EXNTs-Cr30hs-<br>N*L*M_63_3_5-<br>S+R_HCl_10_90m-<br>TT_1mx5 |  | Sonication & reflux (as stated in 27C) and thermal shock for 1 min, 5 times.                         |
| 28A        | EXNTs-Cr30hs-<br>N*L*M_11_1_1-<br>R_HCl_10_90m               | Non-purified MWNTs 15 min synthesis, 28 hs (13.4 mg) and 30 hs (17.9 mg) sonication in concentrated HNO <sub>3</sub> :H <sub>2</sub> SO <sub>4</sub> 3:1<br><b>NH<sub>3</sub>:Li:MWNTs</b> 11.2:1.2:1<br><b>mL:mg:mg</b> 350:37.8:31.3   | Reflux in 100 mL of 10% HCl for 90 min.  |
| 28B        | EXNTs-Cr30hs-<br>N*L*M_11_1_1-<br>R_HCl_10_90m-<br>TT_1mx5   |  | Reflux in 100 mL of 10% HCl for 90 min, followed by thermal shock 1 min at 1000 °C, 5 times.         |
| 28C        | EXNTs-Cr30hs-<br>N*L*M_11_1_1-<br>R_HCl_10_90m-<br>TT_300m   |  | Reflux in 100 mL of 10% HCl for 90 min, followed by thermal treatment 300 min at 1000 °C, once.      |
| 29         | EXNTs-2ND-<br>N*M*L_20_1_5-<br>R_HCl10_90m-TT_1mx5           | Second intercalation. Product from experiment 21. Fine powdered MWNTs for 15 min in agata mortar (no acetone used). Addition of MWNTs. Homogenization for 14 min 56 sec, then addition of lithium. Ammonia was evaporated as a result of homogenization and soft heating of the external surface of the reactor with acetone, in order to set the desired stoichiometry. Soft magnetic stirring (#5, Barnstead stirring hot plate). Left in a 2 L Dewar flask with insulating PS "fritures" and Al foil, from 15:15.<br><b>NH<sub>3</sub>:Li:MWNTs</b> 19.7:1:5.3<br><b>mL:mg:mg</b> 350:94.7:17.8 | Reflux in 10% HCl for 90 min, followed by sudden thermal treatment, 1 minute at 1000 °C, five times. |
| 22<br>BIS  | EXNTs-2ND-<br>N*M*L_21_10_2-<br>R_HCl10_90m-TT_1mx5          | Second intercalation. Product from experiment 21. MWNTs ground in agata mortar for 15 min. Addition of MWNTs, followed by 30 min homogenization. Addition of Li. Homogenization continued for 18 more min. Vigorous magnetic stirring (no.8) for 5 min, then turned slow (no. 5).<br><b>NH<sub>3</sub>:Li:MWNTs</b> 10.5:4.9:1<br><b>mL:mg:mg</b> 270:125:25.6   | Reflux in 10% HCl for 90 min, followed by sudden thermal treatment, 1 minute at 1000 °C, five times. |

## Legends:

CN<sub>x</sub>-Cp51h – CN<sub>x</sub> nanotubes sonicated in HNO<sub>3</sub>:H<sub>2</sub>SO<sub>4</sub> 3:1 for 51 hours  
S – Sonication  
R – Reflux

#m – Number of minutes

N\*L\*M – Addition order – otherwise stated - of NH<sub>3</sub>:Li:MWNTs (following numbers show stoichiometry mL:mg:mg)

TT\_1mx5 – Thermal shock, 1 minute, 5 times.

Table A.3.3. Exfoliation data for selected experiments.

| Exp. No | Code   | Counted Tubes | % ex-MWNT | % Partially Exfoliated | % Damaged | % Intact |
|---------|--|---------------|-----------|------------------------|-----------|----------|
| 1       | EXNTs-p_S_THF_120m-N*L*M*_8_10_1-R_HCl30_120m  | 73            | 0.0       | 41.1                   | 43.8      | 15.1     |
| 2       | EXNTs-p-S_THF_120m-N*L*M*_8_10.5_1-S_HCl30_120m  | 71            | 0.0       | 38.0                   | 55.0      | 7.0      |
| 3       | EXNTs-p-N*L*M*_7_10_2-S_HCl30_120m   | 110           | 0.0       | 52.7                   | 47.3      | 0.0      |
| 4       | EXNTs-S+R_HNO <sub>3</sub> H <sub>2</sub> SO <sub>4</sub> _120m-N*L*M*_1_5.4_10-S+R_HCl30_120m | 74            | 0.0       | 41.9                   | 17.6      | 40.5     |
| 8       | EXNTs-r4ms-S_HNO <sub>3</sub> _120m-N*L*M*_10_10_1-S+R_HCl37_15+120m                           | 56            | 1.8       | 42.9                   | 41.1      | 14.2     |
| 9       | EXNTs-Cp12hs-N*L*M*_8_10.5_1-S+R_HCl37_15+120m   | 75            | 14.7      | 58.7                   | 20.0      | 6.6      |
| 11      | EXNTs-r2ms_6M_H <sub>2</sub> SO <sub>4</sub> _120m-N*L*M*_5_10_1-S+R_HCl37_120m                | 42            | 2.4       | 45.2                   | 42.9      | 9.5      |
| 12      | EXNTs-<4mm-N*L*M*_12_10_1-S+R_HCl135+128m  | 59            | 0.0       | 3.4                    | 47.5      | 49.1     |
| 13      | EXNTs-S_THF_5m-N*L*M*_10_14_1-S+R_HCl30_120m   | 8             | 0.0       | 25.0                   | 50.0      | 25.0     |
| 14      | EXNTs-2ND-E12-S_THF_4m-N*L*M*_5_10_1-S+R_HCl30_255+120m-MS+S_1M_NaOH_37.5hs+50m                | 19            | 5.3       | 78.9                   | 15.8      | 0.0      |
| 15A     | EXNT-Cp28hs-S_THF_15m-N*L*M*_7_10_1-S_HNO <sub>3</sub> 60+1M_NaOH_60m                          | 59            | 7.0       | 53.0                   | 23.0      | 17.0     |
| 15B     | EXNT-Cp28hs-S_THF_15m-N*L*M*_7_10_1-S_HNO <sub>3</sub> 60+1M_NaOH_60m-TT_1m                    | 49            | 34.7      | 38.8                   | 20.4      | 6.1      |
| 16A     | EXNT-Cp24hs-S_THF_30m-N*L*M*_6_10_1-1WK-S_HNO <sub>3</sub> _60_120m                            | 75            | 6.7       | 40.0                   | 33.3      | 20.0     |
| 16B     | EXNT-Cp24hs-S_THF_30m-N*L*M*_6_10_1-1WK-S_HNO <sub>3</sub> _60_120m-TT_1m                      | 46            | 37.0      | 50.0                   | 10.9      | 2.1      |
| 17A     | EXNT-2ND-N*L*M*_35_20_1-HNO <sub>3</sub> :H <sub>2</sub> SO <sub>4</sub> _3:1-90m              | 153           | 49.0      | 28.1                   | 18.3      | 4.6      |
| 17B     | EXNT-2ND-N*L*M*_35_20_1-HNO <sub>3</sub> :H <sub>2</sub> SO <sub>4</sub> _3:1-90m-TT_1m        | 106           | 45.3      | 28.3                   | 14.1      | 12.3     |
| 18A1    | EXNTs-Cr28hs-N*L*M*_9_9_1-S_HCl10_120m   | 111           | 45.0      | 29.7                   | 17.2      | 8.1      |
| 18A2    | EXNTs-Cr28hs-N*L*M*_9_9_1-S+R_HCl10_120m+110m  | 145           | 46.2      | 24.8                   | 22.8      | 6.2      |
| 18A4    | EXNT-Cr28hs-N*L*M*_9_9_1-S+R_HCl10_120+110m-TT_1m  | 38            | 47.4      | 44.7                   | 2.6       | 5.3      |
| 18C     | EXNT-Cr28hs-NOTHF-N*L*M*_10_10_1-TT_2mx3   | 68            | 41.2      | 35.3                   | 22.0      | 1.5      |
| 21      | EXNTs-Cr28hs-N*L*M*_6_4_1-R_HCl10_120m-TT_1mx5   | 94            | 35.1      | 37.2                   | 24.5      | 3.2      |
| 22      | EXNTs-2ND-N*L*M*_14_5_1-R_HCl10_90m-TT_1mx5  | 51            | 64.7      | 17.6                   | 15.7      | 2.0      |
| 23      | EXNTs-Cr28hs-N*L*M*_14_6_1-R_HCl09_107m-TT_1mx5  | 65            | 58.5      | 15.4                   | 18.5      | 7.6      |
| 26      | EXNTs-Cr28hs-N*L*M*_33_1_2-R_HCl09_90m-TT_1mx5   | 116           | 43.1      | 25.0                   | 19.0      | 12.9     |
| 29      | EXNTs-2ND-N*L*M*_20_1_5-R_HCl10_90m-TT_1mx5  | 80            | 41.2      | 37.5                   | 21.3      | 0        |



## Appendix A.4 Characterization Techniques

### A.4.1 Scanning Electron Microscopy

This is one of the most important, non-destructive characterization techniques commonly used for studying bulk specimens. A modern SEM microscope is composed of three main parts: an electron gun or emitter, which produces an electron beam or probe that will hit the sample; an array of electromagnetic lenses, which keeps electrons in the beam path, focus the beam, and scans the sample; and a chamber in which the sample is placed, as depicted in [figure A.4.1](#).

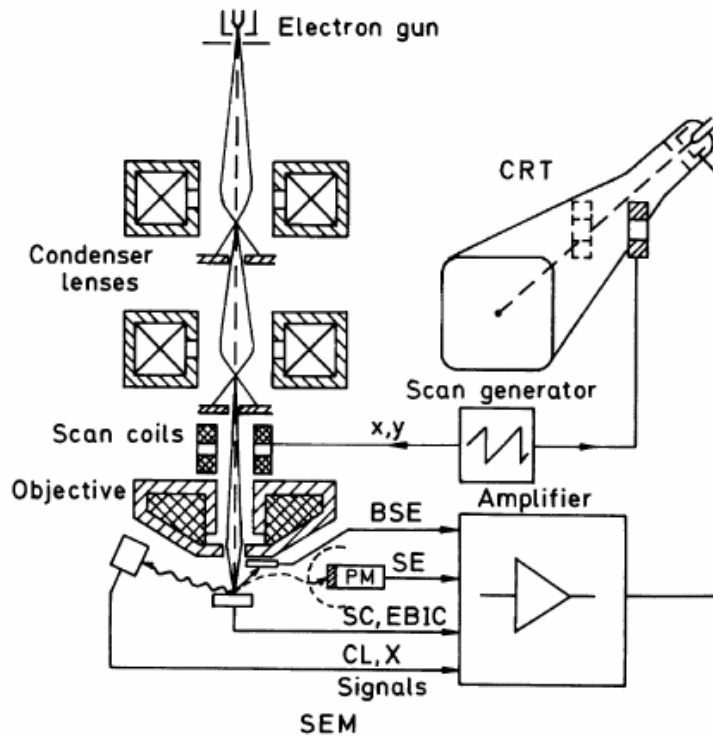


Figure A.4.1. Schematic ray path for a scanning electron microscope (SEM) [1].

The whole system is purged with an inert gas (typically, nitrogen) and then evacuated by means of a rotary pump and a diffusion pump until a “high” vacuum is reached ( $10^{-3}$  Pa). A turbo-molecular pump or turbine fan may replace the diffusion

pump or be used as an additional pump. An ion pump is used to achieve pressures below  $10^{-4}$  Pa. A high vacuum is required in order to operate an emission or electron source. The electron source can be a tungsten filament, a lanthanum hexaboride ( $\text{LaB}_6$ ) or Schottky emitter, or a tungsten field-emission tip. The electron gun in an SEM is small and requires less insulation than that of a TEM, since the maximum accelerating voltage is lower than that of a TEM (30 kV). A field-emission source is often more desirable, since it can give a resolution of 1 nm, which is defined by the diameter of the electron beam or spot size ( $\sim 1$  nm in such case). Next, the electron beam passes through a series of two or three electromagnetic lenses generated by tubular electromagnets. This beam is focused into a small-diameter (2–10 nm) electron probe by means of these electromagnetic lenses, the last being called the objective lens. These primary electrons do not hit the sample simultaneously; instead, the electron probe is scanned horizontally across the specimen by two scan generators in two perpendicular directions sequentially, pretty much in the way that images are formed on a CRT, in a process known as raster scanning. The outputs of both scans are generated digitally, and the x, y coordinates of each pixel are registered in the memory of a computer and stored into a file [1, 2].

When primary electrons hit the bulk sample, some of them are scattered elastically (backscattered electrons or BSE, repelled by electrostatic interaction with atomic nuclei), others deflected inelastically towards the vacuum (secondary electrons or SE, deflected by interaction with atomic electrons), both in angles  $<90^\circ$ . A small fraction of backscattered electrons is deflected in angles  $>90^\circ$  and can be collected as a backscattered-electron (BSE) signal that can show contrast as a result of changes in the chemical composition of a sample. Most SE are absorbed and brought to rest within the interaction volume. Those created at the surface can be released into the vacuum within a range of energies, and be collected and used for elemental analysis of the sample or for image formation. The SE image is thus a property of the topography of the sample. SE images have a three-dimensional appearance, since electrons emitted from surfaces tilted towards the detector have a greater probability of reaching the detector (they are closer), thus forming brighter images. The detector is composed of a scintillator, which emits visible-light photons when it is bombarded by electrons, and a photomultiplier tube, which senses photons and amplifies the signal [2].

Samples should be conducting, otherwise they should be finely coated with gold (done by means of a plasma or sputtering chamber) to avoid charge buildup in the sample and hence electron deflection. Environmental SEM is also possible; in this case while the whole column is under vacuum, the electron beam is allowed to pass through without letting gas molecules (often water vapor) to interact with the SEM column. The beam interacts within a few millimeter range with the sample at ambient pressure. Thin samples may also be used, usually for Scanning Transmission Electron Microscopy (STEM) mode. Other important parameters are the distance between the specimen and the objective lens or working distance, and the astigmatism, which is due to distortions in the electron probe and that can be corrected by electromagnetic fields.

## A.4.2 Transmission Electron Microscopy

Figure A.4.2 depicts a scheme of a TEM microscope. In a transmission electron microscope, a thin specimen is irradiated with an electron beam of uniform current density. The main difference with a SEM is the acceleration voltage, which typically ranges from 100–200 kV. Medium-voltage instruments work at 200–500 kV for better transmission and resolution, and in high-voltage electron microscopy the acceleration voltage reaches 500 kV– 3 MV (a 3-MV class ultrahigh voltage electron microscope is located at Osaka University, Japan).

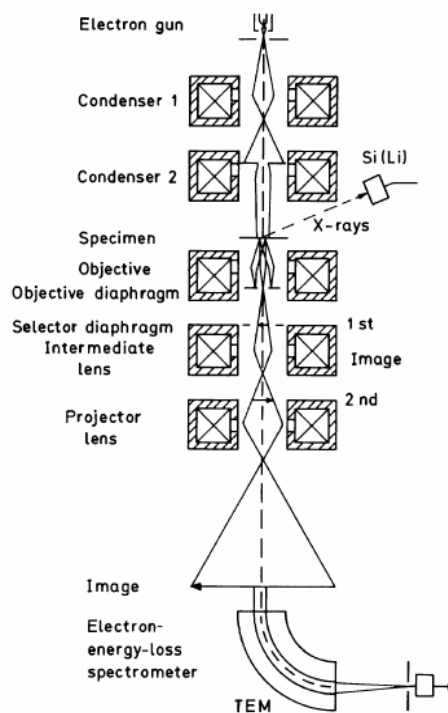


**Figure A.4.2. Schematic ray path for a transmission electron microscope (TEM) equipped for additional x-ray and electron energy-loss spectroscopy [1].**

Moreover, the specimen should be thin (5–100 nm for 100 keV, but it changes according to specimen composition and desired resolution) to allow electrons to cross it.

Since aberrations of the objective lens are huge, very small objective apertures are needed to achieve a resolution of the order of 0.1–0.3 nm. The image can be recorded by direct exposure of a photographic emulsion or an image plate inside the vacuum, or digitally via a fluorescent screen coupled to a CCD camera. High-resolution micrographs can be obtained, but care should be taken when handling organic samples since they can be altered or destroyed by electron irradiation [1]. Moreover, electron diffraction is a valuable tool and its combination with the various imaging modes makes it one of the most powerful features of TEM for research on crystal lattices and defects in a material. Other useful analytical tools are X-ray microanalysis, and electron energy-loss spectroscopy, which relies on the inelastic scattering of electrons that produce inner-shell ionizations that are collected by the spectrometer. Furthermore, high-voltage microscopes (>500 kV), despite the space required by the column (10–15 m height), are useful for studying ceramics and minerals that are difficult to prepare in thin layers. The increased space also makes it easier to install special stages or goniometers (sample holders) for heating, cooling, or stretching. Environmental TEM is also possible.

### **A.4.3 Atomic Force Microscopy**

Atomic force microscopy [2, 3] is a type of scanning-probe microscope inspired in the scanning-tunneling microscope. The first AFM equipment was built in 1986, but it gained interest from the scientific community at the 1990s, in which the instrument was refined to achieve near-atomic resolution. AFM works by scanning with a tip or probe very close to the sample surface, through which it senses and measures the attractive or repulsive forces between the tip and the sample. Initially, the z-motion of the cantilever was detected by using an STM tip above it; modern AFM instruments measure the cantilever z-motion by observing the angular deflection of a reflected laser beam while the specimen is scanned in the x- and y- directions, as schematized in [figure A.4.3](#).

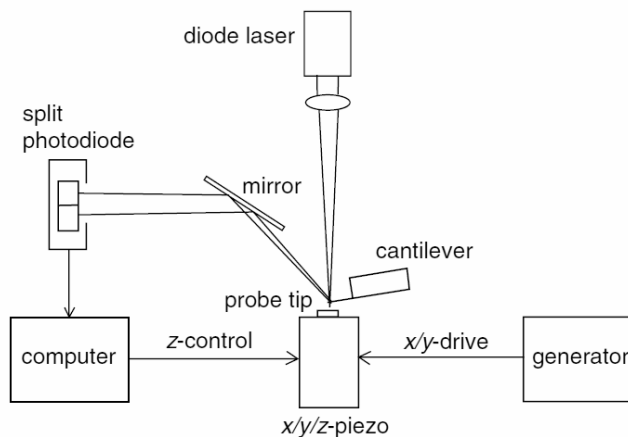


**Figure A.4.3. Block diagram of a laser deflection contact AFM [3].**

AFM cantilevers are made in large quantities from silicon nitride by photolithography. AFM images should be critically evaluated to discern and avoid artifacts such as multiple-tip effects and 'sweeping' generated by dragging of the tip. The main operating modes of AFM make use of repulsive and attractive mechanical forces, which occur if the tip is in direct contact with the sample or at a small distance above, respectively. The primary operation modes are called static or contact mode, and dynamic, intermittent contact, or tapping mode. In the contact mode, the force between the tip and the surface is kept constant during scanning by maintaining a constant deflection. In the dynamic mode, the cantilever is externally oscillated at or close to its fundamental resonance frequency or harmonic. The resonance frequency, oscillation amplitude, and phase change when the tip interacts with the specimen, thus giving information about its features.

Though atomic resolution is difficult to achieve in AFM (in contrast to STM) and the scanning speed is low, which makes it inappropriate for large areas, the advantage of AFM is that it does not require a conducting sample. The AFM can work in aqueous media, making it suitable for biological specimens. By using a special tip, it is also possible to map the magnetic field of data-storage media materials. The use of a photodetector enables torsional motion sensing of the AFM cantilever and thus imaging of the local coefficient of friction. Moreover, AFM offers true three-dimensional effect equivalent to viewing the specimen surface at an oblique angle rather than perpendicularly to the surface, which provides a surface profile.

## A.4.4 Raman Spectroscopy

The Raman effect [4, 5] is a phonon-scattering phenomenon discovered by Chandrasekhara Venkata Raman (1888–1970, Nobel laureate in physics) in 1928. Raman scattering is an inelastic two-photon process due to the polarizability of a molecule, that is, the ability of an applied electric field to induce a dipole moment in a molecule and to distort the electron cloud. Polarizability in molecules depends on the molecular symmetry, which defines the allowed molecular vibrational modes. The energy of the scattered radiation may be equal to that of the incident light, which is called Rayleigh scattering, or different, as in the Stokes and anti-Stokes lines. These lines are shown at figure A.4.4.

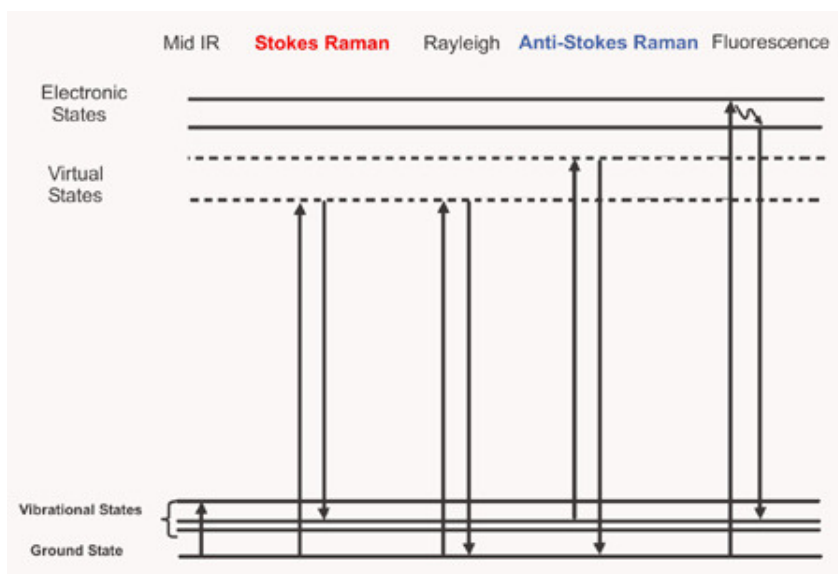


Figure A.4.4. Jablonski energy diagram for Raman scattering [5].

In the Stokes line, the energy of the scattered radiation is less than that of the incident radiation, and the opposite occurs for the anti-Stokes line. The wavenumber of the Stokes and anti-Stokes lines are a direct measure of the vibrational energies of the molecule. In Raman spectroscopy, only the more intense Stokes line is measured. The energy loss in the Stokes line is characteristic of particular bonds, and hence can be used as a spectral fingerprint. In addition, Raman spectroscopy is not limited to organic molecules, since it has proved to be useful for elements and inorganic compounds such

as silicon [6], iron carbides [7], and carbon nanotubes [8]. The experimental setup is shown at figure A.4.5.

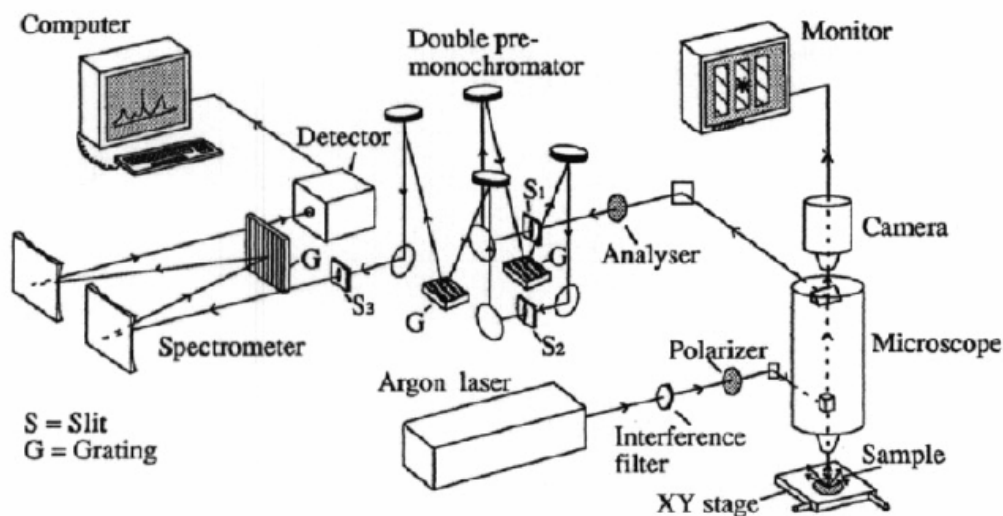


Figure A.4.5. Experimental setup of a micro-Raman spectrometer [6].

A high-energy, monochromatic light source is required (a laser beam) to determine the energy (wavenumber) difference between the excitation and the Stokes lines, since the Raman scattering is not a very efficient process. In micro-Raman spectroscopy the light is focused on the specimen through a confocal microscope. The microscope allows different surface areas to be analyzed, from  $\sim 1 \mu\text{m}$  to a few  $\mu\text{m}$  (100x–10x objective). The scattered light is collected by back-scattering through the microscope, addressed towards a double pre-monochromator, and directed to the spectrometer. Since about one photon in  $10^{12}$  is inelastically scattered, very sensitive detectors are required, and a double monochromator is used to reject the Rayleigh-scattered light. Both the pre-monochromator and the spectrometer contain computer-controlled spherical mirrors, gratings and slits that define the resolution and the intensity of the signal. At the exit of the spectrometer, a photomultiplier, multichannel detector or CCD detector is mounted.

Raman spectroscopy is complementary to infrared spectroscopy. Nonetheless, it offers some advantages as: no interference from water absorption, the sample requires little or no preparation, and is not affected by materials such as glass. Moreover, the use of a microscope (micro-Raman mode) provides a very high level of spatial resolution and depth discrimination, often unavailable in infrared methods.

## A.4.5 Thermogravimetric Analysis

Thermogravimetric analysis (TGA) [9] is a method for determination of mass changes of a specimen under a heating procedure. The mass changes may be ascribed to functional groups, or to intrinsic properties of the specimen. A thermobalance is used for measuring changes of the order of 1  $\mu\text{m}$ , and it consists in a combination of an electronic microbalance, a furnace, a temperature programmer, and a computer that allows full control and register of heating and cooling rates, gases, mass, time, and temperature. The microbalance should be enclosed in order to maintain a reproducible atmosphere at its surroundings. Figure A.4.6 schematizes a TGA system.

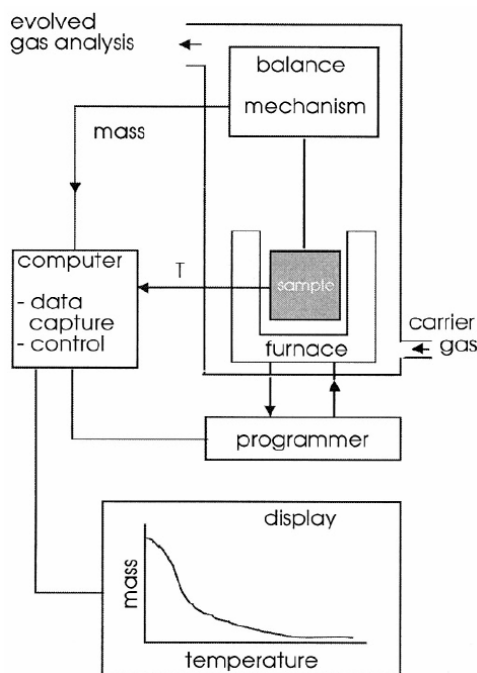
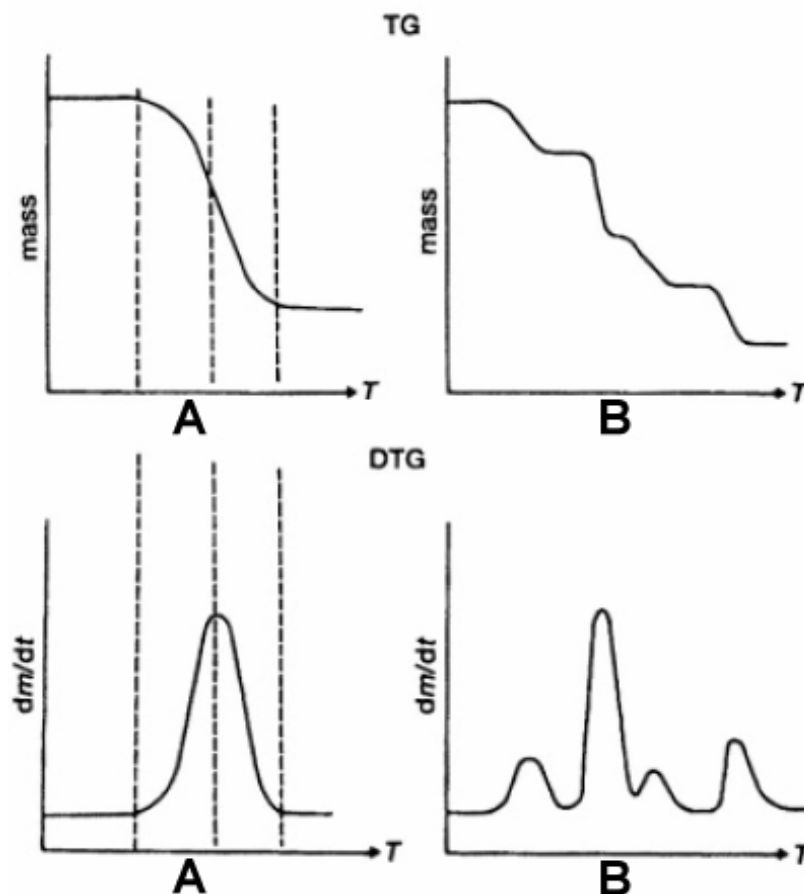


Figure A.4.6. Schematic of a thermobalance [9].

There are three important parameters in thermogravimetric analysis: the temperature where sample oxidation or decomposition starts ( $T_{\text{ONSET}}$ ), the temperature with the fastest decomposition rate ( $T_0$ ), and the residual mass ( $M_R$ ). In addition, what is obtained at the computer is an output of mass loss percent of the original sample mass. Sometimes it is more adequate to use the first derivative of mass loss as a function of temperature (derivative thermogravimetry or DTG), since it allows easy identification of

the  $T_0$ . DTG curves can be compared with other derivative measurements such as DTA, DSC, or EGA. From TGA curves several changes can be observed: desorption of gases, single- or multi-step decomposition, and mass gain or loss due to reaction of the sample with the surrounding atmosphere. In addition, DTG curves allow better resolution of the individual stages of complex TGA curves. Examples of TGA and DTG curves for single- and multi-step decompositions are shown at [figure A.4.7](#).



**Figure A.4.7. Comparison of TGA and DTG curves. (A)** Single-step decomposition, the dotted lines represent (from left to right) the temperature in which decomposition begins ( $T_{\text{ONSET}}$ ), the temperature of maximum decomposition rate ( $T_0$ ), and the temperature which marks the end of decomposition. **(B)** Multi-step decomposition, the derivative mass loss clearly shows  $T_0$  for each decomposition step [9].

## A.4.6 X-Ray Powder Diffraction

The diffraction phenomenon [10] of X-rays was first observed by the German physicist Max Theodor Felix von Laue (1879-1960, 1914 Nobel Prize in physics) on copper sulfate crystals, and followed by the English physicist, W. L. Bragg (1890–1971, 1915 Nobel Prize in physics) who solved the crystal structures of NaCl, KCl, KBr, and KI, and who formulated the Bragg's law:

$$n\lambda = 2d' \cdot \sin\theta \quad \text{A.4.1}$$

This relation states the fundamental condition which must be met in order for diffraction to occur. A beam of certain wavelength (figure A.4.8) strikes all atoms in an angle  $\theta$  with respect to the plane of the crystal; the beam is strongly scattered (diffracted) at the same angle  $\theta$ . The order of diffraction  $n$ , is equal to the number of wavelengths in the path difference between rays scattered by adjacent planes;  $d'$  is the interlayer distance between adjacent planes. For fixed values of  $\lambda$  and  $d'$ , there may be several angles of incidence (which satisfy Bragg's law) at which diffraction may occur. The rays scattered by all the atoms in all the planes are completely in phase and reinforce one another (constructive interference) and form a diffracted beam in the direction shown. In all other directions, the scattered beams are out of phase and cancel each other (destructive interference). The intensity of the diffracted beam is extremely weak in comparison to that of the incident beam, due to the small fraction of incident energy being scattered by atoms.

Moreover, the angle between the diffracted beam and the transmitted beam (the diffraction angle) is always  $2\theta$ , and is usually measured experimentally. For diffraction to occur, the wavelength of the incident beam should be of the same order of magnitude as the repeat distance between scattering centers. From Bragg's law, it follows that  $\lambda < 2d'$ .

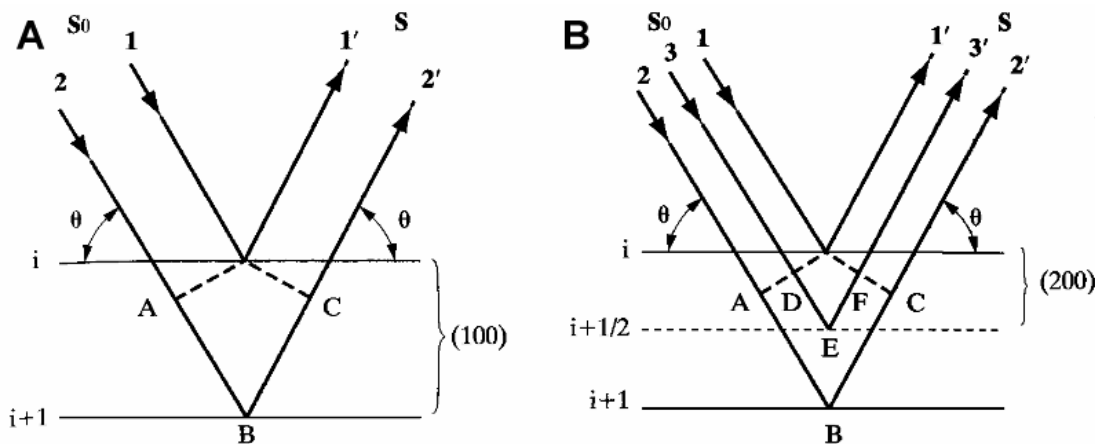


**Figure A.4.8. X-ray diffraction by a crystal.** Equivalence of (A) a second-order 100 reflection, and (B) a first-order 200 reflection. The incident and diffracted beam directions are  $S_0$  and  $S$ , respectively, and the  $i$ th,  $(i+1/2)$ th and  $(i+1)$ th planes are labeled. Note that the angle with the plane  $i$  for both  $S_0$  and  $S$  is the same [10].

Bragg's law is often written as  $\lambda = 2d \cdot \sin\theta$  with  $d = d'/n$ , since a reflection of any order can be considered as a first-order reflection from planes spaced at a distance  $1/n$  of the previous spacing. Experimentally, Bragg's law can be used in two ways: X-ray spectroscopy, in which a crystal with planes of known spacing  $d$  can be used to measure  $\theta$  and thus to determine the wavelength  $\lambda$  of the radiation used; or in structure analysis, in which X-rays of known wavelength let us to measure  $\theta$  and thus the spacing  $d$  of various planes in a crystal.

There are three main diffraction methods in which either  $\lambda$  or  $\theta$  are continuously varied during the experiment: the Laue method, the rotating-crystal method, and the powder method. In the Laue method, the continuous spectrum of an X-ray tube hits a fixed single crystal. The Bragg angle  $\theta$  is fixed for every set of planes in the crystal, and each set selects and diffracts that particular wavelength which satisfies Bragg's law for the particular values of  $d$  and  $\theta$  involved. Hence, each diffracted beam has a different wavelength. There are two variations of the method: the transmission Laue method, in which the crystal is placed between the X-ray source and a photographic film; and the back-reflection Laue method, in which the film is placed between the source and the sample. In any case, curved arrays of spots are obtained on the film. The spots are reflections from planes belonging to a certain zone, and are located on imaginary cones. The Laue methods are used for determination of crystal orientation and for quality

assessment on crystals. In the rotating crystal method, a single crystal is mounted with one of its axes or crystallographic directions normal to a monochromatic X-ray beam. A cylindrical film is placed around it, and the crystal is rotated about the chosen direction; the axis of the film coinciding with the rotational axis of the crystal. As the crystal rotates, a particular set of lattice planes will, for an instant, make the correct Bragg angle for diffraction of the monochromatic incident beam, and at that instant a diffracted beam will be formed. The spots lie on imaginary “horizontal” layer lines, since the axes of the diffraction cones coincide with the rotation axis. This method is primarily used for analyzing diffraction patterns in polymers.

In the powder method, the crystal to be examined consists of a very fine powder or is in the form of loss or consolidated microscopic grains, placed in a beam of monochromatic X-rays. Each particle powder is or contains crystals randomly oriented with respect to the incident beam. Each crystal will diffract the beam in a specific orientation, that is, in a crystallographic plane. If we rotate the crystal while keeping  $\theta$  constant, the diffracted beam will form a diffraction cone, as depicted in [figure A.4.9](#).

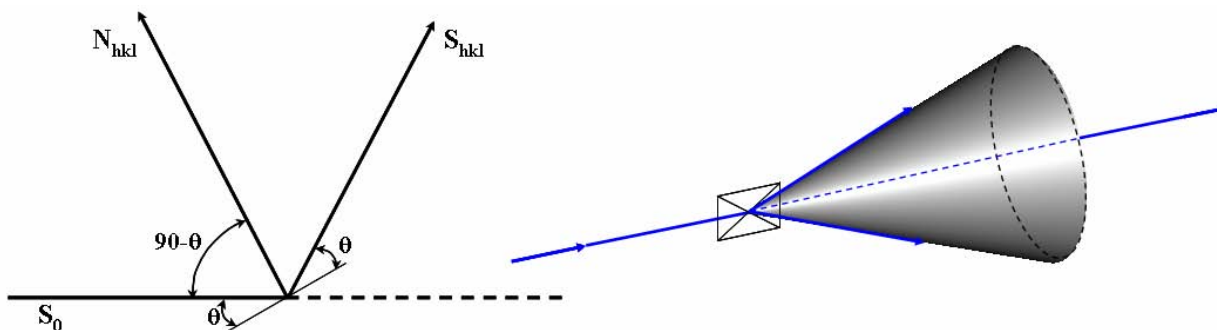


**Figure A.4.9. Formation of a diffracted cone of radiation in the powder method.**  $N_{hkl}$  is the normal to the sample;  $S_0$  and  $S_{hkl}$ , the incident and diffracted beams, respectively. The angle  $\theta$  lies between the plane and each beam ( $S_0$  and  $S_{hkl}$ ). For practical reasons, a diffractometer measures an angle twice that of the  $\theta$  angle [10].

Real powder samples are not rotated, since there are a great number of crystals in different positions and the mass powder is then equivalent to a single crystal rotated about all possible axes. Hence, the  $hkl$  reflection from a motionless powder specimen also forms a diffraction cone, and a separate cone is generated for each set of differently spaced lattice planes.

An X-ray spectrometer, shown at [figure A.4.10](#), is composed of the next basic features: an emission tube, a target crystal sample which may be set at any angle to the incident beam by rotation and placed at the center of the spectrometer, and a detector which measures the intensity of the diffracted X-rays and that can also be rotated about the center at any angular position. Usually, the crystal is cut or cleaved in a way that certain planes of known spacing are parallel to its surface.

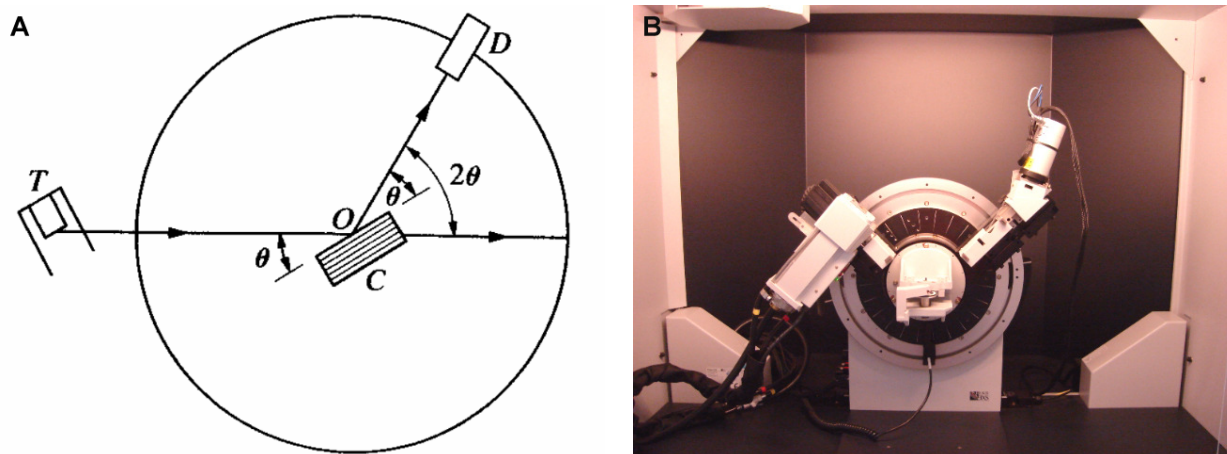


**Figure A.4.10. An X-ray spectrometer [10]. (A)** Schematics. **(B)** A modern Bruker D8 Advance X-ray equipment used for powder diffraction at IPICyT, showing the emission tube at left and the detector at right; in this case, the sample (center) remains fixed, while the X-ray source and the detector rotate around the sample.

X-rays are generated at the emission tube (T) as follows [11, 12]. Photoelectrons are emitted by heating a metal filament. These photoelectrons are accelerated towards a target, usually copper, by applying a voltage between the filament and the copper target (located at the tube). Photoelectrons hit and displace inner-shell electrons from copper atoms, then electrons from upper energy levels fill those vacancies and emit X-rays of specific wavelengths characteristic for copper. X-rays are collimated and directed towards the specimen. Since the sample and the detector are rotated (or the emission tube and the detector are rotated about the sample, which remains fixed), the intensity of the reflected X-rays is recorded. Every time the Bragg equation is satisfied by the geometry of the incoming X-rays on the sample, constructive interference occurs, which produces a peak in intensity. This signal is detected, converted to a count rate and directed to a computer.

The powder method [10] is widely used in the study of materials, and is the only method that can be employed when a single-crystal specimen is not available. The method is specially suited for determining lattice parameters with high precision and for the identification of single or mixed phases in a wide variety of products and materials.

## References

- [1] L. Reimer, H. Kohl. *Transmission Electron Microscopy - Physics of Image Formation*. W. T. Rhodes. Springer series in optical sciences. Springer: Münster, Germany, 2008.
- [2] R. F. Egerton. *Physical principles of electron microscopy - An introduction to TEM, SEM, and AEM*. Springer: Edmonton, Alberta, Canada, 2007.
- [3] G. Kaupp. *Atomic force microscopy, scanning nearfield optical microscopy and nanoscratching - Application to rough and natural surfaces*. P. Avouris, B. Bhushan, K. v. Klitzing, H. Sakaki and R. Wiesendanger. Springer Series on Nanoscience and Technology. Springer: Berlin, Germany, 2006.
- [4] Raman Spectroscopy. L. G. Anderson. Last access on: March 24, 2010. From: <http://carbon.cudenver.edu/public/chemistry/classes/chem4538/raman.htm>.
- [5] Raman tutorial. HORIBA Scientific. Last access on: March 24, 2010. From: <http://www.horiba.com/us/en/scientific/products/raman-spectroscopy/tutorial-faqs/raman-tutorial/>.
- [6] I. De Wolf. Micro-Raman spectroscopy to study local mechanical stress in silicon integrated circuits. *Semicond. Sci. Technol.* **11** (1996) 139-154.
- [7] E. Park, J. Zhang, S. Thomson, O. Ostrovski, R. Howe. Characterization of phases formed in the iron carbide process by X-ray diffraction, Mossbauer, X-ray photoelectron spectroscopy, and Raman spectroscopy analyses. *Metall. Mater. Trans. B* **32B** (2001) 839-845.
- [8] M. S. Dresselhaus, G. Dresselhaus, R. Saito, A. Jorio. Raman spectroscopy of carbon nanotubes. *Phys. Rep.* **409** (2005) 47-99.
- [9] M. E. Brown. *Introduction to thermal analysis - Techniques and applications*. J. Simon. Hot topics in thermal analysis and calorimetry. Kluwer Academic Publishers: USA, 2004.
- [10] B. D. Cullity, S. R. Stock. *Elements of X-ray diffraction*. Prentice-Hall: Upper Saddle River, New Jersey, USA, 2001.
- [11] X-Ray Generation. The University of Oklahoma Chemical Crystallography Lab. Last access on: March 25, 2010. From: <http://xrayweb.chem.ou.edu/notes/xray.html>.
- [12] X-ray Powder Diffraction (XRD). B. L. Dutrow, C. M. Clark. Science Education Resource Center at Carleton College. Geochemical instrumentation and analysis. Last access on: March 25, 2010. From: [http://serc.carleton.edu/research\\_education/geochemsheets/techniques/XRD.html](http://serc.carleton.edu/research_education/geochemsheets/techniques/XRD.html).



# Ex-MWNTs: Graphene Sheets and Ribbons Produced by Lithium Intercalation and Exfoliation of Carbon Nanotubes

Abraham G. Cano-Márquez,<sup>†</sup> Fernando J. Rodríguez-Macías,<sup>†</sup>  
Jessica Campos-Delgado,<sup>†</sup> Claudia G. Espinosa-González,<sup>†</sup>  
Ferdinando Tristán-López,<sup>†</sup> Daniel Ramírez-González,<sup>†</sup> David A. Cullen,<sup>‡</sup>  
David J. Smith,<sup>‡</sup> Mauricio Terrones,<sup>†</sup> and Yadira I. Vega-Cantú<sup>\*†</sup>

*Advanced Materials Department and Laboratory for Nanoscience and Nanotechnology Research (LINAN), IPICYT, Camino a la Presa San José 2055, Col. Lomas 4a, San Luis Potosí, SLP, 78216, México, and Department of Physics and School of Materials, Arizona State University, Tempe, Arizona, 85287-1704*

Received November 25, 2008; Revised Manuscript Received February 16, 2009

## ABSTRACT

We found that multiwalled carbon nanotubes (MWNTs) can be opened longitudinally by intercalation of lithium and ammonia followed by exfoliation. Intercalation of open-ended tubes and exfoliation with acid treatment and abrupt heating provided the best results. The resulting material consists of: (i) multilayered flat graphitic structures (nanoribbons), (ii) partially open MWNTs, and (iii) graphene flakes. We called the completely unwrapped nanotubes ex-MWNTs, and their large number of edge atoms makes them attractive for many applications.

Carbon nanotubes are usually described as rolled graphene sheets; however, the generation of graphene by unrolling carbon nanotubes has yet to be explored in detail. In this Letter we report an efficient method in which open-ended multiwalled carbon nanotubes (MWNTs) are intercalated with ionic Li in liquid NH<sub>3</sub> thus unfolding concentric tubules into exfoliated graphitic ribbons and stacked sheets (ex-MWNTs). These unwrapped tubes exhibit a large number of exposed edges that could be functionalized and are susceptible of further chemical modification, thus making this material attractive for different applications. Ex-MWNTs could also be easily functionalized and dispersed, using methods developed for carbon nanotubes (CNTs),<sup>1-3</sup> facilitating potential applications.

Single-walled carbon nanotubes (SWNTs) dispersed in liquid NH<sub>3</sub> with Li form “nanotube salts”,<sup>4</sup> in which SWNTs absorb electrons released by Li, and then react with alkyl or aryl halides.<sup>5</sup> This Birch reduction method has also been applied to functionalize MWNTs<sup>6</sup> and as

an approach for in situ polymerization reactions to produce SWNT composites.<sup>7</sup>

While using the nanotube salts method to produce MWNT composites by in situ polymerization of aniline, acrylates, and other monomers, we found by transmission electron microscopy (TEM; Figure 1) several damaged nanotubes and some appearing partially unwrapped and exfoliated. We considered that this effect was a consequence of Li intercalation between the concentric graphene cylinders followed by exfoliation (unwrapping) of the MWNTs. This exfoliation would have taken place when the material was treated with a 10% (v/v) HCl solution, used to remove residual Li in the final step of the nanotube salts method described above. These initial results motivated us to study this phenomenon in more detail, as described below.

Intercalation of alkali metals and other chemical species in graphite has been known since the 19th century.<sup>8</sup> The reaction of MWNTs with Li at high pressures and temperatures has been reported to produce Li<sub>2</sub>C intercalation compounds, or lithium carbide, depending on conditions.<sup>9</sup> Electrochemical intercalation of Li in MWNT has been reported to be reversible, causing little damage to the nanotubes.<sup>10</sup> Other studies have found that, for MWNT produced by chemical vapor deposition (CVD) of acety-

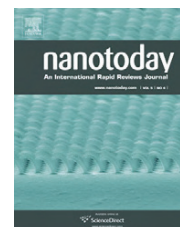
\* Corresponding author: e-mail, yivega@ipicyt.edu.mx; fax, (+) 52 444 834-2010; telephone, (+) 52 444 834-2000 ext 7236.

<sup>†</sup> Advanced Materials Department and Laboratory for Nanoscience and Nanotechnology Research (LINAN), IPICYT.

<sup>‡</sup> Department of Physics and School of Materials, Arizona State University.



ELSEVIER

available at [www.sciencedirect.com](http://www.sciencedirect.com)journal homepage: [www.elsevier.com/locate/nanotoday](http://www.elsevier.com/locate/nanotoday)

## REVIEW

# Graphene and graphite nanoribbons: Morphology, properties, synthesis, defects and applications

**Mauricio Terrones<sup>a,\*</sup>, Andrés R. Botello-Méndez<sup>b</sup>, Jessica Campos-Delgado<sup>c</sup>, Florentino López-Urías<sup>d</sup>, Yadira I. Vega-Cantú<sup>d</sup>, Fernando J. Rodríguez-Macías<sup>d</sup>, Ana Laura Elías<sup>e</sup>, Emilio Muñoz-Sandoval<sup>d</sup>, Abraham G. Cano-Márquez<sup>d</sup>, Jean-Christophe Charlier<sup>b</sup>, Humberto Terrones<sup>b</sup>**

<sup>a</sup> Department of Materials Science and Engineering & Chemical Engineering, Polytechnic School, Carlos III University of Madrid, Avenida Universidad 30, Edificio Betancourt, 28911 Leganés, Madrid, Spain

<sup>b</sup> Institute of Condensed Matter and Nanosciences (IMCN), Université Catholique de Louvain, Place Croix du Sud 1, B-1348 Louvain-la-Neuve, Belgium

<sup>c</sup> Divisão de Metrologia de Materiais, Instituto Nacional de Metrologia, Normalização e Qualidade Industrial (INMETRO), Duque de Caxias, RJ 25250-020, Brazil

<sup>d</sup> Advanced Materials Department, IPICYT, Camino a la Presa San José 2055, Col. Lomas 4a sección, 78216, San Luis Potosí, SLP, Mexico

<sup>e</sup> Department of Mechanical Engineering and Materials Science, Rice University, Houston, TX 77005, USA

Received 16 May 2010; received in revised form 26 June 2010; accepted 28 June 2010

Available online 2 August 2010

## KEYWORDS

Graphene;  
Nanoribbons;  
Nanotubes;  
Synthesis;  
Properties;  
Applications

**Summary** Carbon is a unique and very versatile element which is capable of forming different architectures at the nanoscale. Over the last 20 years, new members of the carbon nanostructure family arose, and more are coming. This review provides a brief overview on carbon nanostructures ranging from C<sub>60</sub> to graphene, passing through carbon nanotubes. It provides the reader with important definitions in carbon nanoscience and concentrates on novel one- and two-dimensional layered carbon (sp<sup>2</sup> hybridized), including graphene and nanoribbons. This account presents the latest advances in their synthesis and characterization, and discusses new perspectives of tailoring their electronic, chemical, mechanical and magnetic properties based on defect control engineering. It is foreseen that some of the structures discussed in the review will have important applications in areas related to electronics, spintronics, composites, medicine and many others.

© 2010 Elsevier Ltd. All rights reserved.

\* Corresponding author. Tel.: +34 91 624 9447; fax: +34 91 624 9430.  
E-mail address: [mttornes@gmail.com](mailto:mttornes@gmail.com) (M. Terrones).